

Reactivity of Metal Oxyhydroxides for Organic Tandem Conversions

Thesis Submitted to AcSIR for the Award of the
Degree of
DOCTOR OF PHILOSOPHY
In
Chemical Science



By
Dnyanesh Vernekar
Registration Number: **10CC15J26008**

Under the guidance of
Dr. Chandrashekhar V. Rode
&
Co-guidance of
Dr. Dinesh Jagadeesan

Chemical Engineering & Process Development Division,
CSIR-National Chemical Laboratory,
Pune - 411008, INDIA

CERTIFICATE

This is to certify that the work incorporated in this Ph.D. thesis entitled “**Reactivity of Metal Oxyhydroxides for Organic Tandem Conversions**” submitted by **Mr. Dnyanesh Vernekar** to Academy of Scientific and Innovative Research (AcSIR) in fulfilment of the requirements for the award of the Degree of **Doctor of Philosophy**, embodies original research work under our supervision. We further certify that this work has not been submitted to any other University or Institution in part or full for the award of any degree or diploma. Research material obtained from other sources has been duly acknowledged in the thesis. Any text, illustration, table etc, used in the thesis from other sources, have been duly cited and acknowledged. It is also certified that this work done by the student, under our supervision, is plagiarism free.



Dr. Chandrashekhar V. Rode
(Supervisor)

Date: 28-04-2020



Dr. Dinesh Jagadeesan
(Co-Supervisor)



Mr. Dnyanesh Vernekar
(Student)

DECLARATION

I hereby declare that the thesis entitled “**Reactivity of Metal Oxyhydroxides for Organic Tandem Conversions**” submitted to Academy of Scientific and Innovative Research (AcSIR) for the award of degree of **Doctor of Philosophy (Ph. D.)** in chemical science is the outcome of experimental investigations carried out by me under the supervision of **Dr. Chandrashekhar V. Rode**, Chief Scientist, Chemical Engineering and Process Development Division, CSIR–National Chemical Laboratory, Pune and Co-supervision of **Dr. Dinesh Jagadeesan**, Assistant Professor, Indian Institute of Technology – Palakkad. I affirm that the work incorporated is original and has not been submitted to any other academy, university or institute for the award of any degree or diploma.

April-2020

Pune



Dnyanesh Vernekar

(Research Student)

CE & PD Division,

CSIR-National Chemical Laboratory,

Dr. Homi Bhabha Road, Pune – 411 008,

INDIA.

Acknowledgement

On the occasion of thesis completion, I take this opportunity beyond the formality, to express my kind gratitude for all those who have contributed in many ways for this success story and made it an indelible experience for me.

*An important league of extra-ordinary gentlemen, who deserve a special mention, and my deep sense of gratitude are my guides. I take the opportunity to acknowledge with pleasure, the guidance, encouragement and unstinted support extended to me by my respected guide, **Dr.Chandrashekhar V. Rode**. Emeritus Scientist, CSIR-National Chemical Laboratory, without whose support and constant guidance, this work would not have seen the light of the day.*

*I also take this opportunity to deeply thank my co-guide **Dr. Dinesh Jagadeesan**, Assistant Professor, IIT-Palakkad, who was the first person to expose me to scientific research and provided me with excellent training, in the formative years of my research career. I would not have been able to finish my PhD without his constant guidance through digital platforms like skype and email till the very end. I would like to thank both guides for the motivation and vast treasures of knowledge that bestowed unto me, apart from the incessant encouragement and prodding during my studies.*

I would like to express my sincere thanks to chairs CEPD, CSIR-NCL, during my PhD tenure. I also wish to express deep sense of gratitude to, Dr. Sourav Pal, Dr. Vijayamohan Pillai, former Directors and Dr. Ashwini Kumar Nangia, current Director CSIR-NCL for allowing me to carry out research and extending all possible infrastructural facilities and permitting me to present this work in the form of a Ph.D. thesis.

I would also like to thank the Doctoral Advisory Committee (DAC) chairman, Dr. Shubhangi Umbarkar and members, Dr. Prakash Wadgaonkar, Dr. C. P. Vinod for the evaluation of my work and for giving valuable suggestions to improve the research. I specially thank my external examiner, Prof. Sulabha Kulkarni (Centre for Materials for Electronics Technology, Pune (C-MET)) for assessment of my work and for valuable discussions and suggestions during my research work. I am also thankful to Dr. C. Gopinath (CSIR-NCL), Dr R. Sai Sathish (Sri Satya Sai Institute of Higher Learning, Dr. Chandra Sekhar Rout (Jain University), Dr Ali Haider (IIT-Delhi), Prof. Masayuki Shirai (Iwate University, Japan) for their valuable help and collaborations. I am also thankful to Dr. Shafeek Mulla and Dr. Sanjay Kamble (CSIR-NCL Pune) for allowing me to use lab space and consumables whenever needed.

I am thankful to CEPD office staff Mr. Hasso Raheja, Mr. Patane and others for their constant cooperation. I thank current and former chairs of Student Academic Office (SAO). I am also grateful to all SAO staff and others for timely documents evaluation and their cooperation. I specially thank AcSIR coordinators, Dr. Chetan Gadgil and Dr. Mahesh Kulkarni for their cooperative evaluation of AcSIR documents.

Special thanks to my colleagues Dr. Garima Jaiswal, Sharad Gupta, Kisalay Kishore & Vivek Jain for setting up our lab in the initial days and assisting me through various procedures and useful scientific inputs. This entire work would never be complete without expressing my sincere gratitude to my senior CVR colleagues, Dr. Sachin Sakate, Dr. Suhas Shinde, Dr. Sumit Kamble, Dr. Sanjay Jadhav, Dr. Mrs. Sharda Kondawar-Parsewar, Dr. Amol Hengne, Dr. Mrs. Rasika Mane-Pol, Dr. Chetana Patil for their help and suggestions. I wish to thank my CVR lab mates Mr. Rajan Pandya, Mr. Bhanupratap Solanki, Mrs. Aarti Jadhav, Dr. Nandan Date, Mr. Shivanand Patil, Mr. Rameshwar Swami, Miss. Gayatri Kasar, Miss. Roopa Parate, Mr. Subhash Magar, Mr. Srinivas. Charate, Mr. Anil Patil, Mr. Rohit Shetty, Miss Komal Tarade, Mr. Ram Mandle, Mr. Angshuman Kathua, Miss. Samrin Shaikh. I would like to thank hard working and sincere master's trainees, Mr P. C. Mahaboob, Mr U. Amrithesh, Miss B Sandhya, Miss P. Varsha, Mr. Ramees Hamsa, Mr. M. Dayyan for their helping hands for accelerating my research work. I am also thankful to Mr. Chinnadurai (Annaji) for his all-time assistance in the lab.

I specially thank all the members of central facilities such as NMR, XRD, HRMS, Raman, XPS and TEM in CMC groups at CSIR-NCL as well as IISER-Pune and SAIF-IIT-Bombay for their help in obtaining the analytical data. I would like to thank staff of administration, accounts, medical, engineering, library, chemical store, purchase, glass blowing departments of NCL for their cooperation.

My sincere thanks go to all dumbbells, barbells, other gym equipment's, gym trainers and fitness enthusiasts at Empire Fitness and Wow Fitness centers. They providing me with the necessary motivation to do the impossible and indirectly kept me in the best of physical and mental health during the course of my PhD life. I always enjoyed their company and the workout sessions helped me to weigh success and failure equally.

*No word would suffice to express my gratitude to my **Parents**. They have been always the source of inspiration and thanks for giving me the opportunity to see this beautiful world. I am very thankful to my Mother, Mrs Mukta and Father Mr Vinayak for their belief in my abilities. Without their constant support, encouragement, positive thinking and inspiration, I cannot stand with this dissertation. I would like to equally thank my younger brother Mr. Yogesh for supporting me in any situation.*

*Finally, I would also like to acknowledge the financial support received from **DST-INSPIRE** "Innovation in Science Pursuit for Inspired Research" in the form of Junior and Senior Research Fellowships.*

Above all, I owe it all to Almighty God for granting me the wisdom, health and strength to undertake this research task and enabling me to its completion.

With many thanks,

Dnyanesh Vernekar

Dedicated

to My

Family

CONTENTS

		Page No.
Acknowledgement		i
Abbreviations		viii
List of Figures		x
List of Schemes		xvi
List of Tables		xvii
<hr/>		
Chapter 1	<i>General Introduction</i>	
1.1	Introduction	1
1.2	Metal Oxyhydroxide (MO(OH))	2
1.3	Structure and Polymorphism in MO(OH)	2
1.4	General Synthesis of MO(OH)	4
1.5	General Applications of MO(OH)	6
1.6	Tandem Catalysis	10
1.7	Multifunctional Heterogeneous catalyst	13
1.8	Classification of Bifunctional Heterogenous catalyst	14
1.8.1	Based on type of active sites	14
1.8.2	Organic, Inorganic and hybrid materials	18
1.9	Material Characterization techniques	22
1.10	Scope and Objectives of Thesis	27
1.11	Organization of Thesis	29
1.12	References	30
<hr/>		
Chapter 2	<i>Role of surface hydroxyl groups on hierarchically condensed phases (Hydroxides, Oxyhydroxides & Oxides) : Insight into surface acidity and basicity</i>	
2.1	Introduction	36
2.2.	Experimental Section	37
2.2.1	Synthesis of metal hydroxides, metal oxyhydroxides and metal oxides	37
2.2.2	Catalysis reaction	39

2.2.3	Determination of surface hydroxyl groups	40
2.3	Results and Discussion	41
2.3.1	Material Characterization	41
2.3.2	Catalytic reactions	45
2.3.3	Acidity and Basicity in M(OH) _n , MO(OH) and M _x O _y	49
2.3.4	Active sites	53
2.3.4.1	Surface -OH groups as the active sites	53
2.4	Conclusions	56
2.5	References	57

Chapter 3a *Tunable acid–base bifunctional catalytic activity of FeO(OH) in an orthogonal tandem reaction*

3a.1	Introduction	59
3a.2.	Experimental Section	60
3a.2.1	Synthesis method of polymorphs of FeO(OH)	60
3a.2.2	Catalytic Reaction	61
3a.2.3	Material Characterization	62
3a.3	Results and discussion	64
3a.3.1	Material Characterization	64
3a.3.2	Acid-Base Catalysis	67
3a.3.3	Acidity & Basicity	74
3a.3.4	Catalyst Recyclability and stability studies	77
3.4	Conclusions	80
3.5	References	81

Chapter 3b *Water-promoted surface basicity in FeO(OH) for the synthesis of Pseudoionones (PS) and their analogues*

3b.1	Introduction	83
3b.2	Experimental Section	84
3b.2.1	General Experimental procedure for the preparation of γ -FeO(OH)	84
3b.2.2	General Experimental procedure for the synthesis of	84

	Pseudoionone (PS)	
3b.2.3	<i>In-situ</i> CO ₂ IR & Methanol dissociation studies	85
3b.2.4	Fluorescence studies using Rhodamine 6G	85
3b.2.5	FeO(OH) activation studies, Hot filtration & Recyclability test	85
3b.2.6	Material Characterization	86
3b.2.7	Analysis of catalysis reaction products	86
3b.3	Results and Discussion	87
3b.3.1	Material Characterization	87
3b.3.2	Knoevenagel condensation	90
3b.3.3	Active sites	94
3b.3.3.1	Basicity in FeO(OH) and role of H ₂ O	94
3b.3.4	Substrate scope	101
3b.3.5	Catalyst recycle study	102
3b.4	Conclusions	104
3b.5	¹H NMR of isolated compounds	105
3b.6	References	110

Chapter 4a *Efficient bifunctional reactivity of K-doped CrO (OH) nanosheets: exploiting the combined role of Cr (III) and surface –OH groups in tandem catalysis*

4a.1	Introduction	112
4a.2	Experimental Section	113
4a.2.1	Preparation of Chromium Oxyhydroxide materials	113
4a.2.2	Material Characterization	115
4a.2.3	Catalytic Reaction	115
4a.2.4	<i>In-situ</i> Infrared Spectroscopy	116
4a.2.5	Cyclic Voltammetry	116
4a.3	Results and Discussion	118
4a.3.1	Synthesis and Characterization of CrO(OH)	118
4a.3.2	Catalytic activity of K- α -CrO(OH)	123
4a.3.2.1	Base property of K- α -CrO(OH)	123

4a.3.2.1.1	Effect of K doping	125
4a.3.2.1.2	Effect of Polymorph	125
4a.3.2.1.3	Nature of basic sites	127
4a.3.2.1.4	Basicity due to Potassium	128
4a.3.2.1.5	Basicity due to Surface Hydroxyl groups	129
4a.3.2.2	Oxidation property of K- α -CrO(OH)	134
4a.3.2.3	Bifunctional activity of K- α -CrO(OH)	138
4a.3.3	Potential Toxicity and Leaching studies	142
4a.3.4	Recyclability and comparison with state of art catalysts	144
4a.4	Conclusions	147
4a.5	NMR of isolated products	148
4a.6	References	152

Chapter 4b *Role of oxide-oxyhydroxide interface in defect MnOx(OH) for redox-base tandem activity*

4b.1	Introduction	156
4b.2	Experimental Section	157
4b.2.1	Material Synthesis	157
4b.2.2	Cyclic Voltammetry	158
4b.2.3	Material characterization	159
4b.2.4	Catalysis reaction	159
4b.3	Results and Discussion	160
4b.3.1	Material characterization	160
4b.3.1	Catalytic Studies on MnOx(OH)	166
4b.3.2.1	Oxidation property of MOx(OH)	166
4b.3.2.2	Base property of MOx(OH)	168
4b.3.2.3	Bifunctional activity of MnOx(OH)	169
4b.3.2.4	MnOx(OH) recyclability and stability	173
4b.3.2.5	Substrate scope	174
4b.4	Conclusions	175
4b.5	¹H NMR of selected compounds	176
4b.6	References	178

Chapter 5 *Amorphous WCoFeO(OH) for oxidant-free liquid phase catalytic conversion of cyclohexane to adipic acid*

5.1	Introduction	180
5.2	Experimental Section	182
5.2.1	Synthesis of mixed metal oxyhydroxides	182
5.2.2	Cyclohexane oxidation	182
5.2.3	Acidity measurements	183
5.3	Results and Discussion	184
5.3.1	Material Characterization	184
5.3.2	Catalyst activity	187
5.3.3	Active sites	189
5.3.3.1	Acidity of WFeCoO(OH)	189
5.3.4	DFT calculations	191
5.3.4.1	Results of DFT studies	193
5.3.5	Recyclability and catalyst stability studies	194
5.4	Conclusions	195
5.5	References	196

Chapter 6 *Summary and Future scope*

6.1	Summary	198
6.2	Salient outcome of the present thesis.	200
6.3	Future scope	201

List of Publications	202
About the Author	203
Plagiarism Report	204

ABBREVIATIONS

aq.	Aqueous
Å	Angstrom
AA	Adipic Acid
BET	Brunauer–Emmett–Teller
¹³ C	¹³ -Carbon
C-C	Carbon-Carbon
C-O	Carbon-Oxygen
cm	Centimeter
CO ₂	Carbon dioxide
CDCl ₃	Deuterated chloroform
Conc.	Concentrated
°C	Degree Celsius
CH ₃ NO ₂	Nitromethane
e.g.	For example
eV	Electron volt
EtOH	Ethanol
EDAX	Energy Dispersive X-ray Analysis
FID	Flame Ionization Detector
FeCl ₃	Iron (III) chloride
FeCl ₃ 6H ₂ O	Iron (III) chloride hexa hydrate
g	Gram
GCMS	Gas Chromatography mass spectroscopy
HCl	Hydrochloric acid
h or hrs	Hours
H ₂ O	Water
H ₂ SO ₄	Sulfuric acid
Hz	Hertz
HPLC	High performance liquid chromatography
¹ H	Proton
ICP-OES	Inductively coupled plasma optical emission spectroscopy
KBr	Potassium bromide
KMnO ₄	Potassium permanganate
Kg	Kilo gram
KA oil	ketone-alcohol oil
mm	Millimeter
mg	Milligram
MHz	Mega Hertz
min	Minute
mL/μL	Milliliter/ Microliter
mmol	Millimole
NaCl	Sodium chloride
NaOH	Sodium hydroxide
NMR	Nuclear magnetic resonance
ppm	Parts per million
Py-FTIR	Pyridine Fourier Transform Infrared spectroscopy
rt	Room temperature

SEM	Scanning electron microscopy
t	Time
T	Temperature
TEM	Transmission electron microscopy
TLC	Thin layer chromatography
TPD	Temperature programmed desorption
TCD	Thermal Conductivity Detector
θ	Theta
u	unit
wt	Weight
XPS	X-ray photo electron microscopy
XRD	X-ray diffraction

List of Figures		
Fig No	Figure Caption	Page No
1.1	a) &b) Thermodynamic stability of Metal Hydroxides, Metal Oxyhydroxides and Metal Oxides	2
1.2	Polymorphism exhibited by FeO(OH).	3
1.3	Crystal changes during synthesis of α -FeO(OH)	5
1.4	A pictorial representation of active sites on a multifunctional catalyst	13
1.5	Classification of various multifunctional catalysts based on nanostructure	18
1.6	Schematic of representation of Bragg's law conditions	23
1.7	Layout of optical components in Transmission Electron Microscopy	25
1.8	Schematic representation of GC-MS	27
2.1	a) &b) Thermodynamic stability of Metal Hydroxides, Metal Oxyhydroxides and Metal Oxides	37
2.2	Different Metal hydroxides, Metal Oxyhydroxides and Metal oxides of Cr, Mn, Co and Al prepared and used in the present work	41
2.3	XRD patterns of 1) Chromium 2) Manganese 3) Cobalt & 4) Aluminium ■ Hydroxides ■ Oxyhydroxide ■ Oxide	42
2.4	Infrared spectrum of the samples 1) Chromium 2) Manganese 3) Cobalt & 4) Aluminium ■ Hydroxide ■ Oxyhydroxide ■ Oxide	44
2.5	Transmission Electron Microscopy images of the samples.	45
2.6	Conversion & Selectivity plots for the Deacetylation-Knoevenagel reaction for Metal Hydroxides M(OH) _x , Metal oxyhydroxides MO(OH) & Metal oxides MO _x	46
2.7	Recyclability studied for the metal hydroxide and metal oxyhydroxide samples for the different metals a) Chromium b) Manganese c) Cobalt d) Aluminium	48
2.8	Ammonia TPD plots for the various Metal Hydroxides M(OH) _x , Metal oxyhydroxides MO(OH) & Metal oxides MO _x a) Cr b) Mn c)Co & d) Al	50
2.9	Trends in acidity from Ammonia TPD for the samples.	50

2.10	CO ₂ TPD plots for the various Metal Hydroxides M(OH) _x , Metal oxyhydroxides MO(OH) & Metal oxides MO _x	51
2.11	Trends in basicity from CO ₂ TPD for the samples.	51
2.12	Brønsted to Lewis acid ratio (B/L) for all the samples.	53
3a.1	a) XRD patterns of FeO(OH), b) FT-IR spectra of FeO(OH) polymorphs. Traces (i) α FeO(OH), (ii) β FeO(OH), (iii) γ FeO(OH) and (iv) δ FeO(OH). * Peaks due to α Fe ₂ O ₃ .	64
3a.2	SEM images (a, d, g and j) and TEM images (b, e, h and k) and crystal structures (c, f and i) of the FeO(OH) polymorphs are shown. (a, b, c) α FeO(OH), (d, e, f) β FeO(OH), (g, h, i) γ FeO(OH), and (j, k) δ FeO(OH). The crystal structures were taken from the website http://shalaleh.blogfa.com/ .	65
3a.3	Nitrogen adsorption-desorption isotherms of FeO(OH) polymorphs. Traces (i) (●) α FeO(OH), (ii) (○) β FeO(OH), (iii) (■) δ FeO(OH) and (iv) (□) γ FeO(OH)	66
3a.4	a) Conversion of deacetalization – Henry condensation reaction of different polymorphs of FeO(OH), b) Selectivity yield of products (2, 3, 4 and 5) obtained from catalysts α FeO(OH), β FeO(OH), γ FeO(OH) and δ FeO(OH). Reaction was carried out under reflux conditions in CH ₃ NO ₂ for 48 h.	67
3a.5	The catalytic activity of the polymorphs of FeO(OH) for in Henry reaction starting from 2 is plotted. Figure a) shows the conversion (%) and b) shows the selectivity of products 3, 4 and 5.	69
3a.6	Time dependent product distribution of (a) β FeO(OH) and (b) γ FeO(OH) catalysts. (■) Reactant 1, (●) Product 2, (□) Product 4 and (○) Product 5.	71
3a.7	Heterogeneous catalytic activity of β and γ FeO(OH)	72
3a.8	Thermogravimetric analysis data for the polymorphs Traces (i) β FeO(OH), (ii) γ FeO(OH), (iii) δ FeO(OH) and (iv) α FeO(OH).	72
3a.9	FT-IR spectra polymorphs of FeO(OH) adsorbed with pyridine. Traces (i) α FeO(OH), (ii) β FeO(OH), (iii) γ FeO(OH), (iv) δ FeO(OH)	75
3a.10	Reusability studies of (a) β FeO(OH), where Conversion % with respect to 1 (■) and selectivity for 4 (■) and (b) γ FeO(OH), where conversion with respect to 1 (■) and selectivity with respect to 4 (■)	77

	for deacetalization-Henry reaction at 80 °C for 12 h are plotted.	
3a.11	XRD patterns of fresh and the used catalysts (after 5 cycles) β FeO(OH) and γ FeO(OH).	78
3a.12	TEM data of fresh and used samples of β and γ FeO(OH)	78
3a.13	a) TGA and b) IR data of fresh and used β FeO(OH)	79
3b.1	a) XRD pattern of γ -FeO(OH) b) Infrared Spectra of γ -FeO(OH) c) Deconvoluted O1s XPS spectra d) Fe 2p XPS spectra of FeO(OH)	87
3b.2	a) Thermogravimetric (TGA) plot of γ -FeO(OH). b) BET surface area isotherm for γ -FeO(OH).	89
3b.3	a) TEM image of γ -FeO(OH) rods b) High magnification TEM image of (I), encircled in Fig 2a c) High resolution TEM images of rods in region (I) & d) Electron diffraction pattern.	89
3b.4	a) Rate of the reaction for the various catalysts screened in the presence and absence of water for the synthesis of the PS. Reaction Conditions: citral (0.152 g, 1 mmol), acetone (0.116 g, 2 mmol), specially dried 1,4-Dioxane (5 mL), H ₂ O (1 mL), time (12 h), reflux, sealed conditions. b) Plot of TON Vs duration of reaction in the presence of γ -FeO(OH) with and without H ₂ O.	93
3b.5	Study of effect of H ₂ O on the activation of γ -FeO(OH) i) in the absence of water ii) hot filtration test: flat line represents no further progress in reaction after the removal of the catalyst iii) in the presence of water iv) reactants introduced after 2 h of stirring FeO(OH) in dioxane-water mixture	94
3b.6	Infrared Spectra of (i) neat FeO(OH) (ii) CO ₂ adsorbed on FeO(OH) and (iii) their difference spectra a) changes in the hydroxyl group stretch b) changes in the C-O stretch	95
3b.7	<i>In situ</i> FT-IR spectra obtained by subtracting MeOH adsorbed FeO(OH) and neat FeO(OH) spectra a) in the absence of water b) in the presence of water. Trace i) ii) & iii) denote scans taken after 5 min, 15 min & 25 min respectively. c) Vibration modes of MeOH dissociation on FeO(OH) surface: Molecularly adsorbed species (1064 cm ⁻¹), Bidentate methoxy species (1092 cm ⁻¹) and Monodentate methoxy species (1115 cm ⁻¹). d) Relative MeOH dissociation on FeO(OH) in the presence and absence of water w.r.t molecularly adsorbed MeOH	96

3b.8	a) structure of Rhodamine -6G b) Interaction between FeO(OH) and Rh-6G c) Fluorescence spectrum for Rh-6G and FeO(OH)-Rh-6G (Excitation-500nm) in water. d) Quantification of amount of dye adsorbed on FeO(OH) in various dioxane: water mixtures. e) FTIR spectra for FeO(OH) and FeO(OH)-Rh-6G complex f) FT-IR spectra for Rh-6G and FeO(OH)-Rh-6G complex	98
3b.9	Calibration plots ((a), (b), (c)& (d)) for dye concentration	99
3b.10	Individual fluorescence spectra ((i), (ii), (iii) & (iv)) in various 1,4-dioxane: water mixtures respectively	100
3b.11	FT-IR results of water treated γ -FeO(OH) (6 h & 12 h) and untreated sample between 4000-2000 cm^{-1}	100
3b.12	Recyclability of γ -FeO(OH) for PS synthesis	103
3b.13	X-ray Diffraction of fresh and 8 th reuse sample	103
4a.1	a) X-Ray Diffraction pattern for K- α -CrO(OH), b) Infrared Spectrum of K- α -CrO(OH) c) TEM image of K- α -CrO(OH) (inset showing the stacks of K- α -CrO(OH) sheets) d) HRTEM image of the K- α -CrO(OH) showing the lattice fringes of (101) plane	119
4a.2	BET Hysteresis plot for K-CrO(OH)	120
4a.3	Atomic Force Micrographs of K α -CrO(OH). Inset of b) shows thickness of sheet along the line between the dotted boundaries	120
4a.4	a) Full scan XPS spectra b) deconvoluted XPS spectra of K 2p signal c) deconvoluted Cr 2p _{3/2} signal (inset Cr Auger Signal) d) deconvoluted O 1s signal of K- α -CrO(OH)	121
4a.5	(a) XRD & (b) Infrared spectrum of i)Cr ₂ O ₃ ii) γ -CrO(OH) iii)K- γ - CrO(OH) iv) α -CrO(OH)	122
4a.6	TEM images of a)Cr ₂ O ₃ b) γ -CrO(OH) c)K- γ -CrO(OH) d) α -CrO(OH)	122
4a.7	Time dependent conversion for Knoevenagel Condensation using K- α -CrO(OH) and Hot filtration test for K- α -CrO(OH) for Knoevenagel Condensation.	125
4a.8	Knoevenagel condensation reaction for K doped and K free α -CrO(OH)	126
4a.9	CO ₂ TPD profiles of (i) Cr ₂ O ₃ (ii) γ -CrO(OH) and (iii) K- γ -CrO(OH) iv) α -CrOOH v) K- α -CrO(OH)	127
4a.10	<i>In situ</i> IR difference spectra of CO ₂ adsorbed on (a) α -CrO(OH) and (b) K- α -CrO(OH) Inset different carbonate & (bi)carbonate vibration modes	128
4a.11	Thermogravimetric (TGA) profiles of (i) K- α -	130

	CrO(OH), (ii) α -CrO(OH), (iii) K- γ -CrO(OH), (iv) γ -CrO(OH) and (v)Cr ₂ O ₃	
4a.12	a) Structure of Rhodamine 6G b) Interaction of Rh-6G with CrO(OH) surface c) Florescence spectroscopy for standard Rh-6G sample and K- α -CrO(OH), α -CrO(OH) adsorbed solutions	132
4a.13	Comparative FT-IR spectra of K- α -CrO(OH)-Rh-6G with bare K- α -CrO(OH) and Rh-6G in two different regions a) & b)	132
4a.14	Deconvoluted O1s spectra of a) α -CrO(OH) b) γ -CrO(OH) c)K- γ - CrO(OH) with the calculated contributions of different Cr(III) species	133
4a.15	Deconvoluted Cr2p _{3/2} spectra of a) α -CrO(OH) b) γ -CrO(OH) c)K- γ - CrO(OH) with the calculated contributions of different Cr(III) species	134
4a.16	Cyclic Voltammograms of a) α -CrO(OH) b)K- α - CrO(OH) c) γ -CrO(OH) d)K- γ -CrO(OH) e) Cr ₂ O ₃	137
4a.17	Time dependent study for K- α -CrO(OH) to yield a) 3a (ii) is an expanded area of (i) after addition of malononitrile b) to yield 3c c) to yield 3d	141
4a.18	Microwave plasma atomic emission spectroscopy results for leaching studies	143
4a.19	Recyclability of K- α -CrO(OH) for one pot oxidative coupling reaction to give 3c	144
4a.20	a) XRD and b) TEM image of used K- α -CrO(OH).	144
4b.1	XRD patterns for i) MnO(OH)-P, ii) MnO _x (OH) iii) Mn ₂ O ₃	160
4b.2	a) FT-IR spectra of i) MnO(OH)-P, ii) MnO _x (OH) iii) Mn ₂ O ₃ . b) A magnified spectra of MnO(OH), MnO _x (OH) and Mn ₂ O ₃ . Yellow bands for Oxyhydroxides features whereas grey bands indicating oxide features.	161
4b.3	a) Raman spectra of i) MnO(OH)-P, ii) MnO _x (OH) iii) Mn ₂ O ₃ b) A magnified spectra of i) MnO(OH)-P, ii) MnO _x (OH) iii) Mn ₂ O ₃ showing a shift for MnO _x (OH)	162
4b.4	EXAFS data for MnO(OH)-P, MnO _x (OH) and Mn ₂ O ₃	163
4b.5	Second derivative a), b) & c) and Fourier transform d), e) & f) of the spectrum for MnO(OH)-P, MnO _x (OH) and Mn ₂ O ₃	163
4b.6	Transmission Electron Microscopy images for a)MnO(OH)-P b) MnO _x (OH) and c) Mn ₂ O ₃	164
4b.7	TEM image (a), ED pattern (b), HRTEM (c) & (d)	165

	Particle sizes of MnO _x (OH) rods and spheroids	
4b.8	Deconvoluted Mn 2p _{3/2} XPS spectra for MnO(OH)-P, MnO _x (OH) & Mn ₂ O ₃	165
4b.9	a) Oxidation step Reaction conditions: 1mmol Benzyl alcohol (1), 5 mL p-xylene, 400mg catalyst at 90 °C, O ₂ balloon, 24h for all the catalysts b) Condensation step: Reaction conditions: 1mmol Benzaldehyde (2), 2mmol acetophenone, 5 mL p-xylene and 400mg catalyst at 90 °C, N ₂ atmosphere, 24h for all the catalysts	166
4b.10	Cyclic Voltammograms for the manganese catalysts	168
4b.11	(a) CO ₂ TPD plots and b) Thermogravimetry plots for i) MnO(OH)-P ii) MnO _x (OH) iii) Mn ₂ O ₃ ,	169
4b.12	Conversion and Selectivity plots for the manganese samples	170
4b.13	a) Deconvoluted O1s XPS spectra of a) MnO _x (OH) b) MnO(OH)-P c) plot of % contribution of O species d) plot of relative ratio of [Mn-O-Mn]/Mn-OH]	171
4b.14	Recyclability of MnO _x (OH) for one pot oxidative coupling reaction to give 3	173
4b.15	a) XRD of Fresh and used MnO _x (OH) b) TEM of used MnO _x (OH)	174
5.1	X-ray Diffraction pattern for (a) WFeCoO(OH) (b) WFeO(OH) (c) WCoO(OH) d) CoFeO(OH) e) CoO(OH) f) FeO(OH)	184
5.2	Infrared Spectrum of (a) WFeCoO(OH) (b) WFeO(OH) (c) WCoO(OH) d) CoFeO(OH) e) CoO(OH) f) FeO(OH)	185
5.3	a) Transmission Electron Microscopy image of WFeCoO(OH) b) Electron Diffraction pattern c) HAADF STEM image and d) elemental mapping of the selected orange portion in c).	186
5.4	XPS spectra of a) full scan of WFeCoO(OH) b) O1s c) Fe2p d) Co2p e) W4f of WFeCoO(OH)	186
5.5	a) Effect of Catalyst amount and b) Effect of reaction temperature on activity:	189
5.6	a) Pyridine IR difference spectra for (vi) WFeCoO(OH) (v) WFeO(OH) (iv) WCoO(OH) iii) CoFeO(OH) ii) CoO(OH) i) FeO(OH) b) Quantified Brønsted and Lewis acidity for the samples	190
5.7	Ammonia TPD plot for (i) FeO(OH) (ii) CoO(OH) (iii)WCoO(OH) (iv)WFeO(OH) (v)CoFeO(OH) (vi) WFeCoO(OH) and their calibrated acidity values	191
5.8	DFT optimized geometries of CoO(OH),	192

	WCoO(OH), FeCoO(OH) and FeWCoO(OH) catalyst surface and respective configuration after deprotonation.	
5.9	A plot of DPE vs adipic acid selectivity for the various catalysts.	194
5.10	Recycle studies for WFeCoO(OH)	195
5.11	XRD before and after the catalytic studies	195
List of Schemes		
Scheme No	Scheme Caption	Page No
1.1	Applications of metal oxyhydroxides	7
1.2	Various terms used for tandem catalysis	10
1.3	Different types of Tandem catalytic processes	11
1.4	Steps to identify Tandem catalytic processes	12
1.5	Oxidative -coupling/ condensation reactions catalysed by base-metal bifunctional catalyst	15
1.6	Acid-base reactions catalysed by bifunctional catalysts	17
2.1	Interaction of pyridine with surface of the catalysts	52
2.2	The probable acid and base sites on a) Metal hydroxides, b) metal oxyhydroxides and c) metal oxides.	55
3a.1	Deacetalization – Henry condensation reaction: Structures of products benzaldehydedimethylacetal (1), benzaldehyde (2), 2-nitro-1-phenylethanol (3), trans-β-Nitrostyrene (4) and 1,3-dinitro-2-phenylpropane (5) are schematically shown.	61
3a.2	Mechanism of deacetalization-Henry condensation reaction occurring on the surface of FeO(OH).	74
3a.3	Representation of different types of surface hydroxyl groups on FeO(OH) in a) single b) double and c) triple coordinated modes	76
3b.1	Flowchart showing the synthesis of ionones from citral via pseudoionones	84
3b.2	a) Crystal structure of γ-FeO(OH) b)The three coordination modes of OH on FeO(OH) surface.	88
3b.3	Plausible reaction mechanism for the synthesis of the Pseudoionones and their analogues.	104
4a.1	a) crystal structure of α-CrO(OH) with Cr as the central atom of the polyhedra b) ordered layers of CrO(OH) stabilized by hydrogen bonding forming the 2D nanostructure	118

4a.2	Two oxidations followed by a coupling reaction in one pot to yield 3c	138
4a.3	Proposed reaction mechanism occurring on K- α -CrO(OH) <i>Oxidation</i> : A) deprotonation of Benzyl alcohol B) oxygen activation on Cr(III) of K- α -CrO(OH) C) formation of Benzaldehyde (1). <i>Coupling/Condensation</i> : D) proton abstraction of active methylene group (2) R=RXH= malononitrile, ethyl cyanoacetate, acetophenone, aniline E) attack of nucleophile on carbonyl carbon of benzaldehyde F) water loss to give the respective products (3)(3a, 3b, 3c, 3d).Activation of O ₂ molecule takes place over Cr(III) sites in Step B. Benzaldehyde (1) is formed in step C. The deprotonated hydroxyl groups (O ⁻) activate the methylene groups of the reactants (2) by abstraction of proton in Step D and ably supported by O ²⁻ ions. Step E involves the attack of the nucleophile to the carbonyl carbon of benzaldehyde and subsequent formation of the desired product (3) by loss of water molecule in Step F.	146
4b.1	Crystal structures of MnO ₂ , Mn ₂ O ₃ and MnO(OH)	161
4b.2	Surface model of MnO(OH)	172
5.1	Industrial process for Adipic Acid production from cyclohexane oxidation	180
List of Tables		
Table No	Table Caption	Page No
1.1	Various Metal Oxyhydroxides their common names and crystallographic descriptions	3
1.2	Reported applications of MO(OH) for adsorption	8
1.3	Use of Metal Oxyhydroxides as sensor components	8
1.4	Oxyhydroxide materials for Photocatalytic applications	9
1.5	Oxyhydroxide materials used as catalyst supports	10
1.6	Various base-metal bifunctional catalysts reported in literature	15
1.7	Various acid-base bifunctional catalysts reported in literature	17
1.8	Advantages and Disadvantages of various Multifunctional Catalysts	21
2.1	Results from XRD and TEM for all hydroxide, oxyhydroxide and oxide materials	42
2.2	Conversion and selectivity trends for the catalytic	47

	studies	
2.3	Surface area and Surface hydroxyl and O ²⁻ concentration using mercurometric titrations and XPS studies.	54
3a.1	Textural parameters of FeO(OH) polymorphs as determined by BET equation.	66
3a.2	Conversion & Yields of deacetalization – Henry condensation reaction of different polymorphs of FeO(OH)	68
3a.3	Table showing the conversion and selectivity of γ and δ FeO(OH) catalysts.	70
3a.4	Table showing the conversion and selectivity of β FeO(OH) catalyst.	70
3a.5	Strength and density of acid and base sites on FeO(OH) catalysts determined using Hammett indicators.	75
3b.1	Optimization of reaction conditions for the synthesis of the pseudoionones	91
3b.2	Condensation reactions of Citral with active methylene compounds using γ -FeO(OH) as catalyst.	101
4a.1	Different base catalyzed reactions tested by K- α -CrO(OH) and other catalysts.	124
4a.2	Textural properties and CO ₂ TPD results of the samples.	128
4a.3	Calculated weight loss of the samples obtained from TGA.	131
4a.4	Table showing the catalytic activity of K- α -CrO(OH) and other catalysts for benzyl alcohol oxidation	135
4b.1	EXAFS data for MnO(OH)-P, MnO _x (OH) and Mn ₂ O ₃	164
4b.2	Analysis of various contributions from Mn 2p _{3/2} XPS spectra for MnO(OH)-P, MnO _x (OH) & Mn ₂ O ₃	166
4b.3	Cyclic Voltammetry data for the manganese catalysts	168
4b.4	(a) CO ₂ TPD plots and b) Thermogravimetry plots for MnO(OH)-P, MnO _x (OH) & Mn ₂ O ₃ ,	169
4b.5	Substrate Scope exhibited by MnO _x (OH)	175
5.1	Cyclohexane to Adipic Acid conversion using various catalysts	188

Chapter 1

General Introduction

1.1 Introduction

Heterogeneous catalysis started as an empirical discipline two centuries ago. Berzelius and Mitscherlich were probably the first to observe heterogeneous catalysis who determined that the reactions could be accelerated by certain solids.[1] The term contact catalysis was introduced at that time.[2] Earlier, only simplified ideas about the mechanism of the reaction and its chemical thermodynamics; specific reactants and its interactions with catalytic materials existed. [3] With time, significant achievements amalgamated to industrially important chemical processes involving solid inorganic catalysts. Prominent among the processes involved production of inorganic chemicals such as sulfuric acid, nitric acid and ammonia.[4-6] This field has been pivotal in contributing to major economic transformations. For example, the Haber-Bosch process[7] developed by Fritz Haber and Carl Bosch in early 1900s efficiently converted N_2 to NH_3 using Fe catalyst promoted with K_2O , CaO , SiO_2 , and Al_2O_3 . [8] Another breakthrough has been the development of zeolites for refining crude oil to yield useful distillates in 1970s.[9] Similarly, Methanol synthesis processes developed by BASF and Fischer Tropsch were key defining industrial processes for synthetic fuels and fine chemicals.[10] A successful heterogeneous catalyst is characterized by high selectivity, high turnover numbers, cost effectiveness, high stability and reusability.[11, 12] To achieve these goals, it is important to develop new catalysts as well as gain insights into chemical synthesis, characterization and identification of the active sites. Computational studies have also been performed to ideally predict a catalytic system and understand the catalytic mechanism.[13]

In the present thesis, an improvement in the field of heterogeneous catalysis was attempted by utilizing various metal oxyhydroxides as active catalysts for different organic tandem conversions. The subsequent sections deal with metal oxyhydroxides, their structural and chemical properties along with their typical synthesis methods and applications. Later a brief literature survey of reported solid materials for tandem catalysis is also presented. The scope and objectives of the present thesis are also highlighted.

1.2 Metal Oxyhydroxides (MO(OH))

Metal oxohydroxides or Metal-oxyhydroxides are metastable intermediates between metal hydroxides and metal oxides. Though they are termed metastable, they exist in their crystallographic forms upto 250-300 °C and tend to disintegrate into metal oxides at higher temperatures. These materials were earlier referred to as metal oxide-hydroxide. These phases can be seen as B and C in Fig 1.1a and as phases 2, 3 and 4 in Fig 1.1b. Hence, according to Ostwald's rule, solids first formed on crystallization of solution/ melt would be least stable. Since metal hydroxides are formed first, they have poor stability whereas, metal oxyhydroxides have intermediate stability with metal oxide which are highly condensed and show very high stability. Metal oxyhydroxides are represented as MOOH or MO(OH) where, M is the metal in trivalent state. Each Metal atom is surrounded by three O^{2-} and three OH- which form the basic structural unit (octahedra): $MO_3(OH)_3$. Thus, MO(OH) has surface hydroxyl groups as in metal hydroxides along with condensed M-O-M linkages similar to metal oxides.

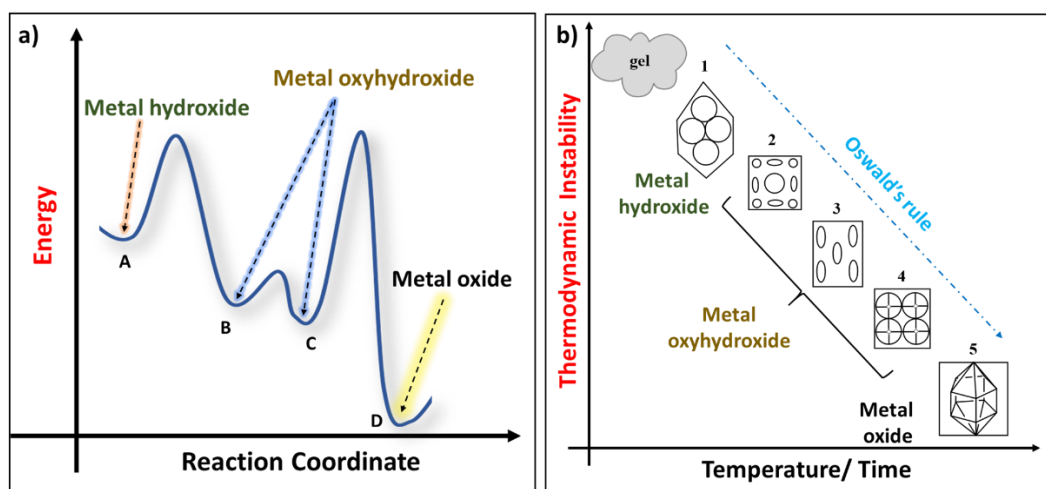


Fig 1.1 a) &b) Thermodynamic stability of Metal Hydroxides, Metal Oxyhydroxides and Metal Oxides

1.3 Structure and Polymorphism in MO(OH)

Metastable phases of a metal oxyhydroxide are known to exhibit polymorphism. It can have same chemical composition but exist in different crystal structures. This arises due to difference in arrangement of $M(O)_6$ octahedra. The building unit which is common to almost all oxyhydroxide materials is octahedron $MO_3(OH)_3$, where M

is the metal surrounded by three O^{2-} and three OH^- ligands. These entities are either linked by corners, edges or faces or even by a combination of these linkages to form desired structural arrays. In the case of $FeO(OH)$, five polymorphs have been identified (α , β , γ , δ , high pressure). In α - $FeO(OH)$, double chains of octahedra are formed by edge sharing which run parallel to $[100]$ direction. There is also a linkage between adjacent double chains via corner sharing as seen in Fig 1.2 leading to orthorhombic symmetry.

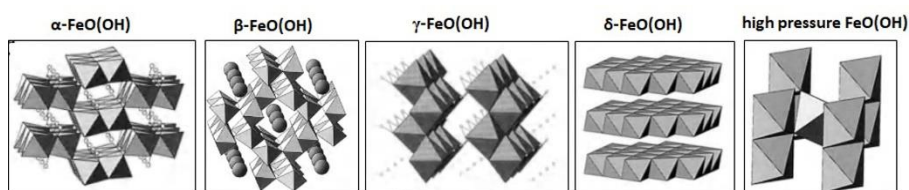


Fig 1.2: Polymorphism exhibited by $FeO(OH)$.

Table 1.1: Various Metal Oxyhydroxides their common names and crystallographic descriptions

Sr.No	MO(OH)	Common name/ mineral name	Crystallographic System	Space group	Stacking of closed packed anions
1.	α - $FeO(OH)$	Geothite	orthorhombic	Pnma	ABAB[001]
2.	β - $FeO(OH)$	Akaganéite	monoclinic	12/m	bcc
3.	γ - $FeO(OH)$	Lepidocrocite	orthorhombic	Bbmm	ABCABC[015]
4.	δ - $FeO(OH)$	Feroxyhyte	Hexagonal	P3ml	ABAB[001]
5	High pressure $FeO(OH)$	-	orthorhombic	Pn2 ₁ m	
6	α - $CrO(OH)$	grimaldiite	rhombohedral	R3m	
7	β - $CrO(OH)$	guyanaite	orthorhombic	Pnma	
8	γ - $CrO(OH)$	bracewellite	orthorhombic	Bbmm	
9	α - $MnO(OH)$	groutite	Orthorhombic	Pnma	
10	γ - $MnO(OH)$	manganite		2P1/c	
11	$CoO(OH)$	heterogenite	Hexagonal		
12	γ - $AlO(OH)$	boemite			
13	α - $AlO(OH)$	diaspore			
14	β - $NiO(OH)$	-		P $\bar{3}$ m1	ABCA
15	γ - $NiO(OH)$	-		R -3 m	
16	$TiO(OH)$	-			
17	$VO(OH)$	-			

Thus α -FeO(OH) has two kinds of O atoms labelled as O_I and O_{II} . O_I is the oxygen shared between octahedra of two different double chains whereas, O_{II} is shared between octahedra in the same chain and is also linked to hydrogen atom. β -FeO(OH) has a body centered cubic array instead of hcp or ccp. In this, the double chains consisting of edge shared octahedra run parallel to the fourfold symmetric axis as shown in Fig1.2. Corner sharing between adjacent double chains provide a 3D structure containing tunnels surrounded by double chains of octahedra with a cross section of 0.5 nm^2 . Cl^- ions are reported to be present in the tunnels with levels ranging between 2 – 7 mol% to stabilize the charge. Unlike, α and β FeO(OH), γ -FeO(OH) is a layered material. Fe(III) ions occupy octahedral interstices with arrays of ccp anions ($\text{O}^{2-}/\text{OH}^-$) stacked along the [150] direction. Adjacent double chains share edges with each chain being displaced by half compared to its neighbour leading to corrugated sheets of octahedra. The sheets are flanked by double rows of empty octahedral sites and the sheets are held together by hydrogen bonds. δ -FeO(OH) has a disordered hcp array of anions with Fe(III) ions distributed over half of the octahedral sites in an ordered manner. High pressure FeO(OH) involves chains of $\text{Fe}(\text{O},\text{OH})_6$ octahedra linked together by edges and running along the c-axis. Corner sharing is present between the neighbouring chains. Most of these oxyhydroxides are found in nature in the form of ores and hence, are known by their mineral names too. Table 1.1 summarizes different metal oxyhydroxides observed in nature their mineral names and crystallographic systems.

1.4. General Synthesis of MO(OH)

Soft Chemistry technique is used for the synthesis of metal oxyhydroxides which normally involve room temperature or around 200-300 °C and hydrothermal conditions. The control of the texture of the solid (porosity and surface area) is also much easier using soft chemistry route. The preparation of MO(OH) can be briefly summarized by the following steps.

i) Hydration of ions:

This step involves dissolution of metal salts in water leading to hydration of ions.
 $[\text{M}(\text{H}_2\text{O})_N]^{z+}$

ii) *Initiation of condensation: By addition of base/acid:* The hydrated ions can be initiated to start condensing by addition of acid or base (dilute mineral acids, or NaOH/NH₃).



iii) *Propagation*



iv) *Termination*

Olation: Condensation of cations taking place by formation of hydroxo (M-OH) bridges

Oxolation: Process of creation of oxo bridges (M-O-M) between cations that do not have aqua ligands in their coordination sphere.

Thermohydrolysis: Hydroxylation of hexa-aqua complexes of trivalent metals usually takes by heat treatment. E.g. heating an acidic solution of Al(III) ions at 80-100 °C leads to formation of boehmite γ -AlO(OH).

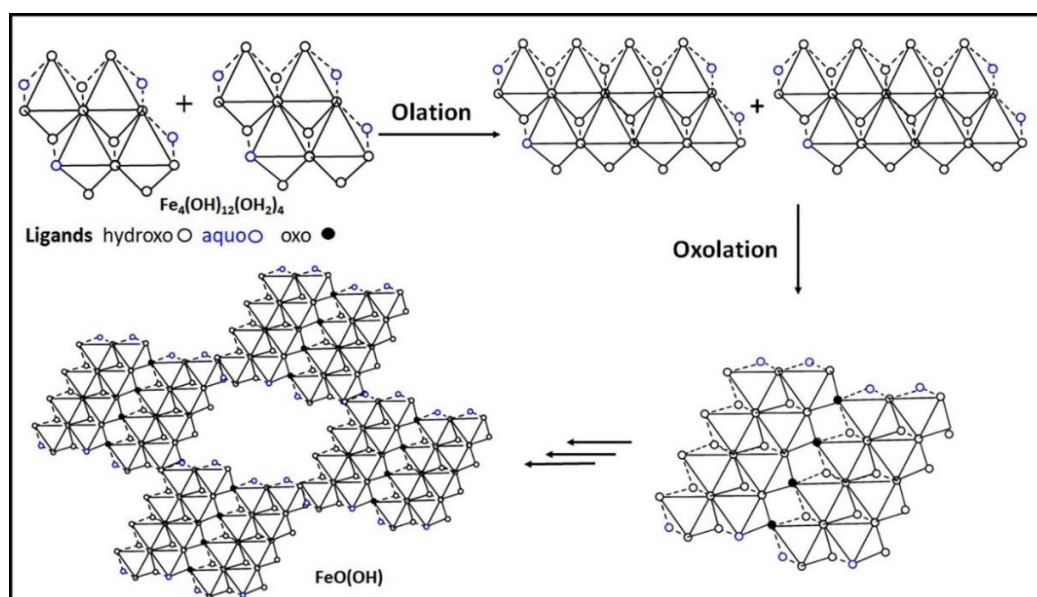
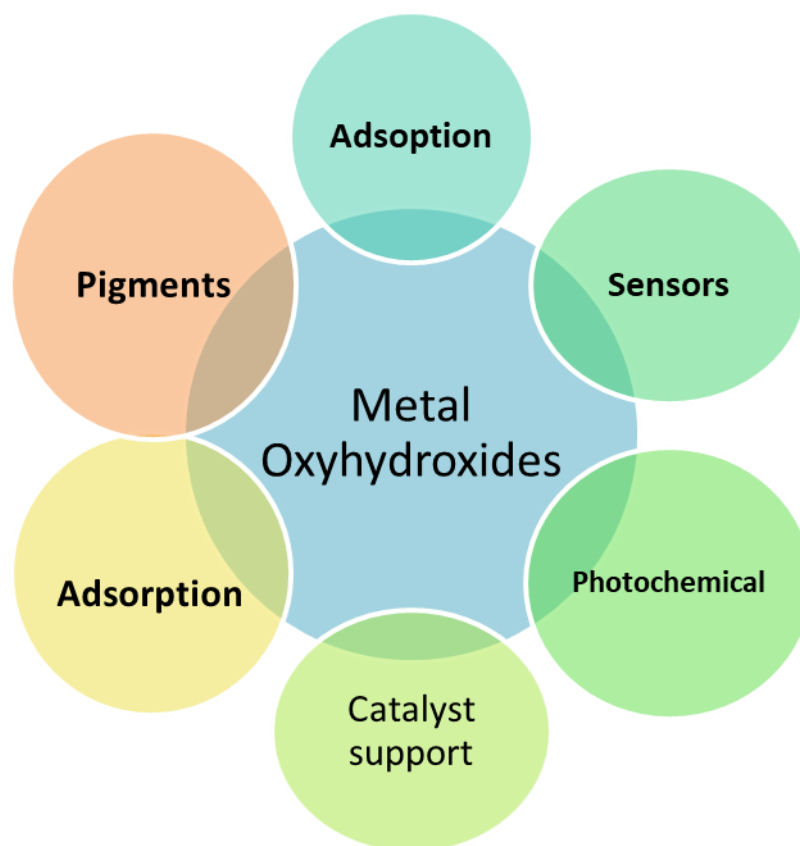


Fig 1.3. Crystal changes during synthesis of α -FeO(OH)

The example of preparation of α -FeO(OH) involving various steps is described in Fig 1.3. α -FeO(OH) is produced by precipitation of ferric ions by using a base or via thermohydrolysis in nitric or perchloric acid solutions. However, the nature of the solid phase in terms of its size, and morphology of particles depends mainly on the experimental conditions such as concentration, pH, temperature, aging time and ionic strength of the medium. Addition of base to a ferric nitrate solution leads to the formation of gelatinous precipitate in acidic media (pH- 2-2.5). The condensation of these ferric ions is difficult to limit because of their high lability. Ferric gels contain oxyhydroxides of various degrees of hydration (ferrihydrites). Ageing at room temperature or at moderately elevated temperatures converts ferrihydrites to hematite between pH 5 and 10. However, at pH above 10, we tend to get α -FeO(OH) which probably involves the process of dissolution-recrystallization. Nucleation of the solid phase takes place via the condensation of zero-charge species $[\text{Fe}_4(\text{OH})_{12}(\text{OH}_2)_4]^0$ via ololation. This process directly leads to the formation of double chains of octahedra. These chains further connect with one another via oxolation. Furthermore, the double chains connect via μ_3 bridges and hydrogen bonds between the chains. The growth of chain takes place leading to particles of high anisotropy with the largest dimension corresponding to the direction of the chains.

1.5 General applications of MO(OH)

Metal Oxyhydroxides can be categorized to have important applications in broadly six different categories as under (Scheme 1.1).



Scheme 1.1. Applications of metal oxyhydroxides

- a) **Pigments and colours:** The major synthetic iron oxide pigments are the yellows (α -FeOOH), the oranges (γ -FeOOH), reds (hematite), browns (maghemite). Like natural iron oxide pigments, the synthetics are used for colouring concrete, bitumen, asphalt, tiles, bricks, ceramics, and glass. They are also used extensively in house and marine paints. Iron oxides are especially suitable colorants for floor coverings as their resistance to alkali enables them to withstand strongly alkaline cleaning compounds. Face powder with practically any skin tone can be produced by appropriate combinations of yellow, red and black. Similarly, CrO(OH) is a precursor to chromia pigments. Green chromic oxide pigment shows excellent performance with resistance to corrosion, wear and chemical attacks. They

find wide applications in gum elastic, plastic, coating, printing, and construction

Table 1.1: Reported applications of MO(OH) for adsorption

SR. NO	ADSORBENT	ADSORBATE	REFERENCE
1.	α -FeO(OH)	Ca ²⁺ , Co ²⁺ , Pb ²⁺ , Zn ²⁺	[14-16]
2.	AlO(OH)	Organic macromolecular substances such as Eosin, tannic acid	[17]
3.	Amorphous FeO(OH)	selenate [Se(VI)] and selenite [Se(IV)] ions	[18]
4.	AlO(OH)	radiolabeled sulfate and phosphate ions	[19]
5.	FeO(OH)	CrO ₄ ²⁻	[20]
6.	Sm(III) oxyhydroxides.	NO ³⁻ & OH ⁻	[21]
7.	Mesoporous TiO(OH)	Flouride ion	[22]
8.	γ -AlOOH(Boehmite)@SiO ₂ /Fe ₃ O ₄	Pb(II)	[23]
9	Resin loaded FeO(OH)	Glyphosate containing effluents	[24]
10	α -FeOOH decorated graphene oxide-carbon nanotubes	As (III)	[25]
11	γ -AlOOH/Fe(OH) micro/nanoflowers	Heavy metal ions	[26]

b) **Adsorption:** The presence of large number surface hydroxyl groups on metal oxyhydroxides have prompted the use of these materials for adsorbing heavy metals and anions. A brief overview of the reported uses of metal oxyhydroxides as an adsorbate is presented in Table 1.1.

Table 1.2: Use of Metal Oxyhydroxides as sensor components.

SR. NO	MATERIAL	TYPE OF SENSOR	REFERENCE
1.	Ag/MnO(OH)	H ₂ O ₂ sensor	[27]
2.	CoO(OH)		[28]
3.	Ag/AlO(OH)		[29]
4.	Cu ₂ O on AlOOH/reduced graphene oxide	Amperometric glucose sensing	[30]
5.	Zinc-Doped Cobalt Oxyhydroxide		[31]
6.	Au-doped cobalt oxyhydroxide	CO sensor	[32]
7.	Cobalt oxide CoOOH		[33]

- c) **Sensors:** Most of the metal oxyhydroxides show good conductivity and hence can be used as low temperature sensors. Table 1.2 shows the various oxyhydroxides used as components of low temperature sensors
- d) **Photocatalysis:** Nanostructured metal oxyhydroxides or specifically two dimensional (2D) materials have been shown to effectively modulate the electron transportation and have been shown to reduce water -redox barriers and enhance catalytic current.

Table 1.3: Oxyhydroxide materials for Photocatalytic applications

SR. NO	MATERIAL	PHOTOCATALYTIC APPLICATION	REFERENCE
1.	Au/GaO(OH)	Methanol fuel cell	[34]
2.	FeO(OH)/TiO ₂	2-propanol decomposition	[35]
3.	β-CoOOH	Photocatalytic hydrogen evolution	[36]
4.	Nanostructured d-FeOOH:	Water splitting	[37]
5.	FeO(OH)/Fe ₂ O ₃	Water splitting	[38]
6.	of BiVO ₄ electrodes with an iron oxyhydroxide (FeOOH) catalyst layer	Oxygen evolution	[39]
7.	GaO(OH)		[40]
8.	InO(OH)	Benzene degradation	[41]
9.	FeOOH polymorphs	Dye degradation	[42]
10.	Se-doped InO(OH)	Dye degradation	[43]

Bulk oxyhydroxides are termed poor and only nanostructured /ultrathin oxyhydroxide materials have been shown to be good photocatalytic materials for hydrogen evolution and oxygen evolution reactions. A brief review of such oxyhydroxides as photocatalytic materials is given in Table 1.3

- e) **Catalyst Supports:** Metal oxyhydroxides and more specifically AlO(OH) has been used as a catalyst support due to its inert nature, high surface area and anchoring surface hydroxyl groups. In addition to the impregnation of the metal nanoparticles, attempts have been made to graft the surface with specific organic functionalities to catalyze several varieties of organic

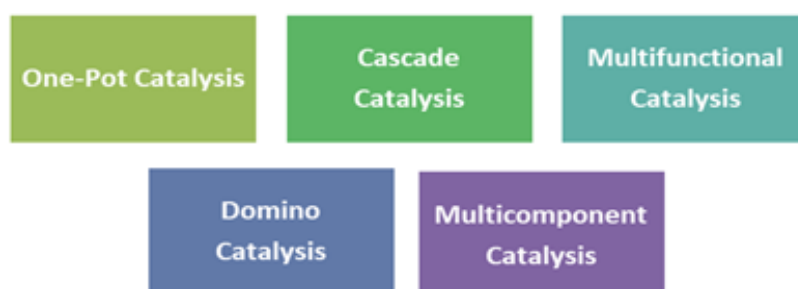
transformations. Table 1.4 gives a brief summary of the use of MO(OH) as a catalyst support for organic transformations.

Table 1.4: Oxyhydroxide materials used as catalyst supports

SR. NO	MATERIAL	ORGANIC TRANSFORMATION	REFERENCE
1.	Ru-Sn-Co/AlO(OH)	hydrogenation of dimethyl adipate to 1,6-hexanodiol	[44]
2.	boehmite silica sulfuric acid	synthesis of polyhydroquinoline and 2,3-dihydroquinazolin-4(1H)-one	[45]
3.	(Pt/AlOOH)	removal of formaldehyde	[46]
4.	Ru-Pt/AlOOH	Hydrogenation of methyl propionate	[47]
5.	Au/ γ -AlOOH	aerobic oxidation of α , ω -diols to lactones	[48]
6.	Pd/ γ -AlOOH@Fe ₃ O ₄	Heck coupling reaction	[49]
7.	Pd/AlOOH/Al-Fiber	CO Coupling to Dimethyl Oxalate:	[50]
8.	Ag/AlOOH	epoxidation of 1,3-butadiene	[51]
9.	(CNTs)- α -FeOOH	Fenton like oxidation	[52]

1.6 Tandem Catalysis

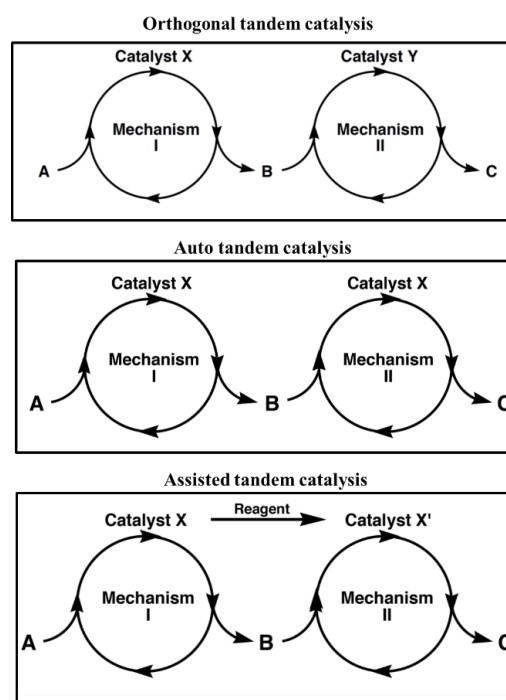
Tandem Catalysis is defined as sequential transformations of the substrate occurring via two or more distinct processes with all the catalytic species either apparent or masked are present from the beginning. [53] Following are a few terms which are often used interchangeably to identify sequential transformations (Scheme 1.2), though all the terms do not convey the same tandem process. These terms have been defined below and their mechanistic representation is presented in Scheme 1.3. Also, the ways to identify these tandem processes is demonstrated using a flowchart (Scheme 1.4).



Scheme 1.2: Various terms used for tandem catalysis

One pot reaction (Multicatalytic):[53] These are sequential processes where all the catalysts or precatalysts are not present from the start of the reaction sequence.

Domino (Cascade) catalysis:[54] Two or more bond-forming transformations which take place under the same reaction conditions, without adding additional reagents and catalysts, and in which the subsequent reactions result as a consequence of the functionality formed in the previous step.



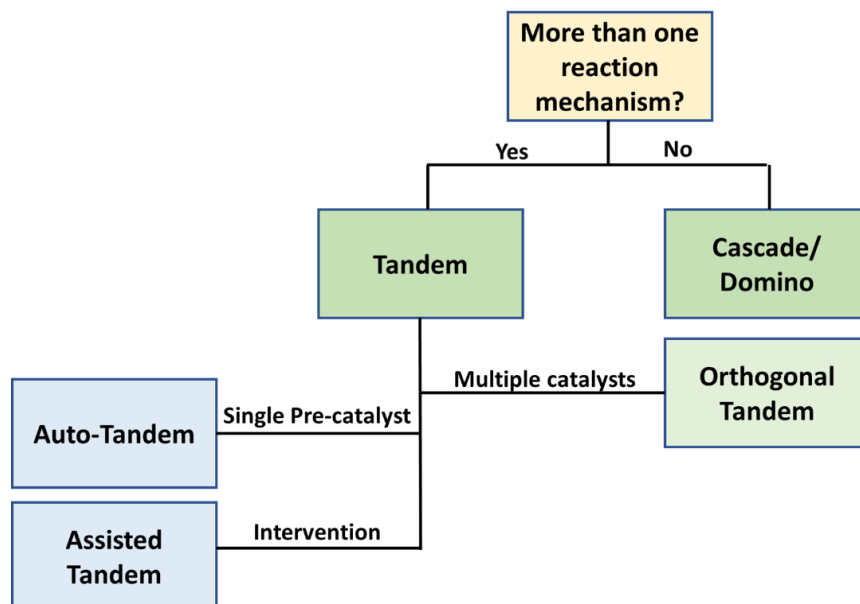
Scheme 1.3: Different types of Tandem catalytic processes

Orthogonal tandem catalysis:[53] This is a subclass of tandem catalysis where sequential transformation occurs involving two or more functionally distinct (non-interfering) catalysts /active sites.

Auto tandem catalysis:[14] In this subclass of tandem catalysis, a single catalyst promotes two or more distinct reactions. The catalytic processes occur spontaneously by cooperative interaction of species present from the outset of reaction.

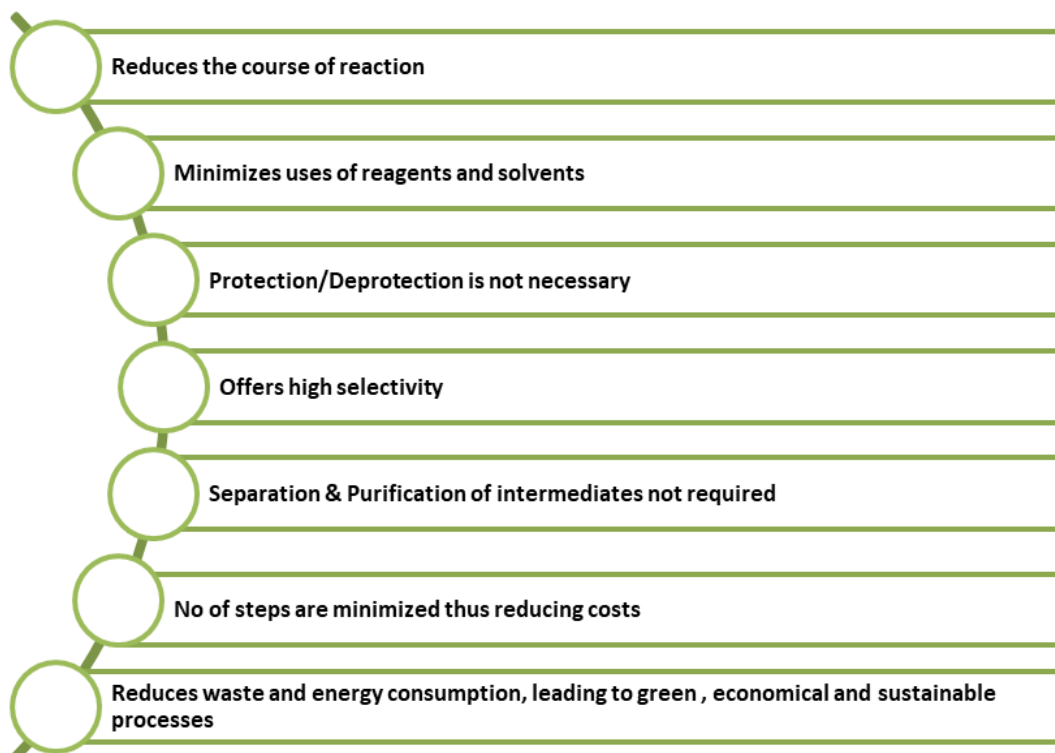
Assisted tandem catalysis:[55] This is a subclass of tandem catalysis where a change in the reaction conditions (except for catalyst addition) leads to a shift from one

catalytic mechanism towards another different mechanism. Also, the transformations are not concurrent.



Scheme 1.4. Steps to identify Tandem catalytic processes [86]

Advantages of Tandem catalytic process



1.7 Multifunctional Heterogeneous Catalysis:

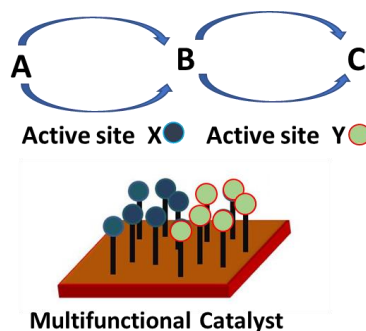


Fig 1.4. A pictorial representation of active sites on a multifunctional catalyst

Natural enzymes act on substrates in a sequential manner leading to products with high selectivity. In the past decade, enormous efforts have been made to mimic this nature's strategy to develop multifunctional heterogeneous catalysts. Multifunctional catalysts are used to perform tandem reactions to improve the economic viability of a chemical manufacturing process by minimizing the steps needed for isolation and purification of intermediates and catalyst. This results in a green, sustainable process with lower energy consumption as well as lower waste production. Though there is a significant progress in this direction, the one pot catalytic reactions haven't got general applications. This is because in general, a multifunctional catalyst should have appropriate active sites for different steps of a multistep reaction. This is primarily due to the difficulty in controlling one pot multistep reactions involving interactions between chemically reactive active sites and components leading to deactivation. Importantly, an active centre on such a multifunctional catalyst must be compatible with the substrates, intermediates, solvents and additives which are present throughout the reaction sequence and also the material must exhibit reaction selectivity. Hence, there is an obvious need to optimize a common operational window combining the individual reactions in the multistep reaction. One solution to this problem seems to be the multisite solid catalysts where the well optimized active sites are isolated spatially and are able to catalyse different steps involved in the reaction sequence. For example, in a bifunctional catalyst possessing different catalytic functions (such as an acidic and a basic site), one can visualize the catalysis of reactions happening in series on different catalytic sites completing a sequence. (Fig 1.4). Thus, it is clear that to design a near perfect multifunctional solid catalyst,

it would involve generating the active sites on a unique support. However, the material synthesis procedure to obtain such a catalyst is quite difficult and challenging. Nevertheless, literature reports different classes of multifunctional catalysts based on the number and types of catalytic active sites. The most common types of active sites encountered on multifunctional catalyst are, acidic, basic and metal sites. These sites and their literature examples are discussed in detail in Section 1.8. In general, acid sites are useful for catalysing reactions steps involving dehydration, hydrolysis, isomerization while the basic sites catalyse condensation / coupling reactions. Metals sites have good redox properties and are useful for oxidation, dehydrogenation and hydrogenation reactions. Those multifunctional catalysts which involve only two active sites are termed as bifunctional catalysts.

1.8 Classification of Bifunctional Heterogeneous Catalysts

1.8.1 Based on type of active sites

a) *Bifunctional Lewis and Brønsted acid sites:*

Zeolites are common examples of materials containing both Brønsted and Lewis acidic sites. The surface hydroxyl groups provide Brønsted acidity whereas the presence of Al^{3+} in the structure gives Lewis acidity. Moreover, the acidity can be modified using isomorphic substitution of trivalent metal ions. Epoxidation of double bonds by Lewis acid sites in the presence of peroxides and subsequent ring opening and rearrangement is catalysed by Brønsted acid sites. Other examples include Ti-Al-Beta and Ti-Al MCM-4.[56]

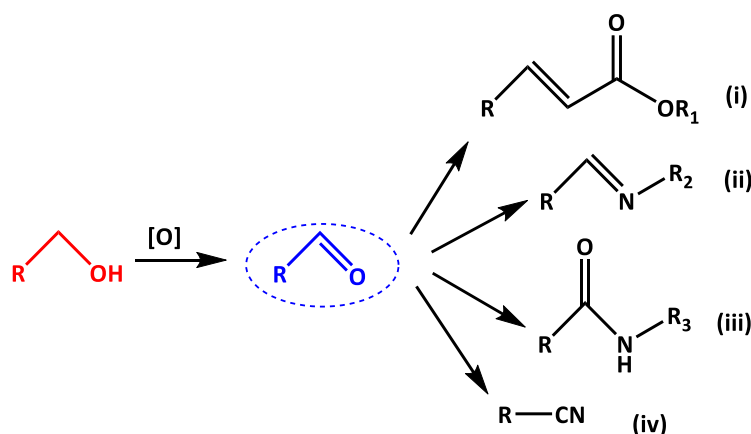
b) *Acid-metal bifunctional catalyst:*

Most of these materials involve supported or core shell structures with zeolites, silica or functionalized carbon supports. Reactions such as isomerization and hydrocracking employ acid-metal bifunctional catalysts. Heavy hydrocarbons are dehydrogenated on metal sites and then isomerized/cracked on acid sites and subsequently hydrogenated on metal sites. Nanoparticles of Cu, Ni, Pd and Pt are preferred for hydrogenation.[57, 58] Also, acid-metal sites help in hydrolysis followed by hydrogenation for biomass transformations. For example, conversion of cellulose or cellobiose to hexitols over metal nanoparticles supported on Al_2O_3 , CeO_2 , SiO_2 ,

TiO₂.^[59] Another process utilizing hydrolysis followed by oxidation using molecular oxygen is also catalysed by acid-metal sites. Fischer-Tropsch process also involves metal nanoparticles such as Co or Ru on acidic zeolites.^[60]

c) *Base-metal bifunctional catalyst:*

Usually a combination of metal nanoparticles (Pt, Pd, Ni and Cu) supported on metal oxides or mixed metal oxides form base-metal bifunctional catalysts. The strong Lewis base sites of the metal oxide O²⁻ catalyse condensation reaction where the weak Mn⁺ ions stabilize the enolate species.



Scheme 1.5. Oxidative -coupling/ condensation reactions catalysed by base-metal bifunctional catalyst

Table 1.1: Various base-metal bifunctional catalysts reported in literature

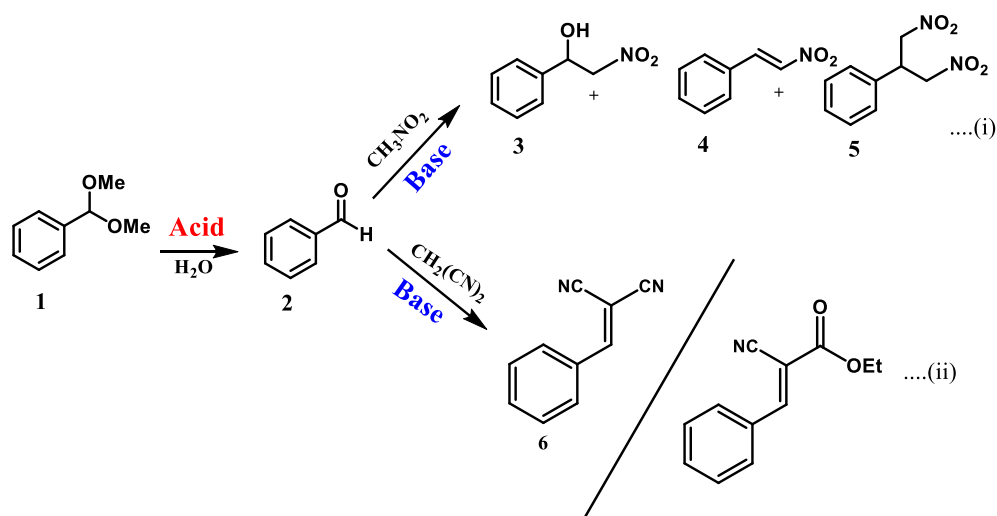
Sr No	Catalyst	Reaction Conditions	Reference
1	Au@Cu(II)-MOF	toluene, 110 °C, 22h	[61]
2	Pd(0)@UiO-68-AP	toluene, 80 °C, 38h,	[62]
3	Tris-LDH-X ₄ (PW ₉) ₂	acetonitrile, H ₂ O ₂ , 80 °C, 6h	[63]
4	CeO ₂	p-xylene, 150 °C, 12h	[64]
5	CeO ₂	mesitylene, 60 °C, 48h	[65]
6	Pd/AlOOH	toluene, K ₃ PO ₄ , 80 °C, 20h	[66]
7	Pd-Au@Mn(II)-MOF	toluene, 110 °C, 24h	[67]
8	Cu _x Ag _{1-x} /HT	xylene, 150 °C, 1h	[68]
9	Pt-Sn/C-Al ₂ O ₃	xylene, K ₃ PO ₄ , 155 °C, 48h	[69]
10	Pd-Si-Pr-NiXantphos/SiO ₂	mesitylene, LiOH, 100 °C, 24h	[70]
11	Au-Pd/HT	xylene, 120 °C, 5h	[71]
12	Co-N-C	H ₂ O/t-BuOH, LiOH, 70 °C, 24h	[72]
13	Ag-Al ₂ O ₃	toluene, Cs ₂ CO ₃ , 115 °C, 24h	[73]

For example, Cu supported on La-Mg oxides show greater promise for one step depolymerization of lignin by hydrogenolysis followed by hydrogenation to bio oils. Another platform for utilizing the base property is layered double hydroxides (LDH) which contain positively charged hydroxide sheets coordinated to metal and charge compensated by anions (carbonate, nitrate, chloride, hydroxide) in the interlayers. Mixed metal oxides derived from thermal decomposition of LDH show homogeneous dispersion of elements, better specific surface areas and basic properties. Also, these metal oxides exhibit weak Brønsted basicity due to -OH group and strong Lewis basicity due to O^{2-} ions. Reaction involving self-condensation of acetone, Michael addition reactions, and transesterification reactions are catalysed by these materials. Use of metal nanoparticles having oxidation property have been used for alcohol oxidation followed by condensation using basic supports. The base catalysed step leads to the formation of C-C, C-O and C-N linkages (Scheme 3). A brief review of such materials with references is presented in Table 1.

d) *Acid-base bifunctional catalyst:*

These sites can chemically interfere and hence they are spatially isolated. The presence of these sites help to catalyse a multistep cascade reaction in a single pot. Most often the catalytic processes involving hydrolysis of acetals over acid sites followed by condensation of the deprotected functional group with an active methylene compound occurs over base sites (Table 1.2). These solid catalysts are extremely advantageous as their homogeneous counterparts require the steps of neutralization. The two standard probe reactions studied for the acid-base activity of the material are:

- i) Deacetylation-Henry reaction
- ii) Deacetylation-Knoevenagel reaction



Scheme 1.6. Acid-base reactions catalysed by bifunctional catalysts

Table 1.2: Various acid-base bifunctional catalysts reported in literature

Sr No	Catalyst Description	Desired product	Reference
1	Sulphonic & amine functionalized mesoporous silica	4	[74]
2	MS-SO ₃ H@MS@MS-NH ₂	6	[55]
3	shell cross-linked micelles	4	[75]
4	Amino- and Sulfo-Bifunctionalized-MOF	6	[76]
5	MIL-101(Al)-NH ₂	6	[77]
6	MS-A@MS-B	6	[78]
7	DMAN grafting on mesoporous silicas containing sulfonic acids.	6	[79]
8	amino-modified silica aerogel	4	[80]
9	microporous MOF with a high density of OMSs and LBSs	6	[81]
10	Microporous organic nanotube-SO ₃ H & -NH ₂	6	[82]
11	Phosphor-doped hexagonal boron nitride Nanosheets	6	[83]
12	ZSM-5@Mg ₃ Si ₄ O ₉ (OH) ₄	6	[84]
13	Functionalized porous polymeric aromatic frameworks	6	[85]

1.8.2 Organic, inorganic and hybrid materials

Multifunctional catalysts can be also classified into three major categories namely Organic, Inorganic and combination of these two, Organic-Inorganic depending upon the components that constitute the material. (Fig 1.5)

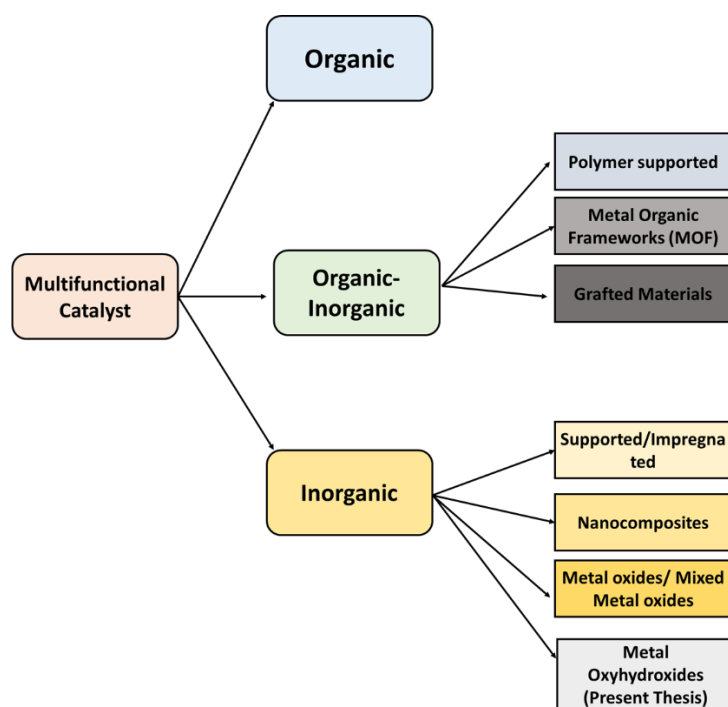


Fig 1.5: Classification of various multifunctional catalysts based on nanostructure[86]

Organic multifunctional nanocatalyst:

These include cross-linked polymeric solids functionalized with organic moieties or metal complexes. A common example of such materials are dendrimers which have been shown to catalyse a tandem Michael addition and nitroaldol condensation.[87] Another example includes a polymeric reagent constituting triarylphosphine-tertiary amine catalyst for one-pot Wittig reaction followed by reductive aldol reactions[88].

Organic-inorganic hybrid multifunctional nanocatalysts:

These hybrid materials are typically composed of inorganic component containing a metallic or ceramic nanostructure as well as an organic functionality consisting of a molecule, oligomers or macromolecules. The organic component may play a direct or an indirect role in catalysis. The materials where the organic group play a direct

role in catalysis are termed as grafted nano catalysts. An example of polymer supported nano catalyst is gold nanoclusters immobilized on cross linked polystyrene copolymers useful for aerobic oxidation of alcohols. Au nanoclusters on polymers were also shown to be active for tandem oxidative esterification followed by Michael addition of allylic alcohols with the Au clusters catalysing the oxidative esterification step whereas traces of Boron from NaBH₄ carrying out the Michael addition step.[89]

Covalent Organic Frameworks (COFs) are porous, crystalline materials containing light elements such as H, C, N & B. They do not contain any metal ions and have shown great promise as gas storage and photonic materials. Chemical functionalization of COFs is also possible. COF hybrids have been reported for numerous catalytic applications involving Suzuki coupling, C-H activation, nitro reduction, glycerol oxidations etc.[90] Recently, the multifunctional application of Pd (0) nanoparticles and organopalladium (II) complex supported on COF is reported for Cu free sequential Heck-Sonogashira cross coupling reactions under basic conditions.[91]

Metal Organic Frameworks (MOFs) are crystalline porous materials with metal ions/clusters and organic ligands bonded by coordinate bonds. A number of structures are possible by changing the metal ions and organic ligands. Bi, tri and tetrapodal organic carboxylates, N-heterocycles and phosphanates are the common ligands.[92] The catalytic applications of these materials arise due to coordinative unsaturation of metal ions, oxidation states, metal nanoparticles and basic nitrogen functionalities. The main advantage of these materials is high surface area and large pore volume, low framework density and distinct structural features. Multifunctional catalysts involving noble metals supported on MOFs and core shell nanostructures where the metal nanoparticles form the core surrounded by MOF shell have also been reported. Enormous work has been done to utilize MOFs for tandem catalysis involving oxidation / hydrogenation, oxidation / esterification, oxidation / condensation, deacetylation / condensation, coupling / cyclization and many such process. A thorough study on MOFs and its applications to tandem catalysis is presented in a review article by Dhakshinamoorthy et al. [93]

Grafted or encapsulated catalysts are materials where a covalent bonding between an organic molecule (active site) with an inorganic solid is achieved by means of sol-gel chemistry with surface hydroxyl groups being the anchoring site. This leads to heterogenization of a traditional homogeneous species thus preventing separation and recycling problems. The grafted organic molecules are usually accessible to the reactants to diffuse through the porous channels of the inorganic material. Many techniques have been improvised to precisely control the location of organic moieties on the surface of the supports. A key achievement in the field of grafted multifunctional catalysts is grafting chemically orthogonal active sites to catalyse cascade reactions. An example which is vastly studied is acid-base bifunctional sites on mesoporous silicas.[79]

Inorganic Multifunctional Nanocatalysts

Supported/Impregnated Catalysts: These catalysts consist of two components namely, a high surface area material called as a support along with a metal nanoparticle. These nanoparticles are distributed on the support which prevents agglomeration of the metal nanoparticles especially, at severe conditions of temperature and pressure. In most cases the support is inert. However strong chemical interactions between the support and metals have an influence on chemisorption properties for the reactant molecules. Au/CeO₂ is an excellent example for the synthesis of propargylamine.[94] The synthesis involves two steps namely, N-alkylation of alcohol followed by reaction of the secondary amine with an aldehyde and an alkyne. The Au⁰ atoms were shown to catalyse the N-alkylation step whereas the Au⁺¹ and Au⁺³ were required for the second step.[95, 96] A few other uses of Au supported materials were used for synthesis of azo compounds from nitro benzene and synthesis of benomidazolquinoxaline formed by oxidative coupling of glycerol with o-phenylenediamine derivatives.[97, 98] The use of bimetallic nanoparticles are generally preferred due to improved electronic properties. In these, generally noble metals such as Pt, Pd, Ir, Ru are combined with less expensive metals such as Al, Co, Fe, Mn and Cu. Bimetallic nanoparticles of Cu-Pd on graphene were shown to be active for the conversion of polyols to lactic acid.[99]

Nanocomposites: These have definite architecture containing domains of nano sized inorganic phases present on an interface with difference in chemical properties. This difference in chemical properties leads to distinctly different domain spaces making nanocomposites suitable for applications in multifunctional catalyst. CeO₂-Pt-SiO₂ was fabricated using Langmuir-Blodgett method. This material was used to catalyse a tandem reaction where methanol to CO and H₂ was decomposed over CeO₂-Pt interface whereas the Pt-SiO₂ interface used the CO and H₂ formed to hydroformylate ethylene.[100]

Metal oxides / Mixed metal oxides: These are non-noble metal nanocomposites catalysts synthesized using sol-gel method or coprecipitation method. For example Cu-ZrO₂ was effectively used for γ -valerolactone synthesis from levulinic acid.[101] This process involves a two-step hydrogenation followed by cyclization. Many such value-added products have been obtained from biomass using metal oxide catalysts.[102, 103]

Table 1.3: Advantages and Disadvantages of various Multifunctional Catalysts[86]

Multifunctional Catalyst	Advantages	Disadvantages
Organic nanocatalyst	Colloidal stability	Chemical stability, Difficulty in separation
Polymer Supported	Colloidal stability	Leaching, complex synthesis methods
Covalent Frameworks	Organic Organic reactions	Poor thermal stability, difficulty in preparation, poor diffusion and low catalyst yields
Metal frameworks	Organic Homogeneous active sites, rational synthesis methods	Expensive synthesis, poor chemical stability, poor diffusion
Grafted catalysts	Possibility of rational synthesis	Multiple steps in synthesis, leaching, possible deactivation of functional groups
Supported catalysts	inorganic Thermal stability	Leaching, sintering
Nanocomposites	Rational design, use of non-catalytic functionalities	

Major challenge faced in the development of multifunctional heterogeneous catalyst is that the chemically interfering active sites must remain active throughout the reaction sequence. Acid and base sites are commonly introduced by functionalizing the support. Protecting agents are commonly used during the functionalization of the support with $-\text{SO}_3\text{H}$ (acid sites) and $-\text{NH}_2$ (base sites). The main disadvantage of synthesizing such multifunctional materials is complex steps of preparation, use of toxic alkoxy grafting agents and non-uniformity of active sites. Also, there should not be leaching of active sites during the reaction processes (Polymer supported and nanoparticle supported catalysts). The use of noble metals enhances the costing of catalyst manufacture and in some cases toxic bases are used to assist the main catalyst, leading to environmental issues. These present interesting challenges in materials chemistry to develop new materials with robust and efficient bifunctional active sites without spatially isolating acidic and basic groups on a surface.

We believe that the inorganic metastable phases such as metal oxyhydroxides could be a practical option to make robust, inexpensive and easily scalable multifunctional catalyst. These materials are usually prepared by hydrolytic sol-gel technique and are intermediates between metal hydroxides and completely condensed metal oxides. As a result of this, metal oxyhydroxides have surface hydroxyl groups as well as metal oxygen linkages.

1.9 Material Characterization techniques

The work in this thesis mainly focuses on preparation of variety of materials hence, their characterization becomes inevitable to gain some knowledge about the active sites close to reality though, not actually prevailing under the reaction conditions. Some of the techniques used in this work are described below.

X-ray Diffraction: This is the most important characterization technique for identification of $\text{MO}(\text{OH})$ to confirm its phase purity. This technique involves interaction of electromagnetic radiation with a wavelength of 1 \AA with atoms of the solid. Crystalline materials such as metal oxyhydroxides can diffract X-rays due to comparable distances between the atoms in the crystal structure and incident wavelength of radiation. Based on the angle of incidence, the diffracted rays can interfere constructively leading to an enhanced intensity. This can be expressed by

the Bragg equation which relates the angle θ , wavelength of the rays (λ) and the lattice spacings (d_{hkl}) (Fig 1.6).

$$n\lambda = 2 d_{hkl} \sin\theta$$

A plot of the observed diffraction intensity against the Bragg angle θ is presented in a X-ray diffraction pattern of a powdered material. Based on the interference conditions each atom plane produces a series of reflections. From these, the interplanar spacings (d_{hkl}) is calculated from the Bragg equation. Each metal oxyhydroxide has a unique specific set of d values and intensities which are useful in the identification of the phase. Since XRD deals with long range order of the atoms, it is one of the most reliable ways to identify crystalline MO(OH) materials. In the present thesis, small and wide-angle X-ray analysis on the solid powder catalysts were analysed. The instrument specification are provided in the experimental section of each working chapter.

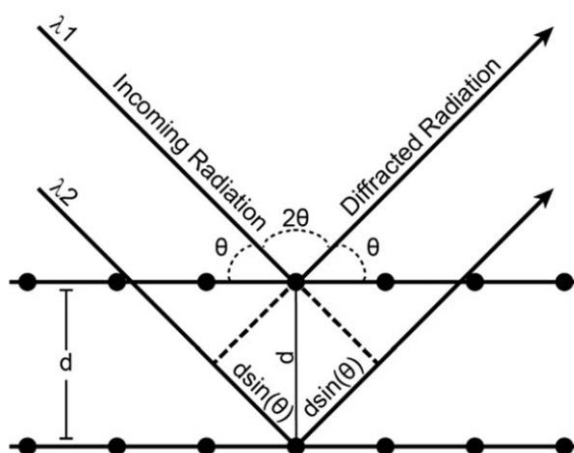


Fig 1.6: Schematic of representation of Bragg's law conditions[104]

Infrared spectroscopy: An infrared spectrum results due to the interaction of MO(OH) with electromagnetic radiation in the wavelength range 1-300 μm (10000-33 cm^{-1}). In this range, we observe excitation of vibration, rotation of molecules in the ground electronic state associated with stretching changes of the interatomic bonds and bending modifications of the interbond angles. Rotational energy levels and force constant of bonds are the basis of the frequency of radiation absorbed. A typical plot gives the frequency of incident radiation (either in cm^{-1} or μm) versus

percent radiation absorbed. This spectroscopy helps to identify shifts in vibrational state adsorbed molecules, investigate the nature of surface hydroxyl groups and adsorbed water. In the present thesis, the FT-IR measurements were carried out using Perkin Elmer FT-IR equipped with a ZnSe crystal as a detector. *In-situ*-FTIR measurements and Pyridine FTIR measurements were carried out using the same instruments with an additional Praying Mantis accessory developed by Harrick Scientific Products Inc.

Raman Spectroscopy: Raman spectroscopy deals with inelastic light scattering in a material and provides vibrational, rotational information about the material. Horiba JY make LabRAMHR800 spectrometer with a laser of 632nm was used for characterization in the present thesis. The average power used was 0.6mW.

X-ray Photoelectron spectroscopy (XPS): Detection and analysis of photoelectrons ejected after interactions of solid with MO(OH) forms the basis of photoelectron spectroscopy. The radiations are generally X-rays (X-ray photoelectron spectroscopy), which removes single core level electron. The overall expression for the kinetic energy E_k can be given by

$$E_k = h\nu - E_B - \phi$$

E_B : binding energy of the ejected electron

$h\nu$: photon energy

ϕ : work function of spectrophotometer.

Each element has its own distinct set of binding energies. Thus, the spectral lines arising out of the plot of measured photoelectron intensity as a function of binding energy can be correlated to atomic orbital energies. The advantage of this technique is the information about oxidation state and surface composition such as doping and contributions due to -OH group and M-O-M linkages to a depth of 8-10nm. XPS studies were performed using VG Microtech Multilab ESCA 3000 spectrometer under Mg $K\alpha$ X-ray source ($h\nu = 1253.6$ eV) and Thermo Kalpha+ spectrometer using Al $K\alpha$ radiation ($h\nu = 1486.6$ eV).

Electron Microscopy: All MO(OH) prepared in this work have small particle sizes and hence are routinely examined using transmission electron microscopy (TEM) and scanning electron microscopy (SEM). SEM provides a 3D image and information regarding morphology and microtopography whereas TEM provides a 2D image. High Resolution TEM (HRTEM) helps to study phase transformations and structural information. In this thesis TEM images were obtained on Tecnai F-20 instrument operating at 200kV. Also, HR-TEM images were obtained on JEOL JEM F200. (CMC, CSIR-NCL). SEM images were obtained on Quanta 200 instrument equipped with energy dispersed X-ray detector (EDS) at CSIR NCL.

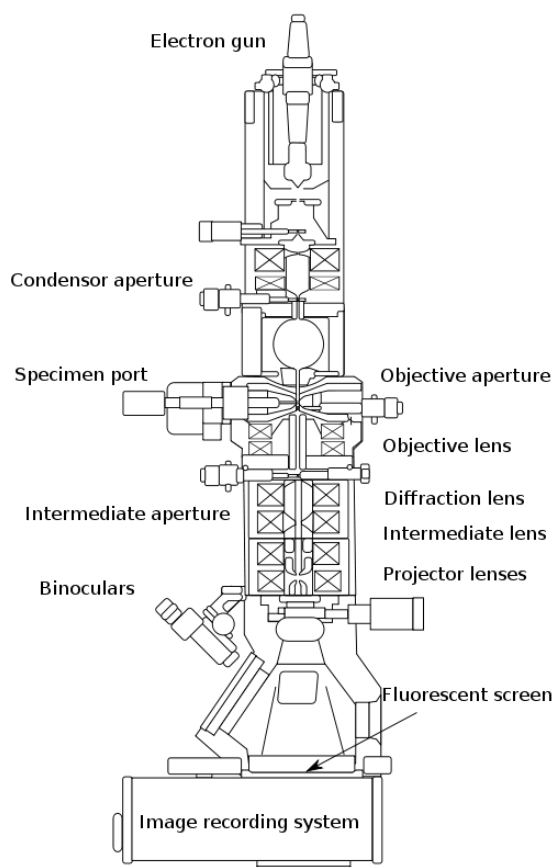


Fig 1.7: Layout of optical components in Transmission Electron Microscopy [105]

Thermogravimetric analysis (TGA): Temperature dependent weight loss is provided by gravimetric thermograms. These are obtained by gradually heating a sample at constant rate (2-10 °C/min) with its weight being measured continuously

throughout the process using a balance. Metal Oxyhydroxides contain -OH and hence lose weight between 250-400 °C due to the dehydroxylation reaction.



Fine grained sample also contains appreciable amount of adsorbed water which gives weight loss between 100 -200 °C and is distinct from dehydroxylation. TGA was done on TGA-7 PerkinElmer instrument under N₂ up to 800 °C with the heating rate of 10 °C /minute

Temperature Programmed Desorption (TPD): To study the acidity and basicity of materials, NH₃ and CO₂ TPD studies, respectively, were carried out. These molecules interact with the acid and base sites of the materials and are desorbed depending upon the strength of interaction on applying steady increase in temperature. The desorbed probe molecule is detected by a TCD (Thermal Conductivity Detector) and is quantified. Samples were analysed on Micromeritics chemisorbed 2120 instrument with Helium as the carrier gas.

Gas Chromatography (GC) & GCMS: Gas chromatography (GC) is an analytical tool used to separate and analyze samples that are vaporized without thermal decomposition. The instrumentation involves an injector which is maintained above the boiling points of all the volatile liquid products to be analysed. The vapours are carried by a carrier gas such as helium or nitrogen and the different products are separated by a column based on the retention times. The vapours are then directed towards a detector which can be an FID (Flame ionization Detector) or Mass Spectrometer. The reactions were monitored using an Agilent 7890B Gas Chromatograph using HP-5 column and N₂ as a carrier gas using standards. The products were further confirmed using QP-Ultra 2010 GC-MS Shimadzu instrument on a RTX-5 column using helium as a carrier gas, at an ionization source temperature of about 200 °C and interface temperature of 210 °C in EI mode.

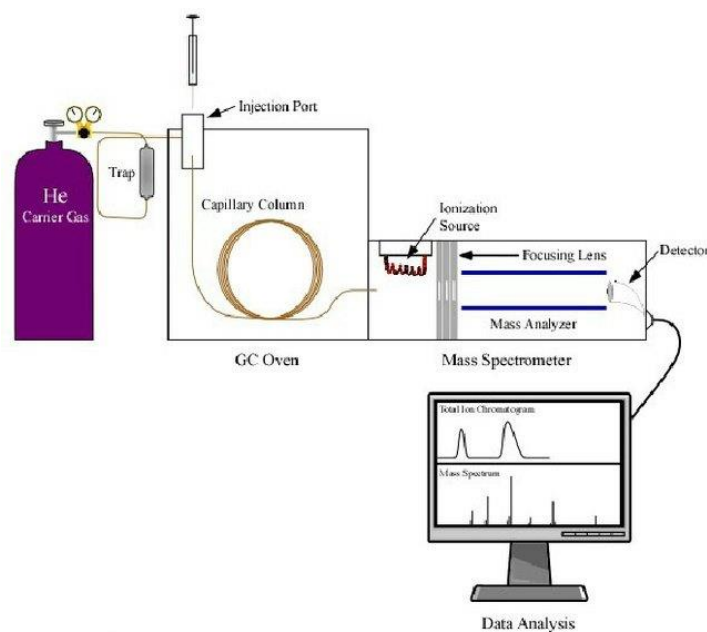


Fig 1.8 : Schematic representation of GC-MS[106]

High Performance Liquid Chromatography (HPLC): This is an analytic tool used to separate and identify liquid mixtures by passing the mobile phase at high pressures through a packed column. This technique is useful for those liquids which have high boiling points and cannot be eluted in GC. The reaction products in chapter 5 were analysed by Agilent HPLC RP-18 column using water: Methanol 9:1 with a phosphate buffer (0.001M) as the mobile phase.

Nuclear Magnetic Resonance (NMR): NMR is a physical phenomenon happening when an atomic nucleus is subjected to external magnetic field along with an electromagnetic radiation of specific frequency. By detecting the absorption signals, the NMR spectra can be obtained. In the present thesis, isolated products were characterized by ^1H -NMR and ^{13}C -NMR using CDCl_3 (0.01% TMS) as solvent using a Bruker instrument (200 MHz & 500MHz frequency).

1.10 Scope and Objectives of thesis

There are several types of heterogeneous catalysts developed for various reactions. However, the need for catalysts with better functionalities, reliable performance and exceptional stabilities are always sought after. Multifunctional heterogeneous

catalysts for one-pot organic transformations is one of the recent challenges, for which several groups contributed many worthy ideas. However, the literature presented the pros and cons of these different types of multifunctional heterogeneous catalysts. One of the major drawbacks in the existing approaches is the use of multiple steps of protection and deprotection synthetic strategies to prepare the catalysts. MO(OH) are special class of materials that is very well known to mankind from very early times due to their uses as pigments. Moreover, the literature on metal oxides for catalysis is enormous whereas metal oxyhydroxides haven't been used as active catalyst materials before our work. Besides, the synthesis of metal oxyhydroxides involve relatively easy soft chemistry techniques like sol-gel, hydrothermal, unlike functionalized materials. Also, metal oxyhydroxides containing different metals can be synthesized, choice of metal atom can even introduce redox behaviour in the material for catalysing oxidation reactions. Thus, metal oxyhydroxides can have acid, base as well as redox behaviour and can be cheap and simpler multifunctional catalysts compared to other surface functionalized and noble metal-based materials. The abundant presence of surface functional groups and the existence of chemical equilibrium between surface -OH and -O⁻ sites presented a perfect ground for multiple functionalities. Realizing the opportunity and need to exploit the multiple functionalities of MO(OH) in catalysis, we prepared several oxyhydroxides and studied their efficiency in catalyzing multi step organic transformations in one-pot. Although, we conducted our study to use the organic transformations to probe the catalyst to gain insights about the active sites, we also explored the substrate scope of the catalyst wherever possible. The specific objectives of the present thesis are:

- Synthesis and characterization of metal oxyhydroxide materials viz. (FeO(OH), CoO(OH), MnO(OH), CrO(OH), AlO(OH), WFeCoO(OH)).
- Exploring the use of various Metal oxyhydroxides as an active catalyst.
- Study of bifunctional activity of metal oxyhydroxides for Deacetylation-Knoevenagel condensations, Deacetylation-Henry reaction, C-N and C-C coupling reactions and cyclohexane oxidation reactions.

- Identifying the origin of bifunctional activity in catalysis using spectroscopic and chemisorption techniques and thereby improving the activity by chemical methods.
- To elucidate plausible reaction pathways / understand structure-activity relationships in respective catalysts and reactions

1.11 Organization of thesis

The thesis is divided into a total of 6 chapters and the organization of each chapter is given below.

Chapter 1: This chapter gives introduction to Metal Oxyhydroxides, their structures, synthesis method, available applications. A literature review of heterogeneous tandem catalysis is also discussed with comparative study on the active sites responsible for catalysis. This chapter also deals with analytical tools required for characterization of metal oxyhydroxides and the tandem catalysis products. This Chapter also provides the blueprint about the intent of the thesis.

Chapter 2: A study of acid-base behaviour of hierarchically condensed phases consisting of Hydroxides, Oxyhydroxides and Oxides of Cr, Mn, Co, Al was done. All the three phases $M(OH)_x$, $MO(OH)$ and $M_x(O)_y$ show acid-base bifunctional behavior to varying extent. The strength of acid sites is stronger on $MO(OH)$ while the strength of basic sites is stronger on $M(OH)_x$. $MO(OH)$ are versatile due to its stability and two types of active sites OH/O^- and O^{2-}

Chapter 3 is divided into two sub chapters **3a** & **3b** dealing with acid-base properties of $FeO(OH)$

Chapter 3a: A study of acid-base behaviour of polymorphs of $FeO(OH)$ was undertaken in this chapter. Within a same $FeO(OH)$, its polymorphs α , β , γ and δ all show bifunctional acid-base reactivity. The origin of acid and base bifunctional property is due to the surface chemical equilibrium between $FeO(OH)$ and $FeOO-$ groups. The difference in the selectivity with the polymorphs is probably due to the different types of $FeO(OH)$ sites and the density of the sites present on the crystal facets of the polymorphs.

Chapter 3b: In this chapter, γ - $FeO(OH)$ was demonstrated as an efficient solid base catalyst for the synthesis of pseudoionones (PS). High activity can be attributed to the formation of chemically stable Brønsted basic sites ($-O^-$) of the surface hydroxyl

groups. In the presence of water, there was an enhancement of catalytic activity by several folds due to the generation of basic sites.

Chapter 4 is sub divided into **4a** & **4b** dealing with redox-base property of metal oxyhydroxides

Chapter 4a: This chapter deals with sequential transformation of benzyl alcohol to a variety of C-C and C-N coupling products on layered K- α -CrO(OH). The transformations were feasible because of the co-existence of redox Cr(III) and basic sites (O⁻ and O²⁻) on the surface of the K- α -CrO(OH). The presence of electron rich sites (O²⁻) due to doping of K and the surface hydroxyl groups were found to be the basic sites on the catalysts using spectroscopy and thermal probe studies.

Chapter 4b: A study on usefulness of oxide-oxyhydroxide interface was carried out over a defect manganese oxyhydroxide sample MnO_x(OH). An oxide impurity in MnO_x(OH) was identified and thoroughly characterized. Its effect on sequential oxidation-condensation reaction was studied and its superiority over a pure MnO(OH) catalyst was explored. The oxide impurity increased O²⁻ basic sites on MnO_x(OH).

Chapter 5: This chapter studies a mixed metal oxyhydroxide WFeCoO(OH) for catalytic conversion of cyclohexane to adipic acid conversion in one pot. A high surge in Lewis acidity was obtained by W doping in Co-Fe matrix. The high acidity and W sites are responsible for activity. DFT calculations indicated a decrease in deprotonation energies for WFeCoO(OH) as compared to undoped CoO(OH).

Chapter 6: This chapter to gives summary and future scope of the present work.

1.12 References

- [1] J. Wisniak, *Educación química*, 2010, **21**, 60-69.
- [2] R. Winderlich, *Journal of Chemical Education*, 1949, **26**, 358.
- [3] J. K. Nørskov, F. Abild-Pedersen, F. Studt and T. S. Bligaard, *Proceedings of the National Academy of Sciences*, 2011, **108**, 937-943.
- [4] V. Pattabathula and J. Richardson, *Chem. Eng. Prog*, 2016, **112**.
- [5] G. B. Taylor, T. H. Chilton and S. L. Handforth, *Industrial & Engineering Chemistry*, 1931, **23**, 860-865.
- [6] L. N. Arthur, *U.S. Patent No. 2,142,855*, 1939.

- [7] F. Haber, *Zeitschrift für Elektrochemie und angewandte physikalische Chemie*, 1913, **19**, 53.
- [8] M. Appl, *A century of chemical engineering*, New York, 1982, 29-53.
- [9] A. Primo and H. Garcia, *Chemical Society Reviews*, 2014, **43**, 7548-7561.
- [10] H. Schulz, *Applied Catalysis A: General*, 1999, **186**, 3-12.
- [11] C. N. Satterfield, *Heterogeneous catalysis in practice*, McGraw-Hill New York, 1980.
- [12] C. N. Satterfield, *Heterogeneous catalysis in industrial practice*, 1991.
- [13] N. Mizuno and M. Misono, *Chemical Reviews*, 1998, **98**, 199-2[18]
- [14] P. Trivedi, L. Axe, J. Dyer, *Colloids and Surfaces A: Physicochemical and Engineering Aspects*, 2001, **191**, 107-121.
- [15] M. M. Benjamin, J. Leckie and I. Science, *Journal of Colloid and Interface Science*, **83**, 410-419.
- [16] J. D. Ostergren, G. E. Brown Jr, G. A. Parks, P. Persson and I. Science, *Journal of Colloid and Interface Science*, 2000, **225**, 483-493.
- [17] A. S. Lozhkomoev, G. Savel'ev, N. V. Svarovskaya and M. Lerner, *Russian Journal of Applied Chemistry*, 2009, **82**, 581-586.
- [18] L. S. Balistrieri and T. Chao, *Geochimica et Cosmochimica Acta*, 1990, **54**, 739-751.
- [19] G. Horányi and E. Kálmán *Journal of colloid and interface science*, 2004, **269**, 315-319.
- [20] J. M. Zachara, D. C. Girvin, R. L. Schmidt, C.T Resch *Environmental science & technology*, 1987, **21**, 589-594.
- [21] S. Pechenyuk, L. Kuz'mich, E. Kalinkina and S. Matveenko, *Russian chemical bulletin* 1998, **47**, 560-565.
- [22] L. N. Ho, T. Ishihara, S. Ueshima, H. Nishiguchi and Y. Takita, *Journal of colloid and interface science*, 2004, **272**, 399-403.
- [23] Y.-X. Zhang, X.-Y. Yu, Z. Jin, Y. Jia, W.-H. Xu, T. Luo, B.-J. Zhu, J.-H. Liu and X. Huang, *Journal of Materials Chemistry*, 2011, **21**, 16550-16557.
- [24] D. Jia, C. Li and A. Li, *RSC advances*, 2017, **7**, 24430-24437.
- [25] D. Fu, Z. He, S. Su, B. Xu, Y. Liu and Y. Zhao, *Journal of colloid and interface science* 2017, **505**, 105-114.
- [26] Y. Zhang, X. Zhou, Z. Liu, B. Li, Q. Liu and X. Li, *RSC advances*, 2016, **6**, 6695-6701.
- [27] W. Bai, J. Zheng and Q. Sheng, *Electroanalysis*, 2013, **25**, 2305-2311.
- [28] K. K. Lee, P. Y. Loh, C. H. Sow and W. S Chin, *Biosensors and Bioelectronics* 2013, **39**, 255-260.
- [29] Z. Yang, C. Qi, X. Zheng and J. Zheng, 2015, *Journal of Electroanalytical Chemistry*, **754**, 138-142.
- [30] Z. Yang, X. Yan, Z. Li, X. Zheng and J. Zheng, *Analytical Methods* 2016, **8**, 1527-1531.
- [31] J.-W. Wang and Y.-M. Kuo, *Journal of Nanomaterials* 2013, **2013**, 1.

- [32] S. Zhuiykov and V. Dowling, *Measurement Science and Technology*, 2008, **19**, 024001.
- [33] R.-J. Wu, J.-G. Wu, T.-K. Tsai and C.-T. Yeh, *Sensors and Actuators B: chemical*, 2006, **120**, 104-109.
- [34] Y.-H. Hsu, A. T. Nguyen, Y.-H. Chiu, J.-M. Li and Y.-J. Hsu, *Applied Catalysis B: Environmental*, 2016, **185**, 133-140.
- [35] S. B. Rawal, A. K. Chakraborty and W.-I. Lee, *Bulletin of the Korean Chemical Society*, 2009, **30**, 2613-2616.
- [36] J. Huang, Q. Shang, Y. Huang, F. Tang, Q. Zhang, Q. Liu, S. Jiang, F. Hu, W. Liu and Y. Luo, *Angewandte Chemie International Edition*, 2016, **55**, 2137-2141.
- [37] M. C. Pereira, E. M. Garcia, A. C. da Silva, E. Lorençon, J. D. Ardisson, E. Murad, J. D. Fabris, T. Matencio, T. de Castro Ramalho and M. Rocha, *Journal of Materials Chemistry*, 2011, **21**, 10280-10282.
- [38] J. Y. Kim, D. H. Youn, K. Kang and J. S. Lee, *Angewandte Chemie International Edition*, 2016, **55**, 10854-10858.
- [39] J. A. Seabold and K.-S. Choi, *Journal of the American Chemical Society*, 2012, **134**, 2186-2192.
- [40] X. Xu, K. Bi, K. Huang, C. Liang, S. Lin, W. J. Wang, T. Z. Yang, J. Liu, D. Y. Fan, H. J. Yang, Y. G. Wang and M. Lei, *Journal of Alloys and Compounds*, 2015, **644**, 485-490.
- [41] Z. Li, Z. Xie, Y. Zhang, L. Wu, X. Wang and X. Fu, *The Journal of Physical Chemistry C*, 2007, **111**, 18348-18352.
- [42] A. A. Jelle, M. Hmadeh, P. G. O'Brien, D. D. Perovic and G. A. Ozin, *ChemNanoMat* 2016, **2**, 1047-1054.
- [43] L. Song, C. Chen, S. Zhang and Q. Wei, *Catalysis Communications*, 2011, **12**, 1051-1054.
- [44] H.-B. Jiang, H.-J. Jiang, K. Su, D.-M. Zhu, X.-L. Zheng, H.-Y. Fu, H. Chen and R.-X. Li, *Applied Catalysis A: General*, 2012, **447-448**, 164-170.
- [45] A. Ghorbani-Choghamarani and B. Tahmasbi, *New Journal of Chemistry*, 2016, **40**, 1205-1212.
- [46] Z. Xu, J. Yu and M. Jaroniec, *Applied Catalysis B: Environmental*, 2015, **163**, 306-312.
- [47] Y. Zhou, H. Fu, X. Zheng, R. Li, H. Chen and X. Li, *Catalysis Communications*, 2009, **11**, 137-141.
- [48] J. Huang, Y. Wang, J. Zheng, W.-L. Dai and K. Fan, *Applied Catalysis B: Environmental*, 2011, **103**, 343-350.
- [49] H. Yang, S. Ji, X. Liu, D. Zhang and D. Shi, *Science China Chemistry*, 2014, **57**, 866-872.
- [50] C. Wang, J. Ding, G. Zhao, T. Deng, Y. Liu and Y. Lu, *ACS Applied Materials & Interfaces*, 2017, **9**, 9795-9804.
- [51] E. J. Doskocil and G. M. Mueller, *Journal of Catalysis*, 2005, **234**, 143-150.

- [52] Y. Liu, X. Liu, Y. Zhao and D. D. Dionysiou, *Applied Catalysis B: Environmental*, 2017, **213**, 74-86.
- [53] D. E. Fogg and E. N. Santos, *Coordination chemistry reviews*, 2004, **248**, 2365-2379.
- [54] L.F. Tietze, *Chemical reviews*, 1996, **96**, 115-136.
- [55] P. Li, C.-Y. Cao, H. Liu, Y. Yu and W.-G Song, *Journal of Materials Chemistry*, 2013, **1**, 12804-12810.
- [56] A. Corma, M. Iglesias and F. Sanchez, *Chemical Communications*, 1995, **16**, 1635-1636.
- [57] A. M. Smith and R. Whyman, *Chemical Reviews*, 2014, **114**, 5477-5510.
- [58] S.-C. Qi, L. Zhang, H. Einaga, S. Kudo, K. Norinaga and J.-i. Hayashi, *Journal of Materials Chemistry A*, 2017, **5**, 3948-3965.
- [59] A. Fukuoka and P. Dhepe, 2015, U.S. Patent No. 8,945,309.
- [60] Q. Zhang, K. Cheng, J. Kang, W. Deng and Y. Wang, *ChemSusChem*, 2014, **7**, 1251-1264.
- [61] J.-S. Wang, F.-Z. Jin, H.-C. Ma, X.-B. Li, M.-Y. Liu, J.-L. Kan, G.-J. Chen and Y.-B. Dong, *Inorganic chemistry*, 2016, **55**, 6685-6691.
- [62] Y.-A. Li, S. Yang, Q.-K. Liu, G.-J. Chen, J.-P. Ma and Y.-B. Dong, *Chemical Communications*, 2016, **52**, 6517-6520.
- [63] K. Liu, Y. Xu, Z. Yao, H. N. Miras and Y. Song, *ChemCatChem*, 2016, **8**, 929-937.
- [64] M. Tamura and K. Tomishige, *Angewandte Chemie International Edition*, 2015, **54**, 864-867.
- [65] Z. Zhang, Y. Wang, M. Wang, J. Lu, C. Zhang, L. Li, J. Jiang, and F. Wang, *Catalysis Science & Technology*, 2016, **6**, 1693-1700.
- [66] M. S. Kwon, N. Kim, S. H. Seo, I. S. Park, R. K. Cheedra and J. Park, *Angewandte Chemie International Edition*, 2005, **44**, 6913-6915.
- [67] G.-J. Chen, H.-C. Ma, W.-L. Xin, X.-B. Li, F.-Z. Jin, J.-S. Wang, M.-Y. Liu and Y.-B. Dong, *Inorganic chemistry*, 2016, **56**, 654-660.
- [68] J. Xu, H. Yue, S. Liu, H. Wang, Y. Du, C. Xu, W. Dong and C. Liu, *RSC advances*, 2016, **6**, 24164-24174.
- [69] K. Wu, W. He, C. Sun and Z. Yu, *Tetrahedron Letters*, 2016, **57**, 4017-4020.
- [70] T. T. Dang, S. P. Shan, B. Ramalingam and A. Seayad, *RSC Advances*, 2015, **5**, 42399-42406.
- [71] X. Liu, R. S. Ding, L. He, Y. M. Liu, Y. Cao, H. Y. He and K. Fan, *ChemSusChem*, 2013, **6**, 604-608.
- [72] L. Zhang, A. Wang, W. Wang, Y. Huang, X. Liu, S. Miao, J. Liu and T. Zhang, *ACS Catalysis*, 2015, **5**, 6563-6572.
- [73] K. i. Shimizu, R. Sato and A. Satsuma, *Angewandte Chemie International Edition*, 2009, **48**, 3982-3986.
- [74] Y. Huang, S. Xu and V. Lin, *Angewandte Chemie International Edition*, 2011, **50**, 661-664.

- [75] L.-C. Lee, J. Lu, M. Weck and C. W. Jones, *ACS Catalysis*, 2016, **6**, 784-787.
- [76] H. Liu, F.-G. Xi, W. Sun, N.-N. Yang and E. Gao, *Inorganic chemistry*, 2016, **55**, 5753-5755.
- [77] T. Toyao, M. Fujiwaki, Y. Horiuchi and M. Matsuoka, *Rsc Advances*, 2013, **3**, 21582-21587.
- [78] P. Li, C.-Y. Cao, Z. Chen, H. Liu, Y. Yu and W.-G Song, *Chemical Communications*, 2012, **48**, 10541-10543.
- [79] E. Gianotti, U. Diaz, A. Velty and A. Corma, *Catalysis Science & Technology*, 2013, **3**, 2677-2688.
- [80] X. Feng, L. Wang, X. Yao, H. Dong, X. Wang and Y. Wang, *Catalysis Communications*, 2017, **90**, 106-110.
- [81] H. He, F. Sun, B. Aguila, J. A. Perman, S. Ma and G. Zhu, *Journal of Materials Chemistry A*, 2016, **4**, 15240-15246.
- [82] H. Zhang, L. Xiong, Z. He, A. Zhong, T. Wang, Y. Xu and K. Huang, *New Journal of Chemistry*, 2016, **40**, 7282-7285.
- [83] J. Zhao, B. Lin, Y. Zhu, Y. Zhou and H. Liu, *Catalysis Science & Technology*, 2018, **8**, 5900-5905.
- [84] D. Wang, B. Wang, Y. Ding, H. Wu and P. Wu, *Chemical Communications*, 2016, **52**, 12817-12820.
- [85] E. Merino, E. Verde-Sesto, E. M. Maya, M. Iglesias, F. I. Sánchez and A. Corma, *Chemistry of Materials*, 2013, **25**, 981-988.
- [86] D. Jagadeesan, *Applied Catalysis A: General*, 2016, **511**, 59-77.
- [87] R. van Heerbeek, P. C. J. Kamer, P. W. N. M. van Leeuwen and J. N. H. Reek, *Chemical Reviews*, 2002, **102**, 3717-3756.
- [88] Y. Teng, J. Lu and P. H. Toy, *Chemistry—An Asian Journal*, 2012, **7**, 351-359.
- [89] H. Miyamura and S. Kobayashi, *Accounts of chemical research*, 2014, **47**, 1054-1066.
- [90] R. K. Sharma, P. Yadav, M. Yadav, R. Gupta, P. Rana, A. Srivastava, R. Zbořil, R. S. Varma, M. Antonietti and M. B. Gawande, *Materials Horizons*, 2020, **7**, 411-454.
- [91] J. Liu, L. Chen, H. Cui, J. Zhang, L. Zhang and C.-Y. Su, *Chemical Society Reviews*, 2014, **43**, 6011-6061.
- [92] T.-H. Chen, I. Popov, W. Kaveevivitchai and O. Miljanić, *Chemistry of Materials*, 2014, **26**, 4322-4325.
- [93] A. Dhakshinamoorthy and H. Garcia, 2014, *ChemSusChem*, **7**, 2392-2410.
- [94] P. Concepción, S. Carrettin and A. Corma, *Applied Catalysis A: General*, 2006, **307**, 42-45.
- [95] A. Corma, J. Navas and M. Sabater, *Chemistry—A European Journal*, 2012, **18**, 14150-14156.

- [96] X. Zhang and A. Corma, *Angewandte Chemie International Edition*, 2008, **47**, 4358-4361.
- [97] A. Corma and P. Serna, *Science*, 2006, **313**, 332-334.
- [98] A. Grirrane, A. Corma and H. García, *Science*, 2008, **322**, 1661-1664.
- [99] X. Jin, L. Dang, J. Lohrman, B. Subramaniam, S. Ren and R. V. Chaudhari, *ACS Nano*, 2013, **7**, 1309-1316.
- [100] Y. Yamada, C.-K. Tsung, W. Huang, Z. Huo, S. E. Habas, T. Soejima, C. E. Aliaga, G. A. Somorjai and P. Yang, *Nature chemistry*, 2011, **3**, 372.
- [101] A. M. Hengne and C. V. Rode, *Green Chemistry*, 2012, **14**, 1064-1072.
- [102] F. Li, T. Lu, B. Chen, Z. Huang and G. Yuan, *Applied Catalysis A: General*, 2014, **478**, 252-258.
- [103] A. Wang and T. Zhang, *Accounts of Chemical Research*, 2013, **46**, 1377-1386.
- [104] C. V. Stan, C. M. Beavers, M. Kunz and N. Tamura, *Quantum Beam Science*, 2018, **2**, 4.
- [105] D. B. Williams and C. B. Carter, in *Transmission electron microscopy*, Springer, 1996, pp. 3-17.
- [106] G. L. Shubin Wu and R. Lou, *Applications of Gas Chromatography*, 2012, 41.

Chapter 2

Role of surface hydroxyl groups on hierarchically condensed phases (Hydroxides, Oxyhydroxides & Oxides) : Insight into surface acidity and basicity

2.1 Introduction

Heterogeneous catalysts for one-pot sequential organic transformations have attracted the attention of both academic and industrial researchers in recent times.[1] Metrics of green chemistry and economic viability of a chemical process are improved in such one-pot transformations as the necessity to remove the catalyst or purify and separate the products after each step is circumvented.[2] Invariably, the presence of catalytic active sites such as an acid and a base could be threatening the efficacy of processes when used in a homogeneous phase. The catalysts used in such processes are expected to contain different types of catalytic active sites in spatially isolated manner on the same material [3-5] without the risk of neutralization in order to reliably catalyze different steps of a reaction sequence in one-pot. [6, 7] Acid-base bifunctional catalysts are traditionally prepared by grafting alkoxyated short organic chains containing acidic $-\text{SO}_3\text{H}$ or basic $-\text{NH}_2$ groups on to silica supports.[8, 9] In addition to the use of toxic alkoxy agents almost all the studies paid special attention to spatially isolate the acidic and basic groups through multiple protection and deprotection steps making the synthesis protocol tedious.[10] Examples of such materials include cross linked micelle [11] uncalcined zeolites[12], core shell $\text{SO}_3\text{H-Si-NH}_2$ [13]. In Chapter 1 of the thesis, robustness of the surface hydroxyl groups on metal oxyhydroxides and its acid-base bifunctionality were discussed. Our hypothesis was that the acid-base equilibrium of surface hydroxyl groups could be the origin of the bifunctional sites. Metal oxyhydroxides being the metastable intermediates between metal hydroxides and metal oxides (Fig 2.1), it would be interesting to understand the activity of surface hydroxyl groups on all these three materials. Hence in this work, the bifunctional catalytic activity of all hierarchically condensed phases such as metal hydroxides, metal oxyhydroxides and metal oxides of different metals such as Cr, Mn, Co and Al and their catalytic activity were explored. Strong evidence for the participation of surface hydroxyl groups in each of the condensed phases is provided. The catalytic activity of these phases were tested for one-pot hydrolysis-condensation reactions where a chemically protected acetal is hydrolysed to form aldehyde (using acidic sites) which subsequently undergoes condensation reactions (using basic sites). The C-C coupling reaction is important industrially and is relevant in the manufacture of pharmaceutical products.[14]

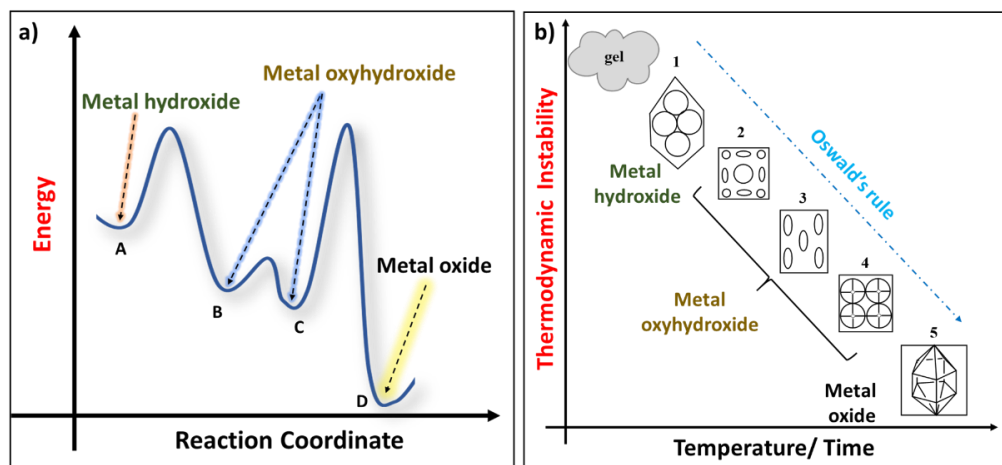


Fig 2.1. a) &b) Thermodynamic stability of Metal Hydroxides, Metal Oxyhydroxides and Metal Oxides

2.2 Experimental Section

Materials

Chromium nitrate ($\text{Cr}(\text{NO}_3)_3 \cdot 9\text{H}_2\text{O}$) manganese chloride tetrahydrate ($\text{MnCl}_2 \cdot 4\text{H}_2\text{O}$), aluminium chloride hexahydrate ($\text{AlCl}_3 \cdot 6\text{H}_2\text{O}$) and sodium hydroxide (NaOH) were obtained from SD fine chemicals. Cobaltous nitrate hexahydrate ($\text{Co}(\text{NO}_3)_2 \cdot 6\text{H}_2\text{O}$) from Himedia chemicals. Cetyl trimethylammonium bromide (CTAB), thionyl chloride (SOCl_2) were purchased from Thomas Baker. Benzaldehydedimethyl acetal, benzaldehyde, malononitrile, mercuric nitrate monohydrate ($\text{Hg}(\text{NO}_3)_2 \cdot \text{H}_2\text{O}$) diphenylcarbazone, bromophenol blue were obtained from Sigma Aldrich Chemicals. Millipore water was used for Mercurometric titration.

2.2.1: Synthesis of metal hydroxides, metal oxyhydroxides and metal oxides

Synthesis of $\text{CrO}(\text{OH})$: [15] 15 g of $\text{Cr}(\text{NO}_3)_3 \cdot 9\text{H}_2\text{O}$ was dissolved in 75 mL of distilled water. 10% Ammonia solution was added dropwise with constant stirring till pH attained was 5. The solution was stirred for further 30 min and then centrifuged and washed to obtain the precipitate. This wet precipitate was transferred into a beaker which was then placed in a teflon lined autoclave containing 2 mL of distilled water. The sample was sealed and heated at 170°C for 6 h. The resultant product was washed, centrifuged and then dried.

Synthesis of Cr_2O_3 : Typically, 15 g of $\text{Cr}(\text{NO}_3)_3 \cdot 9\text{H}_2\text{O}$ was dissolved in 75 mL ultra pure water to which 10% ammonia solution was added at room temperature, at the rate

of 1 mL min^{-1} under vigorous stirring. Addition of ammonia solution was completed when pH of the reaction mixture reached the desired value (5.0) The reaction mixture was then kept under constant stirring in air at room temperature for 0.5 h. The obtained gel was centrifuged and washed at 13000 rpm for 10 min, for three times. The resultant sample was calcined at $800 \text{ }^\circ\text{C}$ for 4h.

Manganese hydroxide $[\text{Mn}(\text{OH})_2]$: 200 mg KMnO_4 , 200 mg NaOH and 200 mg glucose were dissolved in deionized water with total volume 30mL. After stirring, the solution was transferred into an autoclave and heated at $200 \text{ }^\circ\text{C}$ for 72 h and allowed to attain room temperature naturally. The product was repeatedly washed with deionized water and ethanol, and then dried at 80°C for 10 h to get $\text{Mn}(\text{OH})_2$.

Synthesis of $\text{MnO}(\text{OH})$ [16] 300 mL of 0.2 N ammonia solution was added to the mixture of 20 mL of 30% H_2O_2 and 1 L, 0.06 mol/L $\text{MnSO}_4 \cdot 4\text{H}_2\text{O}$. The resultant solution was quickly heated and kept for 6 h at $90 \text{ }^\circ\text{C}$. The resultant solid was filtered while hot, washed with doubly distilled water, dried in oven under vacuum for 2 days at room temperature and stored dry.

Manganese oxide $[\text{Mn}_2\text{O}_3]$: A transparent sol solution was prepared by dissolving 0.1 M of Manganese (II) chloride tetrahydrate ($\text{MnCl}_2 \cdot 4\text{H}_2\text{O}$) in 100 ml methanol under vigorous stirring. And then, an aqueous ammonia solution (10 ml) was added to the above solution by drop wise under stirring. The dropping rate must be well controlled for the chemical homogeneity. The resulting opal gels were filtered and washed with methanol to remove impurities and dried over $120 \text{ }^\circ\text{C}$ for 12 h in order to remove water molecules and thus white colored powders were obtained. Finally, black-brown colored Mn_2O_3 nano powders were formed at $400 \text{ }^\circ\text{C}$ for 2 h.

Synthesis of $\text{Co}(\text{OH})_2$:[2] In a typical synthesis of Cobalt hydroxide nanocrystals, 50 mL of 0.1 M, NaOH solution was added dropwise to 80 mL of 0.05 M, $\text{Co}(\text{NO}_3)_3 \cdot 6\text{H}_2\text{O}$ solution, held in a $45 \text{ }^\circ\text{C}$ oil bath. A pink precipitate formed is filtered and washed with deionized water three times. Then dried, the obtained product is cobalt hydroxide.

Synthesis of $\text{CoO}(\text{OH})$: [15] 50 mL of 0.1 mol/L NaOH solution was added drop wise in to 80 mL of 0.05 mol/L Cobaltous Nitrate solution held in a $45 \text{ }^\circ\text{C}$ oil bath. A pink precipitate was produced which was then filtered and washed with deionized water 3 times. To the filtrate, 5 mL of 8 mol/L NaOH was added along with 2 mL of 30% H_2O_2

and kept at 45 °C for 18 h. The final brown precipitate was filtered and washed with deionized water for 3 times. The precipitate was collected and dried at 65 °C.

Synthesis of Co₃O₄: [15] In a typical synthesis of Cobalt oxyhydroxide nanocrystals, 100 mL of 0.1 M, NaOH solution was added dropwise into 160 mL of 0.05 M, Co(NO₃)₃.6H₂O solution, held at 45 °C in an oil bath. A pink precipitate formed was filtered and washed with deionized water three times. The dried precipitate was annealed at 500 °C for 5 hours to obtain the cobalt oxide.

Synthesis of Al(OH)₃: To 100 mL 0.1M [Al(NO₃)₃.9H₂O] solution, 100 mL of 0.25% ammonia aqueous solution was added at 348K until pH reached 8. The resultant gel was then charged heated under constant stirring at 348K for two days. After cooling to room temperature, the white gel was recovered by filtration, washed with deionised water and dried overnight in an oven at 393K.

Synthesis of AlO(OH): [17] 0.005 mol AlCl₃.6H₂O (1.21 g) was dissolved in 15 mL of distilled water with 0.02 M NaOH. A transparent solution of NaAlO₂ was obtained. To this solution, 10% aqueous surfactant solution of CTAB (2 g in 18 mL water) was added and stirred at room temperature. The solution was further stirred vigorously for 30 min and then sealed in a Teflon lined stainless steel autoclave of 40 mL capacity and heated at 120 °C for 12 h. The obtained white product was collected by filtration and washed several times with distilled water and ethanol. Then dried at 60 °C for 10 h.

Synthesis of Al₂O₃: [17] To 100 mL 0.1M Al(NO₃)₃.9H₂O, 100 mL of 0.25% aqueous ammonia was added 348 K until pH reached to 8 at. The resultant gel was then loaded into a flask and heated under constant stirring at 348 K for two days. After cooling to room temperature, the white gel was recovered by filtration. And washed with deionized water and dried overnight in an oven at 393K. The dried precipitate was annealed at 400 °C for 4 hours to obtain aluminum oxide.

2.2.2 Catalysis Reaction

Deacetylation-Knoevenagel condensation

A reaction mixture composed of benzaldehydedimethyl acetal (5 mmol), malononitrile (5 mmol), acetonitrile (2 mL), H₂O (20 µL) was taken in a 25mL RBF. 50 mg of MO(OH) was added. The reaction mixture was heated at 80 °C for 15 h under nitrogen atmosphere. The catalyst was separated by centrifugation and the supernatant liquid was

analyzed using Gas Chromatography.

Knoevenagel condensation

Benzaldehyde (5 mmol), malononitrile (5 mmol), acetonitrile (2 mL), H₂O (20 μ L) was taken in a 25 mL beaker. 50 mg of MO(OH) was added. The reaction mixture was heated at 80 °C for 15 h under nitrogen atmosphere. The catalyst was separated by centrifugation and the supernatant liquid was analyzed using Gas Chromatography.

2.2.3 Determination of Surface hydroxyl groups

The surface hydroxyl groups were determined with a slight modification of a known procedure.[18] The as prepared MO(OH) was taken and exposed to Thionyl Chloride (SOCl₂) vapours in a sealed autoclave at 60 °C for 1h to convert the surface hydroxyl groups into chlorides. The physisorbed SOCl₂ was removed under vacuum (1mbar). 30 mg of this sample was immediately weighed and dispersed in a 0.1 N NaOH solution to hydrolyze the formed chlorides. The chloride concentration was determined by mercurometric titration. To the NaOH solution, 60 μ L of bromophenol blue indicator was added and the pH was maintained at 3.5 using 0.1 N HNO₃ solution. A 0.5 mL of diphenylcarbazone was added to the above solution and the resultant solution was titrated with 0.028 N mercuric nitrate solution.

2.3 Results and Discussion

2.3.1 Material Characterization

The different types of materials synthesized as per the procedures described above are shown in Fig 2.2 All the materials were thoroughly characterized to ascertain the purity of each phase in the respective samples.

<ol style="list-style-type: none"> 1. Cr(OH)_3 2. CrO(OH) 3. Cr_2O_3 	<ol style="list-style-type: none"> 1. Mn(OH)_2 2. MnO(OH) 3. Mn_2O_3
<ol style="list-style-type: none"> 1. Co(OH)_2 2. CoO(OH) 3. Co_3O_4 	<ol style="list-style-type: none"> 1. Al(OH)_3 2. AlO(OH) 3. Al_2O_3

Fig 2.2: Metal hydroxides, Metal Oxyhydroxides and Metal oxides of Cr, Mn, Co and Al prepared and used in the present work

Fig 2.3 shows the X-ray diffraction patterns for each of the samples synthesized. They can be indexed to the known phases and the appropriate lattice planes. Table 2.1 provides the JCPDS file no of the materials and their miller planes which can be indexed. Pure phases of CrO(OH) (rhombohedral $R\bar{3}m$), MnO(OH) (manganite, $2P_1/c$), CoO(OH) (heterogenite, $R\bar{3}m$) and AlO(OH) (Boehmite, $Cmc2_1$) were identified. A common observation among all hydroxides was broader XRD peaks as compared to their oxyhydroxides. For e.g. in Fig 2.3a, CrO(OH) did not show any sharp peaks except a hump at $2\theta = 20^\circ$. In contrast, CrO(OH) and Cr_2O_3 showed distinct peaks. Moreover, all the respective oxides had sharp narrower peaks as compared to their oxyhydroxide counterparts. This indicated that oxides are highly condensed systems followed by oxyhydroxides and hydroxides that showed decreasing degree of crystallinity.

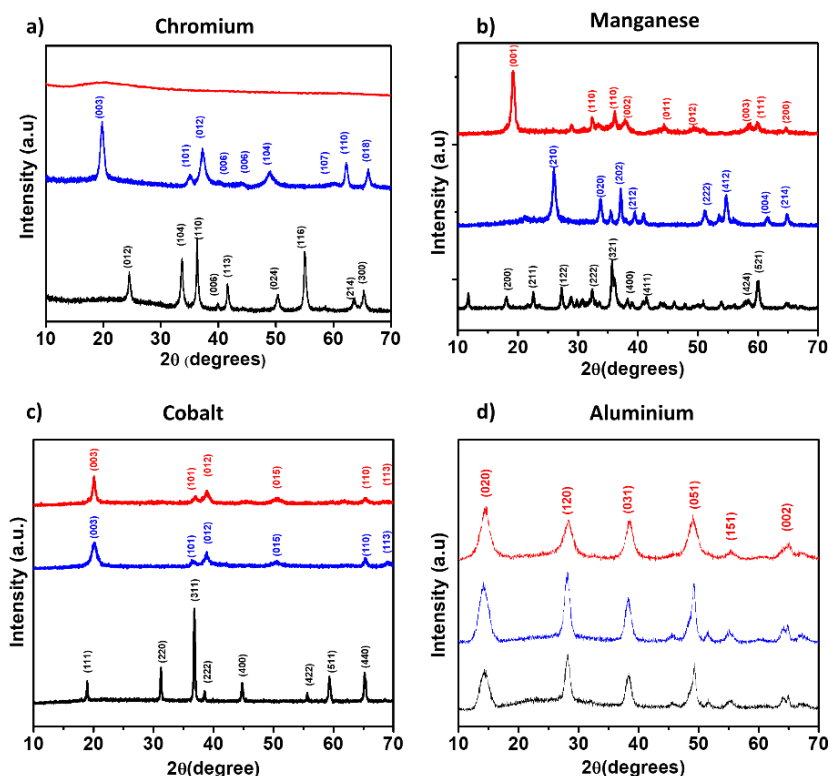


Fig 2.3: XRD patterns of 1) Chromium 2) Manganese 3) Cobalt & 4) Aluminium

■ Hydroxides ■ Oxyhydroxide ■ Oxide

Table 2.1: Results from XRD and TEM for all hydroxide, oxyhydroxide and oxide materials

Sr. No	Sample	JCPDS No	2θ° - Miller indices(hkl) (from XRD)	Morphology (from TEM)
1	Cr(OH) ₃	-	No Crystalline peaks	flake like
2	CrO(OH)	85-1373	20°-(003), 35°-(101), 38°-(012), 50°-(104), 64°-(110), 68°-(018)	polyhedra
3	Cr ₂ O ₃	38-1479	25°-(012), 33°-(104), 40°-(006), 42°-(113), 51°-(024), 56°-(116), 64°-(214), 66°-(300)	spherical
4	Mn(OH) ₂	73-1604	20°-(001), 33°-(110), 36°-(110), 38°-(002), 44°-(011), 49°-(012), 57°-(003), 60°-(111), 65°-(200)	spherical
5	MnO(OH)	41-1379	26°-(210), 34°-(020), 37°-(202), 39°-(212), 51°-(222), 55°-(412), 62°-(004), 65°-(214)	nanorods
6	Mn ₂ O ₃	76-0150	17°-(200), 23°-(211), 27°-(122),	spherical

			33°-(222),36°-(321), 38°-(400), 42°-(411), 57°-(424), 60°-(521)	
7	Co(OH) ₂	00-030-0443	20°-(003), 37°-(101), 39°-(012), 50°-(016), 65°-(110), 68°-(113)	granular
8	CoO(OH)	01-073-1213	20°-(003), 37°-(101), 39°-(012), 50°-(016),65°-(110), 68°-(113)	triangular
9	Co ₃ O ₄	073-1701	18°-(111), 32°-(220),36°-(311), 38°-(222), 45°-(400),56°-(422) 59°-(511), 65°-(440)	bulk
10	Al(OH) ₃	12-0457	14°-(020), 28°-(120), 38°-(031), 50°-(051), 55°-(151), 60°-(002),	needlelike
11	AlO(OH)	21-1307	14°-(020), 28°-(120), 38°-(031), 50°-(051), 55°-(151),60°-(002)	needlelike
12	Al ₂ O ₃	29-0063	14°-(020), 28°-(120), 38°-(031), 50°-(051),55°-(151), 60°-(002)	needlelike

The FT-IR spectra of the synthesized metal hydroxides M(OH)_x, metal oxyhydroxides MO(OH) and metal oxides MO_x were studied in Fig 2.3. In all these materials, the surface hydroxyl groups are characterized by prominent O-H stretching bands between 2800-3500 cm⁻¹. As expected, the position of O-H stretch for the four oxyhydroxides were not at the same frequencies due to the difference in the electronegativity of the metals (Cr = 1.66, Mn =1.55, Co=1.88, Al=1.61) which influences the strength of O –H bond. In Fig 2.3a, Cr₂O₃ showed characteristic absorption bands due to Cr-O-Cr and Cr-O stretching modes at 985 cm⁻¹ and 1188 cm⁻¹ respectively, the latter due to the dissociative chemisorption of oxygen.[19] The broad band centered around 3400 cm⁻¹ is due to the stretching of surface hydroxyl group in CrO(OH). Mn₂O₃ showed bands at 576 cm⁻¹ due to Mn-O stretching vibrations and 539 cm⁻¹ due to Mn-O bending vibrations.[20] In Fig 2.4 d, the main peaks of Al₂O₃ at 459, 595, and 656 cm⁻¹ can be assigned to the Al–O stretching mode.

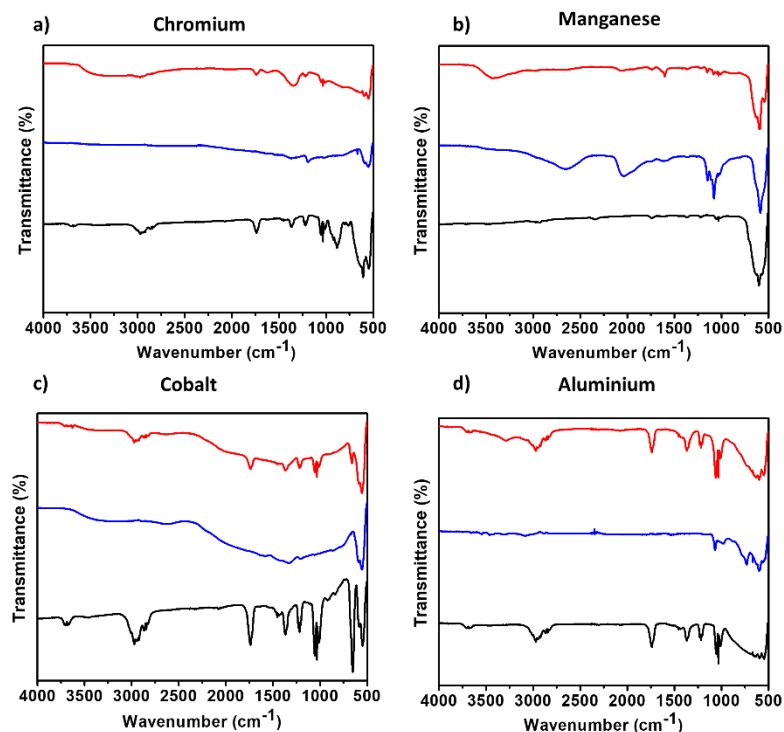


Fig 2.4: Infrared spectrum of 1) Chromium 2) Manganese 3) Cobalt & 4) Aluminium Hydroxides ■ Oxyhydroxide ■ Oxide ■

Bands around 715 cm^{-1} and 1072 cm^{-1} are related to Al–O stretching mode in tetrahedron and symmetric bending of Al–O–H, respectively.[21]

The microstructure of the synthesized metal hydroxides $M(\text{OH})_x$, metal oxyhydroxides $\text{MO}(\text{OH})$ and metal oxides MO_x was analyzed using Transmission Electron Microscopy (TEM) as shown in Fig 2.5. $\text{CrO}(\text{OH})$ showed a platelet like morphology with sizes between 5-8 nm as seen in Fig 2.5. $\text{MnO}(\text{OH})$ formed rod like structures (Fig 2.5) with an average size ranging from 100-400 nm and 50 nm in width. $\text{CoO}(\text{OH})$ was observed to be in the form of hexagonal nanoplatelet fragments (Fig 2.5) ranging from 30-100 nm. In Fig 2.5, $\text{AlO}(\text{OH})$ showed needle like structures with average length of 20-40 nm. All the metal hydroxides show poorly crystalline or amorphous structures. Metal oxides show distinct crystalline features.

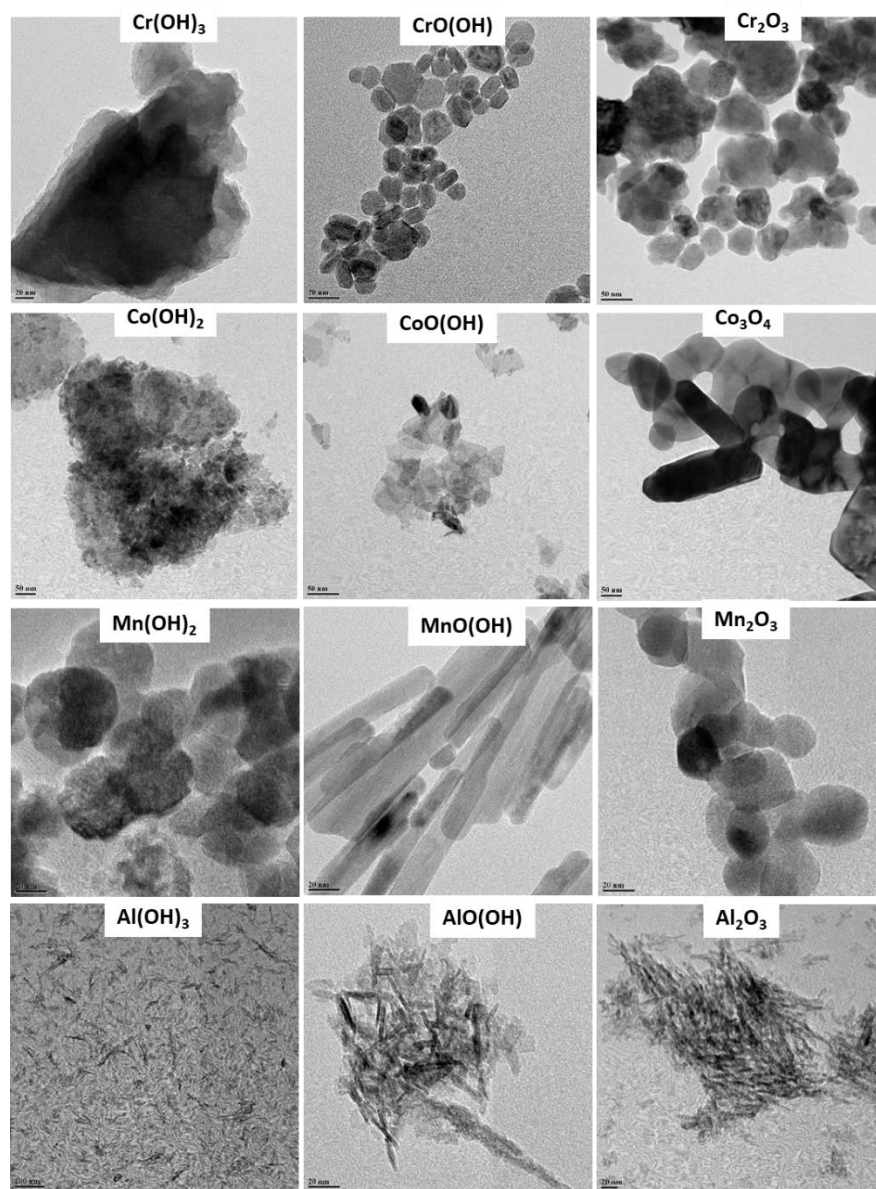


Fig 2.5: Transmission Electron Microscopy images of the samples.

2.3.2 Catalytic reactions

The as synthesized materials were first evaluated for a one-pot tandem deacetalization-Knoevenagel condensation reaction where the first step of the reaction requires an acid for converting benzaldehydedimethyl acetal (**1**) to benzaldehyde (**2**) in the presence of water and base is required for the Knoevenagel condensation of benzaldehyde with malononitrile to form benzylidene malononitrile (**3**) in a single pot. Fig 2.6 summarizes

the results of various samples for bifunctional activity. Formation of product **3** is an indication that catalysts are bifunctional in nature.

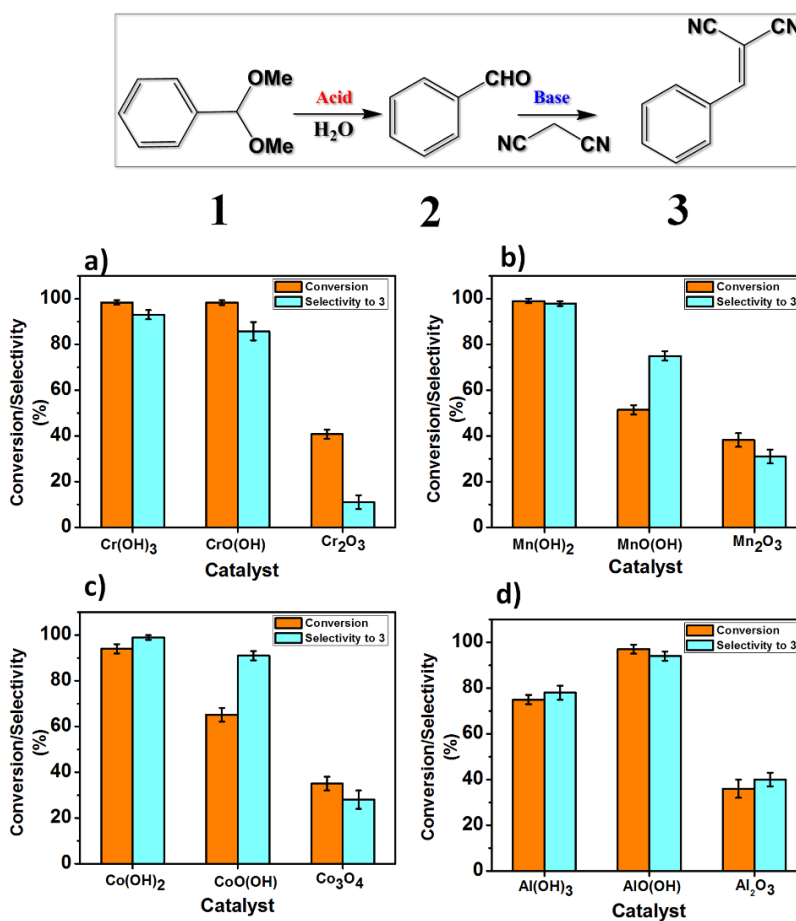


Fig 2.6: Conversion & Selectivity plots for the Deacetylation-Knoevenagel reaction for Metal Hydroxides M(OH)_x, Metal oxyhydroxides MO(OH) & Metal oxides MO_x. Error bars represent deviation from average value in the GC detector response.

In this work, the comparison of catalytic activity is made between samples of the same element. The work focuses on the effect of surface hydroxyl groups on phases such as hydroxide, oxyhydroxide & oxide for a particular metal on the activity. Fig 2.6 and Table 2.2 shows that all the metal hydroxides Cr(OH)₃, Mn(OH)₃ and Co(OH)₂ with an exception of Al(OH)₃ gave better conversion (above 90%) and selectivity (above 95%) for Product **3** as compared to their metal oxyhydroxides and metal oxide counterparts after 15h of the reaction. Metal oxyhydroxides showed a fairly decent conversion and selectivity trends. e.g. CrO(OH) showed a conversion of **1** to 98% with a selectivity to benzylidene malononitrile (**3**) of 92%. MnO(OH) showed a conversion of 56% with

94% selectivity for **3**. Metal oxides show a relatively poor trend less than 40 % conversion with lower selectivity for **3**. E.g., Cr_2O_3 gave selectivity of 15 % for **3**. Essentially Metal oxides are dehydrated metal hydroxides with metal oxyhydroxides as intermediate phases between metal hydroxides and metal oxides.

Table 2.2: Conversion and selectivity trends for the catalytic studies

Sr No	Catalyst	Conversion of 1 (%)	Selectivity to 2 (%)	Selectivity to 3 (%)
1	$\text{Cr}(\text{OH})_3$	98	7	93
2	$\text{CrO}(\text{OH})$	98	14	86
3	Cr_2O_3	40	89	11
4	$\text{Mn}(\text{OH})_2$	99	2	98
5	$\text{MnO}(\text{OH})$	51	25	75
6	Mn_2O_3	38	69	31
7	$\text{Co}(\text{OH})_2$	94	1	99
8	$\text{CoO}(\text{OH})$	65	9	91
9	Co_3O_4	35	72	28
10	$\text{Al}(\text{OH})_3$	75	22	78
11	$\text{AlO}(\text{OH})$	97	6	94
12	Al_2O_3	36	60	40

Reaction conditions: **1** (5 mmol), malononitrile (5 mmol), acetonitrile (2 mL), H_2O (20 μL), 50 mg catalyst, 80 °C, 15 h, under nitrogen atmosphere.

The reusability of metal oxides were not considered due to their poor activity. The reusability trends for metal hydroxides and metal oxyhydroxides are presented in Fig 2.7. Both the metal hydroxides and metal oxyhydroxides showed decent recycling ability. However, a 8-20 % drop in selectivity of **3** was observed for metal hydroxides compared to 2-8% for the case of metal oxyhydroxides in the 4th recycle. This probably indicates possible loss of active sites on metal hydroxides and could be related to structural differences.

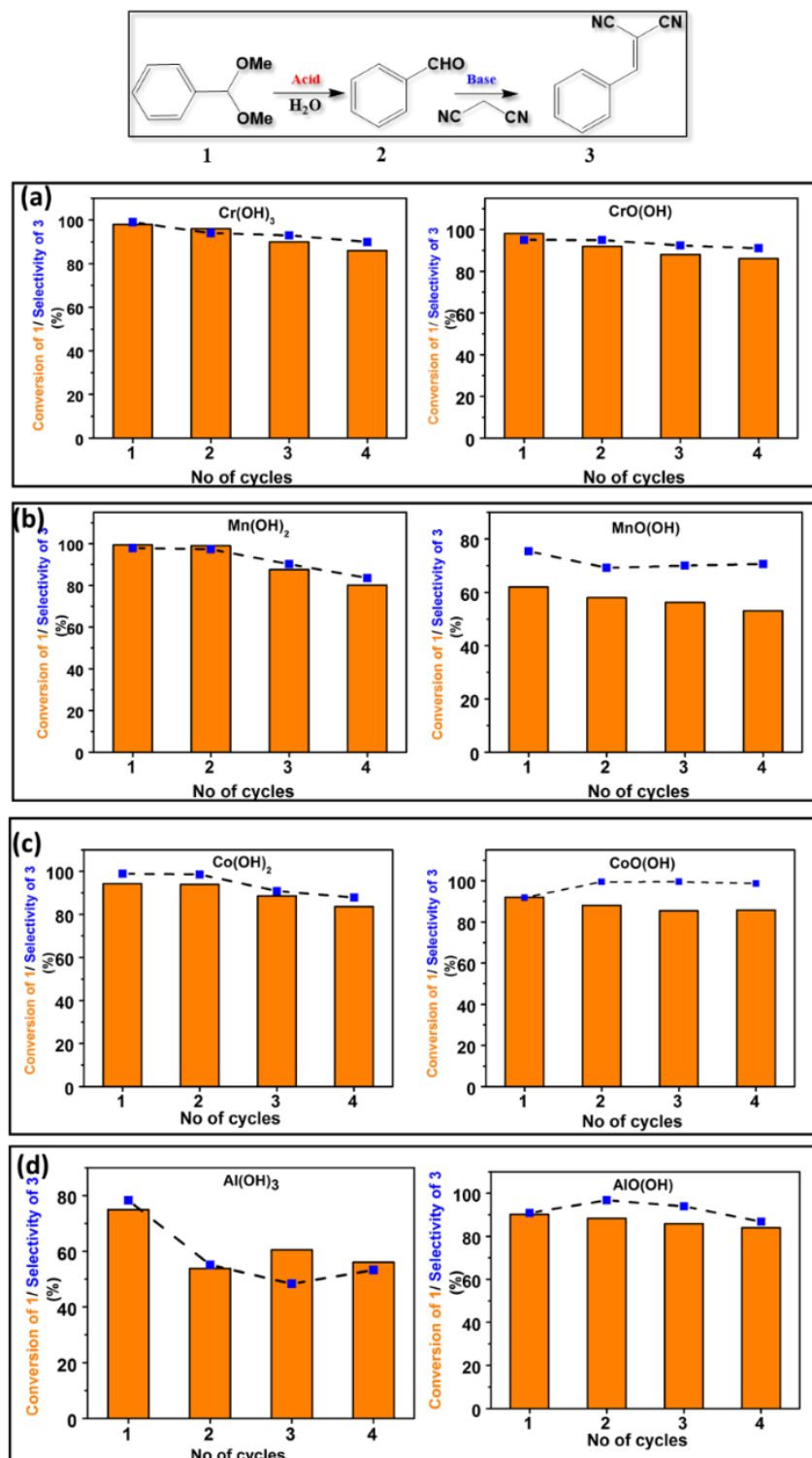


Fig 2.7: Recyclability studied for the metal hydroxide and metal oxyhydroxide samples for the different metals a) Chromium b) Manganese c) Cobalt d) Aluminium

2.3.3 Acidity and Basicity of $M(OH)_n$, $MO(OH)$ and M_xO_y

We probed the acidity of all the samples using temperature programmed adsorption-desorption of NH_3 studies. The maximum temperature set was $400\text{ }^\circ\text{C}$ to avoid the interference due to phase transformation to oxides at a higher temperature. The plots are presented in Fig 2.8 and the trends in acidity for the different materials are shown in Fig 2.9. The oxyhydroxides are highly acidic as compared to the metal hydroxides and metal oxides in all cases except $Cr(OH)_3$ ($2.67\text{ mmol/g } NH_3$) which shows only a slight better acid value as compared to $CrO(OH)$ ($2.19\text{ mmol/g } NH_3$). The surface hydroxyl groups provide the acidic nature for the metal oxyhydroxides.

On the other hand, metal hydroxides although have large number of hydroxyl groups but these do not show better acidity value as compared to the metal oxyhydroxides. Structurally the attachment of hydroxyl groups on to the surface of metal oxyhydroxide and metal hydroxides is different. Metal hydroxides are ionic compounds with positively charged cation surrounded by negatively charged OH^- ions. Whereas there is coordinate bonding between the surface hydroxyl groups with the metal ion in the case of metal oxyhydroxides. Hence this asserts the fact that the hydroxyl groups in metal hydroxides are basic in nature. These trends are perfectly reflected in the CO_2 TPD data presented in Fig's 2.8 and 2.9 indicating better basicity for metal hydroxides as compared to metal oxyhydroxides and oxides. Also the lower activity of $Al(OH)_3$ for the tandem reaction in Fig 2.6 is due to the low basicity of $Al(OH)_3$ as compared to $AlO(OH)$.

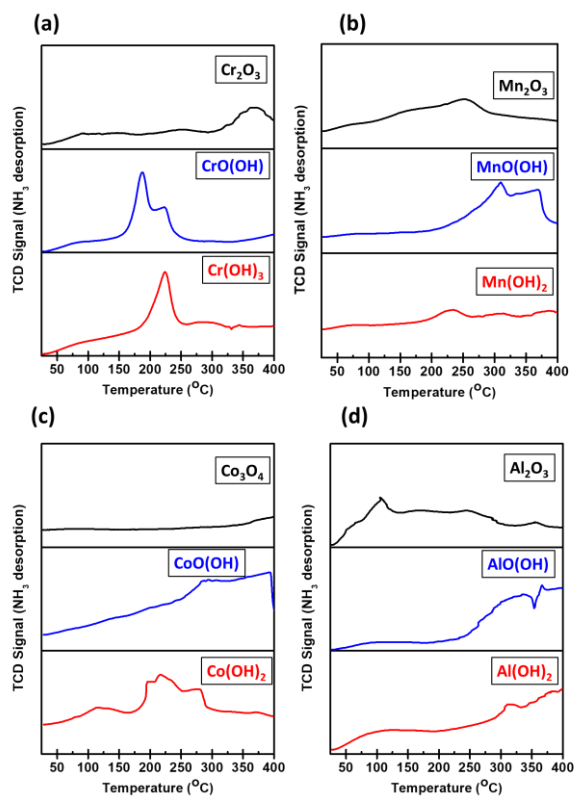


Fig 2.8: Ammonia TPD plots for the various Metal Hydroxides $M(OH)_x$, Metal oxyhydroxides $MO(OH)$ & Metal oxides MO_x a) Cr b) Mn c)Co & d) Al

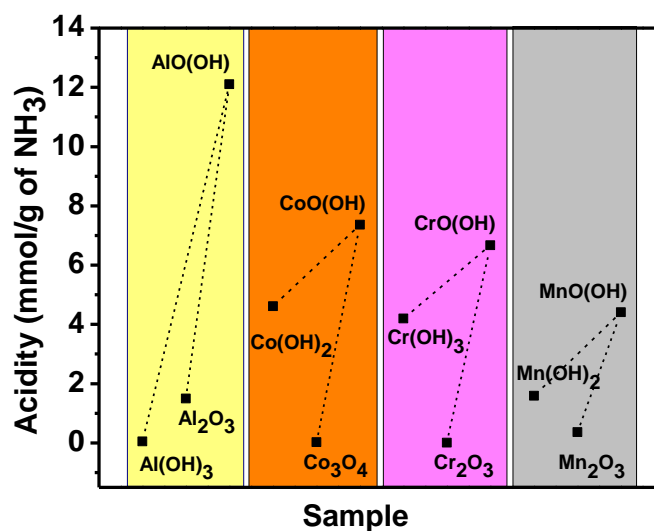


Fig 2.9: Trends in acidity from Ammonia TPD for the samples.

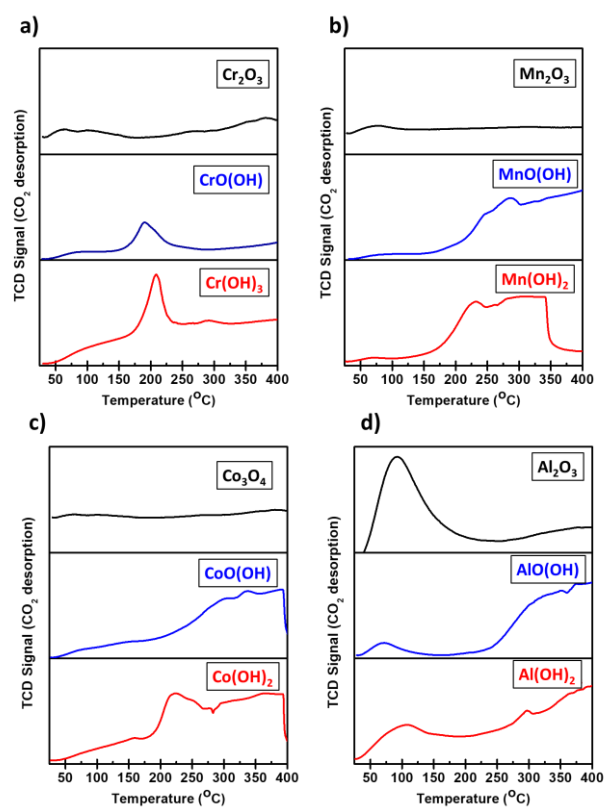


Fig 2.10: CO₂ TPD plots for the various Metal Hydroxides M(OH)_x, Metal oxyhydroxides MO(OH) & Metal oxides MO_x

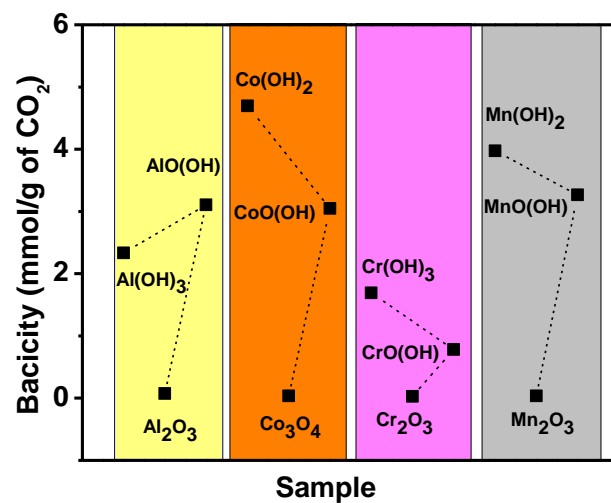


Fig 2.11: Trends in basicity from CO₂ TPD for the samples.

We performed pyridine IR of all the samples to identify the pyridine adsorption on the surface. Scheme 2.1 shows the possible interaction of pyridine molecule on the surface of metal hydroxide, oxyhydroxide and oxide. There are basically two vibration bands of interest. a) interaction with surface hydroxyl group at 1540 cm^{-1} and the interaction with Lewis acidic metal at 1450 cm^{-1} . We quantified these interactions and the calculations were based on the Emeis algorithm which is given below.[22] The Brønsted to Lewis acid ratio (B/L) was presented in Fig 2.11

Emeis Equations

$$C_L = K_L \times A_{1450} = (\pi / \text{IMEC}_L) \times (r^2/w) \times A_{1450} \quad \text{----- (I)}$$

$$C_B = K_B \times A_{1540} = (\pi / \text{IMEC}_B) \times (r^2/w) \times A_{1540} \quad \text{----- (II)}$$

Where,

C_L and C_B = concentration of pyridine on Lewis and Brønsted acid sites.

A_{1450} and A_{1540} = integrated area of band at 1450 cm^{-1} and 1540 cm^{-1}

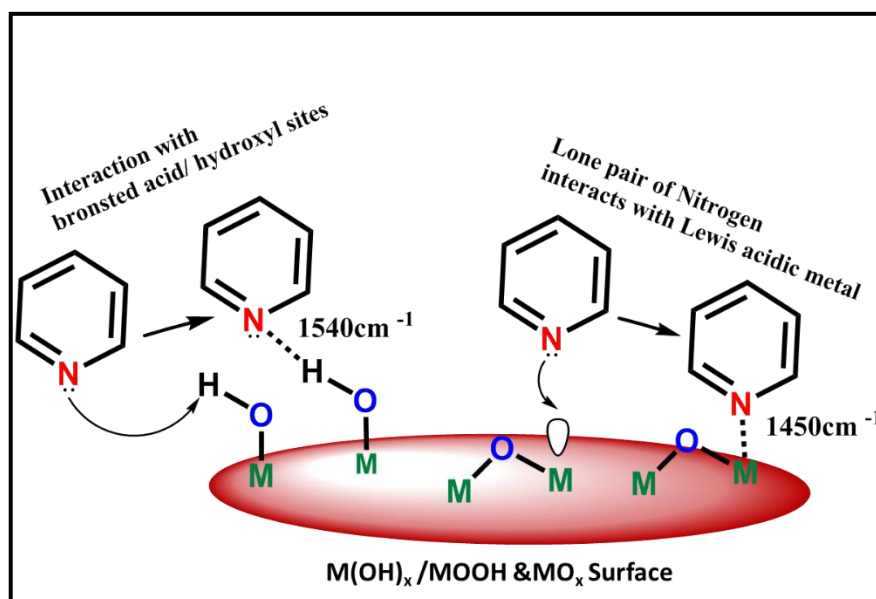
K_L and K_B = molar extinction constant for Lewis acid sites and Brønsted acid sites

IMEC_L = integration molar extinction coefficient ($2.22\text{ cm}/\mu\text{mol}$) for Lewis acid sites

IMEC_B = integration molar extinction coefficient ($1.67\text{ cm}/\mu\text{mol}$) for Brønsted acid sites

r = radius of self-supporting disk of praying mantis assembly

weight of sample pressed into self-supporting disk of praying mantis assembly.



Scheme 2.1: Interaction of pyridine with surface of the catalysts

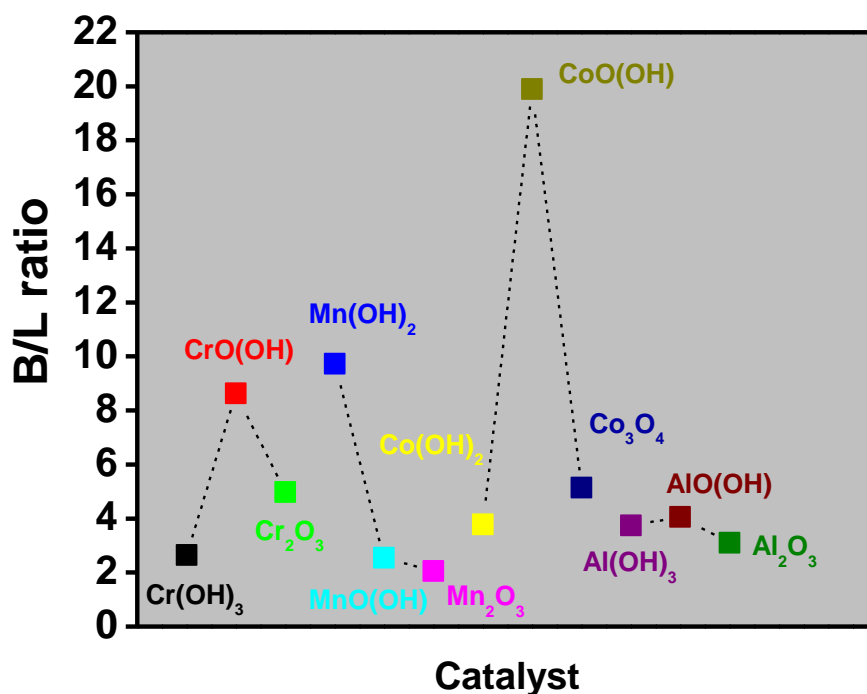


Fig 2.12: Brønsted to Lewis acid ratio (B/L) for all the samples.

From the pyridine IR measurements and Fig 2.12, the metal oxyhydroxides for all the metals invariably show higher B/L value at room temperature. For example CrO(OH) shows B/L value of 8.3 compared to 2.2 & 4.3 for Cr(OH)₃ and Cr₂O₃ respectively. Similarly AlO(OH) gives 4.2 in comparison to 3.8 & 3.2 for Al(OH)₃ and Al₂O₃ respectively. However MnO(OH) is an exception as it shows lower B/L ratio for MnO(OH) as compared to Mn(OH)₂ which interestingly accounts for the far lower conversion as shown in Fig 2.6. CoO(OH) shows the highest B/L ratio of 20.1. The higher B/L ratio of metal oxyhydroxides confirm the acidic nature of surface hydroxyl groups present on them.

2.3.4 Active Sites:

Surface -OH groups as the active sites:

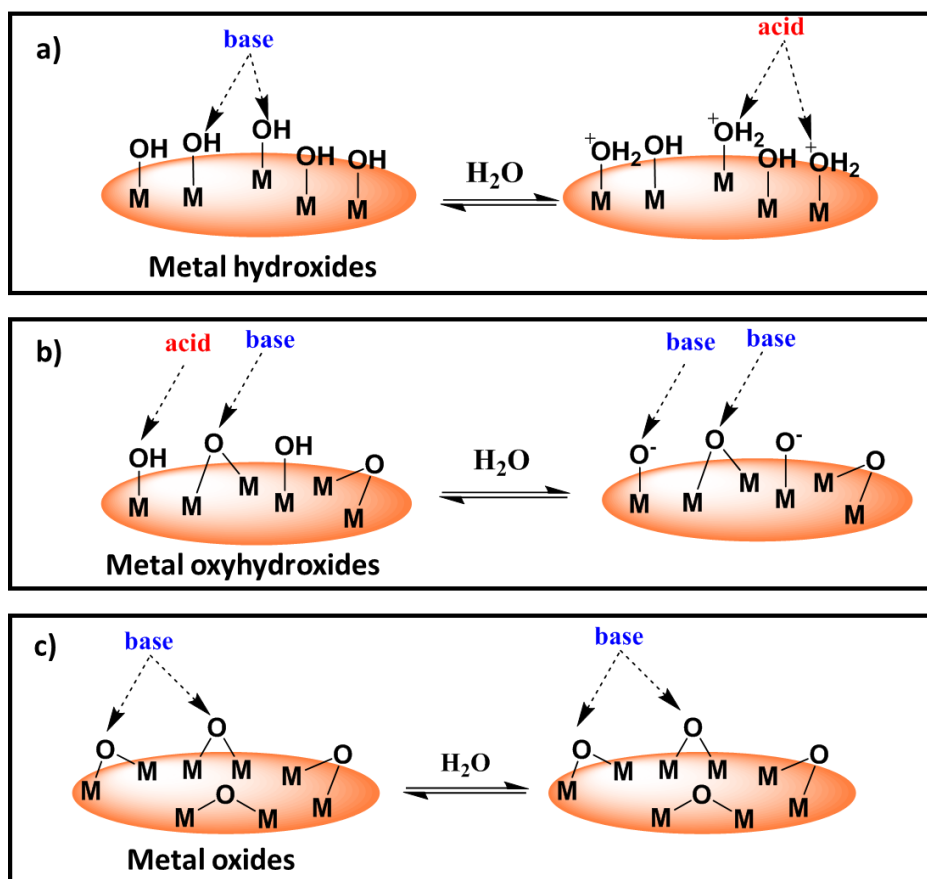
All the samples studied contain only metal and surface hydroxide linkages (M-OH) and metal oxygen linkages (M-O-M). Hence the source of activity of the tested materials are governed by these active sites alone. XPS studies show that the number of surface hydroxyl groups on metal hydroxides are large in number (Table 2.2, columns 5 and 6) as compared to metal oxyhydroxides. These results were supported by mercurimetric

titrations (Table 2.2, column 4). This is natural as metal hydroxides are the least condensed phases (Fig 2.1).

Table 2.3: Surface area, Surface hydroxyl, O^{2-} concentration using mercurometric titrations and XPS studies and acidity/basicity values from temperature programmed desorption

Sr No	Catalyst	Surface Area (m^2/g)	Concentration of Surface OH groups from Mercurometric titrations (mmol /g)	Contribution of Surface Hydroxyl (OH/O ⁻) groups from XPS studies (%)	Contribution of Oxide (O ²⁻) species from XPS studies (%)	Acidity (mmol/g of NH ₃)	Basicity (mmol/g of CO ₂)
1	Cr(OH) ₃	151.60	22	43	-	2.7	1.7
2	CrO(OH)	112.18	9	39	23	2.2	0.8
3	Cr ₂ O ₃	118.20	0.2	10	68	0.2	0.0
4	Mn(OH) ₂	148.09	26	46	-	0.4	4.0
5	MnO(OH)	134.69	8.5	36	29	4.4	3.3
6	Mn ₂ O ₃	150.88	0.2	11	66	0.1	0.0
7	Co(OH) ₂	126.31	50	48	-	4.6	4.7
8	CoO(OH)	160.51	31	41	22	7.2	3.0
9	Co ₃ O ₄	119.76	2	9	51	0.0	0.0
10	Al(OH) ₃	209.85	16	51	-	0.0	2.3
11	AlO(OH)	111.34	5	39	21	4.7	3.1
12	Al ₂ O ₃	195.97	0.5	6	56	1.5	0.0

However, under normal conditions, as observed from the CO₂ TPD studies, the surface hydroxyl groups on metal hydroxides are basic in nature (Scheme 2.2a). In the presence of water, the basic hydroxyl groups on metal hydroxides get protonated to $-OH_2^+$ (Scheme 2.2a) due to the ionic nature of the bonding. In the case of metal oxyhydroxides, the surface hydroxyl groups are acidic in nature (NH₃ TPD) which get deprotonated in the presence of water to yield basic sites. (Scheme 2.2b) This is because pK_a of water is more than that of surface hydroxyl groups in metal oxyhydroxides.[23] Since the surface hydroxyl groups are getting protonated/deprotonated using H₂O the resultant water derived byproducts OH⁻/H₃O⁺ in the solution could in principle catalyze the steps of the acid-base reaction homogeneously.



Scheme 2.2: The probable acid and base sites on a) Metal hydroxides, b) metal oxyhydroxides and c) metal oxides.

Since, hot filtration tests for the metal hydroxides and oxyhydroxides did not show any improvement in catalytic activity after removal of the catalyst under the reaction conditions. Hence, we can definitely rule out the possibility of catalysis by any homogeneous entities under the present reaction conditions. Apart from OH groups, metal oxyhydroxides also contain M-O-M linkages which provide basicity in the form of Lewis basic O²⁻. Thus, the active sites in metal oxyhydroxides are -OH/O⁻ and O²⁻. In the case of metal oxides, only the metal-oxygen linkages are present, hence the active sites would be O²⁻ species alone. Literature studies on hydrated MgO sample have shown that the basicity provided by OH/O⁻ is highly active for the catalytic [24] reaction such as methanol dissociation compared to the basicity provided by O²⁻ ions which justifies the poor conversion shown by metal oxides in all the cases. Though metal hydroxides show excellent catalytic activity, they seem to suffer from leaching and

stability issues. A more detailed analysis of the acid-base activity of metal oxyhydroxides is provided in the subsequent chapters.

2.4 Conclusions

This chapter discusses the acid-base bifunctional behavior of the three hierarchically condensed phases $M(OH)_x$, $MO(OH)$ and $M_x(O)_y$ to varying extent. CO_2 TPD, NH_3 TPD and Pyridine IR data show presence of acid and basic sites. The strength of acid sites is stronger on $MO(OH)$ while the strength of basic sites is stronger on $M(OH)_x$. Metal oxyhydroxides show better recyclability as compared to $M(OH)_x$. $MO(OH)$ are versatile due to its stability and two types of active sites OH/O^- and O^{2-} . Further studies using computational modelling techniques and dye adsorption studies are in progress.

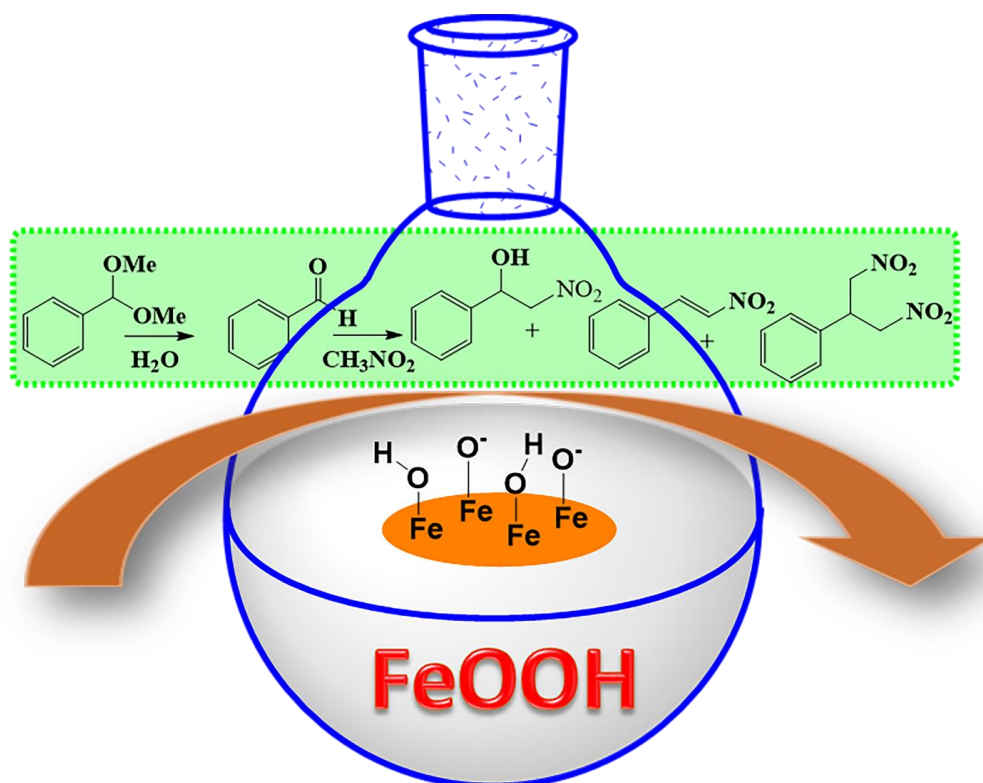
2.5 References

1. F. Diederich and P. J. Stang, *Metal-catalyzed cross-coupling reactions*, John Wiley & Sons, 2008.
2. M. J. Climent, A. Corma and S. Iborra, *Chemical Reviews*, 2011, **111**, 1072-1133.
3. P. Li, C.-Y. Cao, Z. Chen, H. Liu, Y. Yu and W.-G. Song, *Chemical Communications*, 2012, **48**, 10541-10543.
4. E. Gianotti, U. Diaz, A. Velty, A. Corma, *Catalysis Science & Technology*, 2013, **3**, 2677-2688.
5. S. Huh, H. T. Chen, J. W. Wiench, M. Pruski and V. Lin, *Angewandte Chemie International Edition*, 2005, **44**, 1826-1830.
6. A. Dhakshinamoorthy and H. Garcia, *ChemSusChem*, 2014, **7**, 2392-2410.
7. W. Deng, Y. Wang, Q. Zhang and Y. Wang, *Catalysis Surveys from Asia*, 2012, **16**, 91-105.
8. N. A. Brunelli and C. W. Jones, *Journal of catalysis*, 2013, **308**, 60-72.
9. S. Shylesh, A. Wagener, A. Seifert, S. Ernst and W. Thiel, *Angewandte Chemie International Edition*, 2010, **49**, 184-187.
10. S. Shylesh and W. Thiel, *ChemCatChem*, 2011, **3**, 278-287.
11. L.-C. Lee, J. Lu, M. Weck and C. Jones, *ACS Catalysis*, 2016, **6**, 784-787.
12. L. Xu, C.-g. Li, K. Zhang and P. Wu, *ACS Catalysis*, 2014, **4**, 2959-2968.
13. Y. Huang, S. Xu and V. Lin, *Angewandte Chemie International Edition*, 2011, **50**, 661-664.
14. M. Bhuiyan, M. Hossain, M. A. Alam and M. Mahmud, *Chemistry Journal*, 2012, **2**, 30-36.
15. J. Yang, H. Liu, W. N. Martens and R. Frost, *The Journal of Physical Chemistry C* 2010, **114**, 111-119.
16. X. Gao, G. Sheng and Y. Huang, *Science China Chemistry*, 2013, **56**, 1658-1666.
17. D. Kuang, Y. Fang, H. Liu, C. Frommen and D. Fenske, *Journal of Materials Chemistry*, 2003, **13**, 660-662.
18. T. Kawai and K. Tsutsumi, *Journal of colloid and interface science* 1999, **212**, 310-316.
19. P. Ratnasamy and A. Leonard, *The Journal of Physical Chemistry*, 1972, **76**, 1838-1843.
20. S. Gnanam and V. Rajendran, *Journal of sol-gel science and technology*, 2011, **58**, 62-69.
21. K. Djebaili, Z. Mekhalif, A. Boumaza and A. Djelloul, *Journal of spectroscopy*, 2015, **2015**.
22. C. J. Emeis, *Journal of Catalysis*, 1993, **141**, 347-354.

23. R. Cornell, and U. Schwertmann. *The iron oxides: structure, properties, reactions, occurrences and uses*. John Wiley & Sons, 2003.
24. M.-L. Bailly, C. Chizallet, G. Costentin, J.-M. Krafft, H. Lauron-Pernot and M. Che, *Journal of Catalysis*, 2005, **235**, 413-422.

Chapter 3a

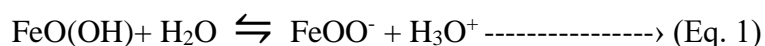
Tunable acid–base bifunctional catalytic activity of FeO(OH) in an orthogonal tandem reaction



Dnyanesh Vernekar, Dinesh Jagadeesan, *Catalysis Science & Technology* 5, 4029-4038, 10, 2015.

3a.1: Introduction

Biosynthetic pathways in living organisms are excellent examples for tandem catalysis. A substrate is acted upon by enzymes in a sequential manner thereby efficiently driving the chemical equilibrium towards products in high selectivity.[1, 2] In last few decades, several attempts have been made to mimic nature's strategy on heterogeneous catalyst systems to develop multi-functional catalysts for orthogonal tandem reactions.[2, 3] Multifunctional catalysts that are capable of carrying out orthogonal tandem reactions are important to the pharmaceutical industry in which significant savings on cost, energy and time can be achieved. From the materials perspective, a multifunctional catalyst must bear suitable active sites for each step of the tandem reaction. A detailed discussion is presented in Chapter 1 Section 1.7.[4-10] It was envisaged that inorganic metastable phases such as metal oxohydroxides are ideal as robust, inexpensive and easily scalable acid-base bifunctional catalysts. In order to develop biocompatible materials, iron oxohydroxides (FeO(OH)) are most desirable and interesting candidates for bifunctional catalytic applications.[11] Some of the unique features of iron based oxides are: (i) FeO(OH) groups existing in chemical equilibrium with FeOO⁻ as described in equation 1.



It may be visualized that -OOH groups and their deprotonated conjugate base -OO⁻ groups may be present in abundance on the surface and on the interiors of the material exhibiting acidic and basic properties respectively, (ii) FeO(OH) has been shown to possess three types of surface sites having different surface coordination. One may expect the p*K*_a values of each of the species to be different and (iii) FeO(OH) is an abundantly available natural mineral and an important raw material in the pigment industry. Therefore, it is interesting to test the bifunctional catalytic activity of FeO(OH) in an industrially important tandem reaction. In this report, we have demonstrated the bifunctional property of FeO(OH) for the first time by catalyzing deacetalization and Henry condensation reactions in tandem (Scheme 3a.1). Interestingly, different crystalline polymorphs of FeO(OH) namely Goethite (α FeO(OH)), Akaganèite (β FeO(OH)), Lepidocrocite (γ FeO(OH)) and δ FeO(OH) showed different trends in the selectivity of products.

3a.2: Experimental section

3a.2.1: Synthesis method of polymorphs of FeO(OH)

Materials

The iron salts used for the synthesis of FeO(OH) polymorphs were ferric nitrate $\text{Fe}(\text{NO}_3)_3$ (Molychem), Ferric Chloride ($\text{FeCl}_3 \cdot 6\text{H}_2\text{O}$) (Molychem), ferrous chloride ($\text{FeCl}_2 \cdot 4\text{H}_2\text{O}$) (Fluka). The alkali hydroxides used were potassium hydroxide (KOH) (Alfa-Aesar) and sodium hydroxide (NaOH) (Sd-fine). H_2O_2 (Merck) was used as an oxidizing agent for the synthesis of δ FeO(OH). For the catalytic reaction, benzaldehyde dimethyl acetal and nitromethane were obtained from Sigma Aldrich. For the Acidity and Basicity measurements, indicators mentioned in the table along with n-butylamine and trichloroacetic acid were obtained from TCI Chemicals. All solutions needed for titration were prepared in dry benzene. All chemicals were used without further purification.

Synthesis of α -FeO(OH).

Ferrihydrite was precipitated by adding 18 mL of 5.0 M KOH to 10 mL of 1M $\text{Fe}(\text{NO}_3)_3$ solution. The suspension obtained was diluted to 200mL with distilled water and held in a closed polypropylene bottle at 70 °C for 60 h. During this time the voluminous red brown ferrihydrite suspension transforms into a compact yellow precipitate of α -FeO(OH) which was filtered, washed and dried at 50 °C.

Synthesis of β -FeO(OH).

500 mL of 0.1 M FeCl_3 solution was held in a closed vessel at 70 °C for 48 h. During this period there was a change in pH from 2.3 to 1 and a compact yellow precipitate was obtained which was filtered and washed with distilled water and dried at 60 °C. This gave β -FeO(OH) with 6 % Chloride. To obtain 4 % Chloride in the β -FeO(OH) channels 0.05 M FeCl_3 solution was used in the synthesis protocol.

Synthesis of β -FeO(OH)(OH⁻ Exchanged).

β -FeO(OH) (6At% Cl^-) was stirred in 100 mL of 0.2 M aq. Ammonia for 2 h to ion-exchange counter anion with OH^- . The solid was centrifuged and washed with distilled water and dried at 60 °C.

Synthesis of γ -FeO(OH).

4 g of $\text{FeCl}_2 \cdot 4\text{H}_2\text{O}$ was dissolved in distilled water. To this, 1 M NaOH was added until the pH of the solution reaches 6.5 - 6.8. After reaching this pH, greenish black

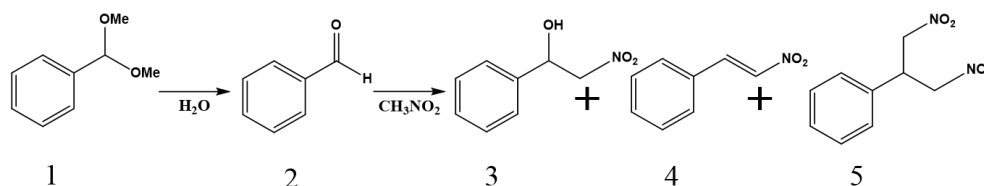
deposits were formed. Oxygen was bubbled through this solution for 20 min to obtain orange deposits i.e. γ FeO(OH) which were separated by filtration and washed with ethyl alcohol and distilled water several times and dried at 60 °C.

Synthesis of δ -FeO(OH).

5 M NaOH solution was added dropwise to 150 mL of 0.1 M FeCl₂ solution till the pH reaches 8. To this, 20mL of 30% H₂O₂ was added in one lot. Upon addition of the oxidizing agent the green suspension rapidly turned reddish brown. The product was centrifuged, washed with distilled water and dried at 40 °C.

3a.2.2: Catalytic Reaction

A reaction mixture composed of 3 mmol benzaldehydedimethylacetal, 2 mL CH₃NO₂ and 3 mmol distilled water was taken in a 25 mL RBF. 0.1 g of the polymorph of FeO(OH) was added. The reaction mixture was refluxed under N₂ atmosphere for 48 h with stirring. Control experiments were carried out by either changing the reaction duration (12h, 24h, 48h,) or by changing the temperature (80 °C, 105 °C) keeping other parameters uniform.



Scheme 3a.1: Deacetalization – Henry condensation reaction: Structures of products benzaldehydedimethylacetal (1), benzaldehyde (2), 2-nitro-1-phenylethanol (3), trans-β-Nitrostyrene (4) and 1,3-dinitro-2-phenylpropane (5) are schematically shown.

Pyridine Adsorption

To identify the presence of Brønsted and Lewis acid sites in FeO(OH), pyridine adsorption study was done by placing the polymorphs in a desiccator concentrated with pyridine vapors for 48 h. The samples were then evacuated at 100 °C to remove physically adsorbed pyridine and were pressed into KBR pellets for FT-IR analysis. To confirm the role of acidic sites on γ -FeO(OH), the Deacetylation-Henry reaction was performed by adding pyridine (0.37 mmol) externally to the reaction mixture containing 3 mmol benzaldehydedimethylacetal, 2 mL CH₃NO₂ and 3 mmol distilled water at the start of the reaction along with 0.1g of γ -FeO(OH). The reaction was run

at 105 °C under N₂ atmosphere for 48 h. The catalyst was separated by centrifugation.

Recyclability Experiment.

The catalyst used for the reaction was separated by centrifugation and repeatedly washed with methanol to remove the adsorbed organic species and then dried at 60 °C. The dried catalyst was used for the next cycle.

3a.2.3: Material Characterization.

X-ray diffraction measurements were made using Phillips PAN analytical diffractometer using Cu K α radiation ($\lambda = 1.5406 \text{ \AA}$). Infrared spectroscopy measurements were done using Bruker FT-IR. The samples were analyzed as KBr pellets. Scanning Electron Microscopy (SEM) were obtained using Quanta 200-3D ESEM microscope. The specimens were prepared by dropping a well-dispersed suspension of the sample in isopropyl alcohol onto a silicon wafer. Once isopropyl alcohol had evaporated, gold was sputtered on the surface for better sample conductivity during SEM analysis. Transmission Electron Microscopy (TEM) images were obtained using FEI Tecnai-20ST electron microscope. Specimens of the samples were prepared by drop-casting well-dispersed isopropyl particle suspensions onto a carbon coated copper grids. The Surface area measurements were performed using Quantachrome Autosorb-iQ gas sorption device.

a) Characterization of catalysts (titrations)

S.No	Indicators	pK _a	Colour	
			Basic (B)	Acidic (BH ⁺)
1.	Neutral red	+6.8	Yellow	Red
2.	Phenylazonaphthylamine	+4.0	Yellow	Red
3.	p-Dimethylaminoazobenzene	+3.3	Yellow	Red
4.	Benzeneazo-diphenylamine	+1.5	Yellow	Purple
5.	Dicinnamalacetone	-3.0	Yellow	Red

The acidity and basicity at various acid base strengths were measured by performing titrations using n-butylamine and trichloroacetic acid respectively using a series of indicators mentioned in the table. Since all FeO(OH) are coloured, we used silica-alumina and aluminium oxide as references. The change in the colour of the indicator was monitored on the white solid. In a typical experiment, 0.1 g of silica

alumina was taken along with 0.015 g of the polymorph in a closed conical flask. 5 mL of the standard indicator solution in dry benzene was added and allowed the adsorption process to take place. The solid was then titrated with 0.1 N n-butylamine solution in dry benzene. The neutralization is followed by noting the gradual disappearance of the indicator colour on the white solid. The end point was taken at the point when the entire white solid regained its original colour. The basicity measurements were done using aluminum oxide as reference and trichloroacetic acid as a titrant.

3a.3: Results and Discussions

3a.3.1: Material Characterization

FeO(OH) catalysts were prepared using sol-gel reaction of iron salts and used without any further functionalization or activation (experimental section).[9,11-12] X-ray diffraction (XRD) patterns of the polymorphs of FeO(OH) in Fig. 3a.1a were used to identify the crystalline structures. Each pattern could be indexed to a pure phase of FeO(OH) polymorph. δ FeO(OH) showed some traces of α Fe₂O₃.

The FT-IR absorption spectra from traces (i) to (iv) in Fig. 3a.1b also confirmed the composition of the polymorphs as α , β , γ and δ FeO(OH) respectively. FT-IR absorption bands due to Fe-O symmetric stretching and O-H bending vibrations occurring in the range of 620 - 680 cm⁻¹ and 750 - 1000 cm⁻¹, respectively, were characteristic of FeO(OH) phases.[13-15] The synthesis conditions of the polymorphs did not employ any organic structure directing agent and therefore, the bulk particle morphology was consistent with the natural crystal growth under those pH conditions.

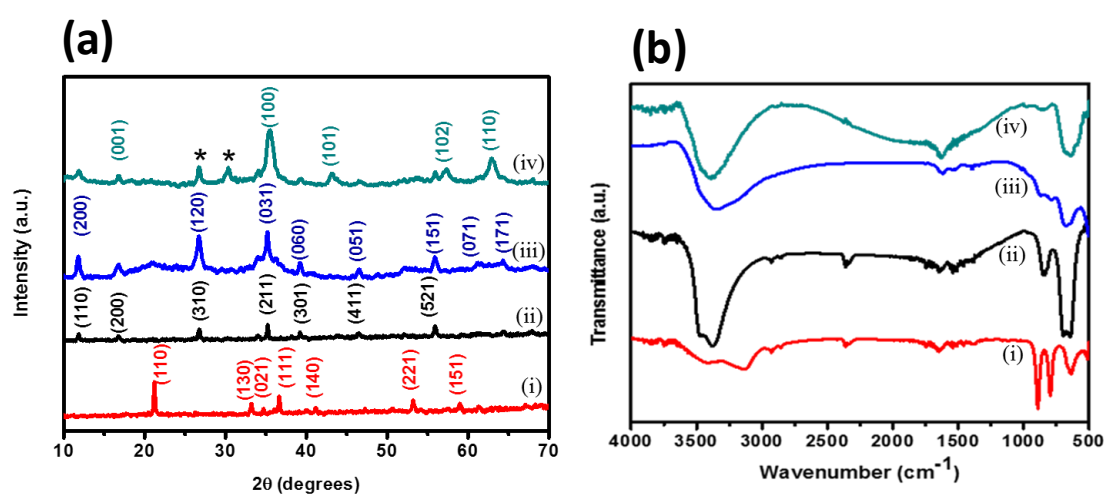


Fig. 3a.1: a) XRD patterns of FeO(OH), b) FT-IR spectra of FeO(OH) polymorphs. Traces (i) α FeO(OH), (ii) β FeO(OH), (iii) γ FeO(OH) and (iv) δ FeO(OH). * Peaks due to α Fe₂O₃.

Morphology and microstructure of FeO(OH) polymorphs were studied using scanning electron microscopy (SEM) and transmission electron microscopy (TEM), respectively. The SEM and TEM images of α FeO(OH) (Fig.s 3a.2a & 3a.b) showed rod shaped microstructures which were 100 – 300 nm in diameter and 250 nm – 1 μ m in length. In Fig.s 3a.2d and 3a.2e, β FeO(OH) showed more uniform rod shaped structures with smaller aspect ratio. The diameter was in the range of 60-70 nm and

length was around 350 nm. Elemental analysis of β FeO(OH) showed the presence of Cl^- ions that are essential for stabilizing the crystal structure. γ FeO(OH) had a layered morphology which was recognized from the shape of the crystals observed using SEM (Fig. 3a.2g). In Fig. 3a.2h, the layers that are standing on its edge can be observed. SEM and TEM images in Fig.s 3a.2j and Fig. 3a.2k showed nanoparticles of δ FeO(OH) which were in the range of 10 – 20 nm. In Fig.s 3a.2c, 3a.2f and 3a.2i, the crystal structure models of α , β and γ FeO(OH) showed the arrangement of $\text{Fe}(\text{O},\text{OH})_6$ octahedra. While, in δ FeO(OH), anions and cations are distributed almost randomly and without a definite arrangement of the octahedra.

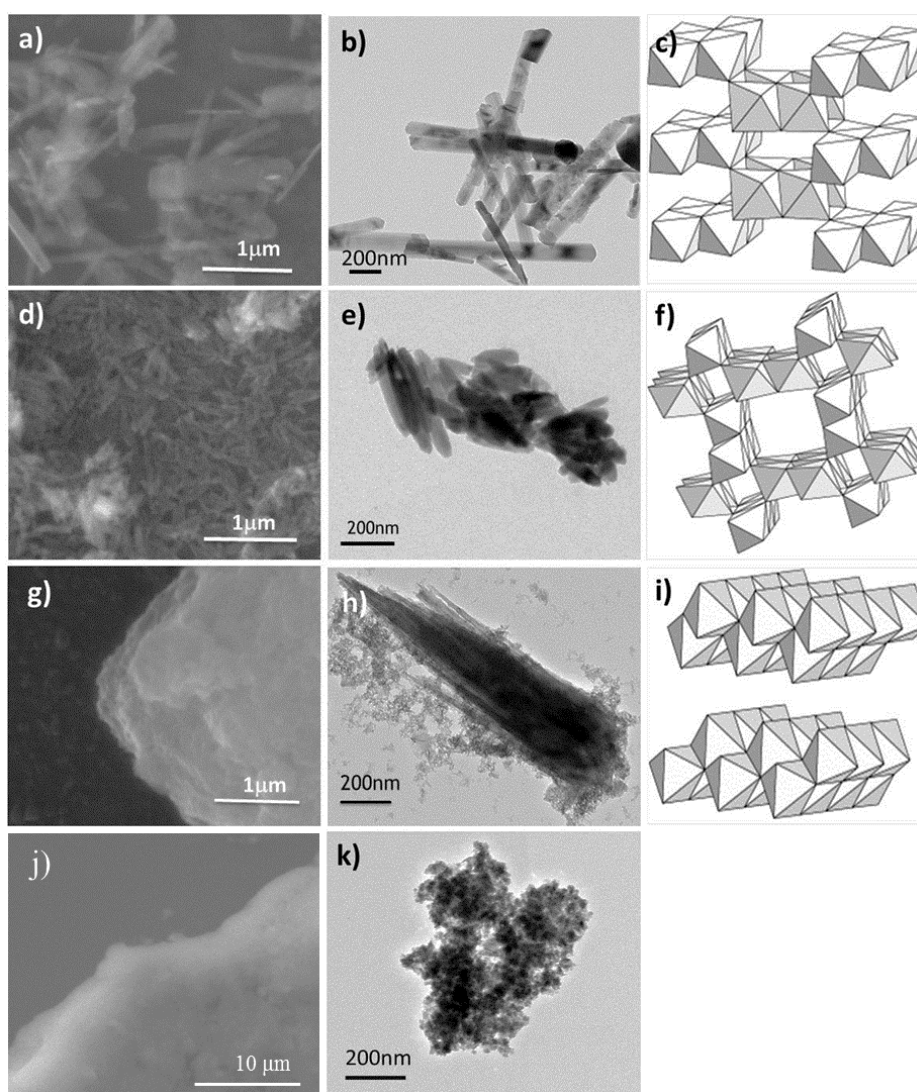


Fig 3a.2: SEM images (a, d, g and j) and TEM images (b, e, h and k) and crystal structures (c, f and i) of the FeO(OH) polymorphs are shown. (a, b, c) α FeO(OH), (d, e, f) β FeO(OH), (g, h, i) γ FeO(OH), and (j, k) δ FeO(OH). The crystal structures were taken from the website <http://shalaleh.blogfa.com/>.

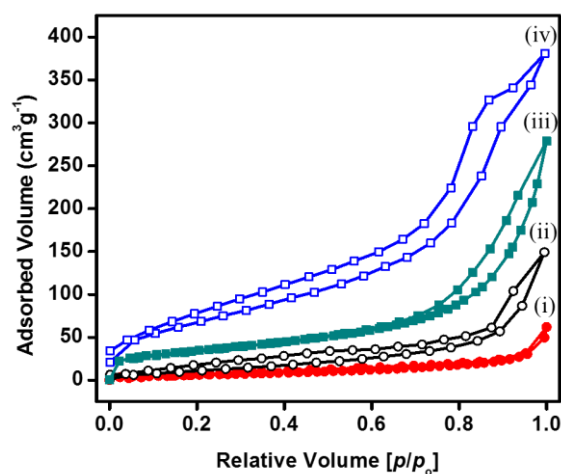


Fig. 3a.3: Nitrogen adsorption-desorption isotherms of FeO(OH) polymorphs. Traces (i) ● α FeO(OH), (ii) ○ β FeO(OH), (iii) ■ δ FeO(OH) and (iv) □ γ FeO(OH)

Textural properties of the FeO(OH) polymorphs were probed using N_2 adsorption isotherms and the results are shown in Fig. 3a.3 and Table 3a.1. BET surface area of the polymorphs differed widely depending on the microstructure of the material. γ FeO(OH) which had a layered structure exhibited the highest surface area of $247 \text{ m}^2\text{g}^{-1}$ and α FeO(OH) with micron sized rod like structures exhibited the least surface area of $24 \text{ m}^2\text{g}^{-1}$. So the surface areas decreased in the order $\gamma > \delta > \beta > \alpha$ FeO(OH) polymorphs. The hysteresis observed could be due to inter particle spaces.

Table 3a.1: Textural parameters of FeO(OH) polymorphs as determined by BET equation.

S. No	Polymorph	Surface area m^2g^{-1}	Pore volume ccg^{-1}	Pore radius \AA
1	α FeO(OH)	24	0.05	13.8
2	β FeO(OH)	44	0.23	17.9
3	γ FeO(OH)	247	0.58	15.8
4	δ FeO(OH)	123	0.32	7.0

3a.3.2: Acid-Base catalysis

FeO(OH) polymorphs were tested for their catalytic activity in deacetalization – Henry reaction as shown in the scheme 3a.1. Mechanistically, benzaldehyde dimethylacetal (**1**) was hydrolysed to form benzaldehyde (**2**) in the presence of an acid catalyst, which further underwent a base-catalyzed Henry condensation with CH_3NO_2 to form 2-nitro-1-phenylethanol (**3**). Dehydration of **3** forms trans- β -nitrostyrene (**4**). In the presence of a base, **3** could further undergo a Michael addition reaction with another molecule of CH_3NO_2 to form 1,3-dinitro-2-phenylpropane (**5**).

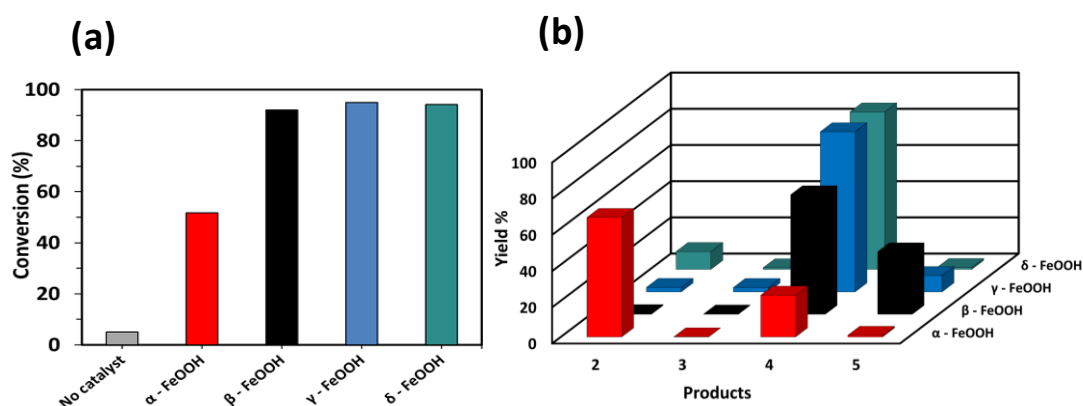
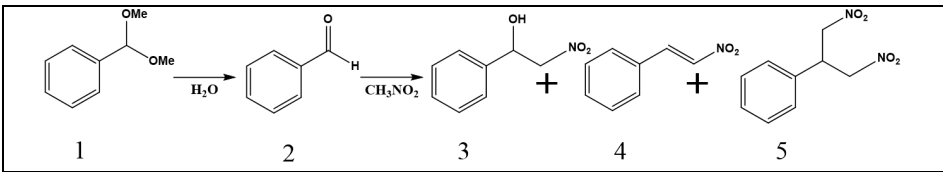


Fig. 3a.4: a) Conversion of deacetalization – Henry condensation reaction of different polymorphs of FeO(OH), b) Selectivity yield of products (**2**, **3**, **4** and **5**) obtained from catalysts α FeO(OH), β FeO(OH), γ FeO(OH) and δ FeO(OH). Reaction was carried out under reflux conditions in CH_3NO_2 for 48 h.

In Fig. 3a.4a and Table 3a.2 the conversion of **1** catalyzed by various polymorphs of FeO(OH) is shown. In the absence of a catalyst, the reaction proceeded with only 5% conversion with **2** as the only product. On the other hand, α FeO(OH) showed a conversion of 52%, and the average conversions of β , γ , and δ FeO(OH) were over 94%. The difference in conversion values shown by different polymorphs of FeO(OH) could be correlated with their respective surface area and morphological aspects. For example, α FeO(OH) with the lowest surface area showed give value conversion in comparison with other polymorphs. The morphology of the catalysts could have had an important role in the catalytic activity of the polymorphs.

Table 3a.2: Conversion & Yields of deacetalization – Henry condensation reaction of different polymorphs of FeO(OH)


Sr.No	Catalyst	Conversion of 1 (%)	GC yield (%)			
			2	3	4	5
1	No Catalyst	5	100	-	-	-
2	α -FeO(OH)	52	72	1	26	1
3	β -FeO(OH)	92	1	2	64	33
4	γ -FeO(OH)	95	1	15	77	6
5	δ -FeO(OH)	94	9	8	82	1

Reactions conditions: **1** (3mmol), H₂O (3mmol), 2mL CH₃NO₂, catalyst 0.1g 105 °C, 48h, N₂ balloon.

The occurrence of α FeO(OH) as micrometer sized particles with a much lower surface to volume ratio compared to other polymorphs is clearly reflected in its poor performance. In addition, the denser octahedral packing of α FeO(OH) could have limited the accessibility of the active sites for the reactant molecules. On the other hand, nanostructured morphology of other polymorphs must have had an advantage in terms of higher surface to volume ratio and easy accessibility of substrate to the active sites. Besides, nanorods of β FeO(OH) crystals are also less dense than α and γ FeO(OH) due to its body centered packing of anions with intracrystalline tunnels. γ FeO(OH) with layered morphology exhibited an interlayer spacing of 2 - 3 nm and a very high surface area. Diffusion of molecules to the active sites along the (100) planes could be easily facilitated through interlayer spacing. It was interesting to note the formation of products **4** and **5** along with **2** and **3** by polymorphs of FeO(OH) (Fig. 3a.4b). Earlier reports have shown that mono-functional acidic or basic catalyst cannot form products **3**, **4** or **5** starting from **1**.^[16] Formation of **4** and **5** strongly suggested the presence of acidic and basic sites on the catalyst surface. Another interesting observation was that the relative ratio of the products formed by each polymorph was different as shown in Fig. 3a.4b. For instance, α FeO(OH) showed a higher selectivity to **2**, while all other polymorphs formed **4** as the major product. Product **3** formation was negligible, under the reaction conditions. Interestingly, β FeO(OH) displayed a unique activity by forming **5** in relatively larger amount than other polymorphs. The products **4** and **5** are important in the

synthesis of pharmaceutical products, fungicides, and herbicides. [17-20] Therefore, a catalyst with a high selectivity to any of these products is highly desirable. Among the polymorphs, γ and δ FeO(OH) formed **4** as the major product.

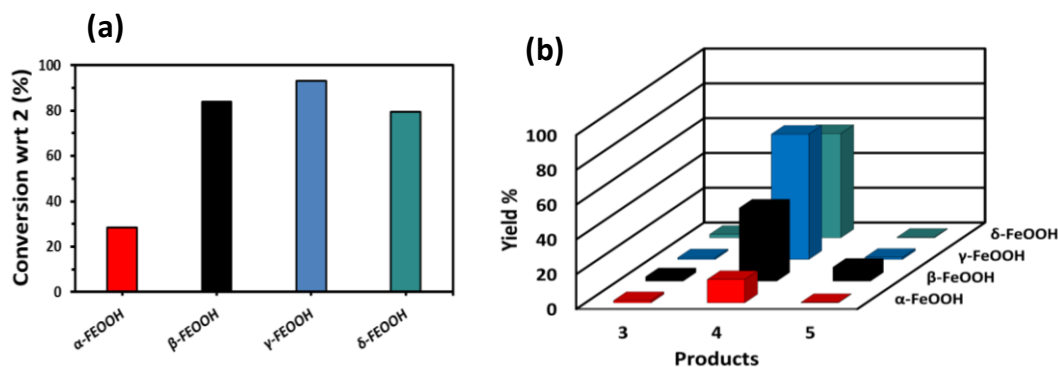


Fig 3a.5: The catalytic activity of the polymorphs of FeO(OH) for in Henry reaction starting from **2** is plotted. Figure a) shows the conversion (%) and b) shows the selectivity of products **3**, **4** and **5**.

In a similar way, the catalytic activities of FeO(OH) polymorphs were studied for Henry reaction starting from **4** as the reactant. The motivation was to study the catalytic behavior of the polymorphs for base-only catalyzed Henry reaction. In Fig 3a.5a, the conversion of **2** is shown for various polymorphs. The conversion and yield of products **3**, **4** and **5** showed similar trend to that shown for the deacetalization-Henry reaction. Table 3a.3 presents the results of the deacetalization-Henry reaction catalyzed by γ and δ FeO(OH). Entries 1 to 4 represent the results of the reactions that were carried out for different duration of time. The yield of **4** was around 93% at the end of 48 h using γ and δ FeO(OH). The difference in the active sites on the surface of FeO(OH) polymorphs became prominent when the reaction was carried out under different conditions. Thus, on decreasing the reaction duration to 12 h, γ FeO(OH) showed a further improvement in the yield of **4**, increasing it to 97.5%, while δ FeO(OH) did not show any improvement. It is interesting to note that although the activity of γ and δ FeO(OH) was similar at 48 h, there was a significant difference in the activity when the reaction was carried out for 12 h. XRD of δ FeO(OH) (Fig. 3a.1a) showed the presence of traces of α Fe₂O₃. However, the observed catalytic behavior of δ FeO(OH) did not have any influence due to the presence of α Fe₂O₃ as the phase impurity. Mainly **2** was obtained in the control experiments under the same conditions when Fe₂O₃ was used as a catalyst. Both γ and δ FeO(OH) did not form **3**

under the reaction conditions. Even under milder conditions at 80 °C, **3** was not observed, probably because the acidic sites of FeO(OH) were active for dehydration of **3** to **4**.

Table 3a.3: Table showing the conversion and selectivity of γ and δ FeO(OH) catalysts.

S.No	Catalyst	Time (h)	Temperature (°C)	Conversion (%)	Yield (%)	
					Product 2	Product 4
1	γ FeO(OH)	48	105	95	2.5	93
2	γ FeO(OH)	12	105	86	0.6	97.5
3	δ FeO(OH)	48	105	94	6	93
4	δ FeO(OH)	12	105	88	21.7	77.7
5	γ FeO(OH)	12	80	71	57	41.6

Reaction conditions: Weight of the catalyst is 0.1 g, 3 mmol of benzaldehyde dimethylacetal, 2 mL of CH₃NO₂ and 3mmol of H₂O. Trace amounts of **5** is also observed. All reactions were carried out in N₂ atmosphere.

Table 3a.4: Table showing the conversion and selectivity of β FeO(OH) catalyst

S.No	Catalyst	[Cl] (At %)	Conversion (%)	Yield ratio
				Product 5 : Product 4
1	β FeO(OH)	1	84	0.1
2	β FeO(OH)	4	95	1.9
3	β FeO(OH)	6	92	0.5
4	β FeO(OH) (OH) [‡]	3	71	1.1

Reactions conditions: Weight of the catalyst is 0.1 g, 3 mmol of benzaldehyde dimethylacetal, 2mL of CH₃NO₂. 3mmol of H₂O. Reflux for 48 h under N₂ atmosphere.
[‡]50 % of the Cl⁻ ions were replaced with OH⁻ ions.

Our attempts to tune the yield of **5** using β FeO(OH) are shown in Table 3a.4. We expected that a higher selectivity to **5** could be obtained due to the presence of Cl⁻ ion in the structure. Accordingly, we prepared β FeO(OH) with different concentrations of Cl⁻ ions without affecting the crystal structure and carried out the reaction under the same conditions. Entries 1 to 3 in Table 3a.4, showed a volcanic relation between Cl⁻ ion concentration and the yield of **5** (relative to **4**). Structural analysis of the used β FeO(OH) catalysts by XRD did not show any significant change in structure due to leaching of Cl⁻ ions. Expecting a dramatic enhancement in the yield of **5**, we exchanged 50% of Cl⁻ ions with more basic OH⁻ ions. However, the result did not show any marked difference.

In order to show the acid-base catalyzed reaction pathway of the catalysts, we chose β and γ FeO(OH) catalyzed reactions and analyzed the products at different time intervals. The reason for choosing these two catalysts was their unique and diverse activity. In Figs. 3a.5a & 3a.5b, the yield (%) of **1**, **2**, **4** and **5** are plotted against time. It was clearly observed that the concentration of starting material **1** decreased while, that of **2** increased with time initially but decreased eventually.

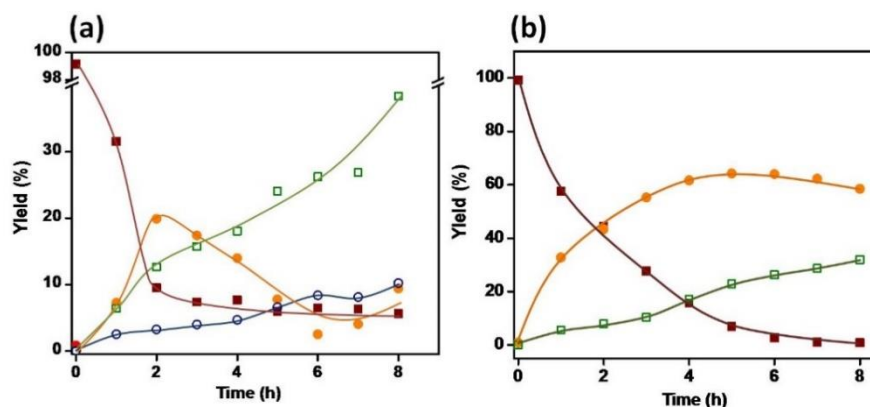


Fig. 3a.6: Time dependent product distribution of (a) β FeO(OH) and (b) γ FeO(OH) catalysts. (■) Reactant **1**, (●) Product **2**, (□) Product **4** and (○) Product **5**.

The decrease in the yield of **2** was accompanied by the increase of **4** in case of γ FeO(OH). Similarly in case of β FeO(OH), an increase in the yield of **4** and **5** occurred with the gradual decrease in the yield of **2**. These observations suggested that **1** was hydrolyzed to **2** progressively with time which underwent condensation with CH_3NO_2 to form products **4** and **5**. In the presence of externally added pyridine, a 63% decrease in the conversion was observed in deacetalization-Henry reaction confirming the role of acidic sites in initiating the first step of the reaction. Thus, acid-base catalyzed reaction pathway starting from **1** leading to **3**, **4** and **5** via **2** as an intermediate is most likely to prevail. It is possible that during the reaction, Fe metal ions leached out of the solid FeO(OH) and behaved as a catalyst for the conversion of **1** to other products such as **2**, **3**, **4** or **5**. In order to prove the heterogeneous nature of FeO(OH) catalysis in deacetalization-Henry reaction, we carried out the reaction using β and γ FeO(OH) starting from **1**. The reaction was carried out for 4 h in the presence of the catalyst during which a conversion of 40-50% was observed with respect to **1**. At this stage, only product **2** was observed in case of both β and γ FeO(OH). Following this, the catalysts were quickly removed by centrifuge and the remaining reaction liquid containing **1**, **2**, CH_3NO_2 and a small amount of H_2O was

subjected to reflux for another 44 h under N_2 atmosphere. The results at the end of 44 h are presented in Fig 3a.7 which showed that the conversion of 1 increased only slightly.

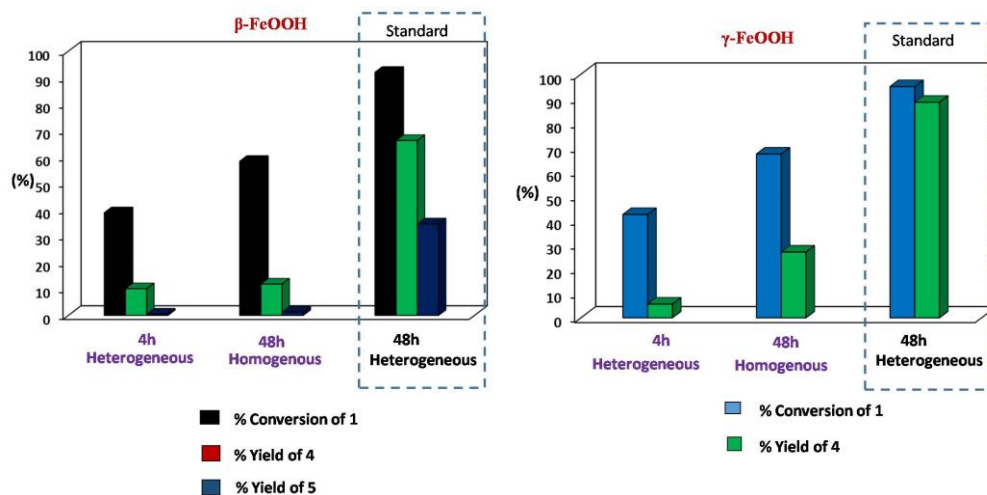


Fig 3a.7 : Heterogeneous catalytic activity of β and γ FeO(OH)

However, the base catalyzed step of the tandem reaction did not proceed at a faster rate. ICP analysis of the reaction crude at the end of the reaction revealed the presence of 0.39 and 6.7 mgL^{-1} of Fe metal. Only a 2 - 8 % increase in the yield of 4 after the duration of 44 h could be due to activity of colloidal nanoparticles of FeO(OH) that were not separated by centrifuge. The experiment clearly proved that the catalytic sites were indeed present on the solid surface of FeO(OH) catalysts.

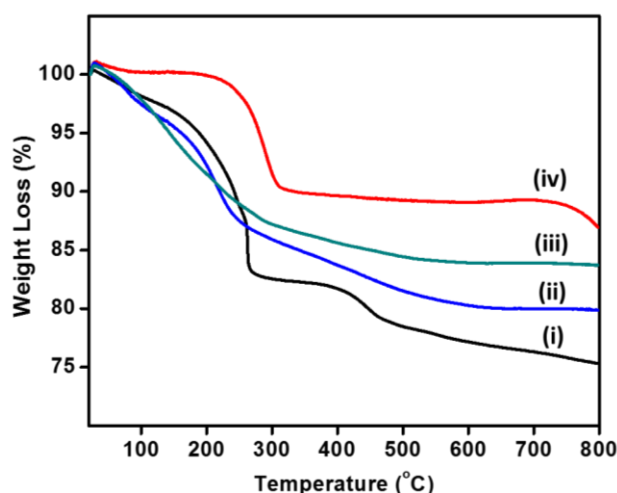
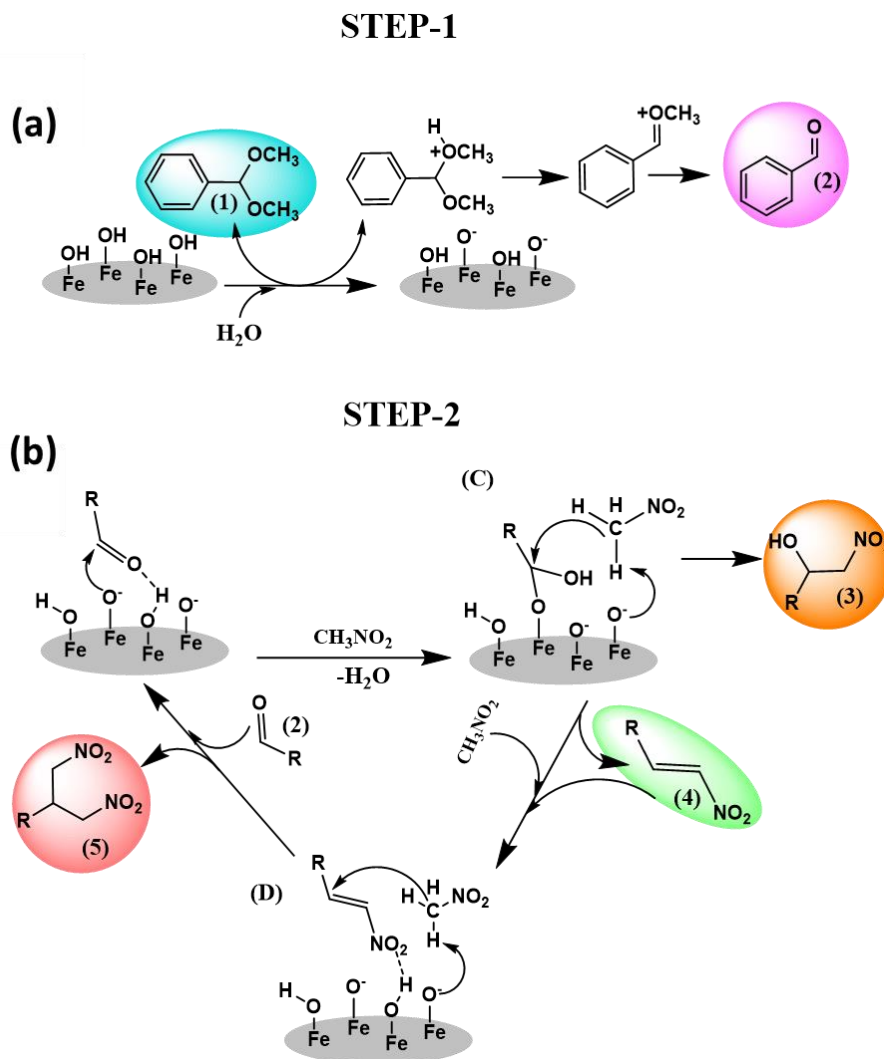


Fig 3a.8 : Thermogravimetric analysis data for the polymorphs Traces (i) β FeO(OH), (ii) γ FeO(OH), (iii) δ FeO(OH) and (iv) α FeO(OH).

The presence of acid-base bifunctional sites on FeO(OH) and their evaluation as catalyst for tandem reaction is an important aspect of this work as it is reported for the first time. The chemical equilibrium existing on the surface of FeO(OH) according to the Eq.1 is probably responsible for the presence of acidic and basic sites together. The surface -OOH groups on FeO(OH) act as Brønsted acid and its conjugate base FeOO⁻ behaves as a Brønsted base. In order to establish the role of H₂O, we carried out control experiments using γ FeO(OH) as the catalyst. In the absence of H₂O, the conversion was found to decrease drastically to 52% (95% in the presence of H₂O). This observation proved that the rate of reaction decreased in the absence of H₂O. On analyzing, it was observed that the yield of **2** was dominant in the absence of H₂O as compared to in the presence of H₂O. A similar kind of behavior was observed in Henry reaction starting from benzaldehyde using γ FeO(OH) as the catalyst. In the presence of water, we observed 94% conversion while, only 49% conversion was observed in the absence of H₂O. The significant amount of conversion even in the absence of external H₂O was intriguing. Thermogravimetric analysis (Fig. 3a.8) of the polymorphs however, revealed that surface adsorbed moisture accounted for nearly 10 – 20 % weight loss in the temperature range below 200 °C which could have played the promotional role in the hydrolysis step of the reaction. Thus, H₂O is crucial in the creation of both acidic and basic sites on the catalyst which were responsible for catalyzing the tandem reaction.

In Scheme 3a.2, the mechanism of reaction on the surface of FeO(OH) is summarized. Step 1 involves the acid (FeO(OH)) catalyzed deacetalization reaction forming **2** while step 2 shows the base (FeOO⁻) catalyzed condensation reaction leading to the formation of products **3**, **4** and **5**.



Scheme 3a.2: Mechanism of deacetalization-Henry condensation reaction occurring on the surface of FeO(OH).

3a.3.3: Acidity and Basicity

In order to probe the nature of the acid and base sites, pyridine was adsorbed on FeO(OH) samples and FT-IR spectra were recorded (Fig. 3a.9). The absorption bands of the FT-IR spectra in the range 1515-1565 cm^{-1} were attributed to the Brønsted acid protons while Lewis acidic sites were detected in the range 1435-1470 cm^{-1} . All polymorphs showed at least three prominent bands in this region around 1560, 1541 cm^{-1} . and 1508 cm^{-1} which was attributed to the formation of pyridinium ion due to Brønsted acid sites. The band at 1457 cm^{-1} could be attributed to the adduct formed by pyridine with the Lewis acid Fe^{3+} . [21, 22]

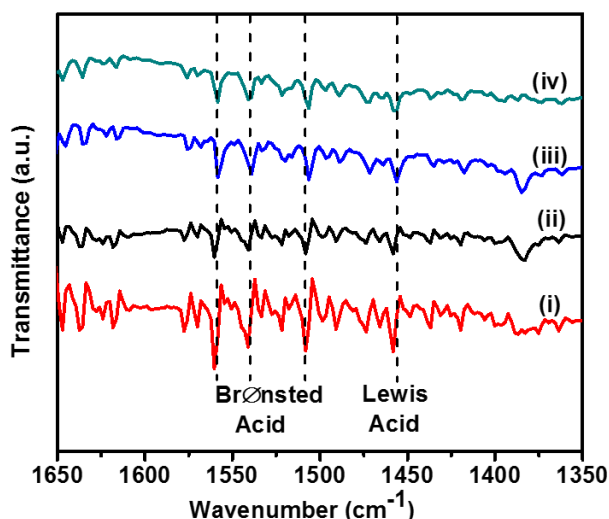


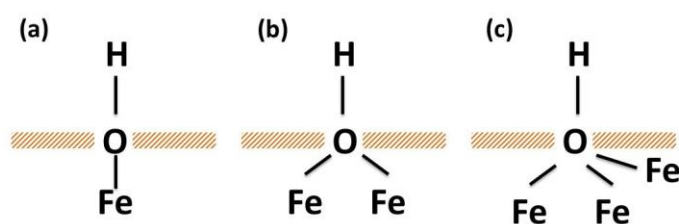
Fig. 3a.9: FT-IR spectra polymorphs of FeO(OH) adsorbed with pyridine. Traces (i) α FeO(OH), (ii) β FeO(OH), (iii) γ FeO(OH), (iv) δ FeO(OH)

Strength of acidic and basic sites and their density on the surface was estimated by acid-base titrations using Hammett indicators of different H_0 values. (See experimental section) The acidity value is represented as the number of acid sites (mmol g^{-1}) whose acid strength is equal to or less than the H_0 value (of the indicator) and the basicity as the number of basic sites (mmol g^{-1}) whose base strength is equal to or greater than the H_0 value (of the indicator). Acidity and basicity are tabulated on a common H_0 scale using an already reported procedure.[23] Low H_0 value referred to a strongly acidic site and a high H_0 value represented a strongly basic site. Table 3a.5 shows the surface acidity and basicity values on a common H_0 value for all the FeO(OH) polymorphs. The polymorphs showed a high number of acid sites of various strengths.

Table 3a.5: Strength and density of acid and base sites on FeO(OH) catalysts determined using Hammett indicators.

Catalyst	Acidity (mmol g^{-1})					Basicity (mmol g^{-1})				
	$H_0 \leq -3.3$	$H_0 \leq 1.5$	$H_0 \leq 3.3$	$H_0 \leq 4.0$	$H_0 \leq 6.8$	$H_0 \geq -3.3$	$H_0 \geq 1.5$	$H_0 \geq 3.3$	$H_0 \geq 4.0$	$H_0 \geq 6.8$
α FeO(OH)	6.03	10.72	10.05	6.7	0.67	0	0.07	0	0	0
β FeO(OH)	1.67	8.71	10.59	4.02	0.34	0	0.33	0	0.01	0.001
γ FeO(OH)	5.36	10.05	10.32	3.35	0.34	0	0.13	0	0.01	0
δ FeO(OH)	4.35	9.38	10.18	3.35	0.4	0	0.33	0	0	0

The numbers of acid sites were comparatively higher than the number of basic sites which could probably mean a low equilibrium constant of reaction in eq. 1. The presence of acid and base sites of different strengths may be due to different types of –OOH groups on the surface of the catalysts. The strengths of –OOH groups could vary due to differences in coordination numbers of O atoms and intermolecular H-bonding specific to the crystal structure. Theoretical calculations in earlier reports have identified at least three sites with different coordination of oxygen atom. [24-26] These are presented in Scheme 3a.3



Scheme 3a.3: Representation of different types of surface hydroxyl groups on FeO(OH) in a) single b) double and c) triple coordinated modes

The results presented in Table 3a.5 are useful to understand the difference in the selectivity of products obtained using FeO(OH) catalysts. For example, α FeO(OH) possessed maximum number of acid sites and least number of basic sites among the polymorphs of FeO(OH). Thus, α FeO(OH) always formed only **2** as the major product as the basic sites were not enough in strength and number to catalyze Henry reaction. Although α FeO(OH) had strong acid sites, the dense crystal structure with a low surface area resulted in poor conversion. Other FeO(OH) polymorphs possessed both acidic and basic sites and therefore, could form condensation products **4** and **5**. Similar trends in the conversion and yield of products were observed for FeO(OH) polymorphs in Henry reaction (Fig 3a.9). Interestingly, α FeO(OH) which formed only **2** in deacetalization –Henry reaction showed the selectivity for **4** in Henry reaction although only less than 20%. This is in agreement with our assumption that α FeO(OH) is predominantly acidic but has some basic sites as $H_0 = 1.5$. However, considering the number of active sites (acid and base), TOF for Henry reaction was higher by two orders of magnitude compared to TOF of deacetalization-Henry reaction. TOF (h^{-1}) of the catalysts for deacetalization Henry

reaction are as follows α FeO(OH) (3.8×10^{-2}), β FeO(OH) (6.9×10^{-2}), γ FeO(OH) (7.3×10^{-2}) and δ FeO(OH) (7.9×10^{-2}). TOF (h^{-1}) for Henry reaction are as follows α FeO(OH) (2.5), β FeO(OH) (1.5), γ FeO(OH) (4.2) and δ FeO(OH) (1.5).

Another interesting observation seen from Table 3a.3 was that γ and δ FeO(OH), which showed a similar activity (conversion and selectivity) at 48 h differed much at the end of 12 h. This observation suggests that γ FeO(OH) possessed more number of accessible active sites than δ FeO(OH) which is clearly evident from the values of acidity and basicity shown in Table 3a.4. The formation of **5** in case of β FeO(OH) was interesting which needs stronger basic sites because of the Michael addition of product **4** with CH_3NO_2 . The presence of trace amounts of strong basic sites of $H_0 = 6.8$ in β FeO(OH) is probably responsible for the enhanced selectivity of **5** by β FeO(OH). The unique feature of β FeO(OH) is the presence of Cl^- ions. The $-\text{OH}$ groups are directed towards the centre of the tunnel which is stabilized by Cl^- ions. Attempts to improve the selectivity by replacing the Cl^- ion with more basic OH^- ions did not have much effect. This suggested that the location of Cl^- or OH^- ions were most likely inaccessible to the reactants. However, it is possible that the strong basic sites on β FeO(OH) could be because of the H-bonding interactions involving Cl^- ions in the crystal structure. Further studies are needed to understand this aspect clearly.

3a.3.4 Catalyst Recyclability and stability studies

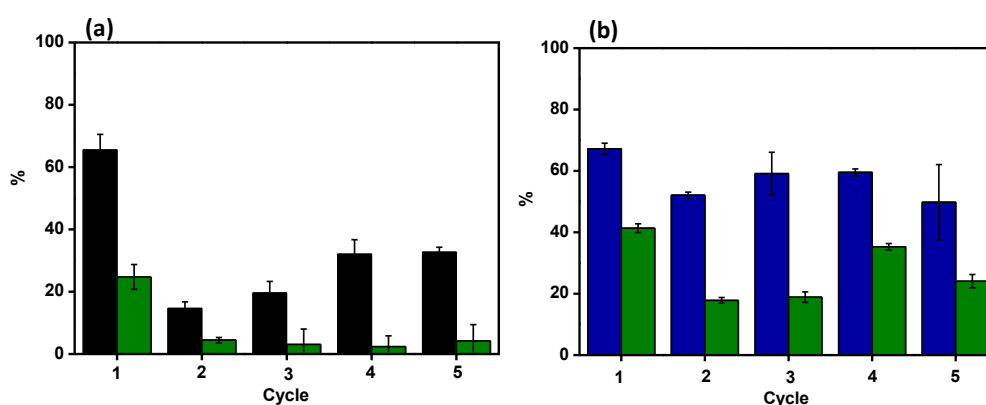


Fig. 3a.10: Reusability studies of (a) β FeO(OH), where Conversion % with respect to 1 (■) and selectivity for 4 (■) and (b) γ FeO(OH), where conversion with respect to 1 (■) and selectivity with respect to 4 (■) for deacetalization-Henry reaction at 80 °C for 12 h are plotted.

The stability of the catalysts was studied for β and γ FeO(OH) and the data is shown in Fig. 3a.10. The recyclability data of β and γ FeO(OH) with conversion (with respect to 1 in 12 h) along with the selectivity of product 4 is plotted as Fig. 3a.10a and 3a.10b, respectively. β FeO(OH) showed a significant decrease in the conversion from second cycle onwards (black bars in Fig. 3a.10a) and it recovered. However, elemental analysis showed only 0.39 mgL^{-1} of Fe in the reaction medium which is insignificant.

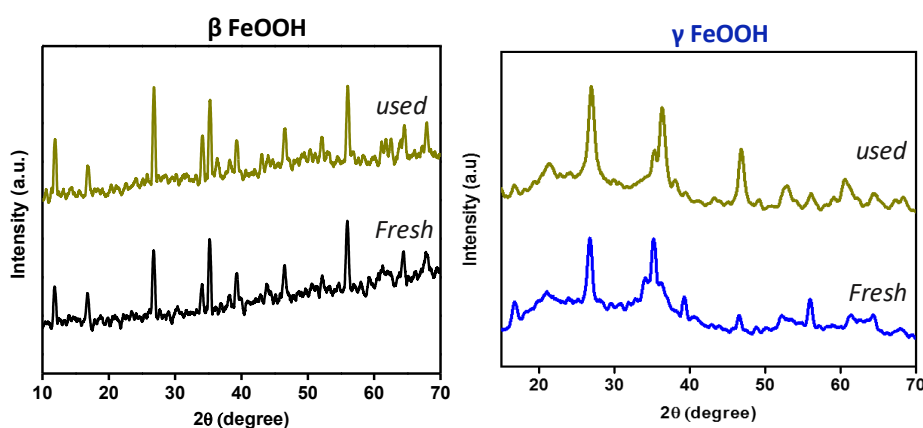


Fig 3a.11: XRD patterns of fresh and the used catalysts (after 5 cycles) β FeO(OH) and γ FeO(OH).

XRD and TEM analysis confirmed the stability of the crystal structure of β FeO(OH) even after five cycles (Fig.s 3a.11 and 3a.12, respectively) suggesting no significant loss of Cl^- ion. On estimating the acid and base functional groups by titration, it was observed that there was a considerable decrease in the values of surface acidic groups. Certainly, the drastic loss in the levels of conversion could be related to the low values of active sites.

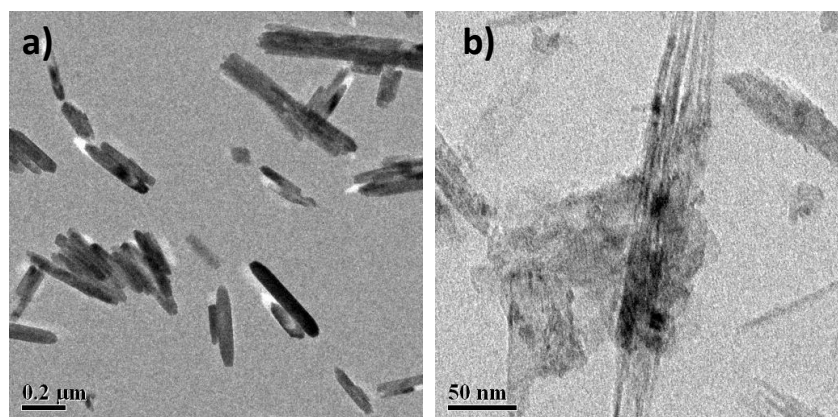


Fig 3a.12: TEM data of fresh and used samples of β and γ FeO(OH)

FT-IR of used β FeO(OH) (after one cycle) was compared with that of the fresh catalyst (Fig 3a.13b). We could observe the appearance of new absorption bands in the region 1400 cm^{-1} suggesting the presence of aromatic C=C functional groups on the used β FeO(OH) catalysts. Among the polymorphs, β FeO(OH) possessed intra crystalline channels of diameter close to 0.8 nm which may be suitable for the diffusion of small molecules such as CH_3NO_2 . However, after reaction, the diffusion of condensation products such as **3**, **4** or **5** away from the active sites could be slower. It is possible that the larger molecules could strongly interact with the acid sites causing deactivation. In order to confirm this, we carried out TGA of used β FeO(OH) and compared it with the fresh sample. Although no any significant weight loss due to adsorbed organic molecules was observed, a weight loss in the temperature region $250 - 400\text{ }^\circ\text{C}$ was observed which is due to loss of Cl^- ions. TGA data suggested that used β FeO(OH) had lesser amount of Cl^- ion compared to the fresh sample but not low enough to affect the structural stability. However, it appears that the loss in Cl^- ion has had its impact in the strength of the acid-base sites and hence the levels of conversion specify. It must also be noted that although the level of conversion (with respect to **1**) seemed to recover by 5-15 % after 2nd cycle, the loss in the selectivity of **4** remains the same. The exact reason for the recovery in conversion of **1** in β FeO(OH) is not clear. On the other hand, γ FeO(OH) showed a relatively stable level of conversion of **1** even after five cycles of reaction (Fig. 3a.10b). The selectivity to **4** was maintained more or less at the same level. XRD pattern and TEM image of the sample after five cycles of reactions showed no changes in the crystalline structure of β and γ -FeO(OH).

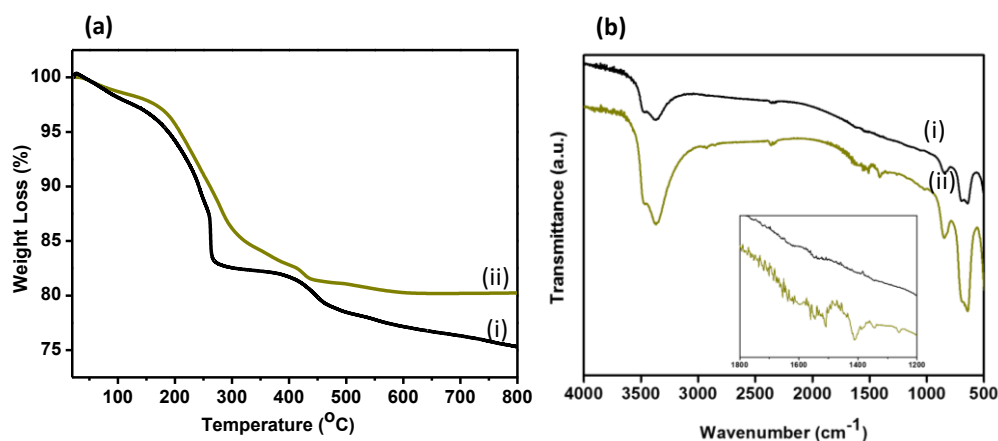


Fig 3a.13: a) TGA and b) IR data of fresh and used β FeO(OH)

3a.4: Conclusions

In conclusion, the acid-base bi-functional catalytic activity of the polymorphs of FeO(OH) namely α , β , γ and δ is described for the first time for deacetalization – Henry condensation reaction . The polymorphs exhibited different selectivity of products which could be tuned to some extent by changing the time of reaction and sample composition. The origin of acid and base bifunctional sites is due to the surface chemical equilibrium between FeO(OH) and FeOO⁻ groups. The difference in the selectivity for the condensation products with different polymorphs is probably due to the different types of FeO(OH) sites and the density of the sites present on the crystal facets of the polymorphs. These results are of great significance because the bifunctional aspects of FeO(OH) polymorphs and their role in the practical applications for deacetalization-Henry reaction are demonstrated. The catalytic property of FeO(OH) also suggests the potential bifunctionality of other hydroxylated metal oxides. The novel properties of this naturally available mineral can be useful for further applications in several catalytic reactions of practical importance.

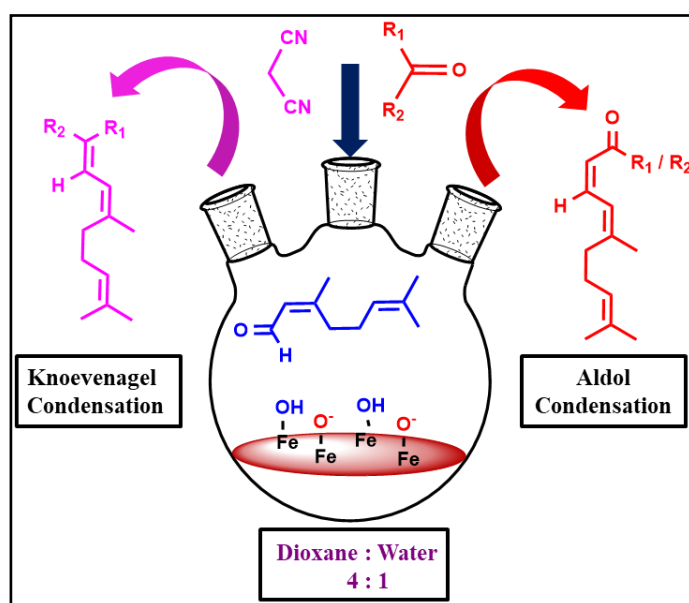
3a.5: References

- [1] I. Oroz-Guinea and E. García-Junceda, *Current Opinion in Chemical Biology*, 2013, **17**, 236-249.
- [2] J. M. Lee, Y. Na, H. Han and S. Chang, *Chemical Society Reviews*, 2004, **33**, 302–312.
- [3] M. J. Climent, A. Corma, S. Iborra and M. J. Sabater, *Green Chemistry*, 2014, **4**, 870-891.
- [4] S. Huh, H-T. Chen, J. W. Wiench, M. Pruski and V. S.-Y. Lin, *Angewandte Chemie, Int. Ed.*, 2005, **44**, 1826 –1830.
- [5] U. Diaz, D. Brunel and A. Corma, *Chemical Society Reviews*, 2013, **42**, 4083-4097.
- [6] K. Motokura, M. Tomita, M. Tada and Y. Iwasawa, *Chemistry–A European Journal*, 2008, **14**, 4017-4027.
- [7] B. Liu, H. Liu, C. Wang, L Liu, S. Wu, J. Guan and Q. Kan, *Applied Catalysis A: General*, 2012, **443–444**, 1-7.
- [8] E. L. Margelefsky, R. K. Zeidan and M. E. Davis, *Chemical Society Reviews*, 2008, **37**, 1118–1126.
- [9] L. Xu, C Li, K Zhang and P Wu, *ACS Catalysis*, 2014, **4**, 2959 –2968.
- [10] A. Corma, U. Diaz, T. Garcia, G.Sastre, and A. Velty, *Journal of the American Chemical Society*, 2010, **132**, 15011-15021.
- [11] R. M. Cornell and U. Schwertmann, in *The Iron Oxides*, Wiley-VCH Verlag GmbH & Co. KGaA, 2003, pp. 222-228.
- [12] G. Lee, S. Kim, B. Choi, S. Huh, Y. Chang, B. Kim, J. Park and S. J. Oh, *Journal of the Korean Physical Society*, 2004, **45**, 1019 –1024.
- [13] P. Cambier, *Clay Minerals*, 1986, **21**, 191-200.
- [14] E. Murad and J. Bishop, *American Mineralogist*, 2000, **85**, 716-721.
- [15] S. Okamoto, *Journal of the American Ceramic Society*, 1968, **51**, 594-599.
- [16] P. Li, C. Cao, Z. Chen, H. Liu, Y. Yu and W. Song, *Chemical Communications*, 2012, **48**, 10541–10543.
- [17] D. Y. Park, K. Y. Lee and J. N. Kim, *Tetrahedron letters*, 2007, **48**, 1633-1636.
- [18] S B. Tsogoeva, *European Journal of Organic Chemistry*, 2007, **11**, 1701–1716.

- [19] N. Milhazes, R. Calheiros, M. Marques, J. Garrido, M. Cordeiro, C. Rodrigues, S. Quinteira, C. Novais, L. Peixe and F. Borges, *Bioorg. Med. Chem Bioorganic & medicinal chemistry*, 2006, **14**, 4078–4088.
- [20] J. M. Betancort, and C. F. Barbas, *Organic Letters*, 2001, **3**, 3737–3740.
- [30] D. Yazici and C. Bilgic, *Surface and Interface Analysis*, 2010, **42**, 959 - 962.
- [31] M. Yurdakoc, M. Akcay, Y. Tonbul and K. Yurdakoc, *Turkish Journal of Chemistry*, 1999, **23**, 319 - 327.
- [32] T. Yamanaka and K. Tanabe, *Journal of Physical Chemistry*, 1976, **80**, 1723–1727.
- [33] P. Venema, T. Hiemstra, P. Weidler, and W. Riemsdijk, *Journal of Colloid and Interface Science*, 1998, **198**, 282-295.
- [34] T. Hiemstra, P. Venema and W. Riemsdijk, *Journal of Colloid and Interface Science*, 1996, **184**, 680 – 692.
- [35] V. Barron and J. Torrent, *Journal of Colloid and Interface Science*, 1996, **117**, 407 - 411.

Chapter 3b

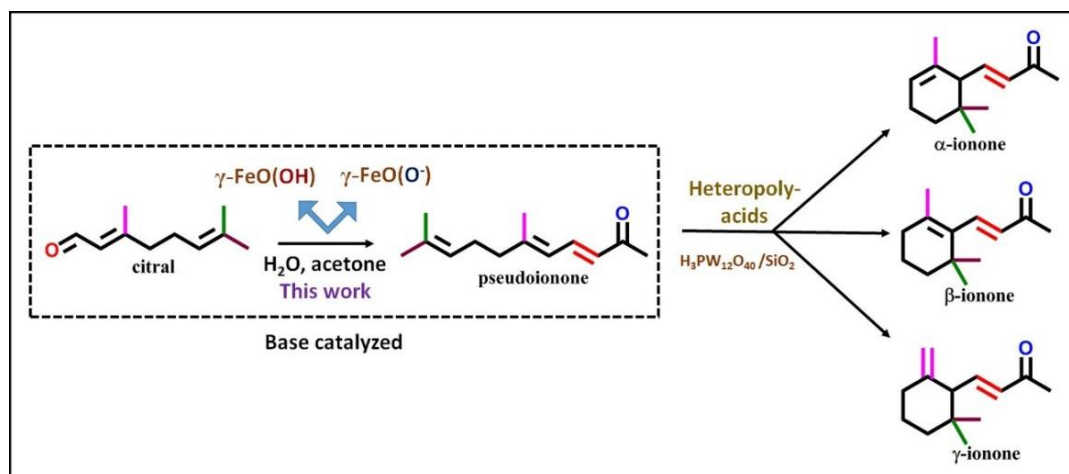
Water-promoted surface basicity in FeO(OH) for the synthesis of Pseudoionones (PS) and their analogues



Dnyanesh Vernekar, Sachin S. Sakate, Chandrashekhar V. Rode, and Dinesh,
Journal of Catalysis, 378, 80-89, 2019

3b.1: Introduction

Pseudoionones (PS) are special monoterpenoids used in the synthesis of industrially important chemical intermediates such as α -, β - and γ -ionones.[1] PS are synthesized on large scale by aldol condensation between citral and acetone in the presence of a base (Scheme 3b.1).[2] The product yields vary between 50-80% depending upon the reaction conditions and the catalysts used. Heterogeneous base catalysts such as alkaline metal oxides [3], basic zeolites [4], and Mg-Al hydrotalcites [5] are preferred over homogeneous bases due to their non-toxicity, non-corrosion, minimal waste and good recyclability. Recently, LiOH.H₂O [6], aluminophosphates (ALPO) [7], anionic clays [8], choline hydroxide/MgO [9], KF-Al₂O₃ [10] and Mg-Al mixed oxides containing rare earth elements [11] have been shown to catalyze the synthesis of PS. Among various catalysts, hydrotalcites are quite interesting as shown by the studies on reconstructed hydrotalcites (Mg₆Al₂(OH)₁₈.4H₂O), because a combination of O²⁻ (Lewis basic) and intercalated OH⁻ anions (Brønsted base) provide higher activity.[12] The presence of charge-compensating Brønsted base (OH⁻ ions) in the Mg-Al hydrotalcite matrix was shown to increase the selectivity of PS from 60% to >90% as compared to the catalysts with just O²⁻ sites. Unfortunately, these intercalated OH⁻ ions have a tendency to leach away into the solvent due to their non-covalent bonding, leading to a severe loss in the activity. Taking a clue from this work, we explored the use of iron oxyhydroxide FeO(OH) as a catalyst for the synthesis of PS. FeO(OH) is a metastable intermediate during the synthesis of iron oxides from its hydroxide gel precursor. It intrinsically possesses significant concentration of potential Brønsted basic sites such as -O⁻ and Lewis basic sites such as O²⁻ in the crystal structure (Scheme 2a). [13] Most importantly, the basic sites (O⁻ & O²⁻) are chemically bonded to the metal and occur in close proximity to O²⁻ sites of FeO(OH) crystal. The structure is therefore suitable for a high and stable activity in the synthesis of PS.[14] For the first time, we report the use of FeO(OH) as stable and highly active catalyst for the synthesis of PS. In addition, we also evidenced that H₂O promotes the catalytic activity of FeO(OH).



Scheme 3b.1. Flowchart showing the synthesis of ionones from citral via pseudoionones[15]

3b.2: Experimental Section.

Materials & Methods

Ferrous chloride ($\text{FeCl}_2 \cdot 4\text{H}_2\text{O}$) and sodium hydroxide (NaOH) were purchased from Thomas-Baker. Citral and other active methylene substrates were obtained from Sigma-Aldrich. Analytical grade acetone was obtained from Merck. Methanol, ethyl acetate, petroleum ether and silica gel (100-230-400 mesh) were obtained from Chem Labs, India.

3b.2.1: General experimental procedure for the preparation of $\gamma\text{-FeO(OH)}$: 4 g of $\text{FeCl}_2 \cdot 4\text{H}_2\text{O}$ was dissolved in distilled water. To this, 1 M NaOH was added until pH of the solution reached 6.5-6.8. At this pH, greenish black deposits were formed. Oxygen was bubbled through this solution for 20 minutes to obtain orange deposit of $\gamma\text{-FeO(OH)}$ which was separated by filtration and washed with ethyl alcohol and distilled water several times and dried at 60°C . All the other control catalysts (CaO , MgO , CeO_2 , AlPO , Al_2O_3) were prepared using standard preparation methods from literature. [3, 7, 9 &10]

3b.2.2: General experimental procedure for the synthesis of PS: In a 50 mL round bottom flask, citral (0.152 g, 1 mmol) and acetone (0.116 g, 2 mmol) were taken along with specially dried 1,4-dioxane (5 mL) as a solvent. H_2O (1 mL) was used as an additive, the catalyst amount was fixed at 0.100 g. The round bottom flask was connected to a water-cooled Liebig condenser which was tightly sealed at the other

end to prevent any evaporation. The reaction mixture was heated up to 100 °C (reflux) in an oil bath. The reaction was monitored by using thin layer chromatography. After the completion of the reaction, reaction mixture was filtered, water removed using anhydrous MgSO_4 and the mixture was analyzed by Gas chromatograph equipped with mass spectrometer as well as isolated using column chromatography and confirmed by ^1H NMR.

3b.2.3: In situ CO_2 -IR & methanol dissociation studies: In situ CO_2/MeOH adsorption/dissociation Infrared Spectroscopy measurements were done using PerkinElmer 2000 Frontier FT-IR equipped with Praying Mantis™ assembly using MCT (HgCdTe) detector. CO_2/MeOH were injected into the port from which the injected molecule was driven under nitrogen flow (50mL/min) and adsorbed on the sample. The samples were then analyzed using the spectrum software and compared with the blank measurements.

3b.2.4: Fluorescence studies using Rhodamine 6G: In a 10 mL volumetric flask, 0.002 M Rhodamine 6G solution was prepared in distilled water. 4 mL of this solution was taken and 10 mg of $\gamma\text{-FeO(OH)}$ was added and the resultant mixture was stirred for 6 h at room temperature. The catalyst was then removed and the resultant filtrate was subjected to fluorescence measurements at the excitation wavelength of 500 nm and emission wavelength centered around 562 nm. The fluorescence emission spectra of Rh-6G were analyzed using PTI Quanta Master™ steady state spectrofluorometer. The resultant FeO(OH)-Rh-6G complex was obtained by thoroughly drying over Buchi rotavap and its FT-IR was recorded and compared with bare FeO(OH) and Rh-6G solids. To quantify the amount of Rh-6G adsorbed in dioxane-water mixtures, four different solutions constituting various ratios of dioxane: water were prepared (10 mL). 20 mg of Rh-6G was dissolved in each of these and 40 mg of FeO(OH) was dispersed in 5 mL of the above prepared Rh-6G solutions and stirred at room temperature for 1 h. The fluorescence measurements were done after removing FeO(OH) and immediately quantified based on the calibration plots for the various solution mixtures.

3b.2.5: FeO(OH) Activation studies, Hot filtration, & Recyclability test: $\gamma\text{-FeO(OH)}$ activation studies were performed by taking a two neck round bottom flask containing 100 mg FeO(OH) , 5 mL 1,4-dioxane and 1 mL distilled water. One neck

of the flask was attached to the Liebig condenser and the other was sealed using a rubber septum. The reaction mixture was refluxed for 2 h. After 2 h of reflux, acetone and citral were introduced in the flask simultaneously using a syringe through the rubber septum. Aliquots were removed hourly and analyzed using GC-MS. For Hot filtration test, the reaction was carried out in a two neck round bottom flask using the same standard reaction conditions and reactant concentrations. The reaction was stopped after 4 h and the catalyst was filtered using a syringe filter and the supernatant liquid was further allowed to reflux without any catalyst. Recycle studies were performed by washing the filtered catalyst with 1,4-dioxane and MeOH after every cycle (12 h reaction) and then dried to be used for next cycle.

3b.2.6: Material characterization: X-ray diffraction measurements were made using Phillips PAN analytical diffractometer with Cu-K α radiation ($\lambda = 1.5406 \text{ \AA}$). Transmission electron microscopy (TEM) images were obtained using FEI Tecnai-20ST electron microscope. Specimens of the samples were prepared by drop-casting well-dispersed isopropyl particle suspensions onto a carbon coated copper grid. The surface area measurements were performed using Quantachrome Autosorb-iQ gas sorption device. The binding energies of the elements on the catalyst were analyzed by X-ray photoelectron spectroscopy (Thermo Fisher Scientific Instruments UK, Model K ALPHA +) with an X-Ray Source- Al K α (Monochromatic) with 6 mA beam current and 12 kV.

3b.2.7: Analysis of reaction products: The catalytic reaction was monitored and the liquid samples were quantitatively analyzed using Shimadzu GC-MS QP 2010 Ultra using Restek FFAP/HP-5 columns with the ion source temperature maintained at 210 °C. The injection and interface temperature were set at 220 °C. The carrier gas used was Helium. The column ramping was 20 °C/min starting from 30 °C till 210 °C with 40 min hold at the final temperature. The catalysis reaction involving different substrates were monitored on TLC (Thin Layer Chromatography) and the products were isolated using column chromatography and confirmed by ^1H NMR.

3b. 3: Results and Discussion

3b.3.1: Material characterization

The crystal structure of FeO(OH) sample was studied using X-ray diffraction pattern and was found to be consistent with the reported pattern of γ -FeO(OH) (JCPDS card no 73-2326) [16] (Fig. 3b.1a). It has an orthorhombic structure with arrays of close-packed anions (O^{2-}/OH^-) stacked along the [150] direction and Fe^{3+} ions occupying the octahedral interstices (Scheme 3b.2a). FT-IR spectra (Fig 3b.1b) showed a broad absorption band in the range of $3350\text{ cm}^{-1} - 3400\text{ cm}^{-1}$ due to O-H stretching characteristic of the FeO(OH) polymorph. Bands in the wave number regions of $620-680\text{ cm}^{-1}$ are due to Fe-O symmetric stretching. Characteristic bands in $750 - 1000\text{ cm}^{-1}$ are due to -OH bending and stretching vibrations.[17]

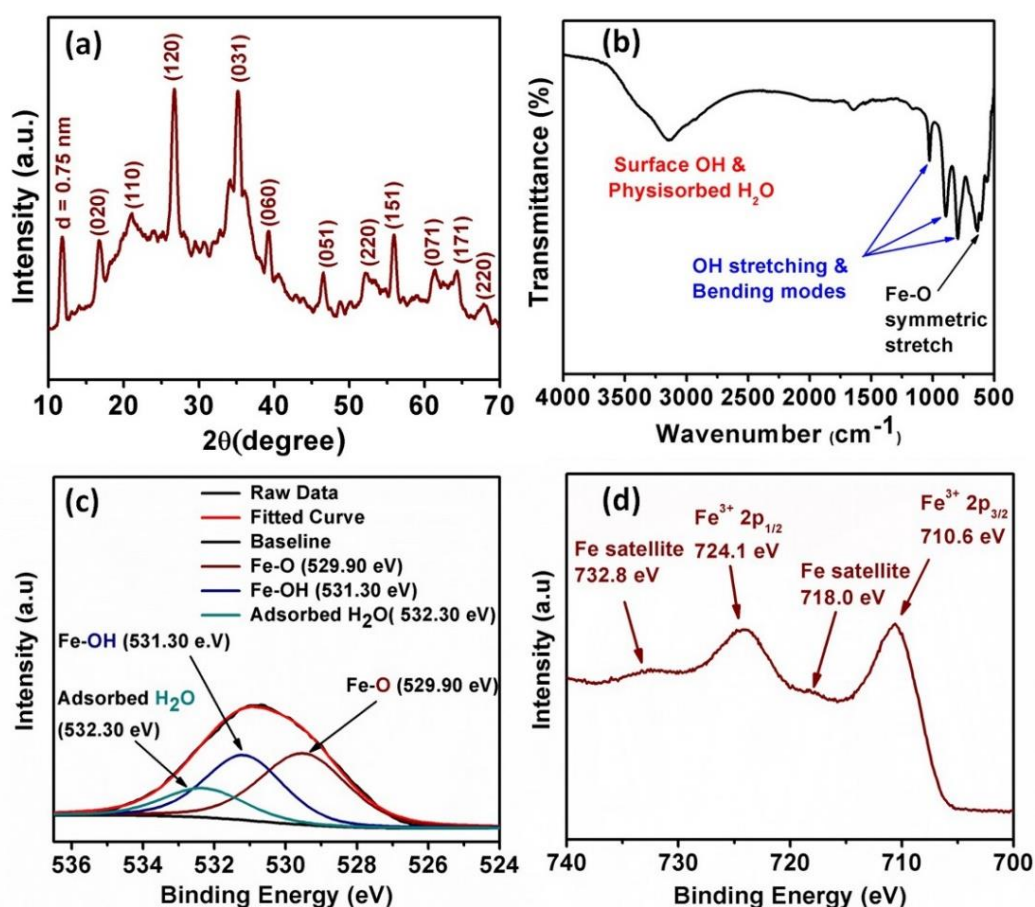
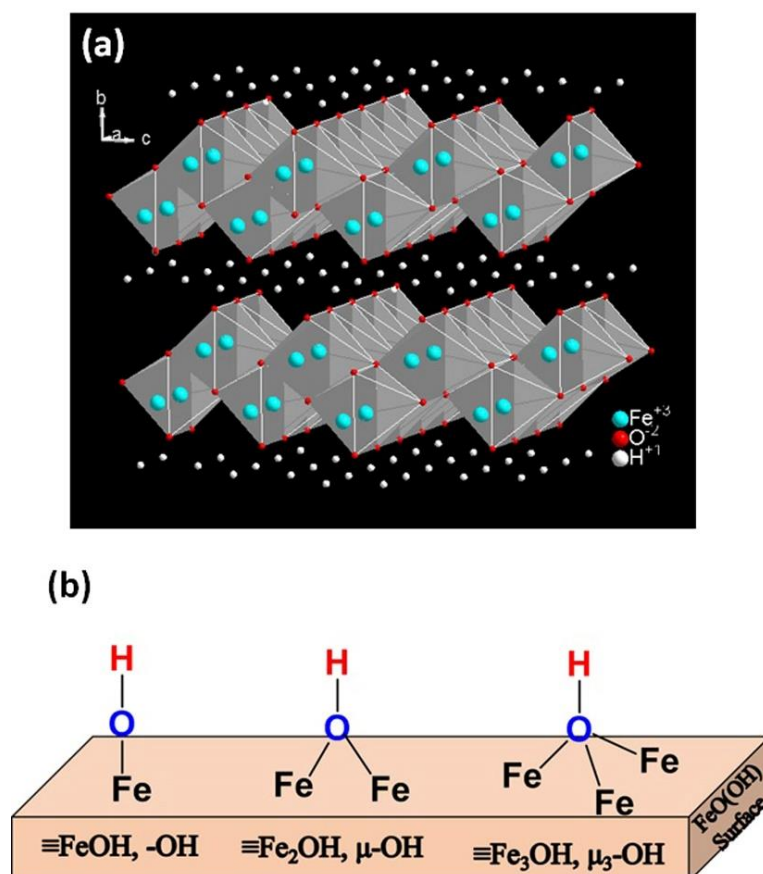


Fig. 3b.1 : a) XRD pattern of γ -FeO(OH) b) Infrared Spectra of γ -FeO(OH) c) Deconvoluted O1s XPS spectra d) Fe 2p XPS spectra of FeO(OH)



Scheme 3b.2: a) Crystal structure of γ -FeO(OH) b) The three coordination modes of OH on FeO(OH) surface.

The surface composition of FeO(OH) was studied using X-ray Photoelectron Spectroscopy (XPS). Deconvoluted O1s XPS spectra (Fig 3b.1c) confirmed contributions due to three kinds of oxygen species a) oxygen involved in Fe-O-Fe (529.9 eV) b) the surface hydroxyl groups Fe-OH (531.3 eV) and c) chemisorbed and physisorbed water (532.3 eV).[18, 19] The XPS signal of Fe2p (Fig 3b.1d) showed two peaks due to Fe2p_{3/2} and Fe2p_{1/2} at 710.6 eV and 724.1 eV respectively. Weak satellite peaks attributed to Fe(III) ions owing to the energy transfer processes of the excited core electrons were observed around 718.0 eV due to Fe2p_{3/2} and at 732.8 eV due to Fe2p_{1/2}. The structure of γ -FeO(OH) was further probed using Thermogravimetric Analyzer (Fig. 3b.2). The thermal decomposition profile of γ -FeO(OH) indicated weight loss due to dehydration in the low temperature region (150-250 °C) and transformation of the phase to α - Fe₂O₃ at higher temperatures (250 °C onwards).[20]

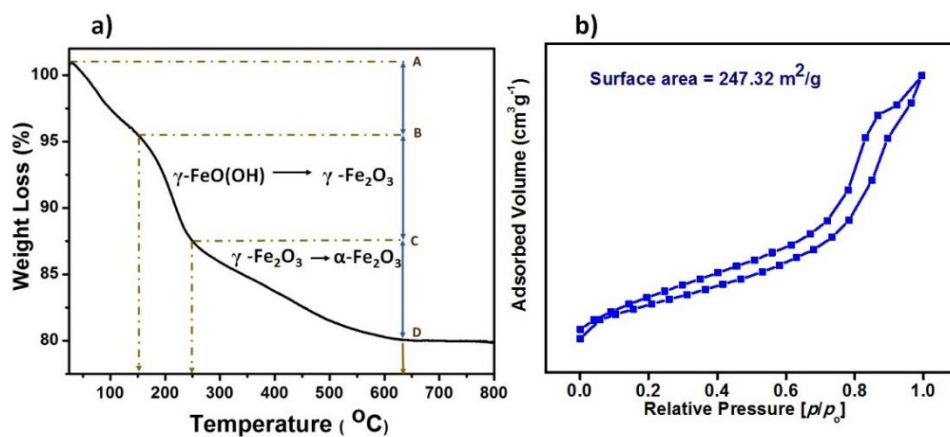


Fig. 3b.2 a) Thermogravimetric (TGA) plot of $\gamma\text{-FeO(OH)}$. b) BET surface area isotherm for $\gamma\text{-FeO(OH)}$.

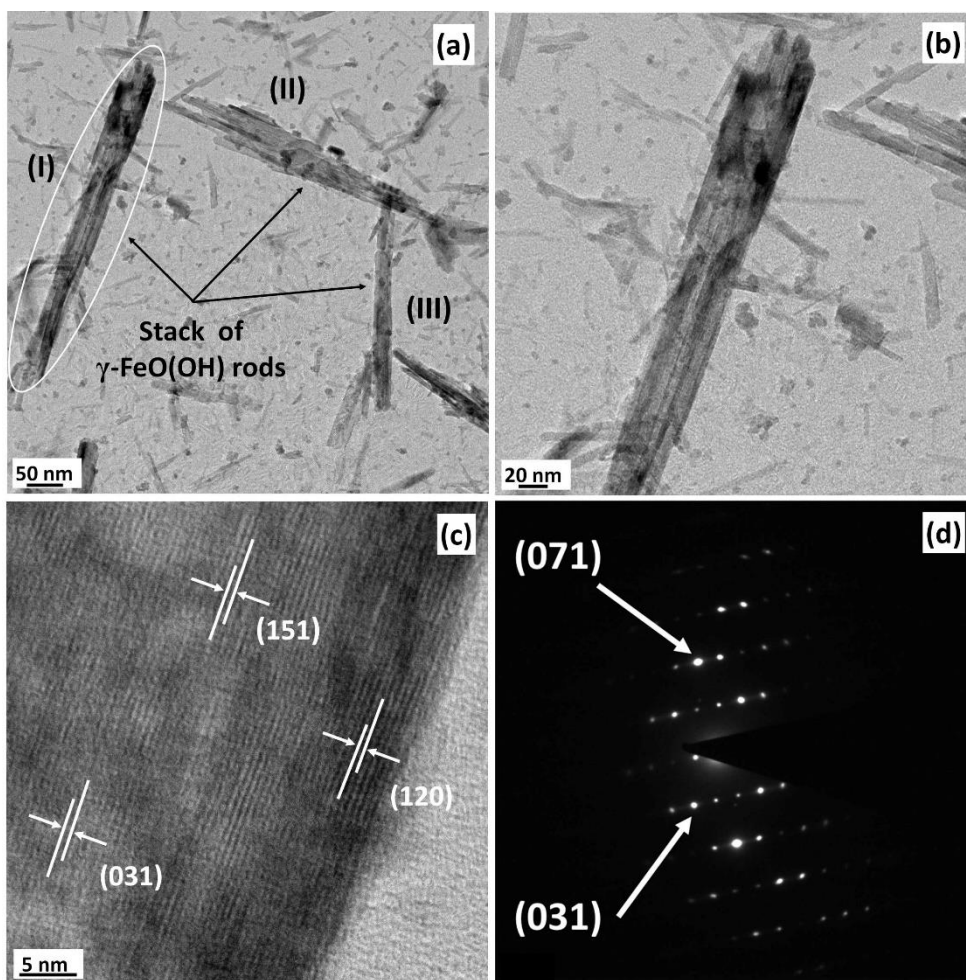


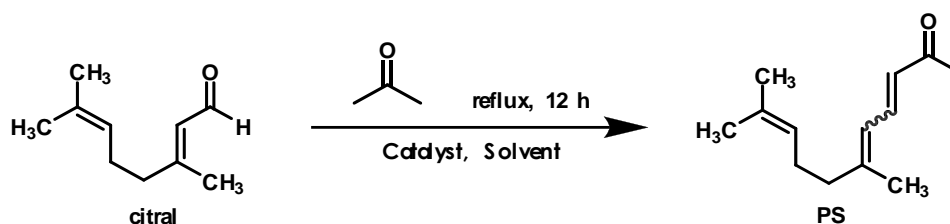
Fig. 3b.3: a) TEM image of $\gamma\text{-FeO(OH)}$ rods b) High magnification TEM image of (I), encircled in Fig 3b.a c) High resolution TEM images of rods in region (I) & d) Electron diffraction pattern.

BET surface area of γ -FeO(OH) was $247 \text{ m}^2 \text{ g}^{-1}$ with a pore volume of 0.58 cc g^{-1} and a pore radius of 15.8 \AA (Fig. 3b.2). The observed hysteresis showed typical type IV characteristics which could be due to interparticle spaces. Microstructure of γ -FeO(OH) was studied using TEM which showed rod-shaped crystals of $250 - 500 \text{ nm}$ in length and $20 - 50 \text{ nm}$ in diameter (Fig 3b.3a, b & c). Frequently, the rods occurred in stacks as shown in the regions (I), (II) and (III) of Fig 3b.3a. In Fig 3b.3b, a magnified image of stack of rods (I) can be seen. Fig. 3c shows the high-resolution TEM image of a nanorod with clearly visible lattice fringes. The spacing between the fringes 0.33 , 0.26 and 0.16 \AA correspond to the (120), (031) and (151) planes of γ -FeO(OH) respectively. The electron diffraction pattern of an isolated stack of FeO(OH) indicated the single crystalline nature of the sample which could be indexed to the planes of γ -FeO(OH) (Fig 3b.3d).

3b.3.2: Knoevenagel Condensation

PS was synthesized by condensation of citral with acetone (and other active methylene compounds). To prevent citral from self-condensation, the acetone and other active methylene compounds were taken twice (2 mmol) as much as citral (1 mmol). The reaction setup was sealed to prevent the formation of the oxidation product nerolic acid. A blank control experiment that involved refluxing of all the reactants for 12 h in the absence of γ -FeO(OH) catalyst (Table 3b.1, entries 1, 2 and 3), did not show the formation of PS in solvents such as CH_3OH , CH_2Cl_2 and $1,4$ -dioxane at their reflux temperatures, respectively. Neither was any activity observed even in the presence of γ -FeO(OH) in solvents such as CH_3OH and CH_2Cl_2 (Table 3b.1, entries 4, 5 & 6). However, the presence of γ -FeO(OH) in $1,4$ -dioxane showed a marginal conversion of 25% . Interestingly, when 1 mL of H_2O was added to 5 mL of $1,4$ -dioxane containing γ -FeO(OH), the conversion of the substrate shot up to 96% with 100% selectivity to PS. In the absence of the catalyst, a mixture of dioxane- H_2O ($5:1$) as solvent showed only 12% conversion under identical reaction conditions (Table 3b.1, entry 9). Thus, γ -FeO(OH) in the presence of H_2O was essential to achieve a high conversion of citral and complete selectivity to PS.

Table 3b.1. Optimization of reaction conditions for the synthesis of the pseudoionones



Entry	Solvent	Water (mL)	Temp. °C	% Conversion
1	MeOH*	-	60	NR ^b
2	Dichloroethane *	-	85	NR ^b
3	1,4-dioxane*	-	110	NR ^b
4	MeOH	-	60	NR ^b
5	dichloroethane	-	84	NR ^b
6	1,4-dioxane	-	110	25
7	MeOH	1	60	8
8	1,4-dioxane	1	110	96
9	1,4-dioxane*	1	110	12

^a Reaction conditions: citral (0.152 g, 1 mmol), acetone (0.116 g, 2 mmol), solvent (5 mL), H₂O (1 mL), Catalyst amount (100mg), time (12 h), reflux temperature, ^b No reaction (NR) * No Catalyst. 1-4 Dioxane was dried over molecular sieves and then used

Calculation of Turnover number

Sr. No	Binding Energy (e.V) O1s signal	Designation	Contribution from deconvoluted O1s XPS (%)
1.	529.9	Fe-O-Fe	45
2.	531.3	Fe-OH	37
3.	532.3	Adsorbed H ₂ O	18

Contribution of surface hydroxyl (OH) groups from XPS = 37%

No of mmols of OH group on 100mg of FeO(OH) = 37/17 = 2.17

Turnover number (TON) = No of moles of reactant converted/No of moles of OH group

= Reactant moles converted /2.17

The reaction rates in presence of γ -FeO(OH) were compared with those in presence of other well-known solid bases both in the presence and the absence of water (Fig 3b.4a). In the presence of conventional solid bases, the reaction rates remained below $0.012 \text{ mmol L}^{-1} \text{ h}^{-1}$ even when water was used. In other words, H_2O caused a marginal decrease in the rates of the reactions when CaO, MgO, AlPO, Al_2O_3 or CeO_2 were used as catalysts. Interestingly, in the presence of water, γ -FeO(OH) showed an impressive four-fold increase in the rate of the reaction making it the most active catalyst. Turnover number (TON) gives the number of reactant molecules converted per minute per catalytic active site present on 1 g of γ -FeO(OH) under given the reaction conditions. The number of sites was calculated based on the concentration of surface -OH groups on FeO(OH) using O1s XPS spectra. The change in the TON of the reaction in the presence of γ -FeO(OH) at the end of 1, 4 and 6 h were compared with the reactions carried out in the absence of water. At the end of 1h, TON of γ -FeO(OH) gave a value of just 15 mmol g^{-1} in the presence of H_2O (Fig 3b.4b). The TON of the reaction increased with time to 161 and 258 mmol g^{-1} after 4 h and 6 h, respectively. Interestingly, at the end of 4h, the increase in TON was 10-fold when the reaction was carried out in the presence of H_2O as compared to 2-fold in the absence of water. This indicated that active sites were generated on the surface of the γ -FeO(OH) by H_2O during the course of the reaction. However, generation of the active sites gradually flattened off after 4 h. A time-dependent plot of catalyst performance in the presence and in the absence of water is presented in Fig 3b.4 (trace i & iii). The dotted line shows the conversion trend in an experiment when the catalyst was filtered off under hot conditions after 6h of reaction (Fig 3b.5, trace ii). Absence of further conversion indicated that there was no leaching of ions from the catalyst, confirming no homogeneous contribution to catalysis under the reaction conditions. The role of water as an activating agent was studied by allowing FeO(OH) to stir in dioxane-water mixture for 2 h at reflux temperature and then introducing the reactants (Fig 3b.5, trace iv). Interestingly, the conversion trends showed an improved spike with 60 % conversion after just 2 h of adding the reactants. On the other hand, almost 7 h was needed to attain this conversion value, when the reactants were present from the beginning of the reaction. This observation strongly suggests that H_2O plays a crucial role in activating γ -FeO(OH) by deprotonating surface -OH to form O^- . A surface concentration of O^- groups builds

up over a period of 2 h which makes γ -FeO(OH) a more efficient catalyst in the condensation reaction. Water appeared to have no such promoting effect in the catalytic activity of other solid bases indicating formation of a different nature of active site on γ -FeO(OH).

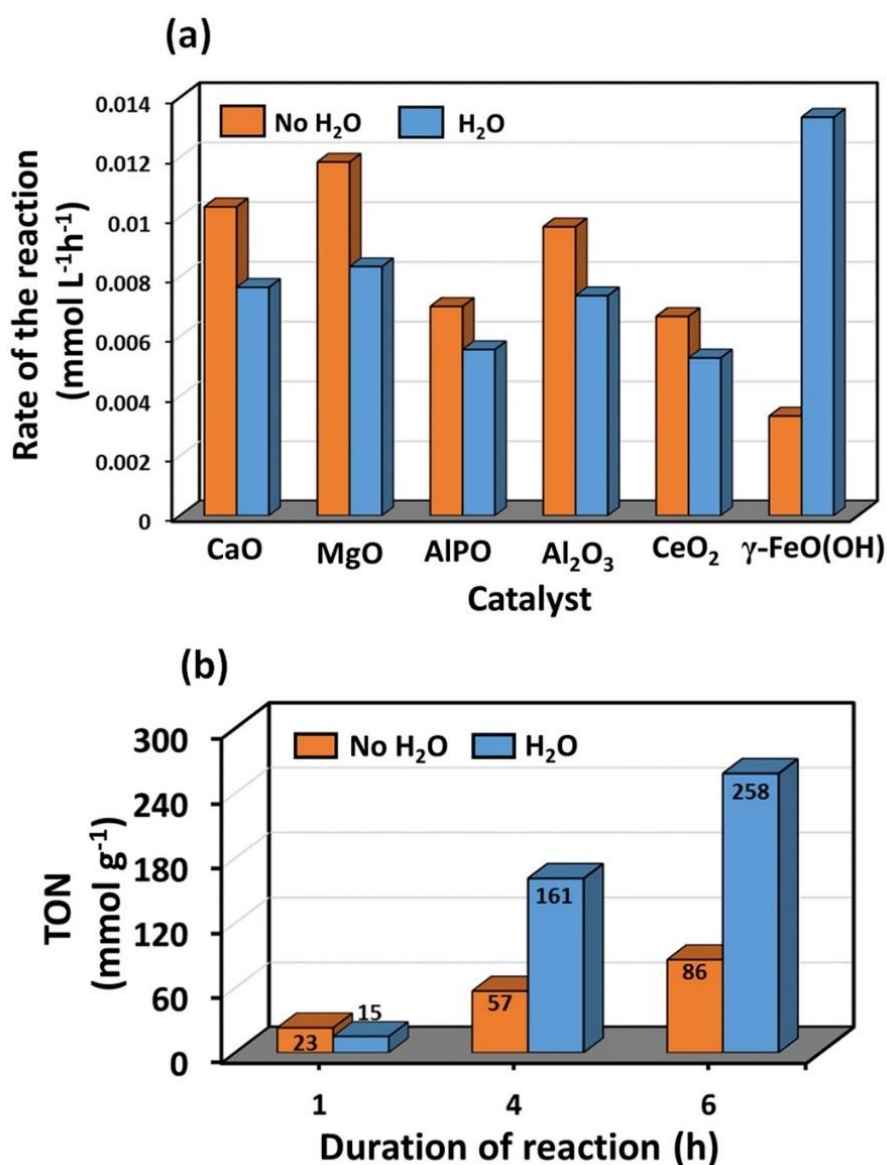


Fig 3b.4: a) Rate of the reaction for the various catalysts screened in the presence and absence of water for the synthesis of the PS. Reaction Conditions: citral (0.152 g, 1 mmol), acetone (0.116 g, 2 mmol), specially dried *1,4*-Dioxane (5 mL), H₂O (1 mL), time (12 h), reflux, sealed conditions. b) Plot of TON Vs duration of reaction in the presence of γ -FeO(OH) with and without H₂O.

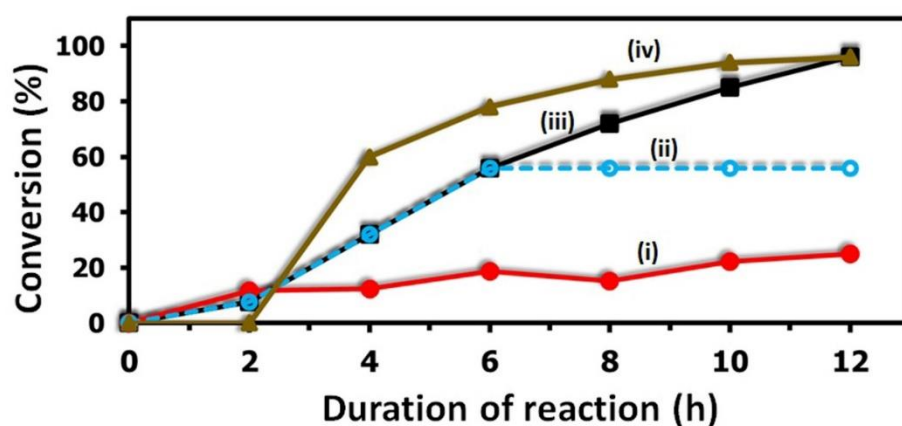


Fig 3b.5. Study of effect of H₂O on the activation of γ -FeO(OH) i) in the absence of water ii) hot filtration test: flat line represents no further progress in reaction after the removal of the catalyst iii) in the presence of water iv) reactants introduced after 2 h of stirring FeO(OH) in dioxane-water mixture

3b.3.3: Active Sites

3b.3.3.1: Basicity in FeO(OH) and role of H₂O

Our previous studies have shown that surface -OH groups on metal oxyhydroxides have a strong role to play in the acid-base catalyzed reactions.[14, 21] To further probe the activity of surface hydroxyl groups, we studied the changes in FT-IR absorption spectra of -OH vibrations due to interactions with CO₂ molecule. It has been shown that interaction with CO₂ can alter the O-H stretching frequencies of FeO(OH) samples upto 150-175 cm⁻¹. [22] The difference spectra (Trace iii in Fig 3b.6 a, b) was obtained by subtracting the absorption bands of neat γ -FeO(OH) sample from that of the CO₂-adsorbed FeO(OH). The anti-symmetric and symmetric modes of the C-O stretching region of carbonate & (bi) carbonate species were formed on the surface of FeO(OH). Interaction of CO₂ with surface -OH and its deprotonated -O⁻ groups resulted in strong bands at 1512 cm⁻¹ and 1314 cm⁻¹ corresponding to the above modes respectively (Fig 3b.6b). [22] This observation confirmed the basicity of the O⁻ sites on the surface. Further, FeO(OH) surface may have three kinds of hydroxo groups 1) singly (\equiv FeOH, -OH) 2) doubly (\equiv Fe₂OH, μ -OH) and 3) triply coordinated (\equiv Fe₃OH, μ_3 -OH) (Scheme 3b.2). [23] From the plot in Fig 3b.6a, one can infer the nature of the surface -OH groups depending on the site at which the carbonate & (bi) carbonate species are coordinated.

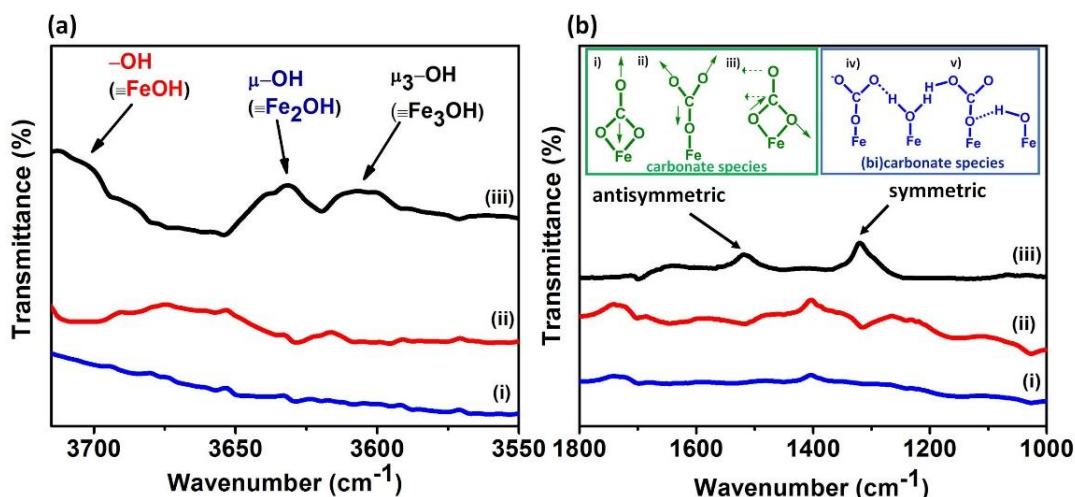


Fig 3b.6: Infrared Spectra of (i) neat FeO(OH) (ii) CO₂ adsorbed on FeO(OH) and (iii) their difference spectra a) changes in the hydroxyl group stretch b) changes in the C-O stretch

At a triply coordinated site ($\equiv\text{Fe}_3\text{OH}$, $\mu_3\text{-OH}$) and at doubly coordinated site ($\equiv\text{Fe}_2\text{OH}$, $\mu\text{-OH}$), the absorption bands appear at 3597 cm^{-1} and 3627 cm^{-1} respectively.[22, 23] The single coordinated ($\equiv\text{FeOH}$, -OH) species which usually shows bands above 3650 cm^{-1} was reasonably intense in our sample suggesting its presence in large number as compared to species with other coordination modes. Due to the difference in the coordination number of the underlying Fe atoms, the surface hydroxyl groups that are bonded to it exhibit difference in basicity and hence difference in reactivity. Past literature reports based on adsorption and charge studies indicate double coordinated hydroxyl groups to be inert, whereas single and triple coordinated species are reactive with highest reactivity for single coordinated species in proton adsorption measured by pressure jump relaxation methods.[24, 25] The presence of all three types of surface -OH groups explains the catalytic activity of $\gamma\text{-FeOOH}$. For example, studies on (001) plane of $\gamma\text{-FeO(OH)}$ had shown equal numbers of single and triply coordinated hydroxyls whereas, (010) plane contained doubly coordinated surface hydroxyls exclusively.[17] Thus, the deprotonated surface hydroxyl groups show exceedingly high conversion as compared to other metal oxide catalysts.



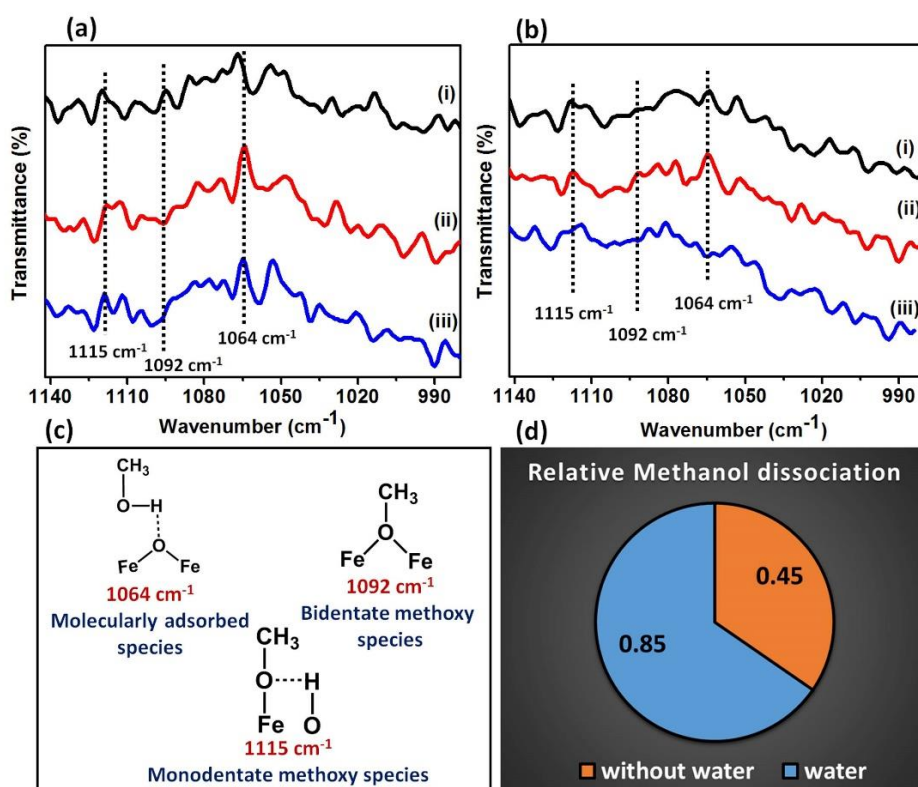


Fig 3b.7: *In situ* FT-IR spectra obtained by subtracting MeOH adsorbed FeO(OH) and neat FeO(OH) spectra a) in the absence of water b) in the presence of water. Trace i) ii) & iii) denote scans taken after 5 min, 15 min & 25 min respectively. c) Vibration modes of MeOH dissociation on FeO(OH) surface: Molecularly adsorbed species (1064 cm^{-1}), Bidentate methoxy species (1092 cm^{-1}) and Monodentate methoxy species (1115 cm^{-1}). d) Relative MeOH dissociation on FeO(OH) in the presence and absence of water w.r.t. molecularly adsorbed MeOH.

Since the pK_a of water ($pK_a = 14$) is higher than the protons on FeO(OH) ($pK_a > 10$), it can deprotonate FeO(OH) to give FeOO^- according to eq 1.[17] The Brønsted basicity was investigated by means of methanol deprotonation followed by *in situ* Infrared Spectroscopy. (Fig 3b.7) Earlier studies on hydroxylated MgO show that MeOH interacts with the surface basic sites forming monodentate and bidentate methoxy species at 1115 cm^{-1} and 1092 cm^{-1} , respectively, whereas molecularly adsorbed methanol involving H-bonding gives an absorption band at 1064 cm^{-1} . [26] The various interactions with FeO(OH) surface can be visualized in Fig 3b.7c. In Fig. s 3b.7a & b, it was observed that the bands were centered at 1064 cm^{-1} and 1115 cm^{-1} indicating molecularly adsorbed MeOH and the formation of monodentate

methoxy species on FeO(OH) surface. The formation of monodentate methoxy species on FeO(OH) is a clear indication of the presence of basic sites O^- . [26, 27] Incidentally, these bands were more intense in the absence of water (Fig 3b.6a). The competitive interaction between MeOH and H₂O with surface hydroxyl groups is probably responsible for the phenomenon. Band at 1092 cm^{-1} due to bidentate methoxy species was not predominant except at the initial 5 min scan in the absence of water (Fig 3b.7a (i)). However, this band disappeared with time because of weak bidentate methoxy interaction with the surface. To quantify the effect of water on basicity, the relative ratio of peak intensities of monodentate methoxy and molecularly adsorbed MeOH in the absence and presence of water were calculated (Fig 3b.7d). The average value gave the measure of methanol dissociation on FeO(OH). We invariably observed that the value was higher (0.85) for the system in the presence of H₂O than in the absence of H₂O (0.45). This shows that H₂O helps to increase the number of monodentate methoxy species by increasing the O^- species on the FeO(OH) surface.

To support the conclusion that H₂O promotes the *in-situ* formation of $FeOO^-$, we carried out the adsorption of a positively charged dye Rhodamine 6G (Rh-6G) as shown in Fig 3b.8a. This dye is known to adsorb on a negatively charged surfaces e.g. on the deprotonated OH on graphene which can be monitored using fluorescence spectroscopy. [28] The details are presented in the experimental section. The $FeOO^-$ species is a negatively charged surface and hence has an affinity to adsorb a positively charged Rh-6G (Fig 3b.8c). The supernatant solution in FeO(OH)-Rh-6G after removing the FeO(OH) from the solution showed a significantly weaker fluorescence as compared to the standard solution. This indicates that the surface of FeO(OH) has negative charge due to the presence of $FeOO^-$ (Fig 3b.8b) and hence, the concentration of Rh-6G in the solution decreased as seen by the weaker fluorescence (red trace, Fig 3b.8c). Fig 3b.8e shows a comparative plot of FeO(OH) and FeO(OH)-Rh-6G complex. One noticeable change is the shift in OH stretching frequency of FeO(OH)-Rh-6G complex from 3134 cm^{-1} in pure FeO(OH) to 3172 cm^{-1} . This red shift can be attributed to the interaction of the deprotonated surface hydroxyl groups with the positively charged nitrogen of Rh-6G similar to that reported for graphene oxide-Rh-6G complex. [28] A comparison of FT-IR bands in the fingerprint region of Rh-6G and FeO(OH)-Rh-6G is shown in Fig 3b.8f. The

bands of Rh-6G showed a slight blue shift in the FeO(OH)-Rh-6G complex, further confirming a strong interaction between the positively charged nitrogen of the dye and the negatively charged FeO(O⁻) species as shown in Fig 3b.8b.

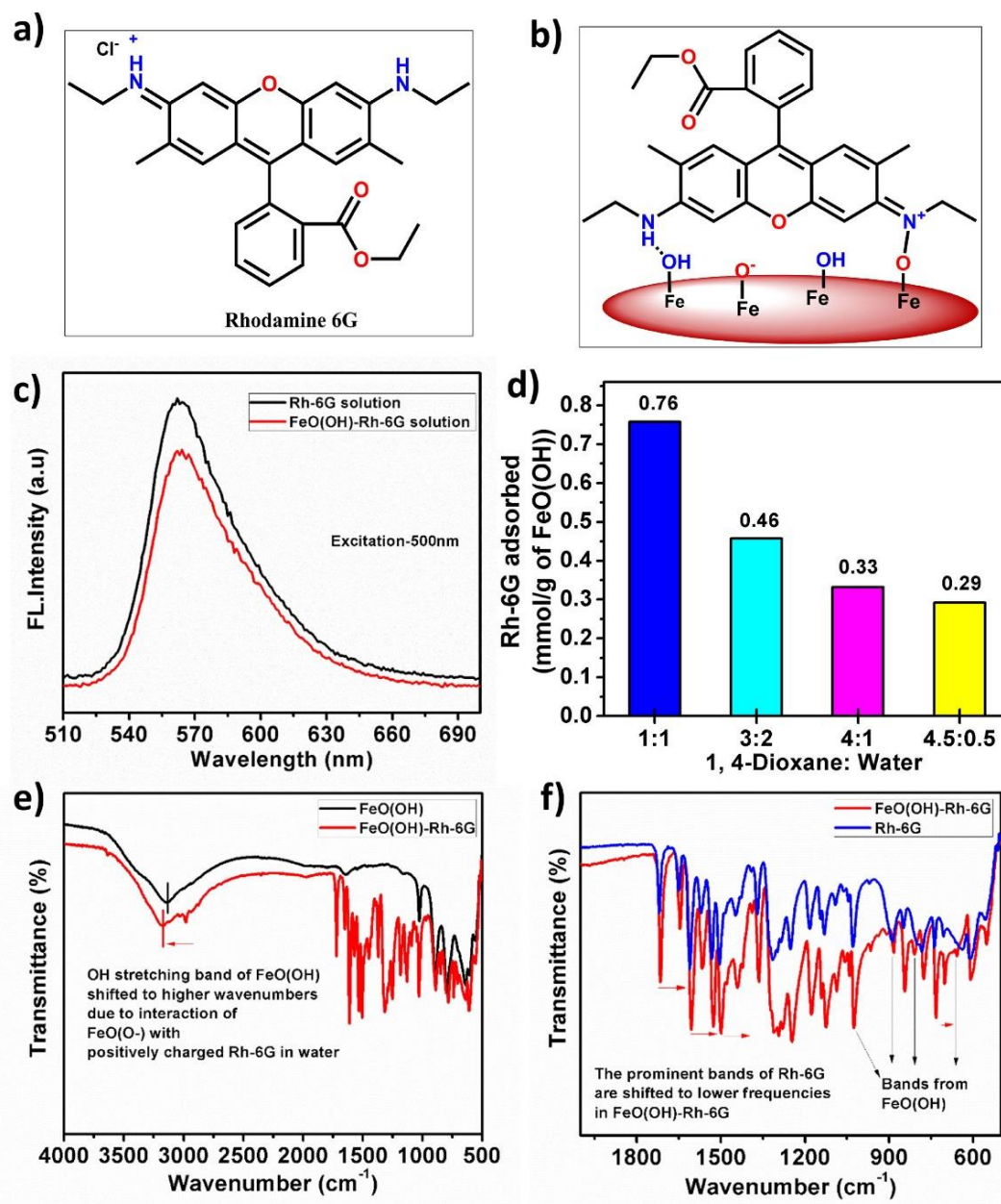


Fig 3b.8 a) Structure of Rhodamine -6G b) Interaction between FeO(OH) and Rh-6G c) Fluorescence spectrum for Rh-6G and FeO(OH)-Rh-6G (Excitation-500nm) in water. d) Quantification of amount of dye adsorbed on FeO(OH) in various dioxane: water mixtures. e) FTIR spectra for FeO(OH) and FeO(OH)-Rh-6G complex f) FT-IR spectra for Rh-6G and FeO(OH)-Rh-6G complex

The dye adsorption on FeO(OH) was also studied using a similar fluorescence experiment in different dioxane-water compositions matching the solvent conditions. The dye concentration in the supernatant decreased from 0.03 mmol to 0.01 mmol as water content increased (Fig 3b.10), indicating that Rh-6G adsorbs more on FeO(OH) in excess water conditions due to formation of FeO(O⁻).

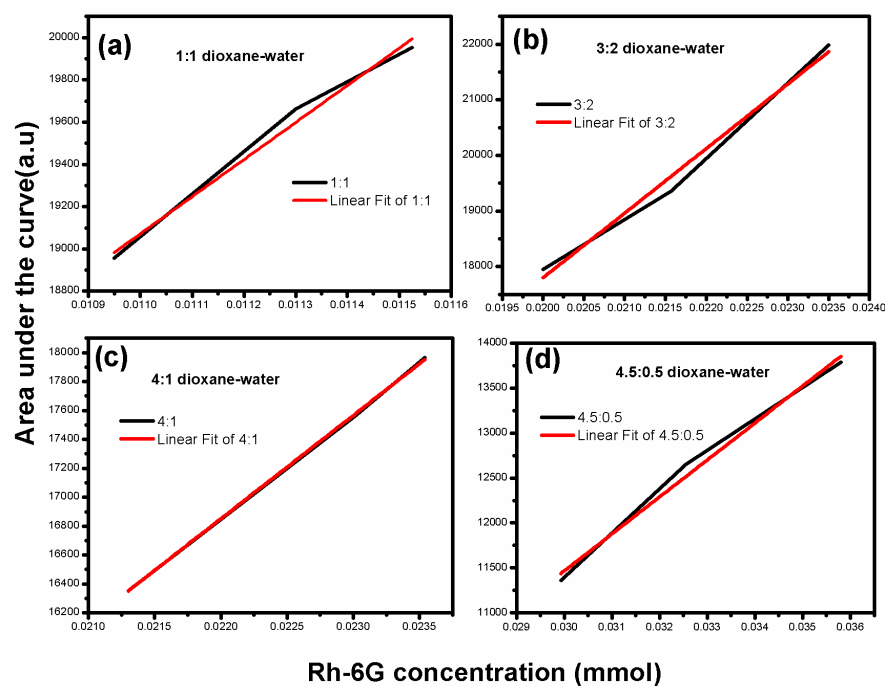


Fig 3b.9: Calibration plots ((a), (b), (c)& (d)) for dye concentration

The amount of Rh-6G adsorbed on FeO(OH) in the dioxane water mixtures was quantified and the results are shown in Fig 3b.8d. The Rh-6G adsorption values showed an increasing trend with increase in water content. For example, 0.29 mmol of Rh-6G was adsorbed per g of FeO(OH) at 4.5:0.5 dioxane-water ratio. This value reached 0.76 mmol/g of FeO(OH) at 1:1 dioxane-water ratio. Thus, it is confirmed that surface -OH group gets deprotonated in the presence of H₂O to form the O⁻ sites responsible for adsorption of Rh-6G. In order to verify if externally added H₂O promoted the catalytic activity in FeO(OH) by introducing additional surface -OH groups, the FeO(OH) sample was stirred in water for 6 and 12 h. Then the solid was filtered and dried. Previous studies on interaction of FeO(OH) with salt water had shown the formation of Fe(OH)₃ and [Fe(OH)]⁺² on FeO(OH) surface.[29] IR transmittance levels of the dried samples between 3670 cm⁻¹ and 2458 cm⁻¹ corresponding to the surface hydroxyl groups and physisorbed water were studied. Interestingly, these bands are consistent with that of bare sample untreated with H₂O

(Fig. 3b.11). Thus, H₂O does not promote activity in FeO(OH) by increasing the number of surface hydroxyl groups on FeO(OH) within the duration of the reaction.

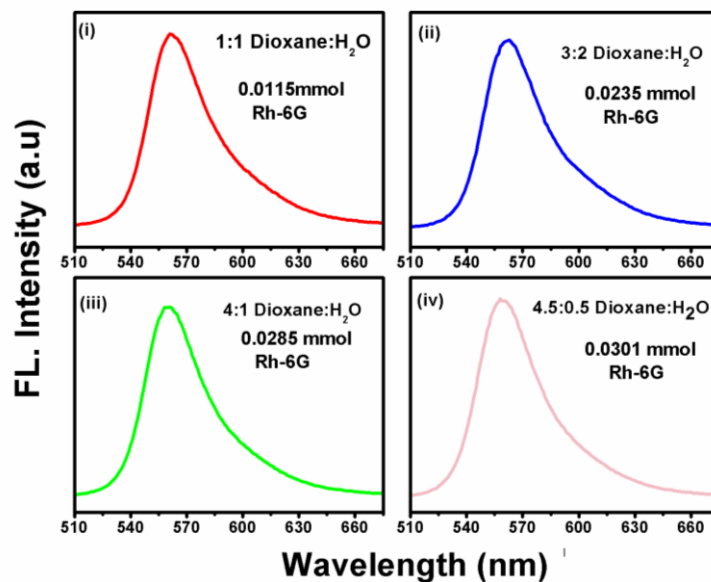


Fig 3b.10: Individual fluorescence spectra ((i), (ii), (iii) & (iv)) in various 1,4-dioxane: water mixtures respectively

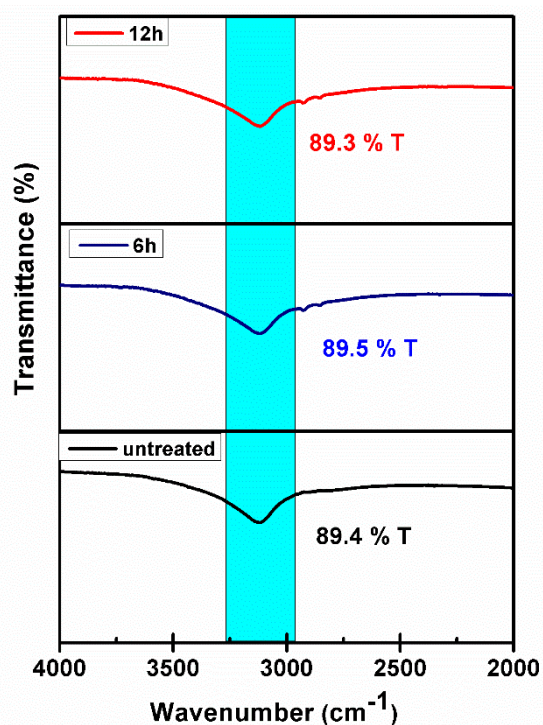


Fig 3b.11: FT-IR of water treated γ -FeO(OH) (6 h & 12 h) and untreated sample between 4000-2000 cm⁻¹

3b.3.4: Substrate scope

Table 3b.2. Condensation reactions of citral with active methylene compounds using γ -FeO(OH) as catalyst.

Entry	Reactant b	Product c	Isolated Yield of Product c (%)
1			84
2			72
3			68
4			74
5			82
6			74
7			70
8			75

Reaction conditions: citral (0.152 g, 1 mmol), Reactant b (2 mmol), 1,4-Dioxane (5 mL), H₂O (1 mL), time (12 h), reflux 1,4-Dioxane was dried over molecular sieves and then used. Products isolated by column chromatography and confirmed by ¹H NMR

To understand the efficiency of the activity of γ -FeO(OH), we tested it for the Knoevenagel condensation reactions of various active methylene group compounds to synthesize PS, their analogues and other products. All the reactions were carried out using specially dried 1,4-dioxane as a solvent with 1 mL of externally added water. The reaction of acetone with the citral (**Table 3b.2, entry 1**) gave the aldol condensation product with 84 % isolated yield in 12h. Encouraged by this, we used substituted acetophenones with various functional groups exerting -I and -R effects to condense with citral. It was observed that the para substituted -Cl group in 4-chloroacetophenone on reaction with citral gave an isolated yield of 72 % due to higher -I as well as -R effect (**Table 3b.2, entry 2**). In comparison, 3-bromoacetophenone gave a 68 % yield (**Table 3b.2, entry 3**) of the condensation product. The activating -NO₂ group in 4-nitro acetophenone gave 74 % yield of condensation product (**Table 3b.2, entry 4**). Further extension of the catalyst activity testing was carried out to study Knoevenagel condensation reactions with compounds having active methylene groups. Firstly, malononitrile on reacting with citral yields 82 % condensation product (**Table 3b.2, entry 5**). Ethylcyanoacetate on reaction with citral gave the condensation product with 74 % yield (**Table 3b.2, entry 6**). Similarly, the Knoevenagel condensation reaction of citral was further studied for nitroethane and nitromethane having active methylene groups which yields up to 70% and 75 % condensation product respectively (**Table 3b.2, entry 7& 8**) under similar reaction conditions.

3b.3.5: Catalyst recycle study

The efficiency of γ -FeO(OH) catalyst was established by its recycle studies (Fig. 3b.12). After completion of the first run, the catalyst was separated by filtration, washed several times with 1,4-dioxane and dried at 100 °C and then used for eight subsequent runs. Fig. 3b.12 shows that the citral conversion was stable (96 - 92%) even after five recycles with minor losses which could be due to handling of small quantity of catalyst during recovery after every use. The selectivity of PS dropped down from 100 to 83% after 8th recycle due to competitive formation of Nerolic acid. Also, the X-ray diffraction pattern of the catalyst appeared stable after 8th recycle under the reaction conditions with minor changes (Fig. 3b.13).

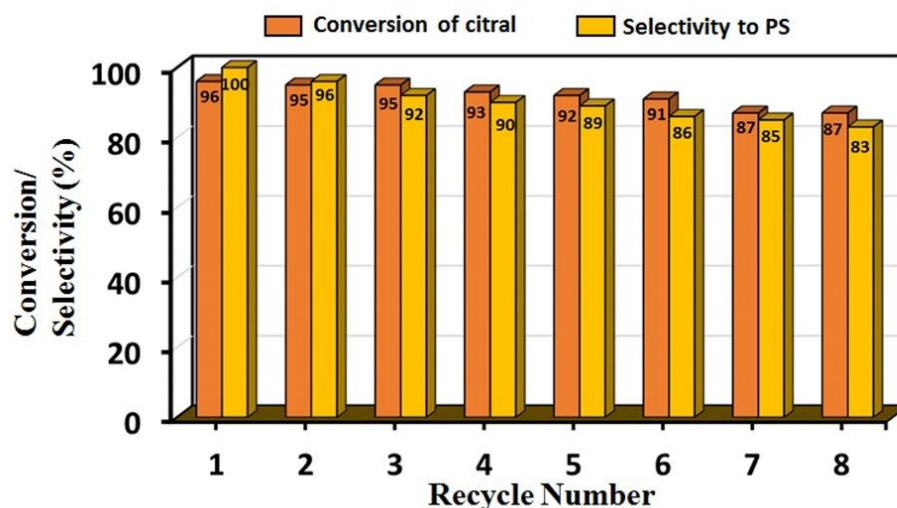


Fig. 3b.12: Recyclability of γ -FeO(OH) for PS synthesis

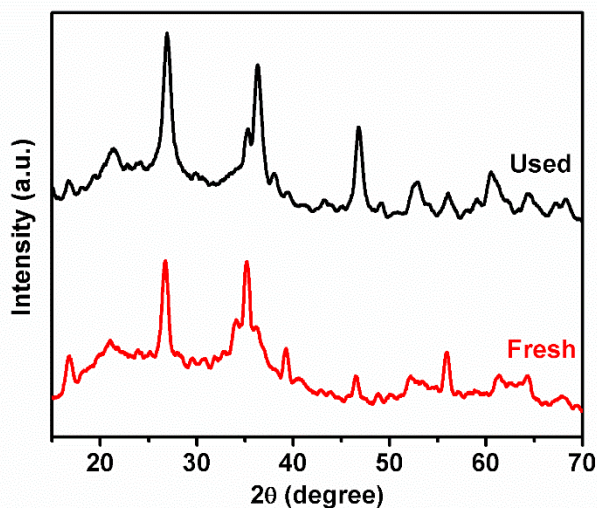
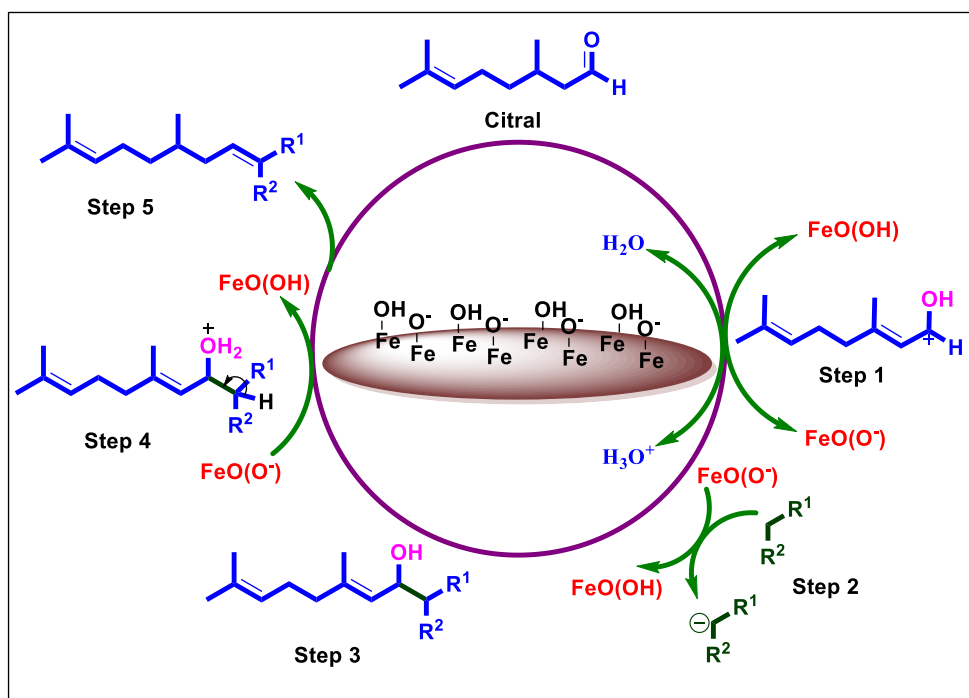


Fig 3b.13: X-ray Diffraction of fresh and 8th reuse sample

In a plausible mechanism shown in Scheme 3b.3, the first step involves the deprotonation of the surface hydroxyl groups of FeO(OH) to give FeOO^- using water. These FeOO^- species act as base centers to abstract the proton from active methylene compounds (Step 2), thus paving way for the attack of the formed carbanion to the carbonyl group of citral (Step 3). Loss of water molecule assisted by FeOO^- finally yields the pseudoionone (Step 5).



Scheme 3b.3. Plausible reaction mechanism for the synthesis of the Pseudoionones and their analogues.

3b.4: Conclusions

This work demonstrates for the first time, the use of FeO(OH) as an environmental friendly, cost effective base catalyst for transformation of citral to PS and its analogues. Combined presence of Brønsted basic O⁻ and Lewis basic O²⁻ is effective for PS synthesis. *In situ* CO₂ adsorption studies confirmed the presence of singly, double and triply coordinated hydroxyl groups with the active singly coordinated species in abundance. Experimental evidences clearly showed that externally added water promoted formation of Brønsted basic O⁻ sites on FeO(OH) by deprotonating the surface hydroxyl groups. This O⁻ was responsible for drastic improvement in activity. The basicity on FeO(OH) obtained by water activation is chemically different from those present on other solid bases explored in literature for PS synthesis. Our studies also indicated, this basicity (O⁻) was superior and easily controllable based on water content in the system. The material also exhibited a decent substrate scope and we went on to isolate PS and its analogues which were hitherto not reported.

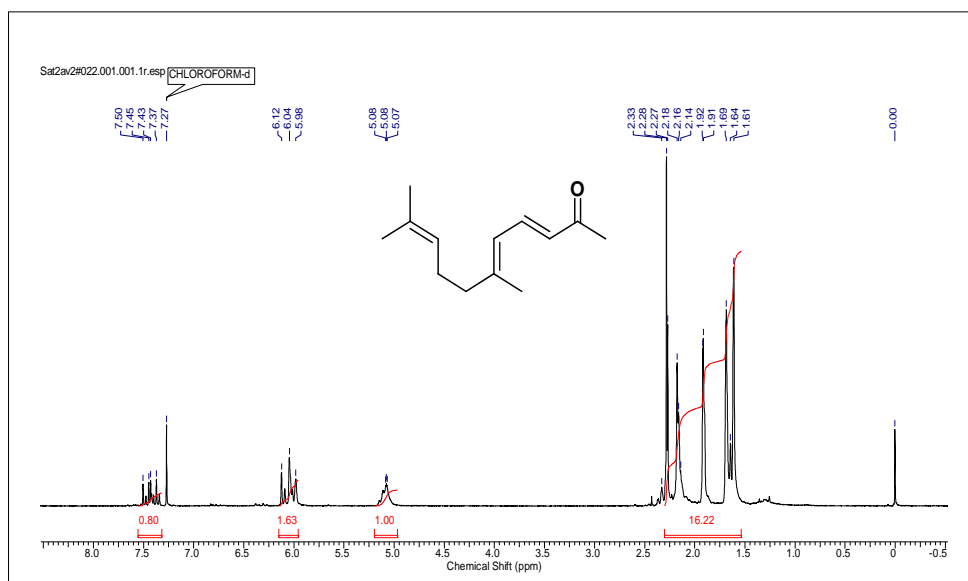
3b.5: ^1H NMR of isolated compounds

Table 3b.2, Entry 1

^1H NMR (200MHz, Chloroform-d) δ : 7.50-7.37 (m, 1 H), 6.12-5.98 (m, 2H), 5.07-5.08 (m, 1H), 2.33-1.61(m, 16H)

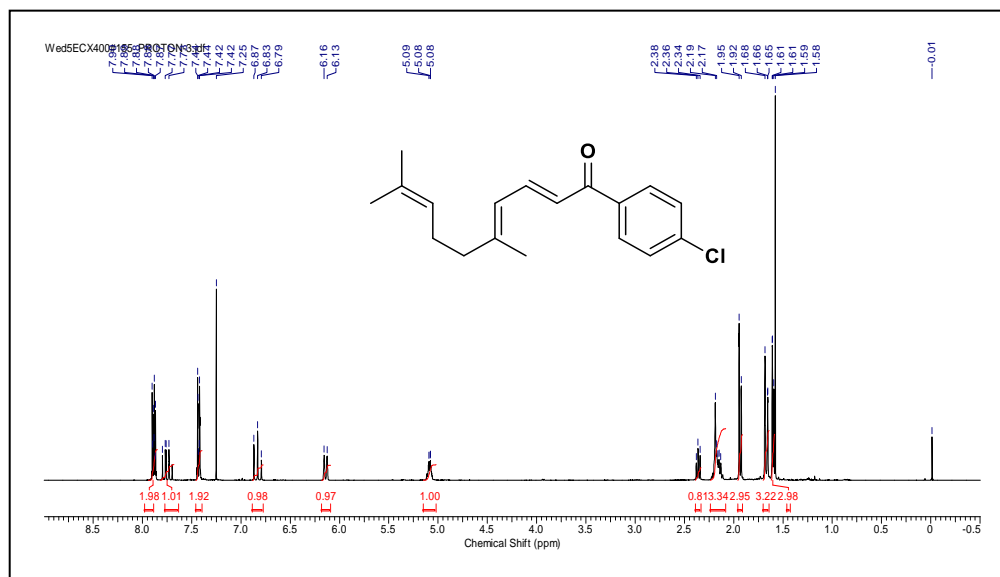


Table 3b.2, Entry 2

^1H NMR (200MHz, Chloroform-d) δ : 7.90-7.87 (m, 2H), 7.77-7.73 (m, 1H), 7.44-7.25 (m, 2 H), 6.87-6.79 (m, 1H), 6.16-6.13 (s, 1H), 5.09-5.08 (m, 1H), 2.38-2.17 (m, 4H), 1.95-1.92 (m, 3H), 1.68-1.58 (m, 6H).

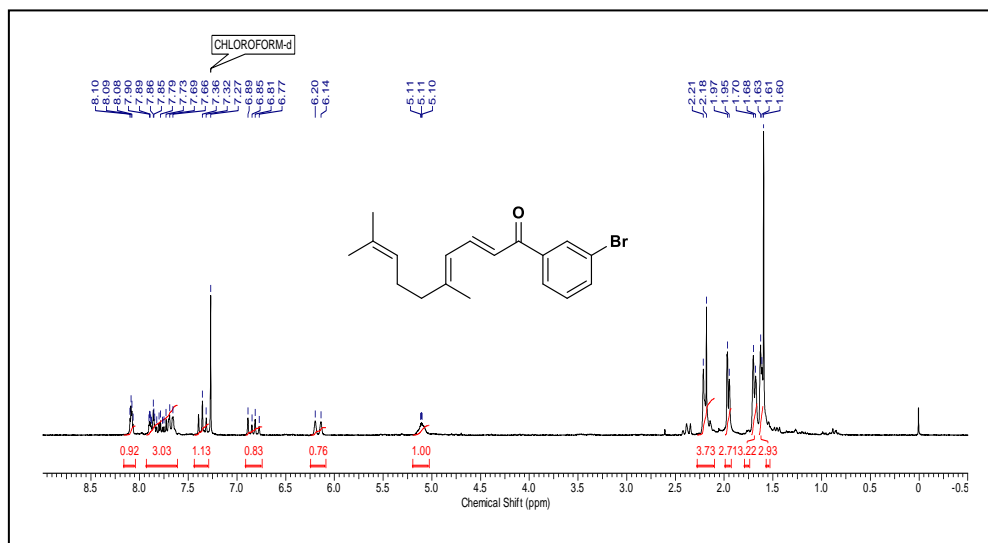


Table 3b.2, Entry 3

¹H NMR (200MHz, Chloroform-d) δ : 8.10-8.08 (m, 1H), 7.90-7.66 (m, 3H), 7.36-7.27 (m, 1H), 6.89-6.77 (m, 1H), 6.20-6.14 (d, 1H), 5.11-5.10 (m, 1H), 2.21-2.18- (m, 4H), 1.97-1.95 (m, 3H), 1.70-1.68 (m, 3H), 1.63-1.60 (m, 3H)

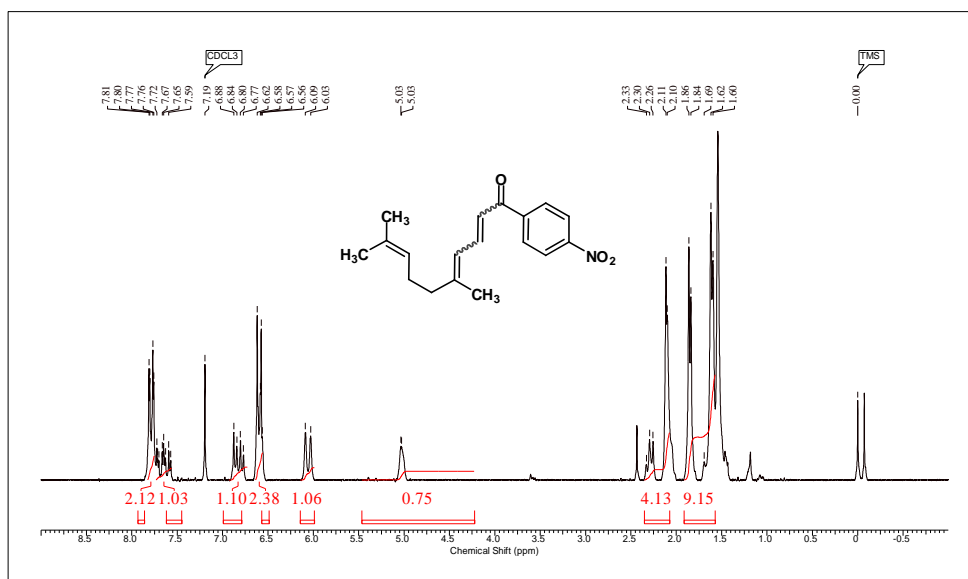


Table 3b.2, Entry 4

¹H NMR (200MHz, Chloroform-d) δ : 7.81-7.76 (d, 2H), 7.72-7.59 (m, 1H), 6.88-6.77 (m, 1H), 6.62-6.56 (d, 2H), 6.09-6.03 (d, 1H), 5.03 (m, 1H), 2.33-2.10 (m, 4H), 1.86-1.60 (m, 9H)

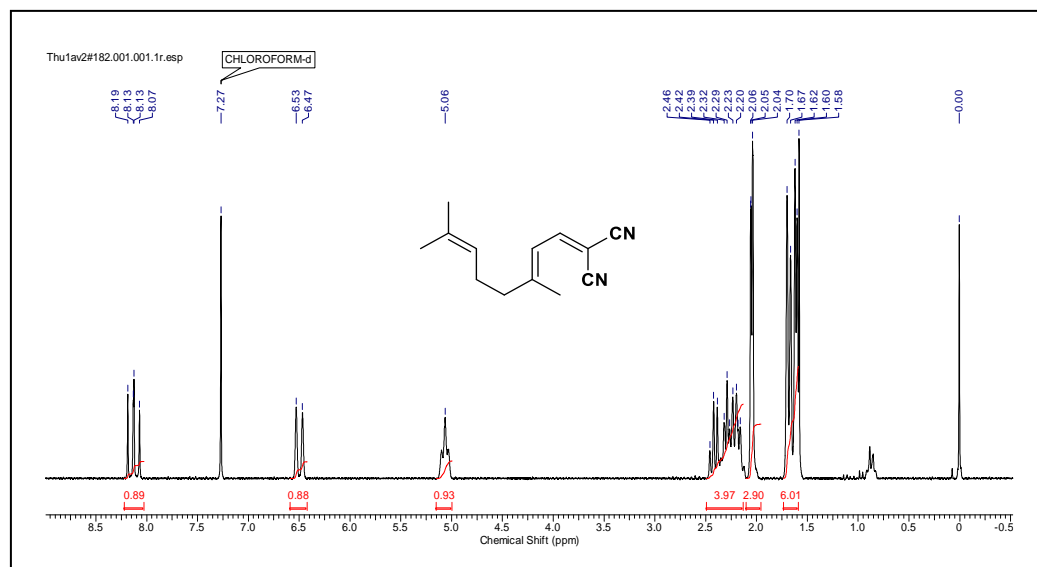


Table 3b.2, Entry 5

^1H NMR (200MHz, Chloroform-d) δ : 8.19-8.07 (m, 1H), 6.53-6.47 (d, 1H), 5.06 (m, 1H), 2.46-2.20 (m, 4H), 2.06-2.04 (m, 3H), 1.70-1.58 (m, 6H)

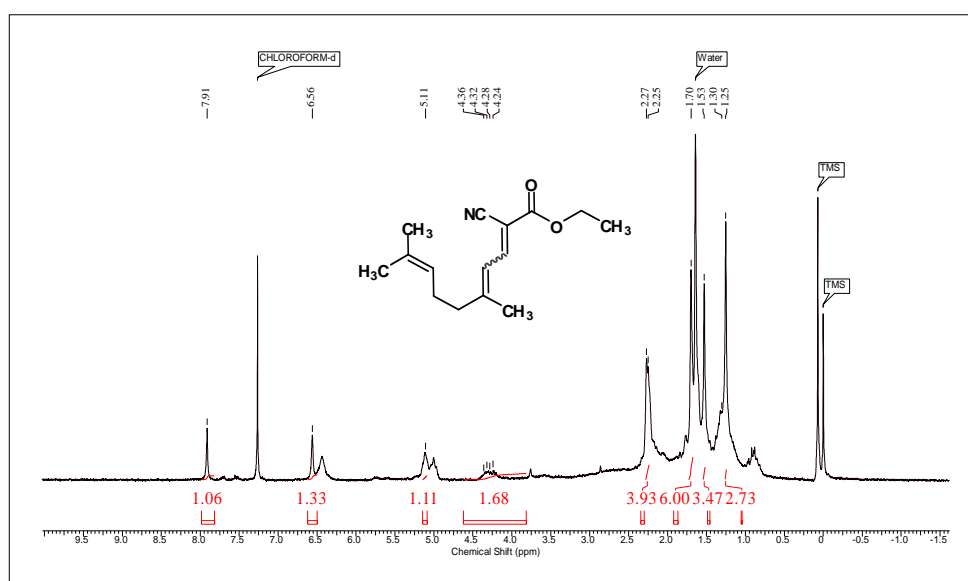


Table 3b.2, Entry 6

^1H NMR (200MHz, Chloroform-d) δ : 7.91 (s, 1H), 6.56 (s, 1H), 5.11 (m, 1H), 4.36-4.24 (q, 2H), 2.27-2.25 (m, 4H), 1.70-1.25 (m, 12H)

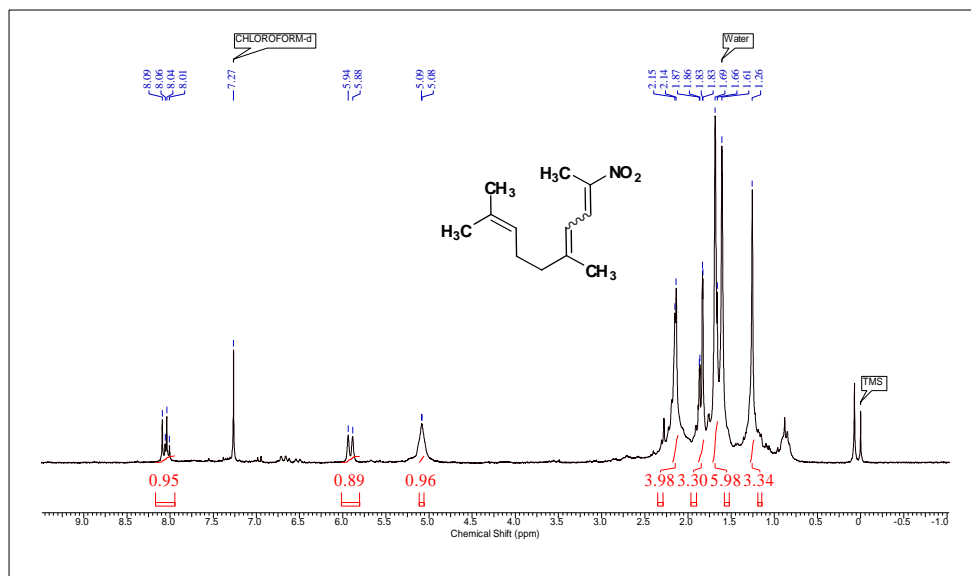


Table 3b.2, Entry 7

¹H NMR (200MHz, Chloroform-d) δ: 8.09-8.01 (m, 1H), 5.94-5.88 (d, 1H), 5.09-5.08 (m, 1H), 2.15-2.14 (m, 4H), 1.87-1.83 (m, 3H), 1.69-1.61 (d, 6H), 1.26 (s, 3H)

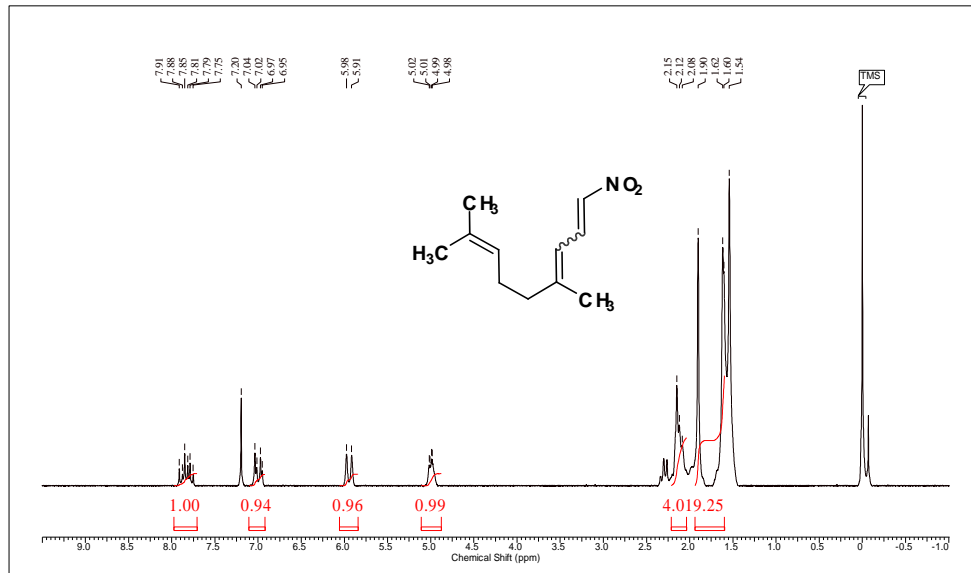
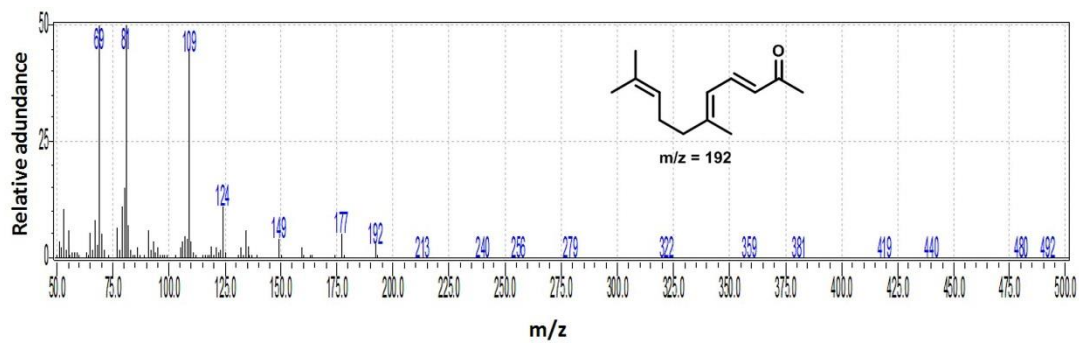


Table 3b.2, Entry 8

¹H NMR (200MHz, Chloroform-d) δ: 7.91-7.75 (m, 1H), 7.20-6.95 (m, 1H), 5.98-5.91 (d, 1H), 5.02-4.98 (m, 1H), 2.15-2.08 (m, 4H), 1.90-1.54 (m, 9H)

GC-MS data of Pseudoionone:



[MS Spectrum]

of Peaks 362

Base Peak m/z 69.05 (Inten : 10,000)

m/z Absolute Intensity

69.05 10000

81.05 8032

109.10 4394

80.05 1497

79.05 1116

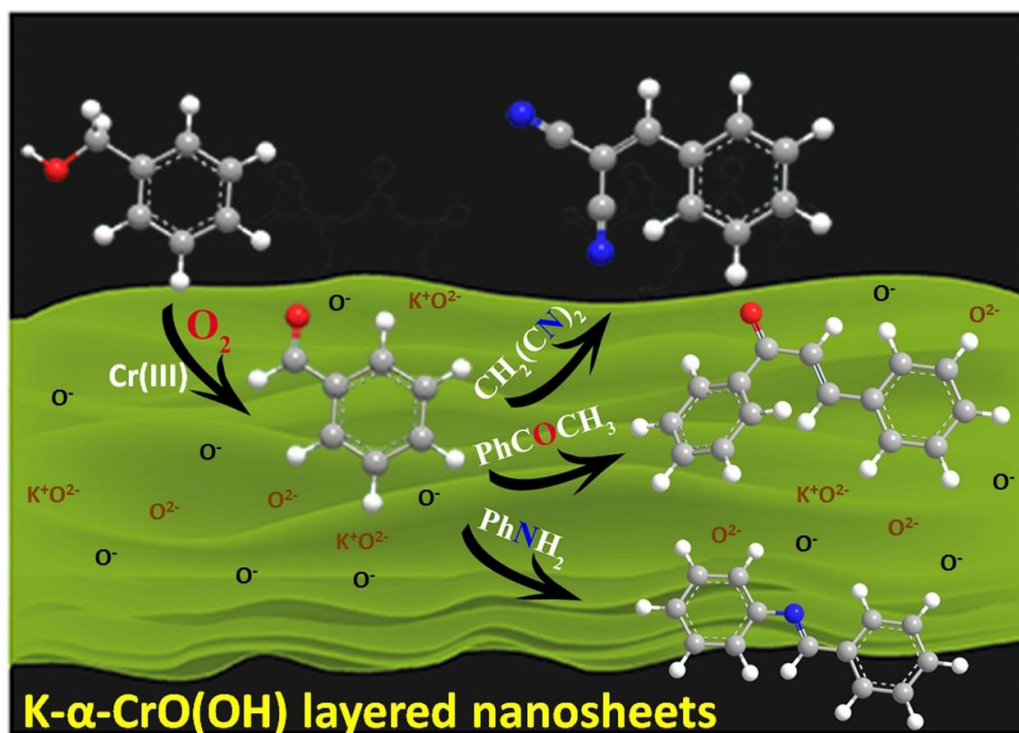
3b.6: References

- [1] P.Z. Bedoukian, *Perfumery and flavoring synthetics*, 1967.
- [2] F. Zhou, H. Liu, Z. Wen, B. Zhang, G. Chen, *Industrial & Engineering Chemistry Research*, 2018, **57**, 11288-11298.
- [3] V. Díez, C. Apesteguía, J. Di Cosimo, *Journal of Catalysis*, 2006, **240**, 235-244.
- [4] M. Climent, A. Corma, S. Iborra, J. Primo, *Journal of Catalysis*, 1995, **151**, 60-66.
- [5] C.N. Pérez, C. Pérez, C. Henriques, J. Monteiro, *Applied Catalysis A: General*, 2004, **272**, 229-240.
- [6] K. Xing, K. You, D. Yin, Z. Yuan, L. Mao, *Catalysis Communications*, **11**, 2009 236-239.
- [7] M. Climent, A. Corma, S. Iborra, A. Velty, *Catalysis letters*, 2002, **79**, 157-163.
- [8] M.J. Climent, A. Corma, S. Iborra, K. Epping, A. Velty, *Journal of Catalysis*, 2004, **225**, 316-326.
- [9] S. Abelló, F. Medina, X. Rodríguez, Y. Cesteros, P. Salagre, J.E. Sueiras, D. Tichit, B. Coq, *Chemical Communications*, 2004, **9**, 1096-1097.
- [10] V. Raju, R. Radhakrishnan, S. Jaenicke, G.K. Chuah, *Catalysis Today*, 2011, **164**, 139-142.
- [11] Z. Wang, G. Lu, Y. Guo, Y. Guo, X.-Q. Gong, *ACS Sustainable Chemistry & Engineering*, 2016, **4**, 1591-1601.
- [12] S. Abelló, S. Dhir, G. Colet, J. Pérez-Ramírez, *Applied Catalysis A: General*, 2007, **325**, 121-129.
- [13] J.-P. Jolivet, M. Henry, J. Livage, *Metal oxide chemistry and synthesis: from solution to solid state*, Wiley-Blackwell, 2000.
- [14] D. Vernekar, D. Jagadeesan, *Catalysis Science & Technology*, 2015, **5**, 4029-4038.
- [15] V.K. Díez, C.R. Apesteguía, J.I. Di Cosimo, *Catalysis Today*, 2010, **149**, 267-274.
- [16] F. Ewing, The crystal structure of lepidocrocite, *The Journal of Chemical Physics*, 1935, **3**, 420-424.
- [17] R.M. Cornell, U. Schwertmann, *The iron oxides: structure, properties, reactions, occurrences and uses*, John Wiley & Sons, 2003.
- [18] V. Jeena, R.S. Robinson, *RSC Advances*, 2014, **4**, 40720-40739.

- [19] M.C. Biesinger, B.P. Payne, A.P. Grosvenor, L.W. Lau, A.R. Gerson, R.S.C. Smart, *Applied Surface Science*, 2011, **257**, 2717-2730.
- [20] P. De Bakker, E. De Grave, R. Vandenberghe, L. Bowen, R. Pollard, R. Persoons, *Physics and chemistry of minerals*, 1991, **18**, 131-143.
- [21] D. Vernekar, S. Ratha, C. Rode, D. Jagadeesan, *Catalysis Science & Technology*, 2019, **9**, 1154-1164.
- [22] X. Song, J.-F.o. Boily, *Environmental science & technology*, 2013, **47**, 9241-9248.
- [23] J.R. Rustad, J.-F. Boily, *American Mineralogist*, 2010, **95**, 414-417.
- [24] T. Hiemstra, P. Venema, W.H.V. Riemsdijk, *Journal of Colloid and Interface Science*, 1996, **184**, 680-692.
- [25] J. Russell, R. Parfitt, A. Fraser, V. Farmer, *Nature*, 1974, **248**, 220.
- [26] M.-L. Bailly, C. Chizallet, G. Costentin, J.-M. Krafft, H. Lauron-Pernot, M. Che, *Journal of Catalysis*, 2005, **235**, 413-422.
- [27] C. Chizallet, H. Petitjean, G. Costentin, H. Lauron-Pernot, J. Maquet, C. Bonhomme, M. Che, *Journal of Catalysis*, 2009, **268**, 175-179.
- [28] H. Ren, D.D. Kulkarni, R. Kodiyath, W. Xu, I. Choi, V.V. Tsukruk, *ACS applied materials & interfaces*, 2014, **6**, 2459-2470.
- [29] K. Kuma, Y. Suzuki, K. Matsunaga, *Water research*, 1993, **27**, 651-657.

Chapter 4a

Efficient bifunctional reactivity of K-doped CrO (OH) nanosheets: exploiting the combined role of Cr (III) and surface –OH groups in tandem catalysis



Dnyanesh Vernekar, Satyajit Ratha, Chandrashekhar Rode, and Dinesh Jagadeesan
Catalysis Science & Technology 9 (5), 1154-1164, 2019

4a.1: Introduction

Synthesis of complex organic molecules usually involves several steps for transformations of various functional groups. Reaction sequences in such synthesis strategies often require separation and purification of intermediate products and use of different catalysts.[1] It is exciting to think of a possibility to carry out the full sequence of synthesis in a single pot so that the yield of the target molecule as well as the environmental benevolence of the reaction are enhanced.[2, 3] One of the strategies to achieve this, may require to carry out all the catalyzed steps of a reaction sequence in a single pot by introducing a common heterogeneous catalyst.[4] For example, a reaction sequence requiring a combination of two or more of the active sites such as an acid, a base, or a reduction or an oxidation site (for reaction steps like hydrolysis, condensation or oxidation) may be tandemly carried out in a single pot in the presence of a single catalyst possessing all such required sites on its surface. One can envisage that such bifunctional catalysts capable of catalyzing a sequence of oxidation and condensation/coupling reactions in tandem shall be useful in efficiently synthesizing biologically active molecules such as chalcones, benzylidene malononitriles and imines.[5-7] Synthesis and applications of multifunctional heterogeneous catalysts are of contemporary interest with promising outcomes.[8] Literature pertaining to the catalysis of sequential oxidation - condensation reactions revealed that majority of the catalysts employed the expensive noble metals and a base.[9, 10] In fact, one could classify the heterogeneous catalysts for the sequential oxidation-coupling organic transformations into two major types. The first type of catalysts are predominantly noble metals on inert oxides such as Ag-Al₂O₃ [11], Pd/AlOOH [12], Pd-Si-Pr-NiXantphos/SiO₂ [13], Pt-Sn/C-Al₂O₃ [14]. These catalysts employ external bases such as K₃PO₄, LiOH, and Cs₂CO₃ to complete the reaction. The second type of catalysts are noble metals on basic oxides or supports with basic functional groups such as amines eg Au@Cu(II)-MOF [15], Pd(0)@UiO-68-AP [16], Au-Pd/HT [17], Cu_xAg_{1-x}/HT [18], Pd-Au@Mn(II)-MOF [19]. There could be only few examples of non-noble metal based bifunctional catalysts without using an external base. Notable ones are Co on N doped carbon [20], Tris-LDH-X₄(PW₉)₂ [21] and CeO₂ [22-23].

In Chapter 3a, we had discussed that $-OH$ and $-O^-$ groups on the surface of iron oxyhydroxides could catalyse organic transformation requiring sequential acid and base catalyzed steps in a single pot.[24] Importantly, we also showed that oxyhydroxides are much simpler acid-base bifunctional catalysts as it does not involve grafting of organic amines and acids on its surface. We were curious to explore if a redox-active metal oxyhydroxide could offer an advantage of the redox property of the metal and basic properties of the surface $-O^-$ groups. In such a case, one could envisage non-noble metal based bifunctional catalyst for sequential oxidation and condensation or coupling reactions. Particularly, we were interested to explore the 2D layered metal oxyhydroxide such as $CrO(OH)$. Layered materials have a higher specific surface as compared to their bulk counterparts or nanoparticles (spherical). [25] This leads to an increase in the number of accessible active sites (Redox and acid-base) on the surface of 2D layered material, thus increasing the chance of efficient catalysis. Besides, the electron mobility in 2D layered materials is excellent leading to ultrafast electron transfer and hence improving their redox ability. [26-28] Thirdly, due to its layered nature, these materials can act as excellent supports with improved catalyst dispersion. [29] In this chapter, we discuss about the K- doped layered $CrO(OH)$ and carried out a detailed study of its activity in a single-pot oxidation followed by coupling reactions.

4a.2: Experimental Section:

Materials used: Potassium chromate K_2CrO_4 , Chromium nitrate nonahydrate $Cr(NO_3)_2 \cdot 9H_2O$, tetraethyl orthosilicate (TEOS), aminopropyl triethoxysilane (APTES), benzyl alcohol, 1-phenyl ethanol, benzaldehyde, balononitrile, Aniline, Ethyl cyano acetate, acetophenone, aniline, acetonitrile, xylene.

4a.2.1: Preparation of oxyhydroxide materials

Synthesis of K- α - $CrO(OH)$: A quartz boat, loaded with K_2CrO_4 particles was placed in a tube furnace over which, hydrogen gas was flown at a constant flow rate to maintain the reductive atmosphere. The reaction temperature was raised by ramping at the rate $10\text{ }^\circ\text{C}/\text{min}$ to $500\text{ }^\circ\text{C}$ and maintained for 1 h and then cooled naturally to the ambient temperature. The product was washed by distilled water several times

until the dissolvable components were completely removed. After that, the black green intermediate was dried at 60 °C.

Synthesis of α -CrO(OH): 1.0 g of K- α -CrO(OH) was taken in 50 mL of 0.01M HCl solution and stirred for 48h at 70 °C and filtered. The obtained residue was stirred again in distilled water, filtered and dried at 60 °C.

Synthesis of γ -CrO(OH): 15 g of Cr(NO₃)₂.9H₂O was dissolved in 75 mL of distilled water. 10% Ammonia solution was added dropwise with constant stirring till the pH attained the value 5. The solution was allowed to stir further for 30 min, centrifuged and washed to obtain the precipitate. This wet precipitate was transferred into a beaker and was placed in a teflon lined autoclave containing 2 mL of water. The sample was sealed and heated for 12 h at 170 °C. The resultant product was washed, centrifuged and dried. Cr₂O₃ was obtained by calcining γ -CrO(OH) in a muffle furnace at 800 °C.

Synthesis of K- γ -CrO(OH): In the synthesis procedure of γ -CrO(OH), 0.5 g KNO₃ was additionally added to the already solution of Cr(NO₃)₂.9H₂O, as mentioned above. 10% Ammonia solution was added dropwise to this solution with constant stirring till the pH attained the value 5. The solution was allowed to stir for further 30 min, centrifuged and washed to obtain the precipitate. This wet precipitate was transferred into a beaker and was placed in a teflon lined autoclave containing 2 mL of water. The sample was sealed and heated for 12 h at 170 °C. The resultant product was washed, centrifuged and dried. The elemental analysis showed K loading of 3.0 wt %.

Synthesis of SiO₂-NH₂: 0.5mL of Ammonia stock solution (30%) was taken along with 3.77 mL of distilled water and 15 mL of isopropanol and stirred for 10min. Then 7.5 mL of tetraethylorthosilicate was added dropwise with stirring. A white silica suspension was obtained which was stirred further for 5h and then centrifuged, washed with ethanol and dried at 150 °C for 5 h. For amine functionalization, 5 mmol of amino propyl triethoxysilane was taken in dry toluene along with 1 g of SiO₂ powder obtained above. This was refluxed overnight at 110 °C then filtered, washed with ethanol and dried to obtain SiO₂-NH₂.

4a.2.2: Material Characterization: Transmission electron microscopy (TEM) images were obtained using FEI Technai TF-20 electron microscope operating at 200kV. Specimens of the samples were prepared by drop-casting well-dispersed ethanol particle suspensions onto a carbon coated copper grids. Infrared Spectroscopy measurements were done using Bruker FT-IR. The samples were analyzed as solids. XRD was measured using PANalytical X'pert Pro diffractometer working under 40kV and 20 mA with CuK α (0.154 nm) radiation using a Ni filter. X-ray photoelectron spectroscopy (XPS) study of K- α -CrO(OH) was done using VG Microtech model ESCA 3000 instrument. The organic reaction was monitored using an Agilent Technologies GC (7890B) equipped with a Flame Ionization Detector using a HP-5 capillary column. CO₂ TPD measurements were performed on Micromeritics ChemiSorb 2720 instrument equipped with a TCD detector.

4a.2.3: Catalytic Reaction

Knoevenagel Condensation: In a typical reaction, 1 mmol of benzaldehyde was taken along with 2 mmol of malononitrile (**2a**) / ethylcyanoacetate (**2b**) in a 25 mL round bottomed flask with 0.1 g of catalyst using 5mL of acetonitrile and heated at 80 °C for required amount of time in nitrogen atmosphere. The reaction mixture was cooled and then centrifuged. The supernatant was analyzed using GC.

C-C and C-N coupling reactions : In a typical reaction, 1 mmol of benzaldehyde (**1**) was taken along with 2 mmol of acetophenone (**2c**) / aniline (**2d**) in a 25 mL round bottomed flask with 0.4 g of catalyst using 5mL of xylene and heated at 110 °C for 12 h in nitrogen atmosphere to yield **3c** & **3d** respectively. The reaction mixture was cooled and then centrifuged. The supernatant was analyzed using GC.

Benzyl alcohol oxidation: In a typical procedure, 1 mmol alcohol and 5 mL xylene was taken in a 25 mL round bottomed flask along with the required amount of catalyst. The suspension was refluxed at 110 °C for suitable time under oxygen atmosphere. The reaction mixture was cooled and then centrifuged and the supernatant was analyzed using GC.

Sequential oxidation-condensation: In a typical procedure, 1 mmol benzyl alcohol and 5 mL xylene were taken in a 25 mL RBF along with 0.4 g of catalyst and

refluxed for suitable time under balloon oxygen pressure. After which, 2 mmol malononitrile/ethyl cyanoacetate was injected into the reaction mixture and the reaction was allowed to proceed further for time. The reaction mixture was cooled and centrifuged with the supernatant liquid analyzed using GC.

One pot Oxidation-C-C coupling reaction: 1 mmol of benzyl alcohol and 2 mmol of 1-phenyl ethanol were taken in a 25 mL round bottom flask dissolved in 5 mL of xylene together with 0.4 g of K- α -CrO(OH). This was refluxed for 48 h under balloon oxygen to give **3c**. The reaction mixture was cooled and then centrifuged and the supernatant was analyzed using GC.

One pot Oxidation- C-N coupling reaction: 1 mmol benzyl alcohol and 2 mmol of aniline were taken in a 25 mL round bottom flask dissolved in 5 mL of xylene together with 0.4 g of K- α -CrO(OH). This was refluxed for 24 h under balloon oxygen pressure (1 atm) to give **3d**. The reaction mixture was cooled and then centrifuged and the supernatant was analyzed using GC.

Reusability: After one pot reaction synthesis of **3c**, the catalyst was separated by centrifugation washed thoroughly with CH₃OH and dried to be used for the next cycle.

4a.2.4: *In-situ* Infrared Spectroscopy: CO₂ adsorption on K- α -CrO(OH)/ α -CrO(OH) was done using a praying mantis assembly equipped to a Perkin Elmer FT-IR using a MCT detector cooled using Liquid Nitrogen. The sample holder and the sample were first degassed under N₂ gas flow at 300 °C. The IR of the bare sample was then recorded. CO₂ was subsequently purged on K- α -CrO(OH)/ α -CrO(OH) held in the sample holder cavity in N₂ flow at room temperature. IR of the CO₂ adsorbed sample was measured. The difference spectra was obtained using the *difference function* inbuilt in the *Spectrum* Software.

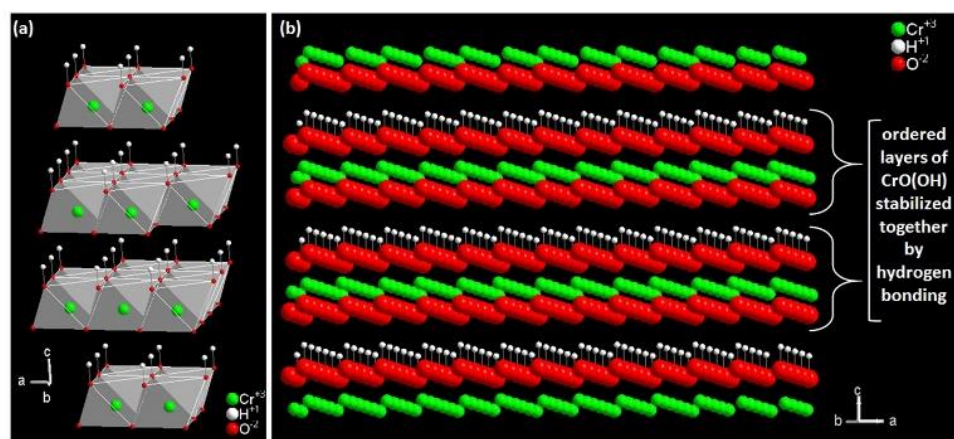
4a.2.5: Cyclic Voltammetry: The electrochemical analysis of all the synthesized samples were carried out by using the cyclic voltammetry technique. Prior to the measurement, glassy carbon electrodes were well polished by alumina slurry (of size 1 μ , 0.3 μ , 0.05 μ sequentially), sonicated in double distilled water and dried in the vacuum desiccator. In the meantime, the sample ink has been prepared by mixing the

powdered sample (1.0 mg) with absolute ethanol (95%) and Nafion followed by ultrasonication for 5 minutes. An optimized amount of the sample ink has been drop casted onto the polished glassy carbon electrode and dried in the vacuum desiccator. The CV profiles were recorded by using Metrohm Electrochemical workstation in a two compartment three electrode electrochemical cell with a bare platinum (as counter electrode), aqueous Ag/AgCl (as reference) and sample modified glassy carbon (as working electrode) in the electrolyte solutions (neutral: Na₂SO₄, acidic: 0.5 M H₂SO₄, and alkaline: 1.0 M KOH) at different sweep rates (10, 50 and 100 mV/s).

4a.3: Results and Discussion

4a.3.1: Synthesis and Characterization of CrO(OH)

According to a reported procedure, [30] one-step reduction of K_2CrO_4 in H_2 at 500 °C resulted in the formation of K doped CrO(OH). X-ray diffraction pattern (XRD) of the sample as shown in Fig 4a.1a confirmed the presence of crystalline grimaldiite (α phase), a mineral phase of chromium oxyhydroxide α -CrO(OH) (JCPDS card no 09-0331) with a space group $R3m$ (Scheme 4a.1a). [31] The amount of K present in the as-prepared sample K - α -CrO(OH), was determined to be 2.7 wt% using inductively coupled plasma atomic emission spectroscopic technique (ICP-AES). An intense peak in the low angle region ($2\theta = 10.5^\circ$) of the XRD pattern corresponded to a d spacing of 0.8 nm. This peak indicated the presence of ordered layers of K- α -CrO(OH) stabilized by an inter-layer hydrogen bonding (Scheme 4a.1b). In Fig 4a.1b, FT-Infrared (IR) spectra of K- α -CrO(OH) showed characteristic absorption bands due to Cr-O-Cr and Cr-O stretching modes at 985 cm^{-1} and 1188 cm^{-1} , respectively, the latter due to the dissociative chemisorption of oxygen. [32] The broad band centered around 3400 cm^{-1} is due to the stretching of surface hydroxyl groups of K- α -CrO(OH) along with non-dissociated water molecules. [30] N_2 sorption isotherm showed type II hysteresis loop with a BET surface area of $61.66\text{ m}^2/\text{g}$ (Fig. 4a.2).



Scheme 4a.1: a) crystal structure of α -CrO(OH) with Cr as the central atom of the polyhedra b) ordered layers of CrO(OH) stabilized by hydrogen bonding forming the 2D nanostructure

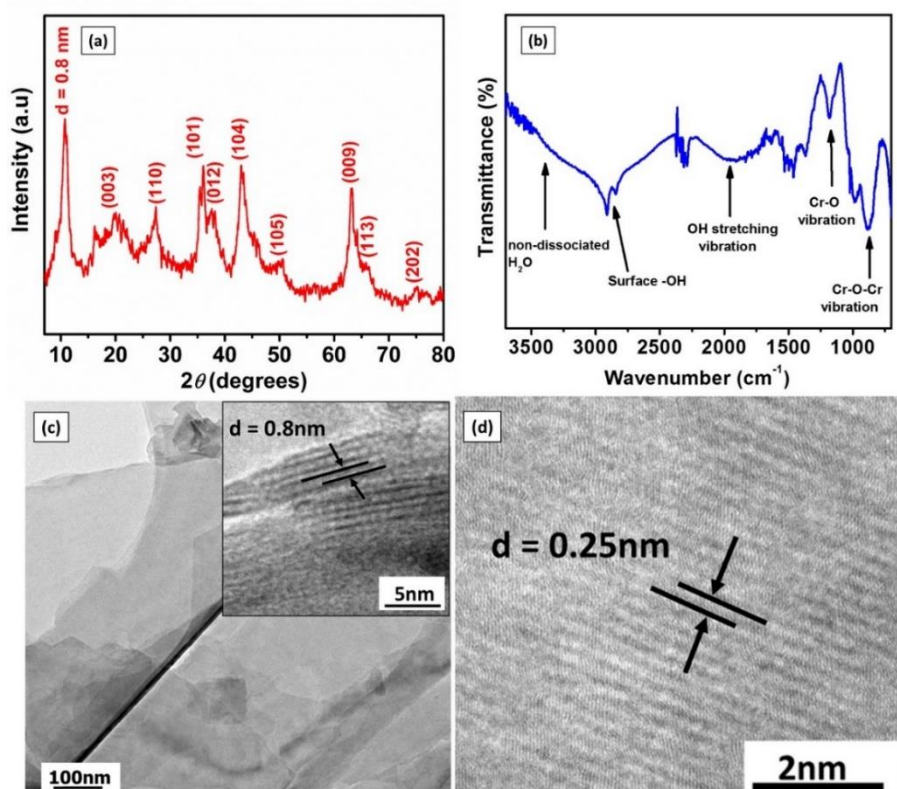


Fig 4a.1: a) X-Ray Diffraction pattern for K- α -CrO(OH), b) Infrared Spectrum of K- α -CrO(OH) c) TEM image of K- α -CrO(OH) (inset showing the stacks of K- α -CrO(OH) sheets) d) HRTEM image of the K- α -CrO(OH) showing the lattice fringes of (101) plane

The microstructure of K- α -CrO(OH) was analyzed using Transmission Electron Microscopy (TEM) (Fig 4a.1c) which showed thin layers of sheet-like structures. The stacks of K- α -CrO(OH) sheets can be observed in the inset of Fig 4a.1c, clearly showing an inter-layer spacing of 0.8 nm. This value of inter-layer separation correlated with the d spacing obtained from the low angle peak in XRD at $2\theta = 10.5^\circ$ (Fig 4a.1a). Atomic force microscopic studies of K- α -CrO(OH) under tapping mode showed K- α -CrO(OH) having a flake-like topology (Fig 4a.3). The height profile measurements of several flakes showed that the average step height was around 50 nm while, the length of each flake varied from 0.3-1 micrometers making it a quasi-two-dimensional nanosheet. HRTEM image of K- α -CrO(OH) (Fig 4a.1d) showed lattice fringes with a d spacing of 0.25 nm corresponding to (101) planes. Chemical analysis of the surface of K- α -CrO(OH) was carried out using X-ray Photoelectron Spectroscopy (XPS). All XPS spectra were charge corrected and referenced to adventitious carbon (284.6eV). Fig 4a.4 shows a full-scan XPS spectra for K- α -

CrO(OH). Peaks due to Cr(2p), O(1s), K(2s, 2p) and Auger peaks due to Cr (LMM) were also observed. The signal of $2p_{3/2}$ at BE of 576.4 eV is due to Cr(III) attached to O^{2-} while, the peaks at BE of 577.6 eV and at 579.0 eV are due to Cr(III) bonded to hydroxyls and Cr(III) coordinated to H_2O , respectively (Fig. 4a.4c).

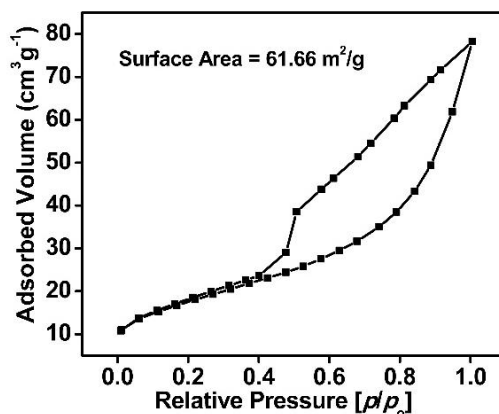


Fig 4a.2: BET Hysteresis plot for K-CrO(OH)

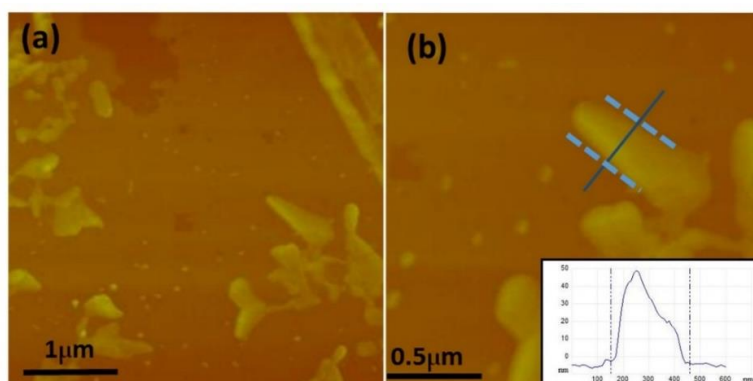


Fig. 4a.3: Atomic Force Micrographs of K- α -CrO(OH). Inset of b) shows thickness of sheet along the line between the dotted boundaries

Inset of Fig 4a.4c shows the Auger signals at BE 972 eV corresponding to LMM transitions in Cr. LMM refers to those processes with the initial vacancy in the L shell and final double vacancy in the M shells. Also, the kinetic energies of the Auger lines are independent of the ionizing radiations. The O1s spectra showed peaks at BE 530.2 eV due to O^{2-} and BE 531.4 eV due to surface OH. The peak at BE 532.4 eV is due to physisorbed moisture (Fig 4a.4d).[31]

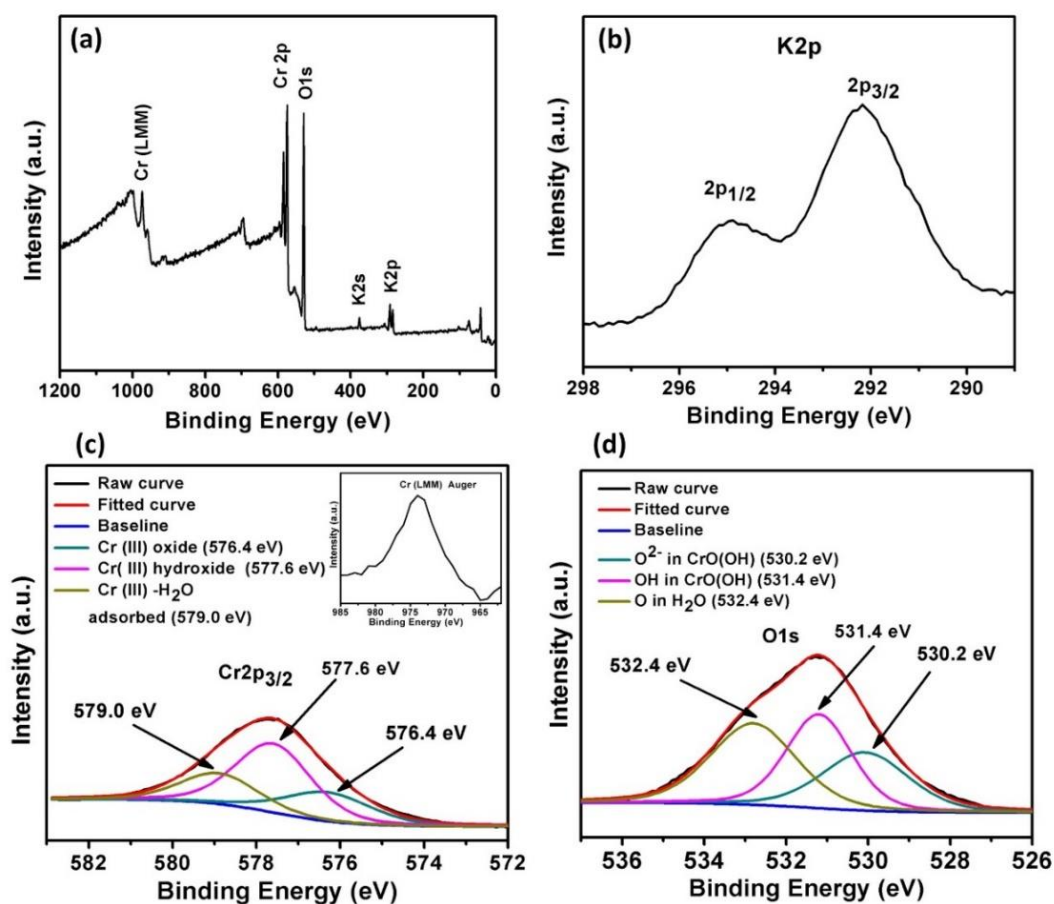


Fig 4a.4: a) Full scan XPS spectra b) deconvoluted XPS spectra of K 2p signal c) deconvoluted Cr 2p_{3/2} signal (inset Cr Auger Signal) d) deconvoluted O 1s signal of K- α -CrO(OH)

XRD analysis (Fig 4a.5a) of the control samples (Cr_2O_3 , γ -CrO(OH), K- γ -CrO(OH) and α -CrO(OH)) showed peaks due to respective phases and no impurity peaks were observed.

α -CrO(OH) - JCPDS-09-0331

γ -CrO(OH) - JCPDS-85-1373

Cr_2O_3 - JCPDS- 38-1479

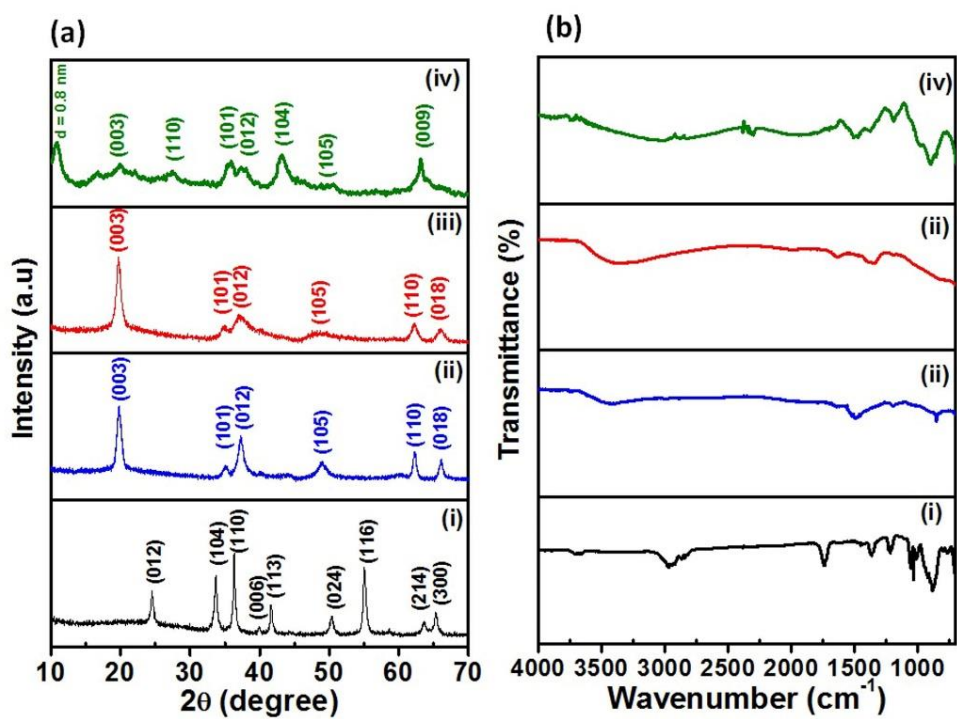


Fig 4a.5: (a) XRD & (b) Infrared spectrum of i) Cr_2O_3 ii) $\gamma\text{-CrO(OH)}$ iii) $\text{K-}\gamma\text{-CrO(OH)}$ iv) $\alpha\text{-CrO(OH)}$

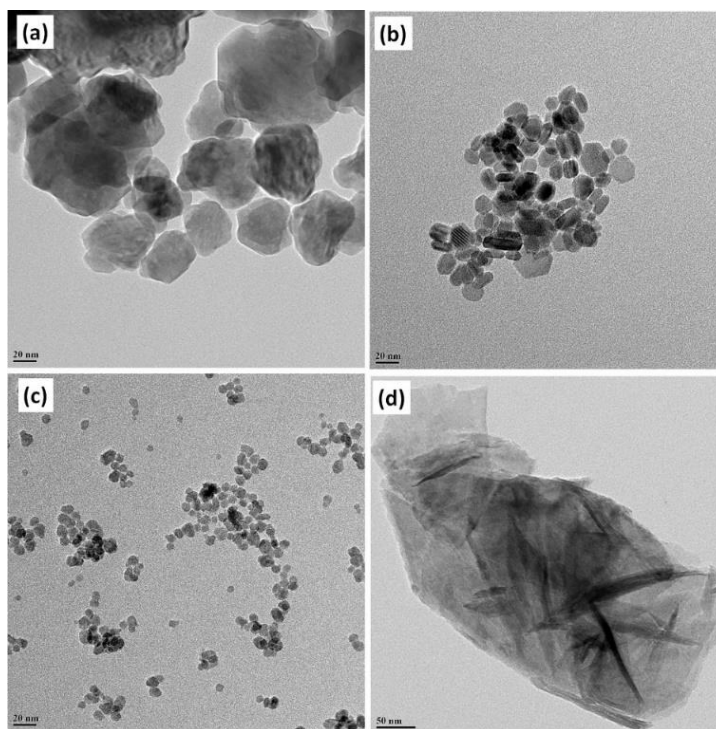


Fig 4a.6: TEM images of a) Cr_2O_3 b) $\gamma\text{-CrO(OH)}$ c) $\text{K-}\gamma\text{-CrO(OH)}$ d) $\alpha\text{-CrO(OH)}$

Characterization of the control catalysts are described in Fig.s 4a.5, Fig 4a.6. Infrared Spectroscopy (Fig 4a.5b) indicated the presence of surface hydroxyl groups ($3000-3700\text{ cm}^{-1}$) in the case of $\gamma\text{-CrO(OH)}$, K- $\gamma\text{-CrO(OH)}$ and $\alpha\text{-CrO(OH)}$. Whereas surface hydroxyl groups are absent in the case of Cr_2O_3 . Cr_2O_3 has larger nanoparticle like morphology (Fig 4a.6a). $\gamma\text{-CrO(OH)}$ and K- $\gamma\text{-CrO(OH)}$ are in the form of smaller nanoparticles (Fig 4a.6b,c). $\alpha\text{-CrO(OH)}$ (Fig 4a.6d) has a nanosheet like morphology intact, similar to K- $\alpha\text{-CrO(OH)}$.

4a.3.2: Catalytic activity of K- $\alpha\text{-CrO(OH)}$

4a.3.2.1: Base property of K- $\alpha\text{-CrO(OH)}$

The basic property of K- $\alpha\text{-CrO(OH)}$ was demonstrated by its catalytic activity for Knoevenagel condensation, C-C and C-N coupling reactions for the first time. Table 4a.1 briefly describes various base catalyzed reactions involving four different active methylene compounds containing aliphatic and aromatic substituents, studied in this work. For example, Knoevenagel condensation reaction between benzaldehyde (**1**) and malononitrile (**2a**) was carried out to give benzylidinemalanonitrile (**3a**) as the product (Table 4a.1, entry 1). K- $\alpha\text{-CrO(OH)}$ showed complete conversion in 6 h at $80\text{ }^\circ\text{C}$ in acetonitrile. The activity of K- $\alpha\text{-CrO(OH)}$ was compared with control catalysts. Cr_2O_3 (Table 4a.1, Entry 2) gave only 21% selectivity for **3a** but more of benzoic acid was formed. In comparison, the standard grafted catalysts such as NH_2 -functionalized silica showed a high selectivity to **3a** but the conversion was limited to only 71% even after 15 h (Entry 5). Similarly, ethylcyanoacetate (**2b**) could be completely converted to ethyl-2-cyano-3-phenylacrylate (**3b**) using K- $\alpha\text{-CrO(OH)}$ (Table 4a.1, entry 6) with 90% selectivity after 12 h in acetonitrile. In another example, benzaldehyde (**1**) could be coupled with acetophenone (**2c**) with complete conversion, to form 1,3-diphenyl-2-propene-1-one (**3c**) (Table 4a.1, entry 6) in the presence of K- $\alpha\text{-CrO(OH)}$. The catalyst showed complete conversion in 24 h with 100% selectivity to (**3c**) (Table 4a.1, Entry 7). In xylene, the selectivity reduced to 95% (Table 4a.1, Entry 8) due to non-polar nature of the solvent. It is important to highlight that the reaction is usually carried out using environmentally unfriendly organic or organometallic coupling partners such as dppe and BuNiXantphos [13] which are air/moisture sensitive, difficult to recycle and are used along with toxic bases such as K_2CO_3 , Cs_2CO_3 , LiOH .

Table 4a.1: Different base catalyzed reactions tested by K- α -CrO(OH) and other catalysts.

Sr. No	Catalyst	Reactant 2	Product 3	Solvent	Time (h)	Conversion of 1 (%)	GC Selectivity of Product 3 (%)
1	K- α -CrO(OH)	2a	3a	CH ₃ CN	6	100	92
2	Cr ₂ O ₃	2a	3a	CH ₃ CN	15	96	21
3	γ -CrO(OH)	2a	3a	CH ₃ CN	15	57	71
4	K- γ -CrO(OH)	2a	3a	CH ₃ CN	15	72	83
5	SiO ₂ -NH ₂	2a	3a	CH ₃ CN	15	71	100
6	K- α -CrO(OH)	2b	3b	CH ₃ CN	12	100	90
7	K- α -CrO(OH)	2c	3c	CH ₃ CN	24	100	100
8	K- α -CrO(OH)	2c	3c	xylene	24	100	95
9	K- α -CrO(OH)	2d	3d	xylene	12	100	100

Reaction conditions: 1 (1 mmol), Entries 1-5 (1: Catalyst weight ratio=1.08) and for Entries 6-7 it was 0.27, 2 (2 mmol), Solvent (5 mL), Temperature of the reaction was 80 °C for acetonitrile and 110 °C for xylene, Nitrogen atmosphere.

Though the time required is slightly higher, it is necessary to recognize the importance of avoiding the usage of soluble bases. N-benzylidene aniline (**3d**), an important intermediate for various pharmaceutical and biological compounds was also synthesized using K- α -CrO(OH) from benzaldehyde and aniline under similar conditions (Table 4a.1, entry 9). Synthesis of **3d** involves the use of strong organic and inorganic bases such as DABCO, NaOH and KOH which leads to the formation of large amounts of undesirable salts. In contrast, K- α -CrO(OH) yielded 100% of **3d** in 12 h without the external base (Table 4a.1 Entry 9). Importantly, 70% higher conversion could be achieved (in the synthesis of **3d**) in 12h in the presence of K- α -CrO(OH). Hot filtration test carried out using K- α -CrO(OH) after 1 h of reaction showed no conversion of **1** to **3a** at 80 °C (Fig 4a.7) in the filtrate devoid of the catalyst, confirming the role of K- α -CrO(OH) as a heterogeneous catalyst.

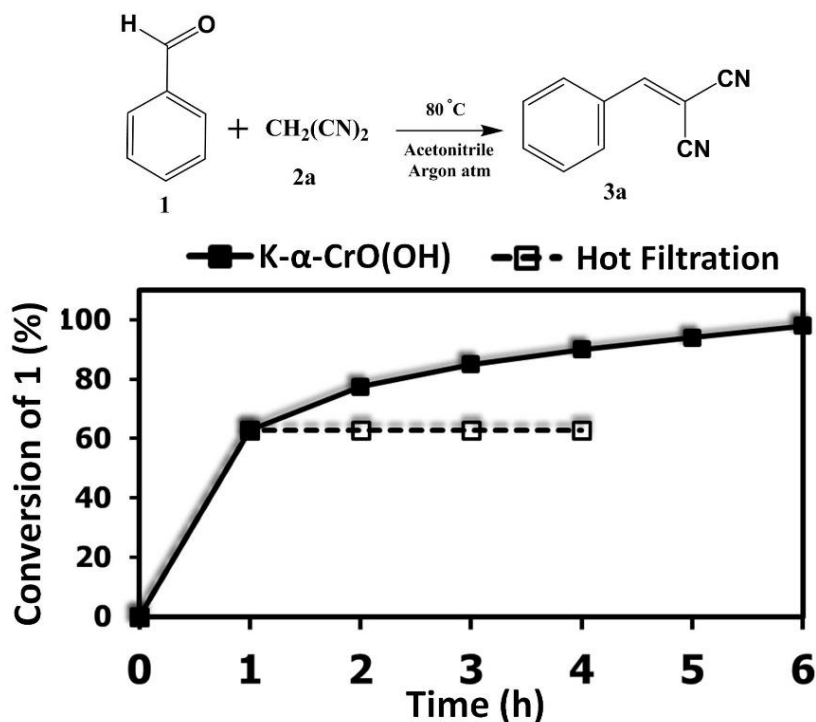


Fig 4a.7: Time dependent conversion for Knoevenagel Condensation using K- α -CrO(OH) and Hot filtration test for K- α -CrO(OH) for Knoevenagel Condensation.

4a.3.2.1.1: Effect of K doping

In order to assess the effect of K doping on the activity of K- α -CrO(OH), we attempted to prepare K-free α -CrO(OH) by treating it with 0.01M HCl at 70°C for 48 h and then washing several times with distilled water. The characterization of K-leached sample (α -CrO(OH)) using X-ray Diffraction, Infrared Spectroscopy, XPS, TEM & elemental analysis data confirmed that the chemical and structural integrity of the sample was preserved (Fig.s 4a.5 and 4a.6). Thus, K doping does not affect the structure of parent CrO(OH). To understand the effect of K on the reaction, the activity of K- α -CrO(OH) with 2.7 wt% K and α -CrO(OH) were compared in the synthesis of 3a at the end of 3h of reaction (Fig 4a.8). The K- α -CrO(OH) with 2.7 wt% K showed a better conversion (67%) and selectivity (95%) to 3a in comparison to α -CrO(OH).

4a.3.2.1.2: Effect of Polymorph

In CrO(OH), each Cr(III) ion is surrounded by three O^{2-} ions and three OH^- to give $CrO_3(OH)_3$ octahedra which is the basic structural unit (Scheme 4a.1). The specific arrangement of these octahedra gives rise to different polymorphs. [33]

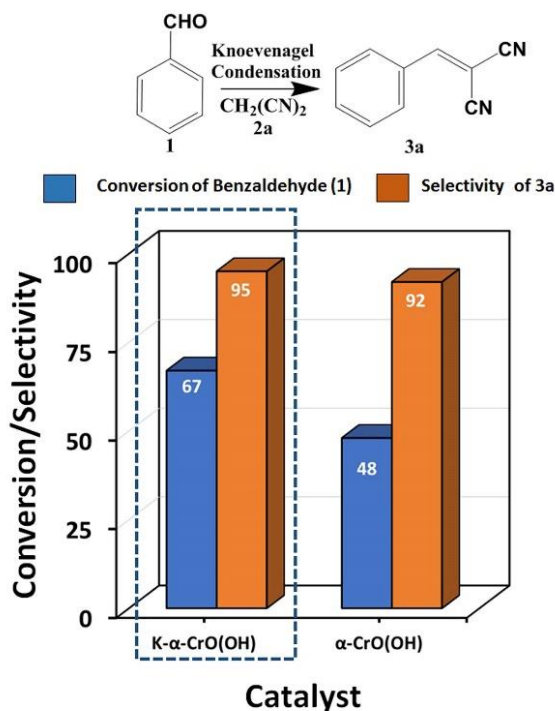


Fig 4a.8: Knoevenagel condensation reaction for K doped and K free α -CrO(OH)

Both K- α -CrO(OH) and α -CrO(OH) have a unique layered structure in which layers of CrO(OH) (with $d = 0.25$ nm) are mesostructurally ordered with a inter-layer spacing of 0.8 nm due to H bonding. Another polymorph of CrO(OH) namely, the γ -CrO(OH) was also prepared by hydrothermal synthesis (Table 4a.1, Entry 3). Interestingly, γ -CrO(OH) differed from α -CrO(OH) in the crystal structure as well as the morphology (Fig.s 4a.5 and 4a.6). K-free γ -CrO(OH) and 3wt % K- doped γ -CrO(OH) were prepared and compared with the catalytic performance of α -CrO(OH) counterparts to understand the effects of polymorphs. K-free γ -CrO(OH) too yielded Knoevenagel condensation product 3a (57% conversion) but the selectivity to 3a was limited to only 71% due to the formation of benzoic acid. Interestingly, K- γ -CrO(OH) (with 3 wt% K) showed an improvement in conversion upto 72% as compared to the K – free γ -CrO(OH) and an increase in selectivity to 83% (Table 4a.1, Entry 4). However, the activity of K- γ -CrO(OH) was far less as compared to K- α -CrO(OH) even though the loading in each case is comparable. One of the reasons for this difference in activity between the polymorphs could be the difference in the exposure of active sites to the reactants.

4a.3.2.1.3: Nature of Basic Sites

The nature and the strength of the basic sites in CrO(OH) catalysts were further probed using Temperature Programmed Desorption (TPD) of CO₂ (Fig 4a.9 and Table 4a.2). The CO₂ desorption from room temperature to 400 °C provided information about weak to moderate basic sites on the surface of K- α -CrO(OH). The CO₂-TPD profiles of K- α -CrO(OH) was compared with those of α -CrO(OH), γ -CrO(OH), K- γ -CrO(OH) and Cr₂O₃. It can be observed that α -CrO(OH) gave a CO₂ desorption amount of 0.59 mmol/g, which was lower than that for K- α -CrO(OH) which desorbed 0.93 mmol CO₂/g. Interestingly, γ -CrO(OH) which is a different polymorph showed an overall basicity of 0.33 mmol/g, which was less than that of both α -CrO(OH) and K- α -CrO(OH). Although, doping of K on γ -CrO(OH) improved its basicity to 0.56 mmol/g, it still remained less in comparison to its layered counterparts. Cr₂O₃ obviously showed a very poor basicity of 0.02 mmol/g of the catalyst. TPD profiles strongly supported the significantly better basicity in layered α -CrO(OH) confirming the role played by the morphology and the enhancement in basicity due to the presence of K (Table 4a.1, Entries 1 and 4).

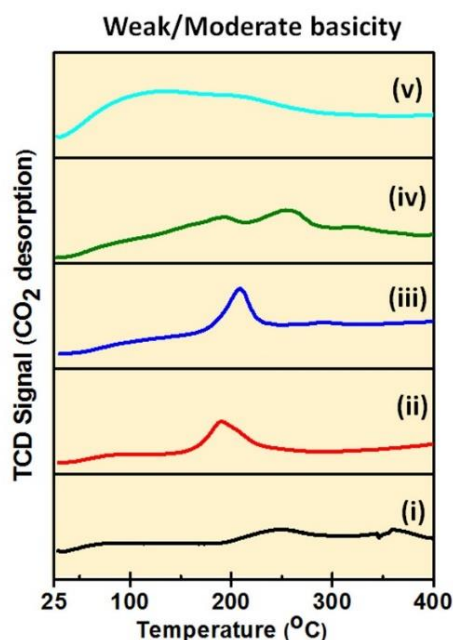


Fig 4a.9: CO₂ TPD profiles of (i) Cr₂O₃ (ii) γ -CrO(OH) and (iii) K- γ -CrO(OH) (iv) α -CrOOH (v) K- α -CrO(OH)

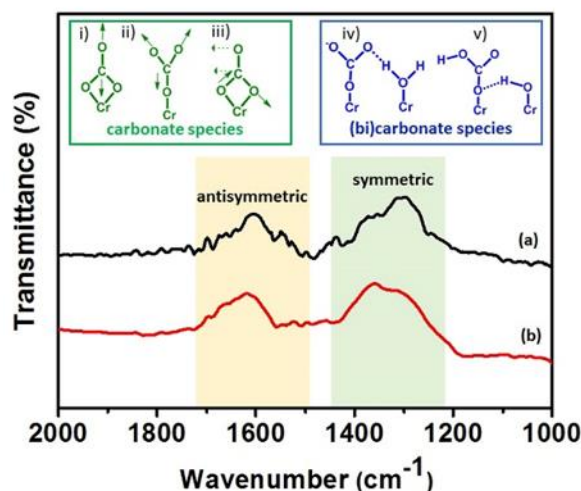


Fig 4a.10: *In situ* IR difference spectra of CO₂ adsorbed on (a) α -CrO(OH) and (b) K- α -CrO(OH) Inset different carbonate & (bi)carbonate vibration modes

Table 4a.2: Textural properties and CO₂ TPD results of the samples.

Sr. No	Sample	Surface area (m ² /g)	Pore Volume cc/g	Weak/moderate Basicity (mmol/g of CO ₂)
1.	Cr ₂ O ₃	118.32	0.089	0.02
2.	γ -CrO(OH)	92.32	0.116	0.33
3.	K- γ -CrO(OH)	83.63	0.098	0.56
4.	α -CrO(OH)	68.35	0.086	0.59
5.	K- α -CrO(OH)	61.66	0.079	0.93

Basicity due to Potassium

The role of potassium (K) in promoting the basicity by electron donation has been well studied in metal oxide catalysts in the context of Fischer-Tropsch and side chain alkylation reactions. [34] Potassium in K- α -CrO(OH) could be in the form of K₂O as the XPS signal due to K2p (Fig 4a.4b) closely matched with this phase. [35] Also, a small peak at BE 530.2 eV in the O1s spectra of K- α -CrO(OH) is attributed to O²⁻ in K⁺₂O²⁻ (Fig 4a.4d). [35] It is possible that K₂O either exists in very small traces or probably in poorly crystalline form thereby could be undetected in XRD. Another possible phase KCrO₂ which may be formed under the synthesis conditions of K- α -CrO(OH)[36] which is highly moisture-sensitive [37] and may react with water to give CrO(OH) and KOH.



Since KOH is completely removed by washing in water, its role in the basicity can be completely ruled out. [30] Analysis of the O1s spectra of the K doped samples in both α & γ polymorphs of CrO(OH) showed that the contribution from O^{2-} (BE 530.2eV) to the XPS signal was 10 – 16% higher in K-doped CrO(OH) compared to their K-free counterparts (Fig 4a.14). *In situ* IR analysis of K- α -CrO(OH) with CO_2 adsorbed was carried out to probe the basic sites on its surface. Fig 4a.10 shows the difference in FT-IR spectra of CO_2 -adsorbed on K- α -CrO(OH) and the bare K- α -CrO(OH). Similarly, the difference FT-IR spectra of CO_2 -adsorbed on α -CrO(OH) with the corresponding bare sample is also shown. The difference spectra gave two strong absorption bands in the range 2000-1000 cm^{-1} due to surface carbonates and (bi)carbonates. The bands in the range of 1200-1300 cm^{-1} and 1600 cm^{-1} are due to symmetric and antisymmetric O-C-O vibrations of the surface carbonates/(bi)carbonates bound to Cr(III), respectively. [38] The probable vibration modes are shown in the inset in Fig 4a.10. Earlier studies on chromium oxides have shown that five-coordinate Cr(III) cations and three-coordinate O^{2-} anions provide strongest basic sites of interaction with CO_2 to form bi-dentate carbonates at room temperature. [38-39] The basicity of O^{2-} sites is well documented in alkaline metal oxides. [40] Consistent with our results, studies on CO_2 -adsorbed intermediates on the surface of metal oxyhydroxides have showed that O^{2-} forms carbonate species whereas, O^- species in the vicinity of surface hydroxyl groups may form (bi)carbonate species ($-O-CO_2H$ or $-(O)_2-COH$).[41] Thus, the results strongly indicate that CrO(OH) has O^{2-} and O^- sites on the surface. Quantifying the carbonate and (bi)carbonate species based on IR absorption is hardly possible as they occur in the same frequency region.

4a.3.2.1.5: Basicity due to surface hydroxyl groups

In addition to the presence of O^{2-} and O^- sites that were probed using FT-IR, we used thermal analysis and fluorescence techniques to study the surface hydroxyl groups and O^- sites. The origin of O^- on the surface of CrO(OH) and its predominant activity could be understood as shown in equation (ii).



The thermogravimetric profiles of the CrO(OH) polymorphs were compared and semi-quantitatively correlated to the presence of surface hydroxyl groups on the respective samples (Fig 4a.11 & Table 4a.3). Weight loss in the temperature region below 150 °C is assigned to the loss of physisorbed water. Continued heating till 350 °C leads to progressive dehydration accompanied by the loss of hydroxyl groups eventually leading to the formation of oxides. Hence, the weight loss in the temperature region between 150 – 350 °C was compared between the samples to understand the presence of surface hydroxyl groups. [42] The fact that K- α -CrO(OH) has a higher weight loss in this thermal regime implies that dehydration of surface hydroxyl groups is a major thermal reaction. As expected, Cr₂O₃ showed the poorest of weight loss i.e. 1.08 wt% indicating negligible surface hydroxyl groups present on the surface. Weight loss in K- α -CrO(OH) (8.48%) and α -CrO(OH) (6.68%) are higher than that for γ -CrO(OH) (4.91%) and K- γ -CrO(OH) (3.71%) (Table 4a.3). Interestingly, this also correlated well with the amount of CO₂ desorbed from the surface of these samples in TPD experiments suggesting that surface hydroxyl groups have a role in surface basicity.

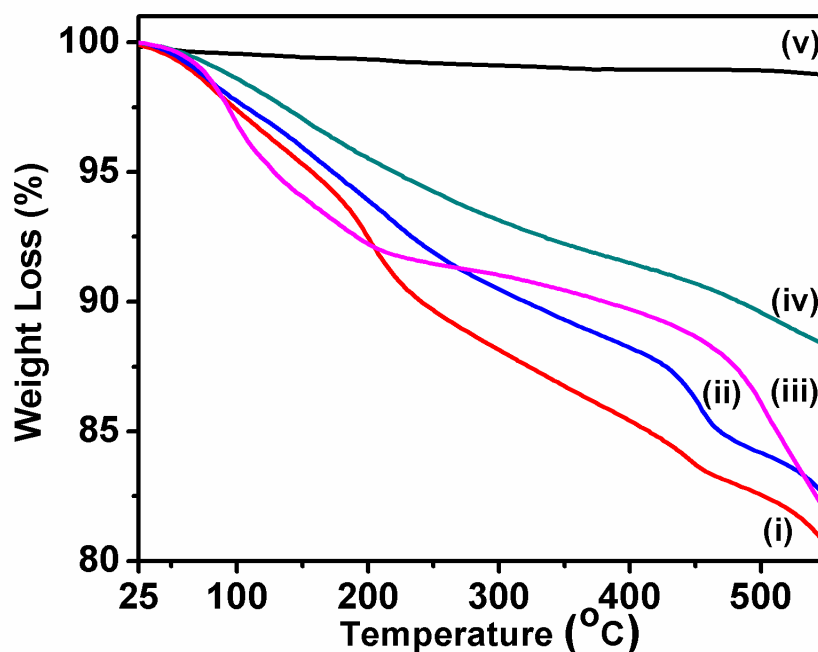


Fig 4a.11: Thermogravimetric (TGA) profiles of (i) K- α -CrO(OH), (ii) α -CrO(OH), (iii) K- γ -CrO(OH), (iv) γ -CrO(OH) and (v) Cr₂O₃

Table 4a.3: Calculated weight loss of the samples obtained from TGA.

Sr No	Catalyst	Weight Loss from TGA (%) at various temperature ranges (°C)					Weight loss due to surface hydroxyl groups 150-350 °C (%)	Total weight loss @ 350 °C (%)
		25-150	150-200	200-250	250-300	300-350		
1.	K- α -CrO(OH)	4.83	2.92	2.67	1.47	1.40	8.48	13.31
2.	α -CrO(OH)	4.09	1.98	2.04	1.43	1.21	6.68	10.77
3.	K- γ -CrO(OH)	5.93	1.82	0.78	0.44	0.65	3.71	9.64
4.	γ -CrO(OH)	2.94	1.56	1.31	1.01	1.02	4.91	7.85
5.	Cr ₂ O ₃	0.63	0.09	0.15	0.12	0.08	0.45	1.08

Surface hydroxyl groups could be in equilibrium with O⁻ ions and exhibit basic property. To conclusively prove the presence of anionic sites, we performed fluorescence studies of dye adsorbed on K- α -CrO(OH) and α -CrO(OH). Rhodamine 6G (Rh-6G), a positively charged dye is routinely used to probe anionic molecules. [43] Specifically, the adsorption of Rh-6G on deprotonated hydroxyl groups of graphene may be detected using fluorescence spectroscopy. [44] The samples were stirred in Rh-6G solution for 3h and then filtered using syringe filter before analyzing the fluorescence of the dye ($\lambda_{ex} = 500\text{nm}$ and $\lambda_{em} = 568\text{nm}$). The intensity of the fluorescence of the Rh-6G solution that had CrO(OH) samples in it was compared with that of the standard Rh-6G solution. It was observed that the intensity of fluorescence of Rh-6G decreased strongly indicating the adsorption of the dye on the negatively charged surface of the CrO(OH) samples due to electrostatic interactions [45-46] (Fig 4a.12c). The complex K- α -CrO(OH) with surface-adsorbed Rh-6G was completely dried on rotavap and its infrared spectrum was recorded (Fig 4a.13). On comparing the IR patterns of K- α -CrO(OH)-Rh-6G complex with bare K- α -CrO(OH) and Rh-6G, a shift in the -OH stretching frequency of the surface -OH groups (non-deprotonated) was observed from 3247 cm⁻¹ to 3452 cm⁻¹ in the case of K- α -CrO(OH)-Rh-6G complex (Fig 4a.13a). Interestingly, a slight shift in the C-N stretching of Rh-6G from 1347 cm⁻¹ to 1321 cm⁻¹ in the fingerprint region of Rh-6G-K- α -CrO(OH) complex was also observed (Fig 4a.13b). [47]

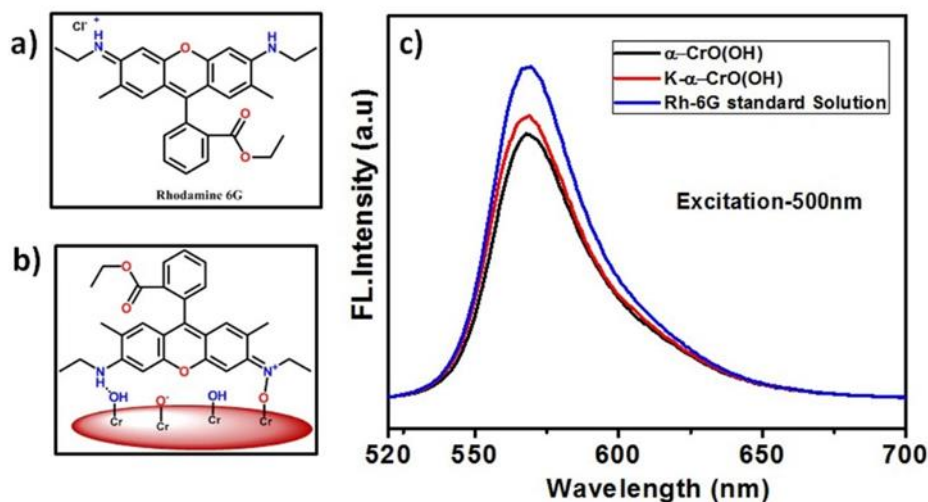


Fig 4a.12: a) Structure of Rhodamine 6G b) Interaction of Rh-6G with CrO(OH) surface c) Fluorescence spectroscopy for standard Rh-6G sample and K- α -CrO(OH), α -CrO(OH) adsorbed solutions

These interactions are graphically represented in Fig 4a.12b. These results were consistent with those observed for Rh-6G-graphene oxide and strongly proving the presence of O^{2-} and O^- sites.[44] In the context of the present work, it must be considered that in comparison to K-doped-CrO(OH), the K-free analogues of the polymorphs have also shown high activity in the condensation reactions. Therefore, K-free analogues of CrO(OH) has intrinsic O^- basic active sites, arising from the deprotonation of surface -OH groups, necessary for catalyzing the condensation reaction.

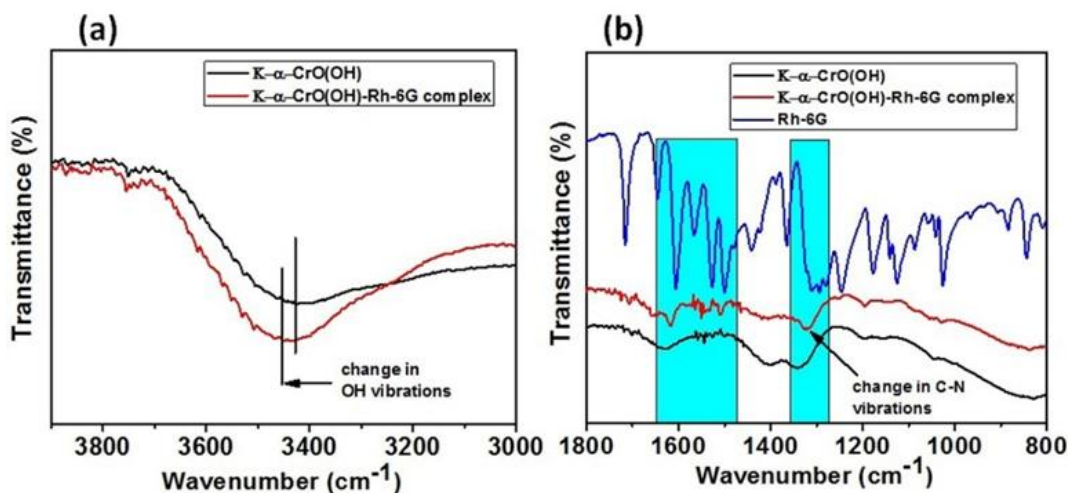
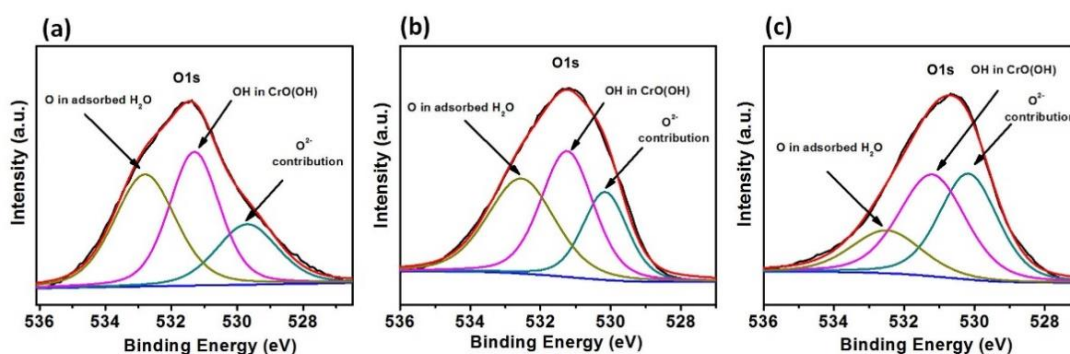


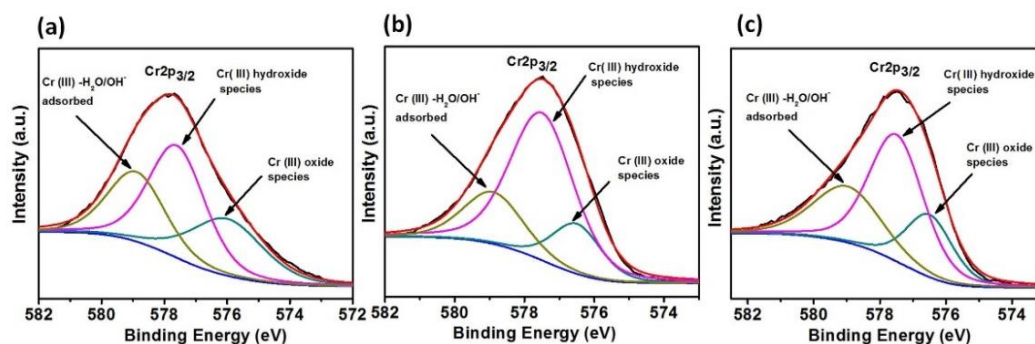
Fig 4a.13: Comparative FT-IR spectra of K- α -CrO(OH)-Rh-6G with bare K- α -CrO(OH) and Rh-6G in two different regions a) & b)

Interestingly, deconvoluted Cr2p_{3/2} XPS spectra of K- α -CrO(OH) in Fig 2c, clearly shows that Cr³⁺ bonded O⁻ species at BE 577.6 eV having a larger contribution to the signal (52%) as compared to the contribution from Cr(III) bonded to O²⁻ at BE 576.4 eV (25%). The contributions of O⁻ species in α -CrO(OH), γ -CrO(OH) and K- γ -CrO(OH) as compared to O²⁻ species (Fig 4a.14) showed similar trends confirming that the O⁻ species were more in density in all the samples. Studies on hydroxylated MgO catalysts have shown that the formation of C-C and C-N linkages are catalyzed by both Brønsted basic sites (O⁻) and Lewis basic (O²⁻) sites.[48] Importantly, Brønsted basic sites (O⁻) are more active than the Lewis basic counterparts (O²⁻). [49] Based on the evidence from CO₂-TPD, CO₂-FT-IR, TGA and XPS, one can conclude that Brønsted sites O⁻ are the major active basic sites for catalyzing the condensation reaction in K-free and K-doped analogues of CrO(OH). However, doping of K increases the concentration of Lewis basic O²⁻ which further increases activity of the catalysts.



Sr.No	Catalyst	O ²⁻ contribution (530.2eV) (%)	OH in CrO(OH) species (531.4 eV) (%)	O in adsorbed H ₂ O (532.4 eV) (%)
1.	α -CrO(OH)	22	38	40
2.	K- α -CrO(OH)	32	34	36
3.	γ -CrO(OH)	23	39	38
4.	K- γ -CrO(OH)	39	37	24

Fig 4a.14: Deconvoluted O1s spectra of a) α -CrO(OH) b) γ -CrO(OH) c)K- γ - CrO(OH) with the calculated contributions of different Cr(III) species



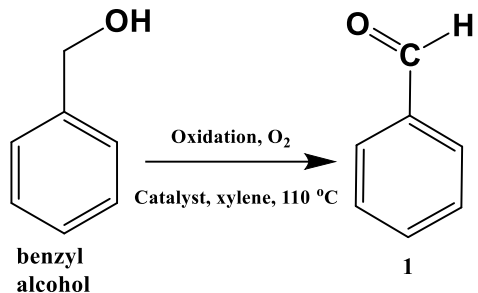
Sr.No	Catalyst	Cr(III)- H ₂ O/OH adsorbed (579.0 eV) (%)	Cr(III) hydroxide species (577.6 eV) (%)	Cr(III) oxide species (576.4 eV) (%)
1.	α -CrO(OH)	28	45	27
2.	K- α -CrO(OH)	23	52	25
3.	γ -CrO(OH)	20	63	17
4.	K- γ -CrO(OH)	28	51	21

Fig 4a.15: Deconvoluted Cr_{2p_{3/2}} spectra of a) α -CrO(OH) b) γ -CrO(OH) c) K- γ - CrO(OH) with the calculated contributions of different Cr(III) species

4a.2.3.2: Oxidation property of K- α -CrO(OH)

Presence of Cr(III) from XPS studies prompted us to test the oxidation ability of K- α -CrO(OH). Oxidation of benzyl alcohol to benzaldehyde (1) using K- α -CrO(OH) was studied and the details are presented in Table 4a.4. Xylene was chosen as the preferred solvent for oxidation of alcohol, due to its non-polar nature. When 1 mmol of benzyl alcohol was used with 0.1 g of K- α -CrO(OH) (benzyl alcohol to K- α -CrO(OH) weight ratio = 1.08) 64% conversion was achieved under O₂ atmosphere at 110 °C (Entry 2) after 15h. When the catalyst amount was increased to 0.4 g (benzyl alcohol to K- α -CrO(OH) weight ratio = 0.27) 100% conversion and 95% selectivity to benzaldehyde was achieved in 15 h (Table 4a.4, Entry 3).

Table 4a.4: Table showing the catalytic activity of K- α -CrO(OH) and other catalysts for benzyl alcohol oxidation

				
Entry	Catalyst	Catalyst amount (g)	Conversion (%)	GC Selectivity (%) [‡]
1	No catalyst	-	0	-
2	K- α -CrO(OH)	0.1	64	99
3	K- α -CrO(OH)	0.4	100	95
4	α -CrO(OH)	0.4	83	96
5	γ -CrO(OH)	0.4	24	98
6	K- γ -CrO(OH)	0.4	38	96
7	Cr ₂ O ₃	0.4	14	90

Reaction conditions: Benzyl alcohol (1 mmol), xylene (5mL), 110 °C, Time of reaction = 15h, [‡]Apart from benzaldehyde, we also observed benzoic acid and benzyl benzoate as side products in low yields.

In comparison, α -CrO(OH) gave a conversion of 83% in 15 h due to the absence of K (Table 4a.4, Entry 4). Similar to the basicity trend, the promotion of oxidation due to K is also more pronounced in α -CrO(OH) than in γ -CrO(OH) (Table 4a.4, Entries 5 and 6). The promotion of oxidation using K doping occurs via the creation of O²⁻ centres on the surface. The role of O²⁻ has been discussed in the context of oxidation of toluene using K-doped vanadia catalysts. [50-52] Most of the literature on tandem reactions involving oxidation reaction of benzyl alcohol reported the use of noble metals such as Pd and Au. It is important to note that 100% conversion of benzyl alcohol was achieved without the use of any expensive noble metal in our case.

Cyclic voltammetry studies were performed for all the samples in 0.5 M H₂SO₄ electrolyte to probe the surface-active oxidation sites (Fig 4a.16). The potential values at which the peaks were obtained suggests the oxidation of Cr²⁺ to Cr³⁺ and subsequent reduction process (from Cr³⁺ to Cr²⁺). As can be observed from the cyclic voltammograms, prominent peaks for oxidation and reduction are at ~0.32 V and ~0.43V, respectively, in the case of α -CrO(OH), K- α -CrO(OH) γ -CrO(OH) and K- γ -CrO(OH) signifying their better reversible redox property. The redox peaks and subsequent potential values in case of all the samples have been found to be consistent and show little deviation which suggests that only chromium species are involved in the reaction. Importantly, smaller FWHM value may be correlated to its faster charge transfer kinetics (i.e. better reduction-oxidation property) in response to the applied potential sweep rate. Though the catalytic property is explicitly shown by the chromium species, the current response in terms of FWHM value and reversibility are significantly influenced by the K- doping. Here, it is expected that both α - and γ -CrO(OH) to show significant change in their electrochemical activities when doped with potassium. In our system, where 0.5 M H₂SO₄ has been taken as an electrolyte, a change in the redox property of both the species (α - and γ -) can be observed. The improved redox property of the K-doped α -species over its pristine counterpart can be observed in terms of the prominent redox couple of the doped species from the obtained cyclic voltammetry data which signifies faster charge transfer rate. In the pristine α -species however, such redox peaks are absent. This might be due to slower kinetics at the catalyst surface resulting in sluggish charge transfer (during oxidation) and subsequent recovery (or reduction). Furthermore, if the cyclic voltammetry data of both K- α -CrO(OH) and γ -CrO(OH) (Fig.s 4a.16, b and c) are compared, there are no visible differences between the curves if slower scan rates (i.e., 10 and 50 mV/s) are considered. However, at a scan rate of 100 mV/s, redox couples generated from K- α -CrO(OH) are more prominent than those obtained from γ -CrO(OH), which suggests its faster current response and better surface kinetics. The ΔE_P values for K- α -CrO(OH), γ -CrO(OH), and Cr₂O₃ samples were calculated to be 72, 75, and 71 mV, respectively. The values are more or less similar for all the three samples, but are greater than the standard reversible ΔE_P value of ~59 mV, thus indicating a quasi-reversible reduction-oxidation process.

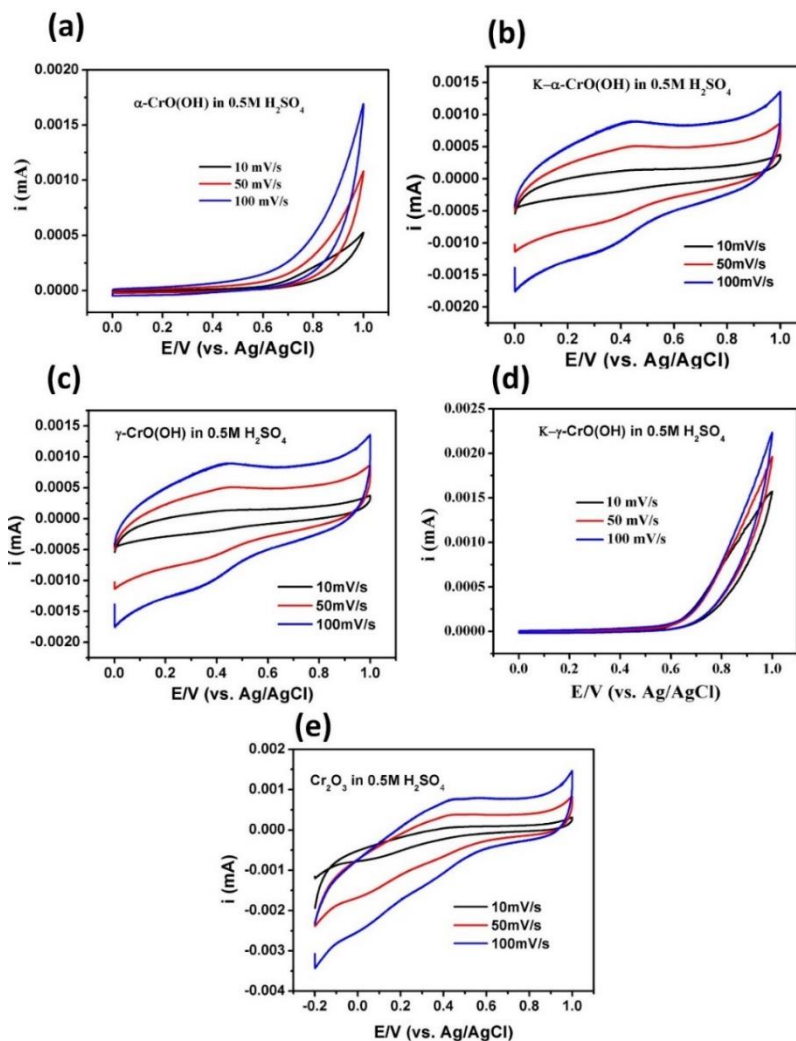


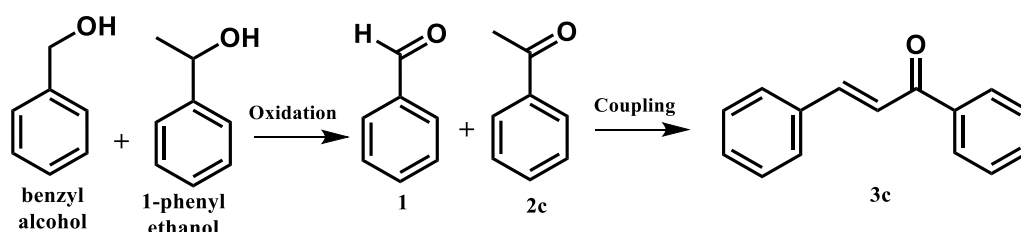
Fig 4a.16: Cyclic Voltammograms of a) α -CrO(OH) b)K- α - CrO(OH) c) γ -CrO(OH) d)K- γ -CrO(OH) e) Cr_2O_3

However, the FWHM value of K- α -CrO(OH) has been found to be the lowest among the three, suggesting its comparatively better charge-transfer kinetics. The ECSA (electroactive surface area) values of K- α -CrO(OH), γ -CrO(OH), and Cr_2O_3 samples were ~ 1.68 , ~ 1.33 , and ~ 1.23 respectively. A comparatively higher value of ECSA, in the case of the K-doped sample, signifies its better electrochemical interaction with the electrolytic content. From the detailed analysis of the voltammograms, the redox activity of the K- α -CrO(OH) was found to be at least 3 fold higher than that of γ -CrO(OH) and K- γ -CrO(OH). This was calculated by taking into consideration, both the electrochemical accessible surface area and the current response values at the redox peaks for each sample. This can be correlated to the significant impact of K-doping on the selectivity of a catalyst in the reaction (primarily due to the chemical structure/composition) in a given electrolytic medium (here acidic). The CrO(OH) showed strikingly different current responses in our controlled

environment (in an acidic electrolytic medium), as α - and γ -CrO(OH) have contrasting physical and chemical properties. [53] Though, γ -species were found to be electrochemically active in 0.5 M H₂SO₄, the anomaly in the same after K-doping needs further analyses in several pH-controlled environments in order to establish its selectivity. However from the cyclic voltammetry studies, we can definitely establish better redox behavior of K- α -CrO(OH) compared to other controls.

4a.3.2.3: Bifunctional activity of K- α -CrO(OH)

Having shown that K- α -CrO(OH) can independently catalyze the oxidation and base catalyzed condensation/coupling reactions and probing the active sites, we proceeded to couple these two steps in a single pot reaction. The sequential conversion of benzyl alcohol to **3** over K- α -CrO(OH) was carried out without separating any intermediates and the results are shown in Table 4a.5. The alcohol oxidation was allowed to take place for 15h followed by the addition of malononitrile. This was done to ensure malononitrile (**2a**) and ethylcyanoacetate (**2b**) do not inhibit the oxidation of benzyl alcohol by blocking the active sites. As seen in entry 6, the conversion was just 20% when ethylcyanoacetate was present from the start of the reaction. α -CrO(OH) naturally showed a lower selectivity of 81% to **3a** (Table 4a.5, Entry 2). Conversions shown by γ -CrO(OH) and K- γ -CrO(OH) were lower than that observed for K- α -CrO(OH) (Table 4a.5, Entries 3, 4). One of the reasons could be the nano-sheet morphology of α -CrO(OH) and K- α -CrO(OH) as compared to γ -CrO(OH) and K- γ -CrO(OH), leading to difference in accessibility of substrate to the active sites on the catalyst surface. Oxidative cross coupling between benzyl alcohol and 1-phenyl ethanol (Scheme 4a.2) required 48 h for 100% conversion of benzyl alcohol with 92% selectivity to (**3c**) (Table 4a.5, Entry 7) with both the reactants present from the start of the reaction.



Scheme 4a.2: Two oxidations followed by a coupling reaction in one pot to yield **3c**

However, lowering the time to 24 h, gave just 62% conversion (Table 4a.5, Entry 8). The formation of N-benzylidene aniline (**3d**) was 95% when benzyl alcohol and **2d** were reacted for 24 h in the presence of K- α -CrO(OH) as the catalyst. Thus, K- α -CrO(OH) showed a great promise with high selectivity and conversion for oxidative condensation/coupling reactions.

Table 4a.5: Table showing the catalytic activity of K- α -CrO(OH) and other catalysts for one-pot tandem Oxidation- Knoevenagel Condensation / Coupling reaction

Entry	Catalyst	Time $t_{ox} + t_{con}$ (h)	Conversion of benzyl alcohol (%)	GC Selectivity (%)	
				1	3 [¶]
1	K- α -CrO(OH)	15+1	100	5	(3a)95(89)
2	α -CrO(OH)	15+1	83	19	(3a)81
3	γ -CrO(OH)	15+6	26	4	(3a)96
4	K- γ -CrO(OH)	15+6	38	3	(3a)99
5	K- α -CrO(OH)	15+1	100	8	(3b)92(80)
6	K- α -CrO(OH) ‡	15	20	4	(3b)96
7	K- α -CrO(OH)*	48	100	4	(3c)92(82)
8	K- α -CrO(OH)*	24	62	22	(3c)78
9	K- α -CrO(OH)	24	100	5	(3d)95(87)

Reaction conditions: Weight of the catalyst is 0.4 g, 1 mmol of benzyl alcohol, 2 mmol of **2**, 5 mL of xylene, 110 °C ‡ethylacynoacetate (**2b**) was present from the beginning of the reaction.*Reactant **2** was 1-phenylethanol. Oxidation carried out in the presence of O₂ balloon. For Entries 1-3, t_{ox} : time for oxidation reaction, t_{con} : time for Knoevenagel condensation. For remaining entries it is the total time of reaction. The products were isolated by column chromatography and characterized by ¹H and ¹³C NMR. ¶Isolated yields presented in parenthesis.

A time-dependent study of the reaction to yield **3a**, **3c** and **3d** was carried out. Fig 4a.17a shows a trace of concentration of the reactants and products during the course of complete reaction. In this case, malononitrile was added after 15h of the start of the reaction. The time was determined based on prior studies probing the completion of the oxidation reaction. Fig 4a.17a (ii) shows the expanded portion of the dotted rectangle in (i) showing the time-dependent formation of **3a**. Fig 4a.17b shows the trace of benzyl alcohol and benzaldehyde along with the formation of **3c**. In 18 h, 80% of benzyl alcohol was converted with 40% selectivity to **3c**. This indicated formation of **3c** was slow at the start of the reaction from **1**. This is because acetophenone (**2c**) was not readily available to react with benzaldehyde and needed to be produced by oxidation of 1-phenylethanol which was the other reactant along with benzyl alcohol (Scheme 4a.2). Thus, K- α -CrO(OH) was used as a catalyst to carry out oxidation of two different substrates and their condensation in a single pot. Despite three reactions occurring in tandem, we achieved a high yield of 92% of **3c** with complete conversion of benzyl alcohol. Fig 4a.17c shows the formation of **3d** from benzyl alcohol and aniline. In 24h, the reaction was completed with 95% yield of **3d**.

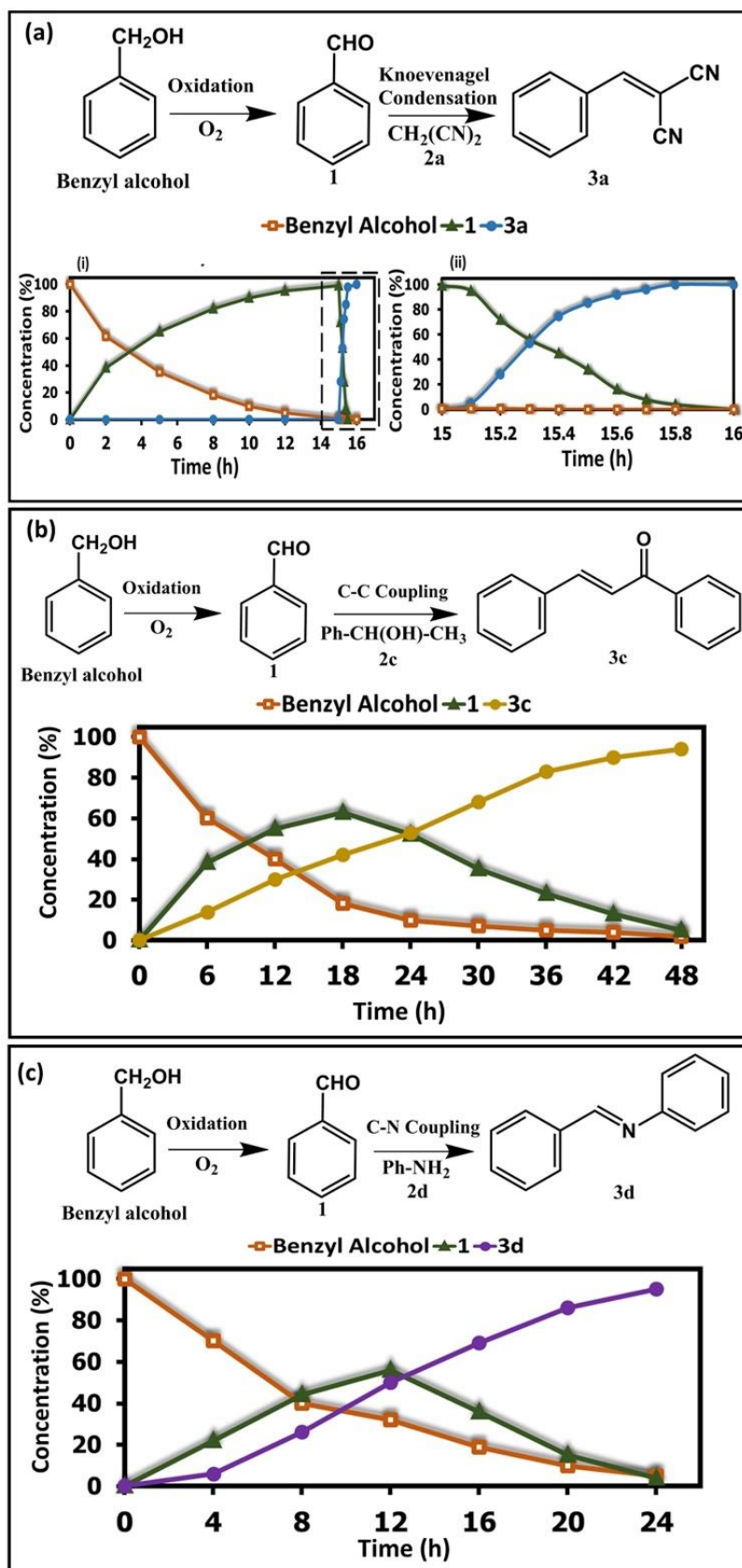
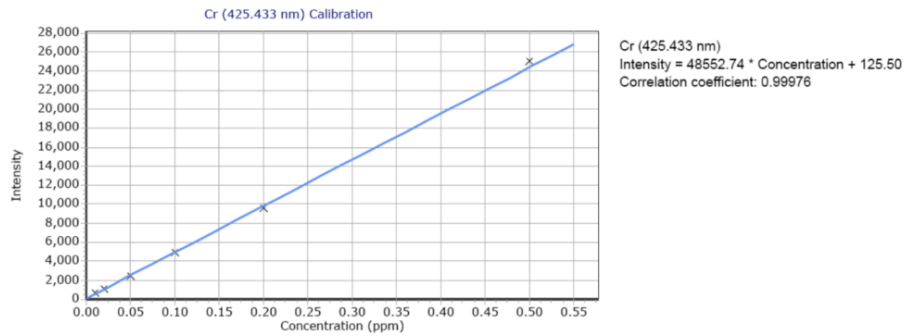


Fig 4a.17: Time dependent study for K- α -CrO(OH) to yield a) **3a** (ii) is an expanded area of (i) after addition of malononitrile b) to yield **3c** c) to yield **3d**

4a.3.3: Potential Toxicity and Leaching studies

Hexavalent chromium Cr(VI) is proven to be hemotoxic, genotoxic, and carcinogenic. [54] Interestingly, chromium (III) is needed as a trace mineral for human nutrition for glucose metabolism [55] and is generally stable and not easily absorbed in the body by any route. Hence, the toxicity of chromium is mainly attributable to Cr(VI). Our materials K- α -CrO(OH), α -CrO(OH) γ -CrO(OH) and Cr₂O₃ are all in Cr(III) state. The experimental reduction of Cr(VI) to lower oxidation states is termed as a detoxification process [54] which is actually utilized in our synthesis of K- α -CrO(OH). Nevertheless, leaching of Cr(III) species during the reaction into the solvent must be avoided at any cost as it can get re-oxidized to Cr(VI) due to natural processes. Hence, microwave plasma atomic emission spectroscopy (MP-AES) analysis of the filtrate was done to test any leaching of Cr(III) species. After 48h refluxing to yield **3c** from benzyl alcohol, the catalyst was removed from the filtrate using a syringe filter and the resultant filtrate was analyzed using MP-AES technique. The calibration plots and the MP-AES data are given in Fig 4a.18. The filtrate did not show any presence of Cr(III)/Cr(VI) whatsoever within the detection limits of the instrument (Sample 1, Fig 4a.18). This is a very important result indicating no leaching of Cr(III) species into the solvent during the reaction. However, the leaching of Cr(III) in the case of other solvents needs further studies.

a) Calibration Curves



Standards	Intensity	Method Concentration	Actual Concentration	% Error
Blank	0.00	0.00	0.00	N/A
Standard 1	735.03	0.01	0.01	0.00
Standard 2	1155.26	0.02	0.02	0.00
Standard 3	2501.42	0.05	0.05	0.00
Standard 4	4920.90	0.10	0.10	0.00
Standard 5	9600.37	0.20	0.20	0.00
Standard 6	25020.43	0.50	0.51	2.00

b) ICP data

Label	Date Time	Element Label (nm)	Concentration	Unit	SD	%RSD
Blank	9/13/2016 14:19:05	Cr (425.433 nm)	0.00	ppm	N/A	N/A
Standard 1	9/13/2016 14:19:56	Cr (425.433 nm)	0.01	ppm	N/A	N/A
Standard 2	9/13/2016 14:20:45	Cr (425.433 nm)	0.02	ppm	N/A	N/A
Standard 3	9/13/2016 14:21:35	Cr (425.433 nm)	0.05	ppm	N/A	N/A
Standard 4	9/13/2016 14:22:27	Cr (425.433 nm)	0.10	ppm	N/A	N/A
Standard 5	9/13/2016 14:23:18	Cr (425.433 nm)	0.20	ppm	N/A	N/A
Standard 6	9/13/2016 14:24:08	Cr (425.433 nm)	0.50	ppm	N/A	N/A
Sample 1	9/13/2016 14:25:59	Cr (425.433 nm)	0.00	ppm	0.00	4.75

Fig 4a.18: Microwave plasma atomic emission spectroscopy results for leaching studies

4a.3.4: Recyclability and Comparison with state of art catalysts

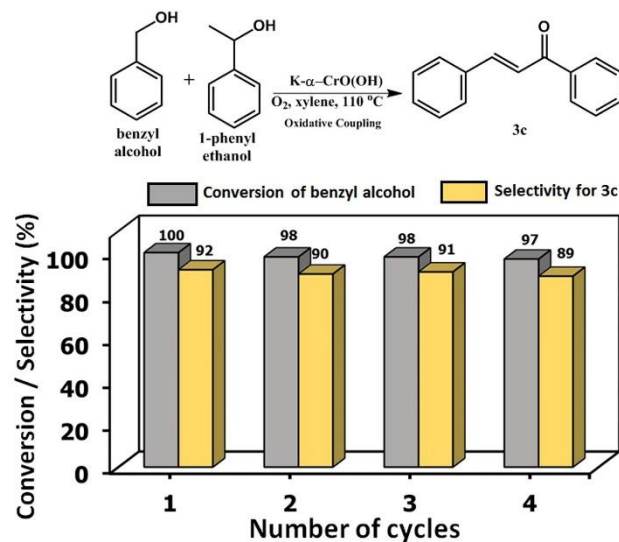


Fig. 4a.19: Recyclability of K- α -CrO(OH) for one pot oxidative coupling reaction to give 3c

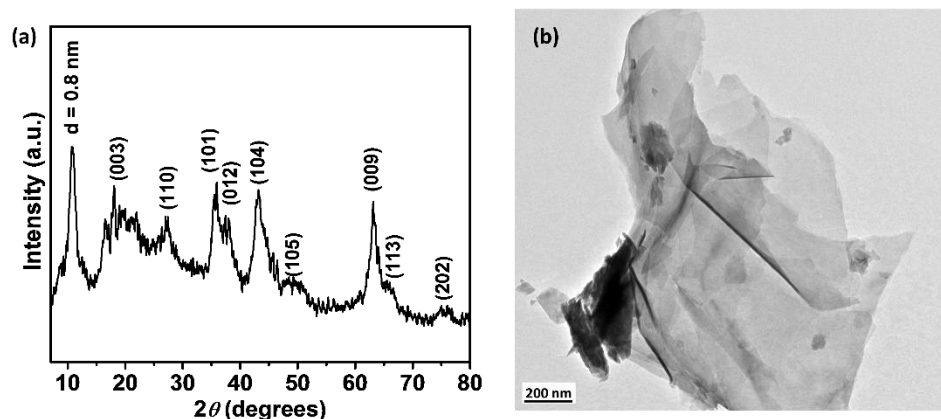


Fig. 4a.20: a) XRD and b) TEM image of used K- α -CrO(OH).

The catalyst was recycled over three cycles for the oxidation-coupling reaction between benzyl alcohol and 1-phenylethanol without appreciable loss in activity as seen in Fig. 4a.19. XRD and TEM of used catalyst after oxidation-coupling reaction did not show any significant changes from the fresh catalysts as seen from Fig. 4a.20. Thus K- α -CrO(OH) acts as a stable catalyst under the reaction conditions.

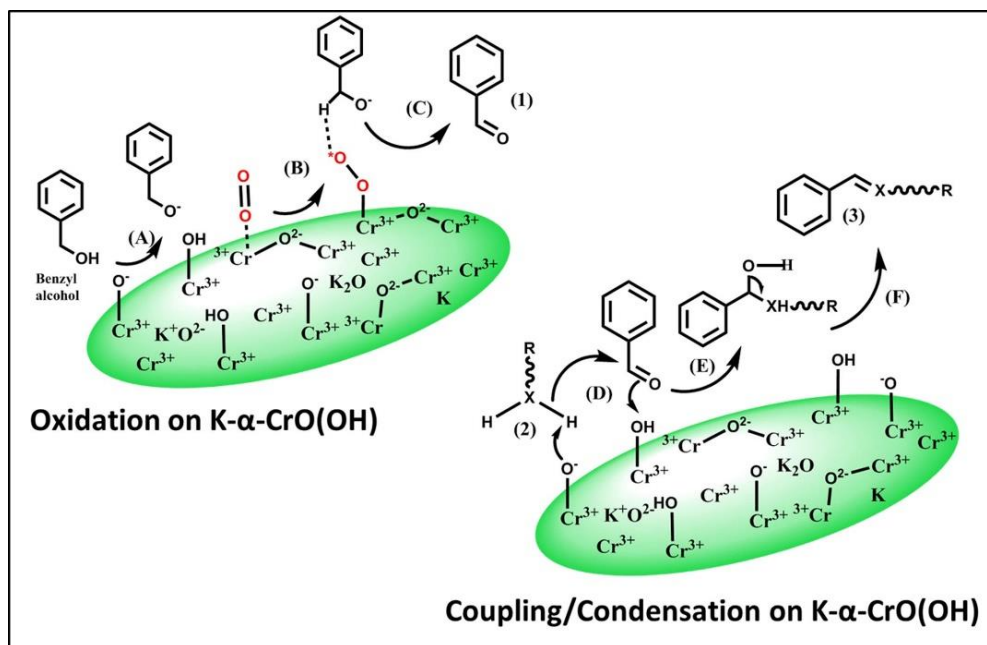
Table 4a.6: Comparing the different catalysts and conditions used in literature for one-pot oxidation coupling reactions

Sr No	Catalyst	Desired product	Reaction Conditions	Reference
1	Au@Cu(II)-MOF	3a	toluene, 110 °C, 22h	[15]
2	Pd(0)@UiO-68-AP	3a,3b	toluene, 80 °C, 38h,	[16]
3	Tris-LDH-X ₄ (PW ₉) ₂	3b	acetonitrile, H ₂ O ₂ , 80 °C, 6h	[21]
4	CeO ₂	3c	p-xylene, 150 °C, 12h	[22]
5	CeO ₂	3d	mesitylene, 60 °C, 48h	[23]
6	Pd/AlOOH	3c	toluene, K ₃ PO ₄ , 80 °C, 20h	[12]
7	Pd-Au@Mn(II)-MOF	3d	toluene, 110 °C, 24h	[19]
8	Cu _x Ag _{1-x} /HT	3c	xylene, 150 °C, 1h	[18]
9	Pt-Sn/C-Al ₂ O ₃	3c	xylene, K ₃ PO ₄ , 155 °C, 48h	[14]
10	Pd-Si-Pr-NiXantphos/SiO ₂	3c	mesitylene, LiOH, 100 °C, 24h	[13]
11	Au-Pd/HT	3c	xylene, 120 °C, 5h	[17]
12	Co-N-C	3c	H ₂ O/t-BuOH, LiOH, 70 °C, 24h	[20]
13	Ag-Al ₂ O ₃	3c	toluene, Cs ₂ CO ₃ , 115 °C, 24h	[11]
14	K- α -CrO(OH)	3a,3b,3c,3d	xylene, 110 °C, 24-48h	This work

Table 4a.6 shows various heterogenous catalysts used for one-pot tandem oxidation-condensation/coupling reactions and the conditions under which the reaction is performed to attain maximum conversion. One can clearly observe that noble metals are commonly preferred to carry out the oxidation step (Entries 1-3, 6-11, 13). The use of soluble bases is also prevalent in most works (Entries 6, 9, 10, 12 and 13). Polyoxometalates (Entry 3) CeO₂ and Co-N-C are rare examples (Entries 4, 5, 12). K- α -CrO(OH) is a promising noble metal free and base free catalyst to attain maximum conversion under similar reaction conditions. The combined role of the reactivity of Cr(III) and surface -OH for tandem reactions is explored for the first time with comparable activities with those reported in literature.

A proposed reaction mechanism on K- α -CrO(OH) is depicted in Scheme 4a.3. Step A involves the proton removal from benzyl alcohol over deprotonated surface hydroxyl groups (O⁻) of K- α -CrO(OH). Activation of O₂ molecule takes place over Cr(III) sites in Step B. Benzaldehyde (1) is formed in step C. The deprotonated hydroxyl groups (O⁻) activate the methylene groups of the reactants (2)

by abstraction of proton in Step D and ably supported by O^{2-} ions. Step E involves the attack of the nucleophile to the carbonyl carbon of benzaldehyde and subsequent formation of the desired product (3) by loss of water molecule in Step F.

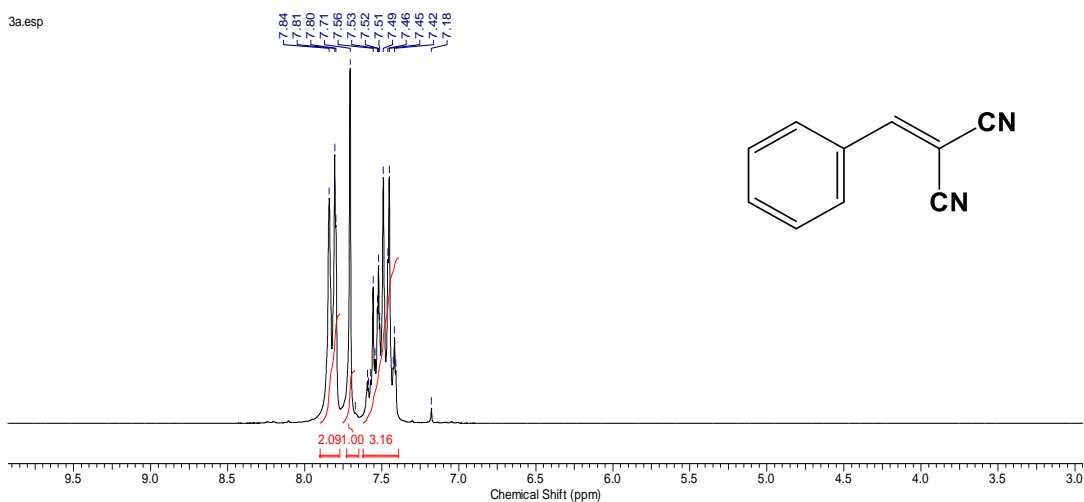


Scheme 4a.3: Proposed reaction mechanism occurring on K- α -CrO(OH) *Oxidation:* A) deprotonation of Benzyl alcohol B) oxygen activation on Cr(III) of K- α -CrO(OH) C) formation of Benzaldehyde (1). *Coupling/Condensation:* D) proton abstraction of active methylene group (2) R=RXH= malononitrile, ethyl cyanoacetate, acetophenone, aniline E) attack of nucleophile on carbonyl carbon of benzaldehyde F) water loss to give the respective products (3)(3a, 3b, 3c, 3d). Activation of O_2 molecule takes place over Cr(III) sites in Step B. Benzaldehyde (1) is formed in step C. The deprotonated hydroxyl groups (O^-) activate the methylene groups of the reactants (2) by abstraction of proton in Step D and ably supported by O^{2-} ions. Step E involves the attack of the nucleophile to the carbonyl carbon of benzaldehyde and subsequent formation of the desired product (3) by loss of water molecule in Step F.

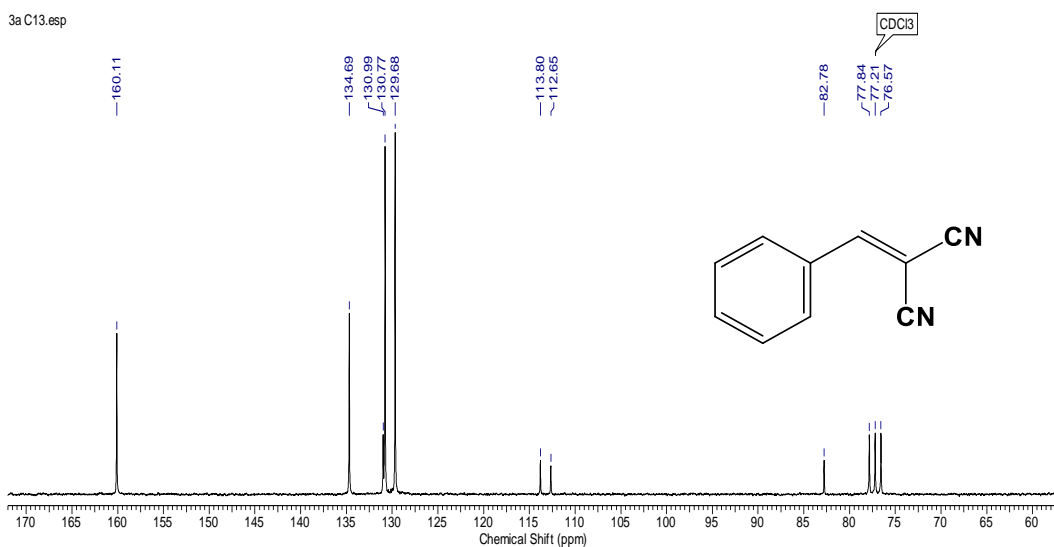
4a.4: Conclusions

The design and utility of K- α -CrO(OH) as a bifunctional catalyst was explored in sequential transformation of benzyl alcohol to a variety of C-C and C-N coupling products. The transformations were feasible because of the co-existence of redox Cr(III) and basic sites (O^- and O^{2-}) on the surface of the K- α -CrO(OH). The presence of electron rich sites (O^{2-}) due to doping of K and the surface hydroxyl groups were found to be the basic sites on the catalysts using spectroscopy and thermal probe studies. This being the first report on use of K- α -CrO(OH) in multifunctional catalysis, there is a promising scope to utilize this material for other catalytic transformations useful in fine chemical and pharmaceutical industries where multistep transformations are needed.

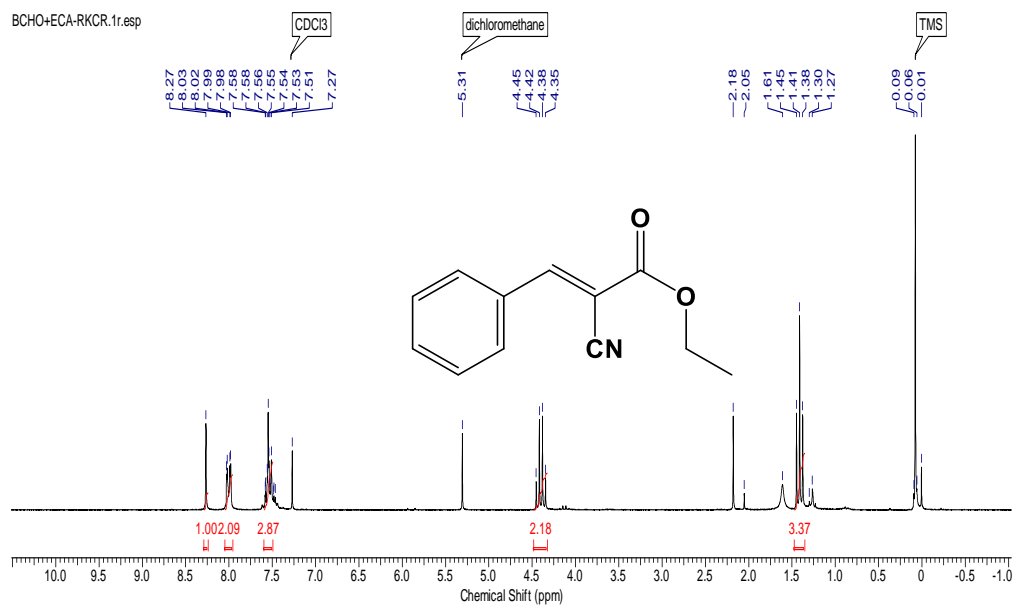
4a.5: NMR of isolated products



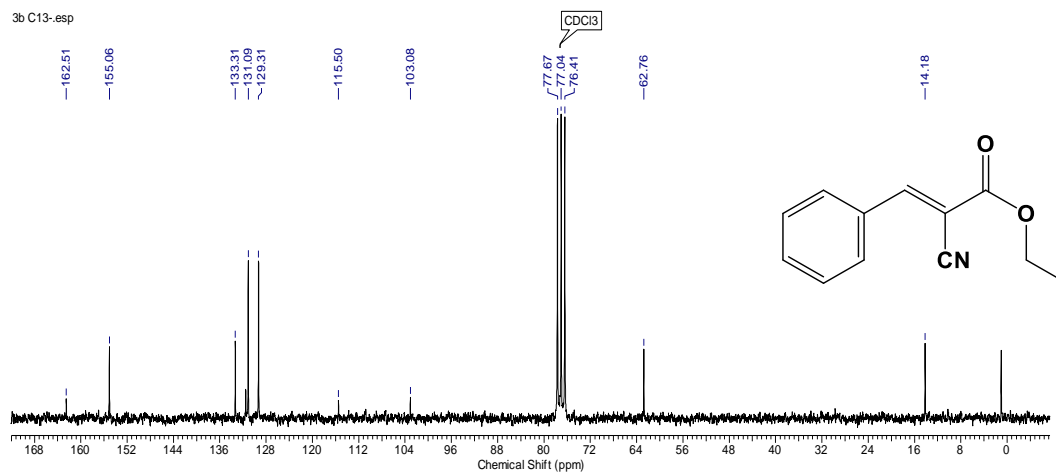
^1H NMR (200 MHz, CHLOROFORM-*d*) δ ppm 7.39 - 7.62 (m, 4 H) 7.71 (s, 1 H)
7.77 - 7.90 (m, 2 H)



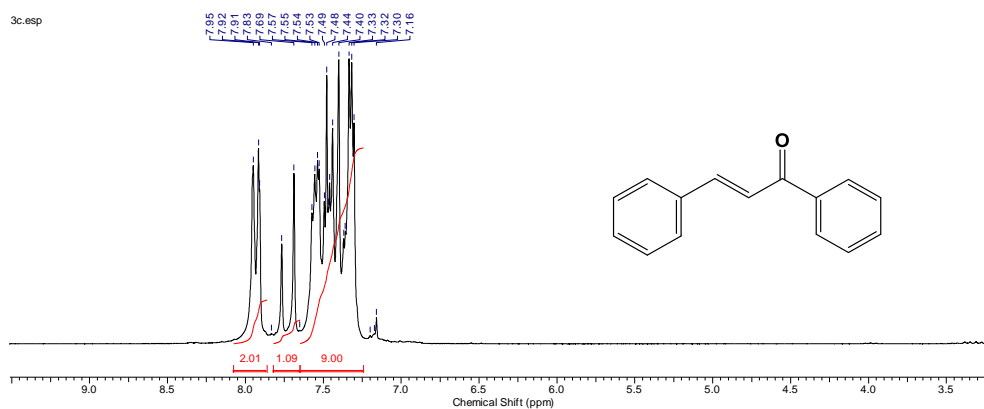
^{13}C NMR (50 MHz, CHLOROFORM-*d*) δ ppm 76.57 (s, 1 C) 77.21 (s, 1 C) 77.84
(s, 1 C) 82.78 (s, 1 C) 112.65 (s, 1 C) 113.80 (s, 1 C) 129.68 (s, 1 C) 130.77 (s, 1 C)
130.99 (s, 1 C) 134.69 (s, 1 C) 160.11 (s, 1 C)



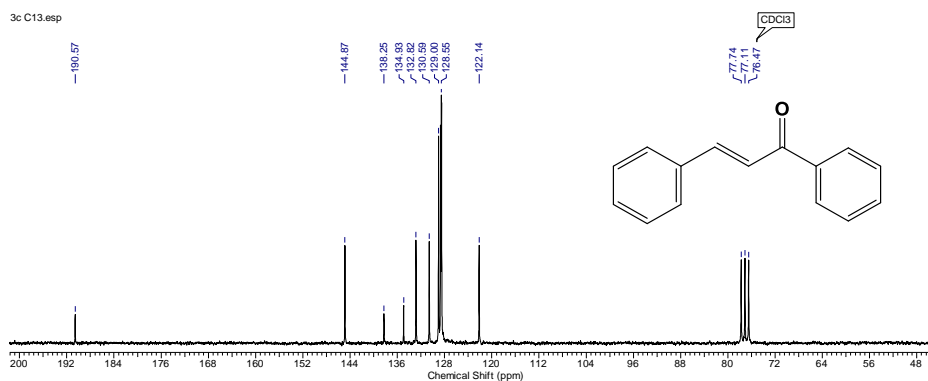
^1H NMR (200 MHz, CHLOROFORM-*d*) δ ppm 1.41 (t, $J=7.14$ Hz, 4 H) 4.40 (q, $J=7.20$ Hz, 2 H) 7.49 - 7.60 (m, 3 H) 8.00 (dd, $J=7.64, 1.71$ Hz, 2 H) 8.27 (s, 1 H)



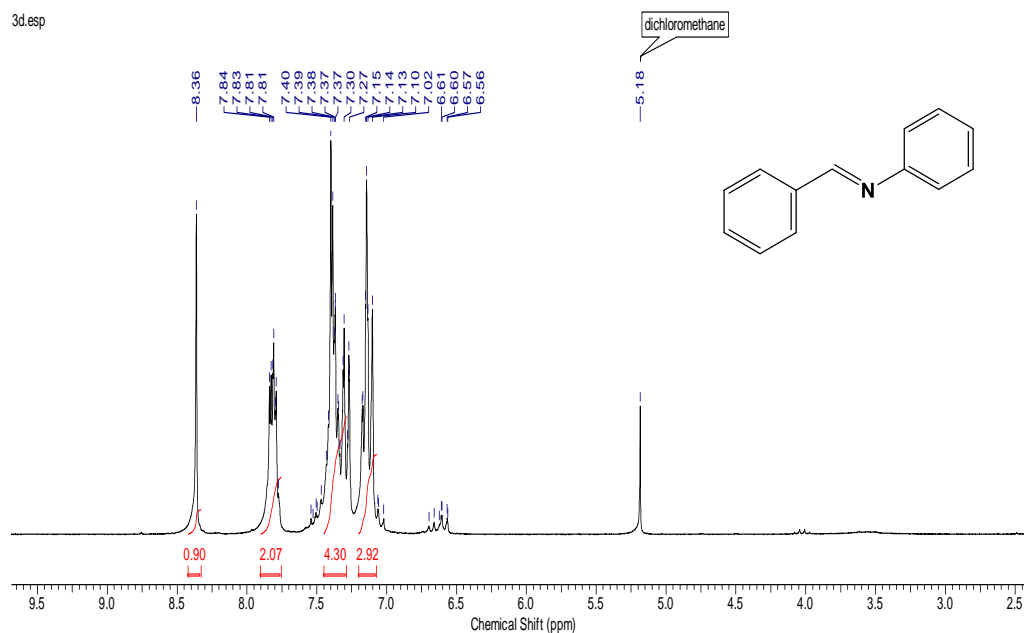
^{13}C NMR (50 MHz, CHLOROFORM-*d*) δ ppm 14.18 (s, 1 C) 62.76 (s, 1 C) 76.41 (s, 1 C) 77.04 (s, 1 C) 77.67 (s, 1 C) 103.08 (s, 1 C) 115.50 (s, 1 C) 129.31 (s, 1 C) 131.09 (s, 1 C) 133.31 (s, 1 C) 155.06 (s, 1 C) 162.51 (s, 1 C)



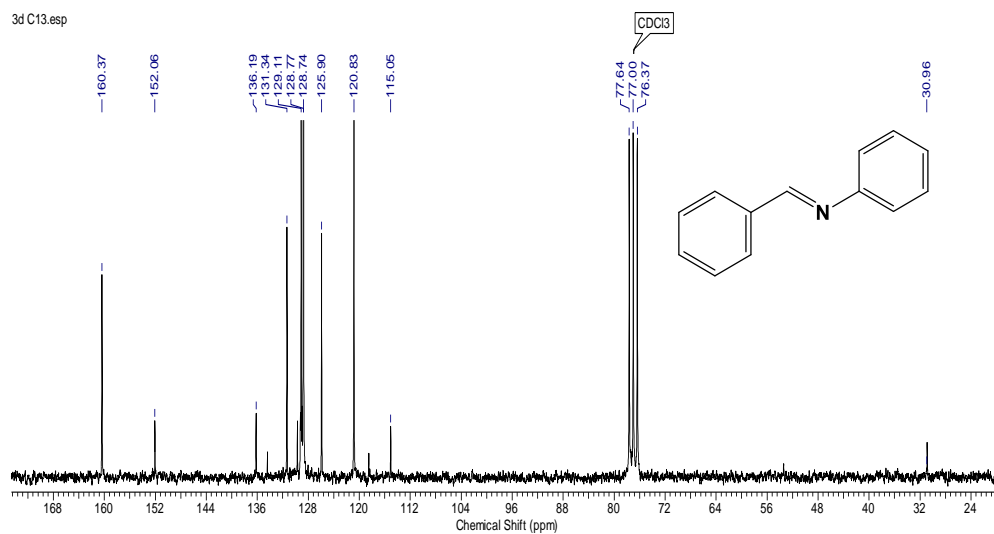
^1H NMR (200 MHz, CHLOROFORM-*d*) δ ppm 7.24 - 7.65 (m, 10 H) 7.65 - 7.82 (m, 1 H) 7.86 - 8.08 (m, 2 H)



^{13}C NMR (50 MHz, CHLOROFORM-*d*) δ ppm 76.47 (s, 1 C) 77.11 (s, 1 C) 77.74 (s, 1 C) 122.14 (s, 1 C) 128.55 (s, 1 C) 129.00 (s, 1 C) 130.59 (s, 1 C) 132.82 (s, 1 C) 134.93 (s, 1 C) 138.25 (s, 1 C) 144.87 (s, 1 C) 190.57 (s, 1 C)



^1H NMR (200 MHz, CHLOROFORM-*d*) δ ppm 7.07 - 7.20 (m, 3 H) 7.29 - 7.45 (m, 5 H) 7.75 - 7.90 (m, 2 H) 8.36 (s, 1 H)



^{13}C NMR (50 MHz, CHLOROFORM-*d*) δ ppm 30.96, 76.37 (s, 1 C) 77.64 (s, 1 C) 115.05 (s, 1 C) 120.83 (s, 1 C) 125.90 (s, 1 C) 128.74 (s, 1 C) 128.77 (s, 1 C) 129.11 (s, 1 C) 131.34 (s, 1 C) 136.19 (s, 1 C) 152.06 (s, 1 C) 160.37 (s, 1 C)

4a.6: References

- [1] K. Nicolaou, D. J. Edmonds and P. G. Bulger, *Angewandte Chemie International Edition*, 2006, **45**, 7134-7186.
- [2] V. Jeena and R. S. Robinson, *RSC Advances*, 2014, **4**, 40720-40739.
- [3] A. M. Faisca Phillips, A. J. Pombeiro and M. N. Kopylovich, *ChemCatChem*, 2017, **9**, 217-246.
- [4] M. J. Climent, A. Corma, S. Iborra and M. J. Sabater, *ACS Catalysis*, 2014, **4**, 870-891.
- [5] M. J. Matos, S. Vazquez-Rodriguez, E. Uriarte and L. Santana, *Expert Opinion on Therapeutic Patents*, 2015, **25**, 351-366.
- [6] V. Yerragunta, T. Kumaraswamy, D. Suman, V. Anusha, P. Patil and T. Samhitha, *PharmaTutor*, 2013, **1**, 54-59.
- [7] S. F. Martin, *Pure and applied chemistry. Chimie pure et appliquee*, 2009, **81**, 195-204.
- [8] D. Jagadeesan, *Applied Catalysis A: General*, 2016, **511**, 59-77.
- [9] N. A. Brunelli and C. W. Jones, *Journal of catalysis*, 2013, **308**, 60-72.
- [10] A. V. Biradar, V. S. Patil, P. Chandra, D. S. Doke and T. Asefa, *Chemical Communications*, 2015, **51**, 8496-8499.
- [11] K. i. Shimizu, R. Sato and A. Satsuma, *Angewandte Chemie*, 2009, **121**, 4042-4046.
- [12] M. S. Kwon, N. Kim, S. H. Seo, I. S. Park, R. K. Cheedraha and J. Park, *Angewandte Chemie*, 2005, **117**, 7073-7075.
- [13] T. T. Dang, S. P. Shan, B. Ramalingam and A. M. Seayad, *RSC Advances*, 2015, **5**, 42399-42406.
- [14] K. Wu, W. He, C. Sun and Z. Yu, *Tetrahedron Letters*, 2016, **57**, 4017-4020.
- [15] J.-S. Wang, F.-Z. Jin, H.-C. Ma, X.-B. Li, M.-Y. Liu, J.-L. Kan, G.-J. Chen and Y.-B. Dong, *Inorganic Chemistry*, 2016, **55**, 6685-6691.
- [16] Y.-A. Li, S. Yang, Q.-K. Liu, G.-J. Chen, J.-P. Ma and Y.-B. Dong, *Chemical Communications*, 2016, **52**, 6517-6520.
- [17] X. Liu, R. S. Ding, L. He, Y. M. Liu, Y. Cao, H. Y. He and K. N. Fan, *ChemSusChem*, 2013, **6**, 604-608.

- [18] J. Xu, H. Yue, S. Liu, H. Wang, Y. Du, C. Xu, W. Dong and C. Liu, *RSC Advances*, 2016, **6**, 24164-24174.
- [19] G.-J. Chen, H.-C. Ma, W.-L. Xin, X.-B. Li, F.-Z. Jin, J.-S. Wang, M.-Y. Liu and Y.-B. Dong, *Inorganic Chemistry*, 2017, **56**, 654-660.
- [20] L. Zhang, A. Wang, W. Wang, Y. Huang, X. Liu, S. Miao, J. Liu and T. Zhang, *ACS Catalysis*, 2015, **5**, 6563-6572.
- [21] K. Liu, Y. Xu, Z. Yao, H. N. Miras and Y. F. Song, *ChemCatChem*, 2016, **8**, 929-937.
- [22] M. Tamura and K. Tomishige, *Angewandte Chemie International Edition*, 2015, **54**, 864-867.
- [23] Z. Zhang, Y. Wang, M. Wang, J. Lu, C. Zhang, L. Li, J. Jiang and F. Wang, *Catalysis Science & Technology*, 2016, **6**, 1693-1700.
- [24] D. Vernekar and D. Jagadeesan, *Catalysis Science & Technology*, 2015, **5**, 4029-4038.
- [25] J. Low, S. Cao, J. Yu and S. Wageh, *Chemical Communications*, 2014, **50**, 10768-10777.
- [26] W. Ye, X. Fang, X. Chen and D. Yan, *Nanoscale*, 2018, **10**, 19484-19491.
- [27] Y. Li, L. Zhang, X. Xiang, D. Yan and F. Li, *Journal of Materials Chemistry A*, 2014, **2**, 13250-13258.
- [28] R. Gao and D. Yan, *Nano Research*, 2018, **11**, 1883-1894.
- [29] M. Arif, G. Yasin, M. Shakeel, X. Fang, R. Gao, S. Ji and D. Yan, *Chemistry – An Asian Journal*, 2018, **13**, 1045-1052.
- [30] Y.-L. Bai, H.-B. Xu, Y. Zhang and Z.-H. Li, *Journal of Physics and Chemistry of Solids*, 2006, **67**, 2589-2595.
- [31] J. Yang, A. G. Baker, H. Liu, W. N. Martens and R. L. Frost, *Journal of materials science*, 2010, **45**, 6574-6585.
- [32] P. Ratnasamy and A. J. Leonard, *The Journal of Physical Chemistry*, 1972, **76**, 1838-1843.
- [33] R. M. Cornell and U. Schwertmann, *The iron oxides: structure, properties, reactions, occurrences and uses*, John Wiley & Sons, 2003.
- [34] W. Wieland, R. Davis and J. Garces, *Catalysis today*, 1996, **28**, 443-450.

- [35] R. Sawyer, H. Nesbitt and R. Secco, *Journal of Non-Crystalline Solids*, 2012, **358**, 290-302.
- [36] P. Li, H.-B. Xu, S.-L. Zheng, Y. Zhang, Z.-H. Li and Y.-L. Bai, *Environmental science & technology*, 2008, **42**, 7231-7235.
- [37] N. Zafar Ali, J. Nuss and M. Jansen, *Zeitschrift für anorganische und allgemeine Chemie*, 2013, **639**, 241-245.
- [38] O. Seiferth, K. Wolter, B. Dillmann, G. Klivenyi, H.-J. Freund, D. Scarano and A. Zecchina, *Surface science*, 1999, **421**, 176-190.
- [39] M. W. Abee, S. C. York and D. F. Cox, *The Journal of Physical Chemistry B*, 2001, **105**, 7755-7761.
- [40] H. Hattori, *Applied Catalysis A: General*, 2001, **222**, 247-259.
- [41] X. Song and J.-F. o. Boily, *Environmental science & technology*, 2013, **47**, 9241-9248.
- [42] S. Musić, M. Maljković, S. Popović and R. Trojko, *Croatica chemica acta*, 1999, **72**, 789-802.
- [43] M. Beija, C. A. Afonso and J. M. Martinho, *Chemical Society Reviews*, 2009, **38**, 2410-2433.
- [44] H. Ren, D. D. Kulkarni, R. Kodiyath, W. Xu, I. Choi and V. V. Tsukruk, *ACS applied materials & interfaces*, 2014, **6**, 2459-2470.
- [45] D. Yan, J. Lu, L. Chen, S. Qin, J. Ma, M. Wei, D. G. Evans and X. Duan, *Chemical Communications*, 2010, **46**, 5912-5914.
- [46] D. Yan, J. Lu, M. Wei, D. G. Evans and X. Duan, *The Journal of Physical Chemistry B*, 2009, **113**, 1381-1388.
- [47] P. R. Griffiths and J. A. De Haseth, *Fourier transform infrared spectrometry*, John Wiley & Sons, 2007.
- [48] M.-L. Bailly, C. Chizallet, G. Costentin, J.-M. Krafft, H. Lauron-Pernot and M. Che, *Journal of Catalysis*, 2005, **235**, 413-422.
- [49] C. Chizallet, H. Petitjean, G. Costentin, H. Lauron-Pernot, J. Maquet, C. Bonhomme and M. Che, *Journal of Catalysis*, 2009, **268**, 175-179.
- [50] D. B. Bukur, D. Mukesh and S. A. Patel, *Industrial & engineering chemistry research*, 1990, **29**, 194-204.
- [51] D. A. Bulushev, L. Kiwi-Minsker, V. I. Zaikovskii, O. B. Lapina, A. A. Ivanov, S. I. Reshetnikov and A. Renken, *Applied Catalysis A: General*, 2000, **202**, 243-250.

[52] R. Grabowski, B. Grzybowska, K. Samson, J. Słoczyński, J. Stoch and K. Wcisło, *Applied Catalysis A: General*, 1995, **125**, 129-144.

[53] S.-t. Liang, H.-l. Zhang, M.-t. Luo, K.-j. Luo, P. Li, H.-b. Xu and Y. Zhang, *Ceramics International*, 2014, **40**, 4367-4373.

[54] A. Dayan and A. Paine, *Human & experimental toxicology*, 2001, **20**, 439-451.

[55] A. Levina and P. A. Lay, *Chemical research in toxicology*, 2008, **21**, 563-571.

Chapter 4b

Role of oxide-oxyhydroxide interface in defect MnOx(OH) for redox-base tandem activity

4b.1: Introduction

Mn based oxides (III/IV) (MnO_2 , Mn_2O_3 and Mn_3O_4) are considered as one of the strongest oxidants capable of transforming a variety of substrates to the corresponding oxidation products [1, 2]. The presence of edge shared $\text{Mn}(\text{O})_6$ has been found to be the active site for the oxidation reaction in manganese oxide samples.[3] The use of manganese oxides has reduced the dependence on the use of expensive noble metals like Au, Pd, and Ru for oxidation reactions. In Chapter 4a, we reported the utility of robustness of redox active metal oxyhydroxide such as K - doped $\text{CrO}(\text{OH})$ for organic tandem reaction. In the case of oxyhydroxides or oxide-hydroxides, the additional presence of surface hydroxyl groups (-OH) was proven to provide excellent base properties.[4] We also exploited the combined action of Cr(III) and surface OH groups for a one-pot sequential oxidation-coupling reaction. Since the synthesis of $\text{CrO}(\text{OH})$ involved reduction of K_2CrO_4 at high temperature, the surface modifications were constrained by the conditions. Hence, we decided to work on another redox metal oxyhydroxide $\text{MnO}(\text{OH})$ where, the synthesis involved sol gel and could be altered to study the surface changes. Most importantly, we were interested in the dynamics of a metal oxyhydroxide catalyst by introducing oxide-oxyhydroxide interface in $\text{MnO}(\text{OH})$ and studying its influence on the one-pot sequential oxidation-coupling catalysis.

Interfaces between two kinds of compounds are an interesting area of research. A recent review highlighted the importance of chemical interaction between metal and support in catalysis. [5] Metal /Metal oxide interfaces have been shown to affect an oxide's chemical and electronic properties within the first few nanometres of the contact, resulting in changes to an oxide's chemical reactivity, conductivity and energy-level alignment. For example, band gap energy was an important parameter for studying the oxidation ability for catalytic propene oxidation by mixed-metal oxides. [6] The metal/oxide boundary in Pd/TiO_2 and Au/TiO_2 has an influence in CO oxidation. Similarly, activity of water-gas shift reaction was enhanced by an order of magnitude over $\text{CeO}_x\text{-Cu}(111)$ interface compared to bare $\text{Cu}(111)$. [7] Thus, the influence of interface has been studied in detail in the case of noble metal nanoparticles supported on reducible supports and mixed-metal oxides. More recent studies have reported the interface confinement effect on coordinatively unsaturated metal/ metal oxides e.g. FeO_x on MnO obtained

from heat treatment of FeO(OH)/MnO₂. [8, 9] In this case, surface to surface electron shuttling between the redox centers showed strong reactivity towards electrophilic oxidation of organic substrates. Interestingly, interface between a metal oxide and metal oxyhydroxide which hitherto not investigated could be a vital tool to modify the activity of metal oxyhydroxides for tandem reactions.

Tandem catalysis is important in the present scenario, because of its advantages of low cost, no isolation of intermediates and better reaction efficiency. Earlier reports have discussed different methodology for aerobic oxidative cross-coupling of primary and secondary alcohols directly to produce α , β -unsaturated ketones. (Table 1.1, Chapter 1) Majority of earlier reports use noble metals which are expensive and also soluble bases which can increase toxicity. Present work on manganese oxyhydroxides not only provides a simpler and easy protocol to prepare the catalyst but also avoids the use of noble metals and external bases for one pot oxidation-coupling reaction to synthesize chalcones. Importantly, the study of oxyhydroxide-oxide interface for tandem catalysis is explored for the first time.

4b.2: Experimental Section

Materials used

Potassium permanganate (KMnO₄), sodium hydroxide (NaOH), glucose, deionised water, 0.2N ammonia solution (NH₃), 30% Hydrogen peroxide (H₂O₂), manganese sulphate tetrahydrate (MnSO₄·4H₂O), 1M HNO₃ solution, sucrose, methanol, manganese (II) chloride tetrahydrate (MnCl₂·4H₂O), isopropanol.

4b.2.1: Material synthesis

a) Manganese hydroxide [Mn(OH)₂]: [10] In a typical preparation, 200 mg each of KMnO₄, NaOH and glucose were dissolved in deionized water with a total volume 30mL. After stirring, the solution was transferred into an autoclave and heated to 200 °C for 72 h. Then the solution was cooled down to room temperature naturally. The product was repeatedly washed with deionized water and ethanol, and then dried at 80 °C for 10 h. to get Mn(OH)₂.

b) Manganese oxyhydroxide (defect) [MnO_x(OH)]: [11] 300 mL of 0.2 N NH₃ solution was added to the mixture of 20 mL 30% H₂O₂ and 1 L 0.06 mol MnSO₄·4H₂O, then quickly heated, and kept for 6 h at 150 °C. The resultant solid

was filtered while hot, washed with doubly distilled water, dried in an oven under vacuum for 2 days at room temperature, and stored dry.

c) Manganese oxyhydroxide (Pure) [MnO(OH)-P]: [12] 1 M HNO₃ solution (40 mL) containing 2 g of sucrose was stirred at room temperature, and 200 mL of water containing 5.89 g of KMnO₄ was added, followed by 4.4 g of MnSO₄·H₂O. The solution was refluxed for 6 h. Hot filtration recovered a brown solid, which was washed with water and air-dried.

d) Manganese oxide [Mn₂O₃]: A transparent sol solution was prepared by dissolving 0.1 M of Manganese (II) chloride tetrahydrate (MnCl₂·4H₂O) in 100 ml methanol under vigorous stirring. And then, an aqueous ammonia solution (10 ml) was added to the above solution by drop wise under stirring. The dropping rate must be well controlled for the chemical homogeneity. The resulting opal gels were filtered and washed with methanol to remove impurities, and dried over 120 °C for 12 h in order to remove water molecules and thus white coloured powders were obtained. Finally, black-brown coloured Mn₂O₃ nanopowders were formed at 400 °C for 2 h.

e) Manganese dioxide [MnO₂]: In a typical procedure for the preparation of MnO₂, 0.18 g of MnCl₂·4H₂O was mixed with isopropanol (50 mL) in a round-bottomed flask equipped with a reflux condenser. The solution was heated to approximately 83 °C with vigorous stirring, and then KMnO₄ (0.10 g) dissolved in 5 mL of deionized (DI) water was added to the above boiling solution rapidly, which gave a large amount of black precipitate. Ten minutes later, the mixture was cooled to room temperature after which centrifugation and washing with DI-water was done followed by drying the precipitate at 60 °C in air, overnight.

4a.2.2: Material Characterization: Transmission electron microscopy (TEM) images were obtained using FEI Technai TF-20 electron microscope operating at 200kV. Specimens of the samples were prepared by drop-casting well-dispersed particle suspensions in ethanol onto a carbon coated copper grids. Infrared Spectroscopy measurements were done using Bruker FT-IR. The samples were analyzed as solids. XRD was measured using PANalytical X'pert Pro diffractometer working under 40kV and 20 mA with CuK α (0.154 nm) radiation using a Ni filter.

X-ray photoelectron spectroscopy (XPS) study of K- α -CrO(OH) was done using VG Microtech model ESCA 3000 instrument. The organic reaction was monitored using an Agilent Technologies GC (7890B) equipped with a Flame Ionization Detector using a HP-5 capillary column. CO₂ TPD measurements were performed on Micromeritics ChemiSorb 2720 instrument equipped with a TCD detector.

4b.2.3: Cyclic Voltammetry: The electrochemical analyses of all the synthesized samples were carried out by using the cyclic voltammetry technique. The analyses were performed with the help of a typical three-electrode electrochemical setup consisting of a working electrode, a counter and a reference electrode. The working electrode (the electrode of interest) is a standard glassy carbon electrode (GCE) modified with the concerned sample. The counter electrode is a high-grade platinum wire and the reference electrode is a standard Ag/AgCl in saturated KCl solution. All the potentials measured in this work are with reference to the Ag/AgCl electrode we have taken. Prior to the measurement, glassy carbon electrodes were well polished by alumina slurry (of size 1 μ , 0.3 μ , 0.05 μ sequentially), sonicated in de-ionised water and dried in a vacuum desiccator. Meanwhile, samples were dispersed in a mixture of ethanol and Nafion (1 mg of each sample mixed with absolute ethanol (95%) and Nafion (5%) followed by ultrasonication for 5 minutes). After thorough dispersion of the samples, the sample ink was drop casted onto the mirror-polished glassy carbon electrode and the modified GCE was dried in the vacuum desiccator. The CV profiles were recorded by using a Metrohm Electrochemical workstation in a two compartment three electrode electrochemical cell. 1 M aqueous solution of KOH was taken as the electrolyte for all the measurements and the cyclic voltammograms were recorded at three different sweep rates (10 (slow sweep), 40 (medium sweep) and 100 mV/s (fast sweep)).

4b.2.4: Catalytic reaction

Oxidation reaction: 1mmol of benzyl alcohol was taken in a 25mL round bottom flask with 5 mL p-xylene as a solvent to which 400mg catalyst was added and the reaction mixture was stirred at 90 °C under O₂ balloon atmosphere for 24h. The products were analyzed using GC.

Condensation reaction: 1mmol of benzaldehyde and 2mmol of acetophenone were taken in a 25mL round bottom flask with 5 mL p-xylene and 400mg catalyst. The resultant reaction mixture was heated to 90 °C under N₂ atmosphere for 24h.

Oxidation-base reaction: 1 mmol of benzyl alcohol and 2 mmol of acetophenone were taken in a 25 mL round bottom flask dissolved in 5mL of p-xylene together with 0.4 g of catalyst. This was refluxed for 48 h under balloon oxygen. The reaction was monitored using GC by removing small aliquots during the course of the reaction.

4b.3: Results and Discussion

4b.3.1: Material characterization

Since the purpose of this work was to study the effect of oxide-oxyhydroxide interface, the materials chosen for this work were pure manganese oxyhydroxide MnO(OH)-P and manganese oxides Mn₂O₃ along with a modified defect manganese oxyhydroxide termed as MnO_x(OH). The synthesized materials were first characterized by X-ray diffraction to ascertain the purity of the crystalline phases. Mn₂O₃ has a rhombohedral structure (Fig 4b.1a, iii). MnO(OH)-P showed octahedral features, where P stands for pure. The synthesis procedure of MnO_x(OH) involved a slight modification to generate oxide phases within by increasing the aging temperature to 150 °C. Thus MnO_x(OH) sample consisted MnO(OH) (CAS-41-1379) phase in addition to MnO₂ and Mn₂O₃ phases. An expanded section of plot (ii) is presented in Fig 1b. Peaks at 2θ= 21.6, 29.0, 51.1, 60.0° could be indexed to MnO₂ (CAS-43-1455) whereas, peaks 2θ= 31.04, 32.26, 44.50 and 58.49 were due to Mn₂O₃ phase (CAS-76-0150).

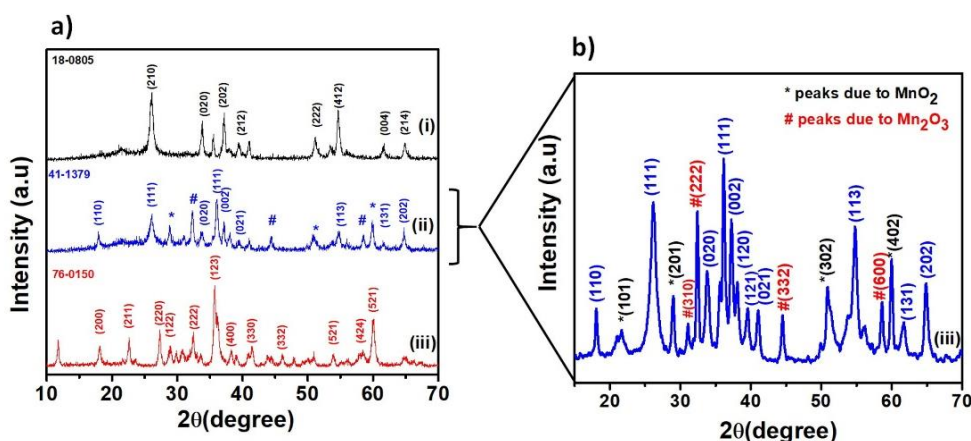
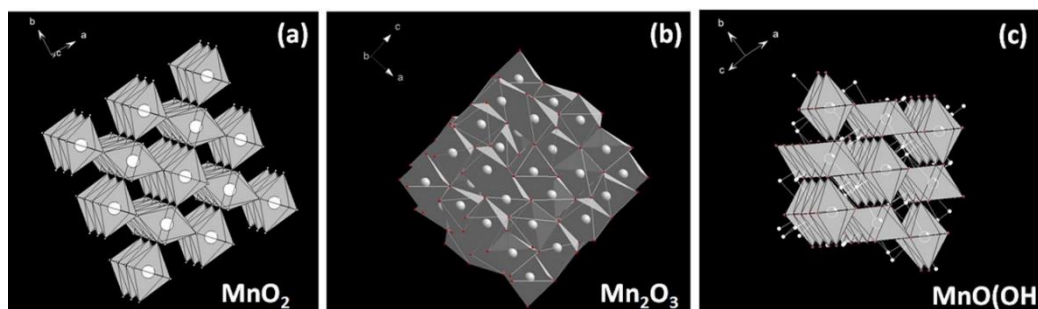


Fig 4b.1: XRD patterns for i) MnO(OH)-P, ii) MnO_x(OH) iii) Mn₂O₃



Scheme 4b.1: Crystal structures of MnO_2 , Mn_2O_3 and $\text{MnO}(\text{OH})$

Scheme 4b.1 shows the crystal structures of Mn oxides and oxyhydroxides. In manganese oxyhydroxides, the $d^4 \text{Mn}^{3+}$ ion is in a weak octahedral field causing Jahn-Teller distortion. This results in a z elongated complex with four short and two long M-O bonds and also hydrogen bonding. [12]

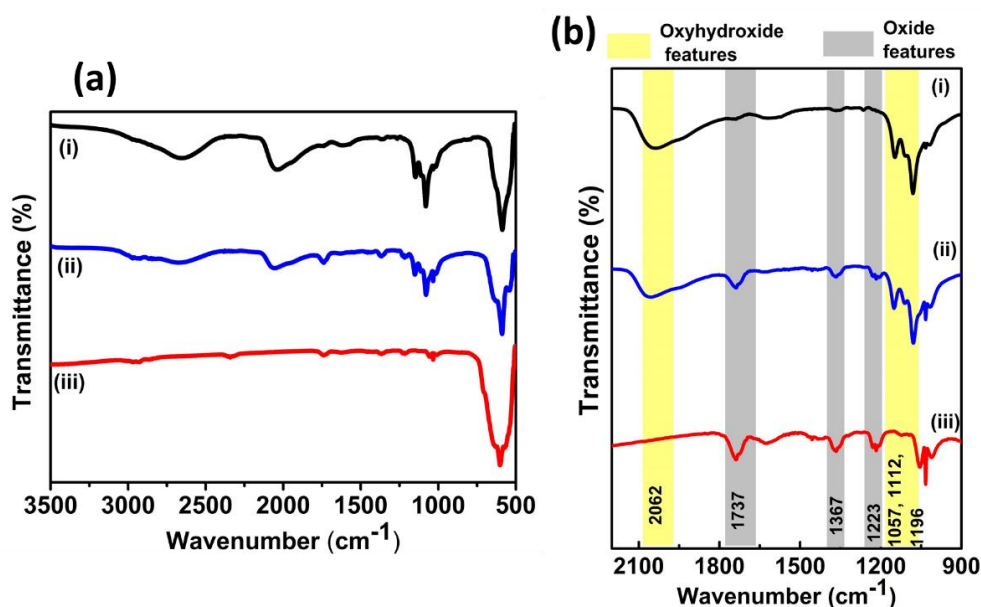


Fig 4b.2: a) FT-IR spectra of i) $\text{MnO}(\text{OH})\text{-P}$, ii) $\text{MnO}_x(\text{OH})$ iii) Mn_2O_3 . b) A magnified spectra of $\text{MnO}(\text{OH})$, $\text{MnO}_x(\text{OH})$ and Mn_2O_3 . Yellow bands for Oxyhydroxides features whereas grey bands indicating oxide features.

Fig 4b.2a gives the FT-IR spectra of the samples. The region between 900-2200 cm^{-1} is enlarged in Fig 4b.2b. Interestingly the $\text{MnO}_x(\text{OH})$ sample shows bands common to both $\text{MnO}(\text{OH})$ (yellow bands) and Mn_2O_3 (grey bands). In the region 2600-2700 cm^{-1} , a broad absorption band was observed due to OH stretching mode of hydrogen bonding. OH bending modes can be assigned to three bands between 1000 and 1150 cm^{-1} , out of which the lowest energy band is due to the γ

mode perpendicular to the OH vector plane whereas, the remaining two are the δ modes in the OH plane.[13] The lattice Mn-O vibrations are observed below 700 cm^{-1} . [14] Mn_2O_3 showed bands at 576 cm^{-1} due to Mn-O stretching vibrations and 539 cm^{-1} due to Mn-O bending vibrations.[15] Infrared spectra of $\text{MnO}_x(\text{OH})$ (Fig 4b.2b (iii)) shows both oxide and oxyhydroxide features. The Raman bands of the samples are presented in Fig 4b.3a. Bands at $620, 554$ and 527 cm^{-1} are due to the stretching mode of MnO_6 octahedra. The peak at 650 cm^{-1} depends upon the number of $\mu\text{-O}$ bridges, their Mn-O-Mn angle, and Mn oxidation state. Long Mn-O bonds occur at higher Raman shift values. [12] The magnified image of the Raman spectra between $610\text{-}690\text{ cm}^{-1}$ in Fig 4b.3b shows a shift for $\text{MnO}_x(\text{OH})$ to higher values as compared to $\text{MnO}(\text{OH})$ and Mn_2O_3 . This confirms the defect nature of $\text{MnO}_x(\text{OH})$ with presence of oxide phases as confirmed by XRD.

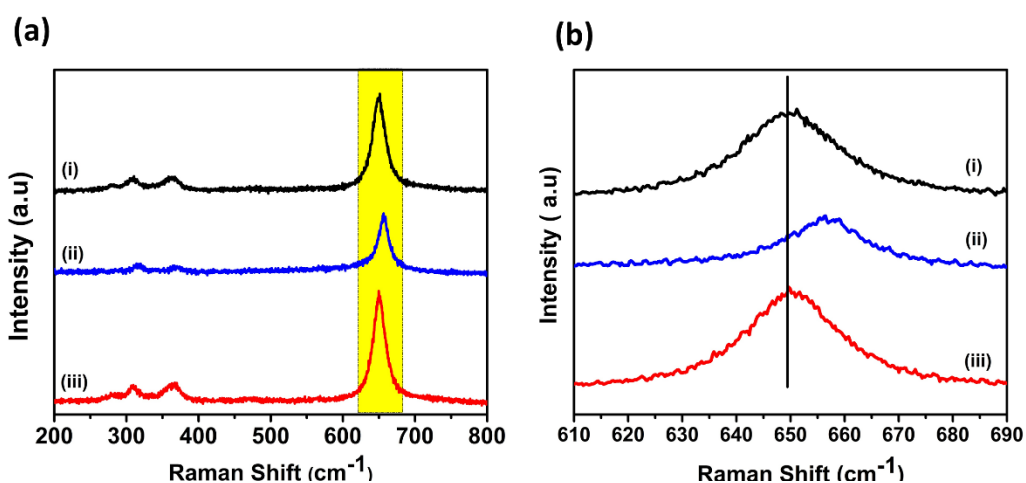


Fig 4b.3: a) Raman spectra of i) $\text{MnO}(\text{OH})\text{-P}$, ii) $\text{MnO}_x(\text{OH})$ iii) Mn_2O_3 b) A magnified spectra of i) $\text{MnO}(\text{OH})\text{-P}$, ii) $\text{MnO}_x(\text{OH})$ iii) Mn_2O_3 showing a shift for $\text{MnO}_x(\text{OH})$

To understand the difference in the bond lengths between the various samples, EXAFS analysis of the samples was carried out, for which cyclotron facility at Tsukuba, Japan was used with the help of Prof. Mayasuki Shirai, Iwate University, Japan. The X-ray absorption spectrum consists of two regimes: X-ray absorption near-edge spectroscopy referred to as (XANES) and extended X-ray absorption fine-structure spectroscopy (EXAFS). XANES studies help to understand the formal oxidation state and coordination structure such as octahedral, tetrahedral of the X-ray absorbing atom whereas, the EXAFS is used to obtain the inter atomic distances, coordination number, and species of the neighbours of the X-ray absorbing atom.

[16] EXAFS spectra (Fig.s 4b.4, 4b.5 and Table 4b.1) indicated longer Mn—O bond length of 1.60 Å in MnO_x(OH) while, it was 1.41 Å in MnO(OH)-P. Also, Mn-Mn bond lengths were elongated to 3.22 Å. Thus MnO_x(OH) shows structural differences from MnO(OH)-P

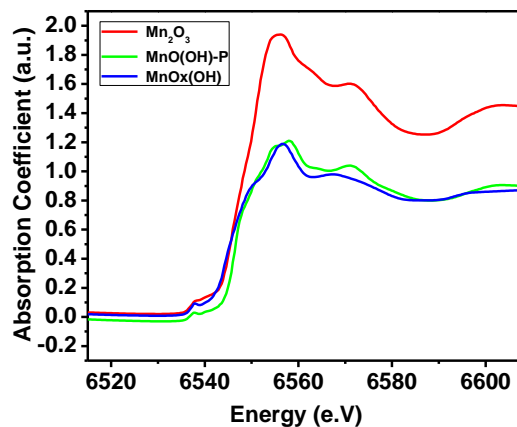


Fig 4b.4: EXAFS data for MnO(OH)-P, MnO_x(OH) and Mn₂O₃

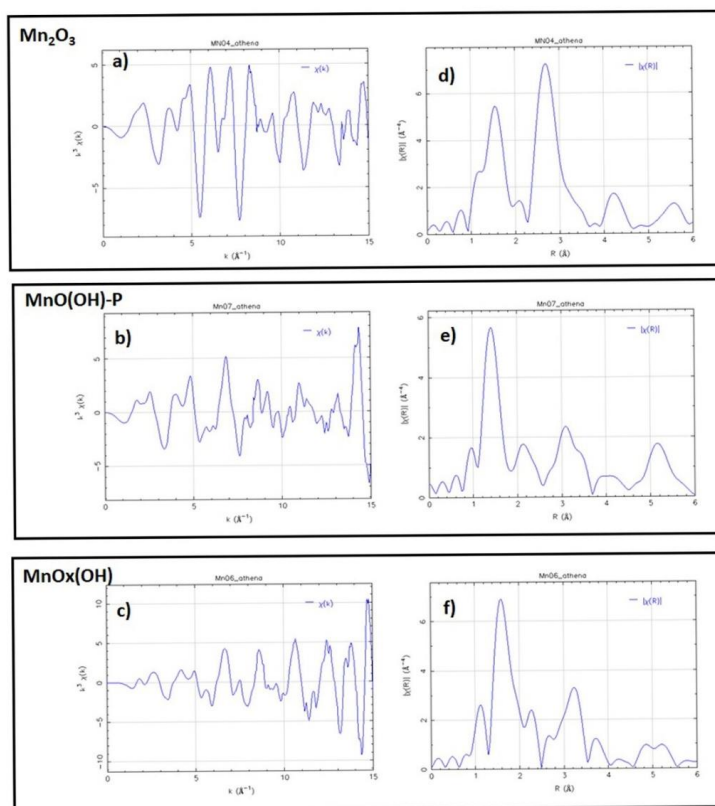


Fig 4b.5: Second derivative a), b) & c) and Fourier transform d), e) & f) of the spectrum for MnO(OH)-P, MnO_x(OH) and Mn₂O₃

Table 4b.1: EXAFS data for MnO(OH)-P, MnO_x(OH) and Mn₂O₃

Sr No	Catalyst	Edge (e.V)	Mn-O	Mn-Mn
			R /Å	R /Å
1.	Mn foil	6536.89	-	-
2.	Mn ₂ O ₃	6550.87	1.58	2.70
3.	MnO(OH)-P	6544.23	1.41	3.08
4.	MnO _x (OH)	6544.23	1.60	3.22

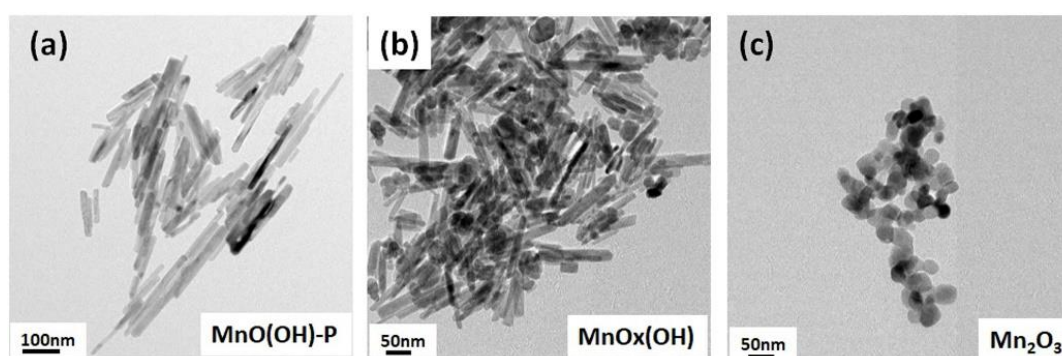
**Fig 4b.6:** Transmission Electron Microscopy images for a) MnO(OH)-P b) MnO_x(OH) and c) Mn₂O₃

Fig 4b.6 shows TEM images of the Mn oxide samples prepared in this work. Mn₂O₃ shows bulk structure consisting of agglomerated particles. MnO(OH)-P shows rodlike morphology whereas, the defect MnO_x(OH) shows both rods and spheroids. Detailed analysis of MnO_x(OH) nanocomposite is presented in Fig 4b.7. Electron diffraction patterns of MnO_x(OH) shows polycrystalline nature of the material with the concentric rings assigned to (113) and (121) planes belonging to MnO(OH) phase. Careful analysis of the MnO_x(OH) spheroids showed presence of fringes corresponding to planes of oxides (MnO₂ and Mn₂O₃ planes). Fig 4b.7c shows MnO_x(OH) spheroids showing d spacing belonging to (332) plane of Mn₂O₃, whereas the rod shows parent MnO(OH) plane (002). Interestingly, the MnO_x(OH) rods in some areas shows presence of oxide planes e.g. (310) plane of Mn₂O₃. On an average, around 45% of the MnO_x(OH) spheroids were 30-35nm in size. Whereas, the length of the MnO_x(OH) rods varied between 50-250 nm. Hence, MnO_x(OH) is a nanostructure with MnO(OH), MnO₂ and Mn₂O₃ phases intermixed.

To understand the presence of oxide components. We carefully analyzed the XPS spectra of MnO_x(OH). We studied the behavior of the asymmetric Mn 2p_{3/2} peak

which is observed at 638.64 ± 0.06 eV with $2p_{3/2}$ to $2p_{1/2}$ splitting of 11.10 ± 0.02 eV. [17] The data is presented in Fig 4b.8 & Table 4b.2. The deconvoluted Mn $2p_{3/2}$ XPS signal of MnOx(OH) showed 40% oxide features at 641.9 eV and 640.8 eV on the surface.

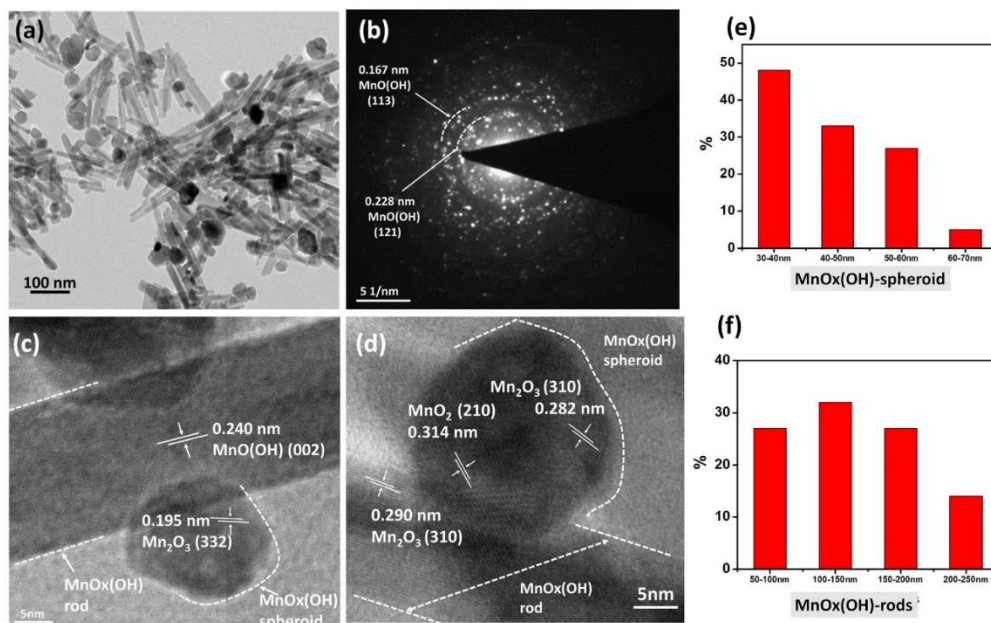


Fig 4b.7: TEM image (a), ED pattern (b), HRTEM (c) & (d) Particle sizes of MnOx(OH) rods and spheroids

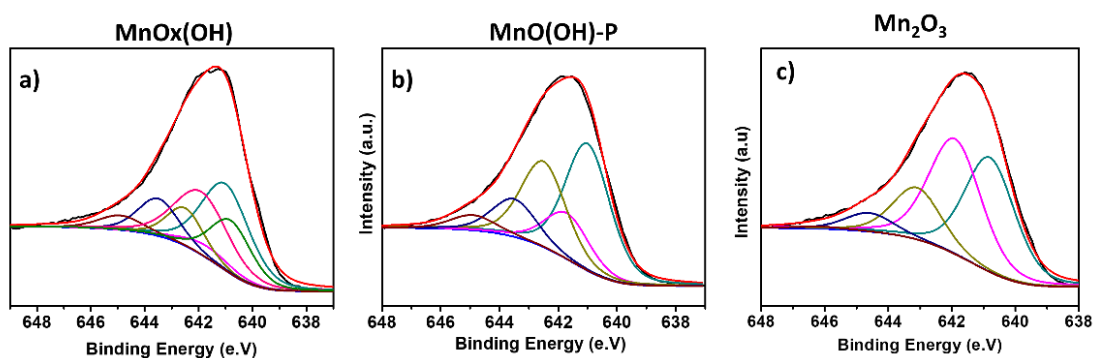


Fig 4b.8: Deconvoluted Mn $2p_{3/2}$ XPS spectra for MnO(OH)-P, MnOx(OH) & Mn₂O₃

Table 4b.2: Analysis of various contributions from Mn 2p_{3/2} XPS spectra for MnO(OH)-P, MnOx(OH) & Mn₂O₃

Mn2p _{3/2} Binding Energy (e.V)					
MnO(OH)-P		MnOx(OH)		Mn ₂ O ₃	
B.E (e.V)	Area (%)	B.E (e.V)	Area (%)	B.E (e.V)	Area (%)
640.99	41	641.00	30	640.8	38
641.69	15	641.7	4	641.9	39
642.49	27	642.5	10	643.1	16
643.49	12	643.5	11	644.6	6
644.89	5	644.9	5	646.2	00
		641.9	24		
		640.8	16		

4b.3.2: Catalytic Studies on MnOx(OH)

4b.3.2.1: Oxidation Property of MnOx(OH)

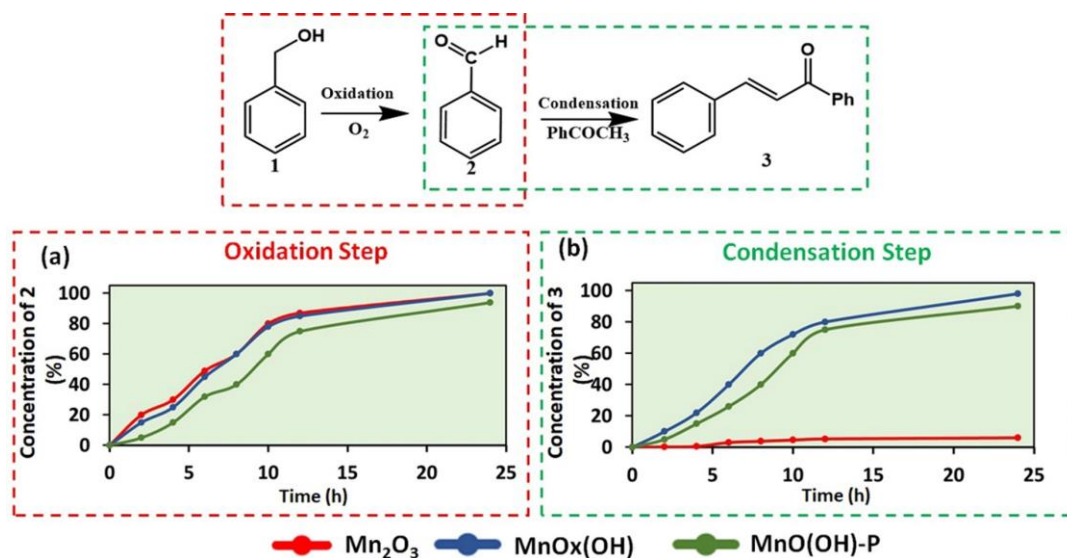


Fig 4b.9: a) Oxidation step Reaction conditions: 1mmol Benzyl alcohol (1), 5 mL p-xylene, 400mg catalyst at 90 °C, O₂ balloon, 24h for all the catalysts
 b) Condensation step: Reaction conditions: 1mmol Benzaldehyde (2), 2mmol acetophenone, 5 mL p-xylene and 400mg catalyst at 90 °C, N₂ atmosphere, 24h for all the catalysts

Since manganese oxides are well-known for their oxidation ability, was oxidation of benzyl alcohol to benzaldehyde was studied using the prepared Mn oxides (Fig

4b.9a). The reaction conditions were optimized based on our earlier work of K-doped CrO(OH). [4] The manganese oxides Mn₂O₃ showed the highest activity with maximum conversion (100%) attained in short time. (Fig 4b.9a) Both the manganese oxyhydroxide samples MnO(OH)-P and MnO_x(OH) also showed significant oxidation property with 60% and 78% conversion, respectively, after 10 h. Importantly, the defect sample MnO_x(OH) showed slightly improved activity of 18% after 10h as compared to MnO(OH)-P. The presence of edge shared Mn(O)₆ has been found to be the active site for the oxidation reaction in manganese oxides.[18] To probe the active sites responsible for oxidation, we performed cyclic voltammetry of the samples. Cyclic voltammetry studies were carried out on Mn₂O₃, MnO₂, MnO_x(OH), MnO(OH) and Mn(OH)₂ (taking 1 M aqueous solution of KOH as the electrolyte), to probe the surface-active sites. These studies were performed by Satyajit Ratha at IIT Bhubaneswar. The data obtained is presented in Fig 4b.10 and Table 4b.3. The reason for taking aqueous solution of KOH as the electrolytic medium is that the manganese-based samples are known to be thermodynamically stable under high pH conditions. As can be observed from the cyclic voltammograms, prominent peaks were found in the case of all the manganese based compounds, signifying their re-dox properties.[Here, the potential values, at which the reduction and oxidation of samples occur, varies within ~0.34-0.36 V and ~0.16-0.18 V, respectively, in the presence of a high pH environment]. Different sets of redox couple were detected for manganese samples, giving their oxidation states in the compound. The different sets of redox couple observed in case of all the samples have been provided in Table 4b.3. The oxidation state of the samples (in the case of MnO(OH), MnO_x(OH), and Mn₂O₃) changes from +3 to +4. The difference in the oxidation potential of the samples is quite small. The redox couples formed by both MnO_x(OH) and MnO(OH) are sharp in contrast to those observed in the case of Mn₂O₃ samples. Additionally, the difference between the redox couple for the MnO_x(OH) sample is lower as compared to MnO(OH), thus indicating better reversible catalytic activity of the former.

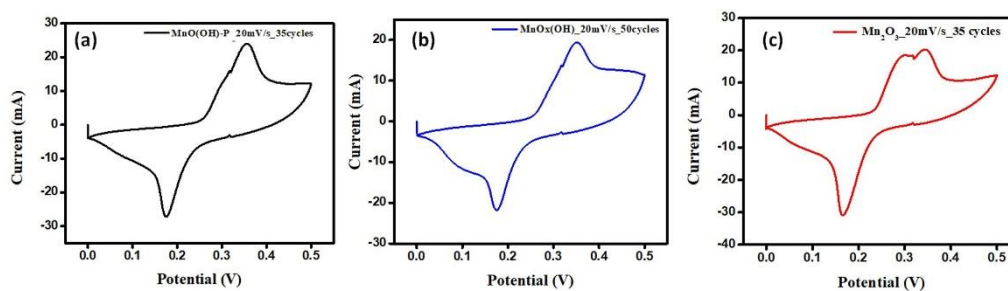


Fig 4b.10: Cyclic Voltammograms for the manganese catalysts

Table 4b.3: Cyclic Voltammetry data for the manganese catalysts

Sr. No	Sample	Oxidation Peak	Reduction Peak	Difference between the peaks (ΔE_p)
1	MnOx(OH)	~0.35 V	~-0.175 V	~0.175 V
2	MnO(OH)	~0.36 V	~-0.175 V	~0.185 V
3	Mn ₂ O ₃	~0.345 V	~-0.160 V	~0.185 V

4b.3.2.2: Base property of MnOx(OH)

OH/O⁻ and O²⁻ have been shown to provide basicity in metal oxyhydroxide materials. Hence, the basicity of MnOx(OH) was explored for the base catalyzed synthesis of chalcones (3) by reacting 1mmol benzaldehyde (2) and 2mmol acetophenone using 0.4g catalyst (Fig 4b.9b). Mn₂O₃ showed poor base activity (below 5%). MnOx(OH) showed best activity in terms of 60% conversion in 8h. While, MnO(OH)-P which does not have any oxide impurities showed 20% lower conversion than that shown by MnOx(OH). CO₂ TPD profiles of the samples are shown in Fig 4b.11 and Table 4b.4. MnO(OH)-P and MnOx(OH) showed similar basicity values of 3.26 and 3.10 mmol/g, respectively. Whereas, manganese oxides Mn₂O₃ showed basicity less than 0.30 mmol/g. Thermogravimetric profiles of the samples showed weight loss region between 100- 250 °C due to water loss of surface hydroxyl groups. MnO(OH)-P showed 4.2% and MnOx(OH) showed 3.9% indicating presence of surface hydroxyl groups. Mn₂O₃ showed less than 1% weight loss due to absence of surface hydroxyl groups. The origin of basicity is discussed in detail in the subsequent section.

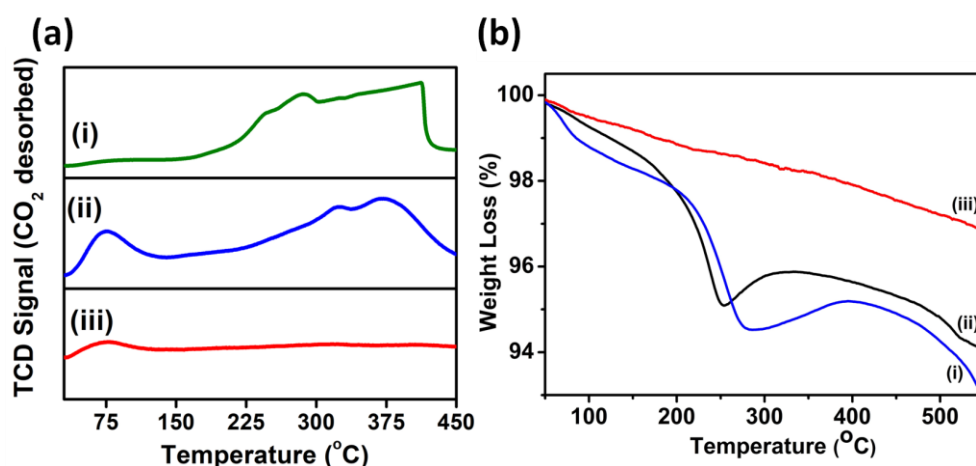


Fig 4b.11: (a) CO₂ TPD plots and b) Thermogravimetry plots for i) MnO(OH)-P ii) MnO_x(OH) iii) Mn₂O₃,

Table 4b.4: (a) CO₂ TPD plots and b) Thermogravimetry plots for MnO(OH)-P, MnO_x(OH) & Mn₂O₃,

Sr. No	Sample	mmol/g of CO ₂	Weight loss due to surface hydroxyl groups 100-250 °C (%)
1.	MnO(OH)-P	3.26	4.2
2.	MnO _x (OH)	3.10	3.0
3.	Mn ₂ O ₃	0.14	0.9

4b.3.2.3: Bifunctional Activity of MnO_x(OH)

Having tested the activity of Mn samples individually for oxidation and condensation reactions and in order to understand the utility of MnO_x(OH) for one pot tandem conversion, the oxidation of benzyl alcohol (1) was studied in the presence of acetophenone so that the resulting oxidation product benzaldehyde would react with acetophenone in the presence of base sites to yield chalcone. (Fig 4b.12) The advantage of such a catalytic approach would reduce isolation of intermediates. Mn₂O₃ and MnO₂ (control catalysts) which showed high oxidation property showed 100% conversion of benzyl alcohol but the yield to (3) was less than 10%, indicating poor ability to catalyze the second base catalyzed condensation step. Another control catalyst Mn(OH)₂ which is basic in nature did not behave as a bifunctional catalyst as it showed poor oxidation ability.

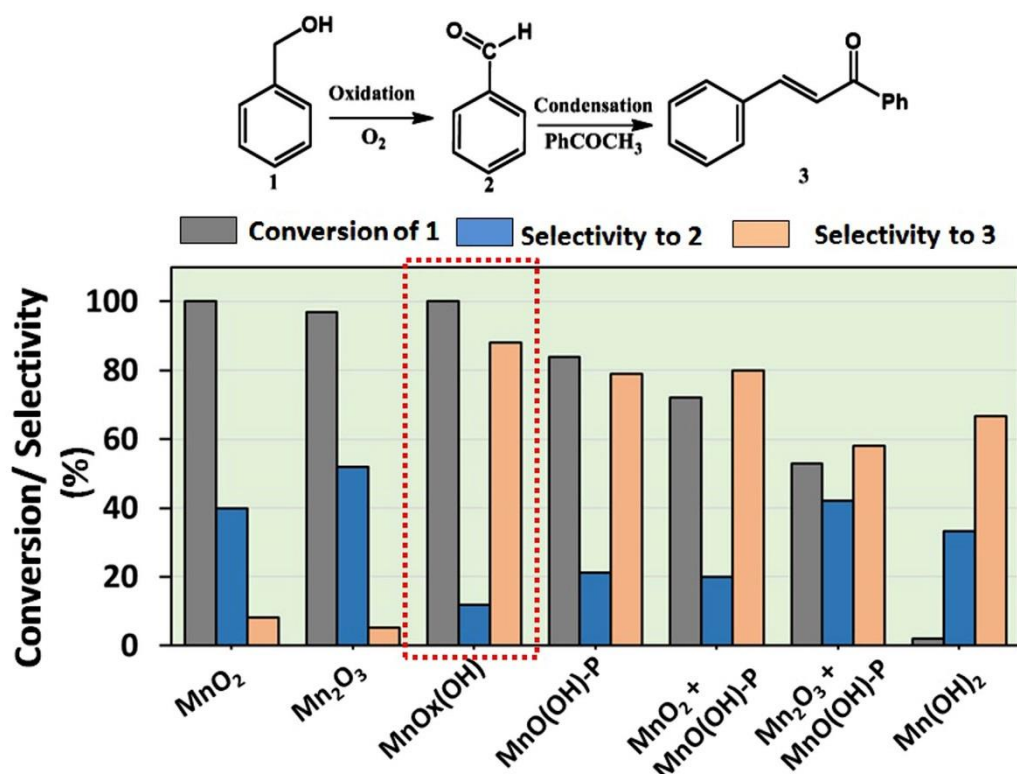


Fig 4b.12: Conversion and Selectivity plots for the manganese samples

MnOx(OH) also showed 100% conversion of (1) with selectivity to (3) as high as 88%. Thus, MnOx(OH) acts as a bifunctional catalyst. In comparison, MnO(OH)-P also showed bifunctional activity with slightly lower conversion 84% and selectivity of 78%. This difference can be attributed to the difference in the composition and structure of MnOx(OH). To understand in detail the difference in the performance of MnOx(OH) and MnO(OH)-P, O1s spectra of these materials were also studied (Fig 4b.13). The surface of any oxyhydroxide material will have contributions from M-O-M (BE of 529.8 eV), the surface hydroxyl group M-OH (531.6 eV) and physisorbed moisture (532.4 eV). [19] The MnOx(OH) sample gave contributions predominantly from Mn-O-Mn (63%) as compared to Mn-OH (30%) (Fig 4b.13c). On the contrary, MnO(OH) showed increased Mn-OH (56%) and a lower Mn-O-Mn (37%). The basicity was quantified in terms of [Mn-O-Mn]/[Mn-OH] ratio. A higher ratio of 2.1 was observed for the MnOx(OH) sample in contrast to 0.7 for MnO(OH)-P (Fig 4b.13d). From the catalysis results, both the Mn-O-Mn and Mn-OH species provide basicity in the form of Lewis basic O²⁻ and Brønsted basic OH/O⁻ respectively. [20, 21] In a pure oxyhydroxide, the contribution of surface hydroxyl groups is always higher than the oxide ion ([Mn-O-Mn]/[Mn-OH] < 1).

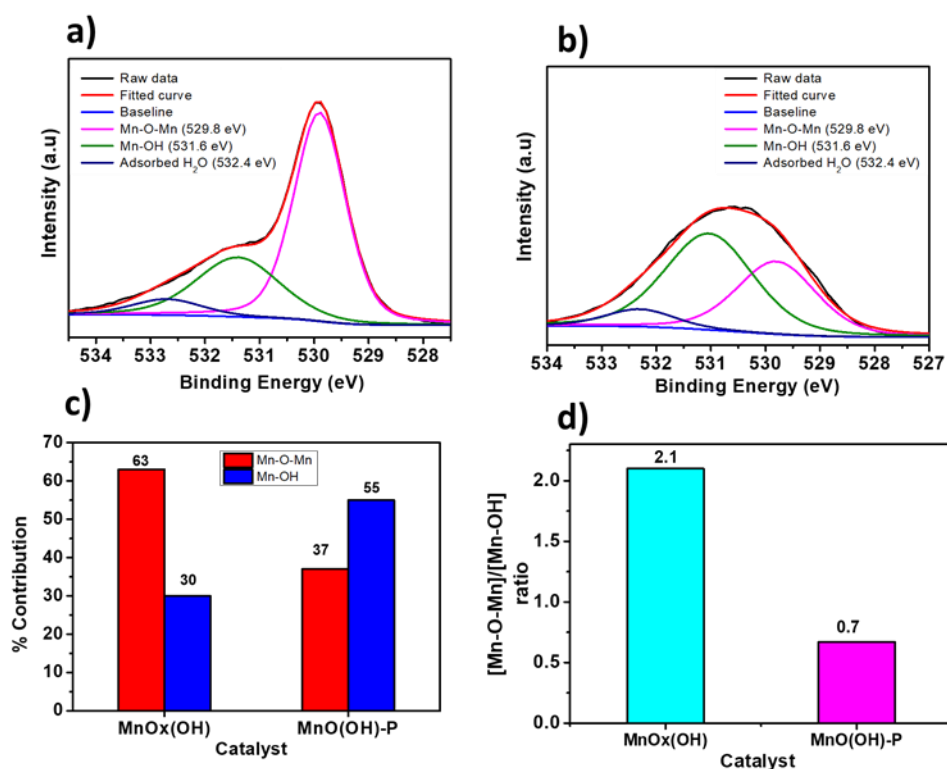
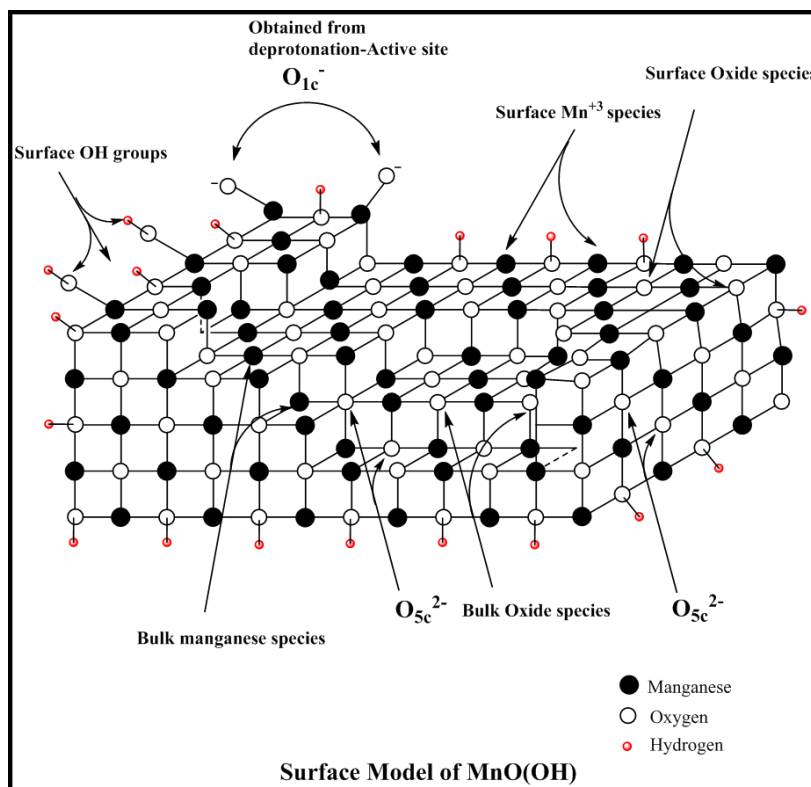


Fig 4b.13: a) Deconvoluted O1s XPS spectra of a) MnO_x(OH) b) MnO(OH)-P c) plot of % contribution of O species d) plot of relative ratio of [Mn-O-Mn]/[Mn-OH]

However, by introducing the oxide impurity in MnO_x(OH) this trend could be reversed because, along with the surface hydroxyl groups, more O²⁻ ions were available as active sites in MnO_x(OH). In the case of manganese oxides (MnO₂) and Mn₂O₃, the basicity is due to O²⁻ ions alone, whereas in the case of Mn(OH)₂, the surface hydroxyl groups are basic in nature, moreover there is no Mn-O-Mn linkage in Mn(OH)₂. The advantage of MnO_x(OH) and MnO(OH)-P is due to the dual basicity of OH/O⁻ and O²⁻. What makes MnO_x(OH) stand apart from the MnO(OH)-P is the additional O²⁻ species which not only help in providing basicity for the condensation step but also help in the oxidation step by activating O₂. In a control experiment, the overall O²⁻ available for the reaction was enhanced by using 1:1 physical mixtures of MnO₂ : MnO(OH)-P and Mn₂O₃:MnO(OH)-P, keeping the weight constant. Though, the activity was found to increase but not to the extent observed for MnO_x(OH) alone (Fig 4b.12). MnO_x(OH) gave a selectivity of 88% with 100% conversion whereas the physical mixtures gave a selectivity of around 80% with a conversion ranging between 70-82%. Thus, the activity of MnO_x(OH) is better than other catalysts due the in-situ generated oxide centers. Since these oxides centers are generated from the same precursors as the surface hydroxyl

groups of MnOx(OH) , there will naturally be a close proximity between the oxide and oxyhydroxide interface. This interface is believed to be responsible for the enhanced activity of MnOx(OH) .



Scheme 4b.2: Surface model of MnO(OH)

Scheme 4b.2 depicts the schematic of postulated surface model of MnO(OH) . The material is made up of surface and bulk species. The exposed surface contains the active sites whereas, the bulk may not directly influence the catalytic property. The surface contains the hydroxyl groups which can be singly, doubly or triply coordinated to Mn atoms. This coordination depends on the linkage of the basic octahedra $\text{MnO}_3(\text{OH})_3$ to each other which can be edge linked, corner linked or face linked. Importantly, the surface hydroxyl groups on metal oxyhydroxides are known to exist in a dynamic equilibrium with their deprotonated counterparts (O_{1c}^-). This O_{1c}^- site is one of the active sites providing basicity. The other basic site is the surface oxide species (O^{2-}) providing lewis basicity. These (O^{2-}) could be penta or tri coordinated. The presence of Mn^{3+} surface sites provide the oxidation ability to the material. In the case of $\text{MnO}_x(\text{OH})$ increases the Mn sites and hence gets a difference in terms of defect sites, oxygen vacancies, and elongated bond lengths.

4b.3.2.4: MnOx(OH) recyclability and stability

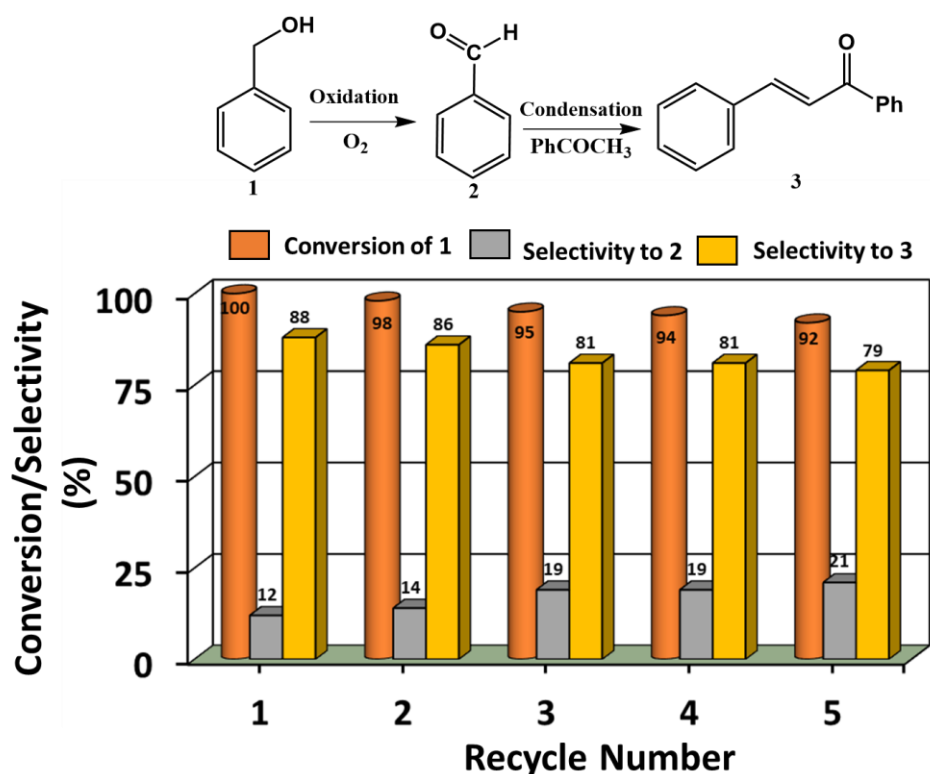


Fig 4b.14: Recyclability of MnOx(OH) for one pot oxidative coupling reaction to give 3

The catalyst could be recycled over four times for the oxidation-coupling reaction between benzyl alcohol and acetophenone without appreciable loss in its activity as can be seen in Fig 4b.14. XRD and TEM of used catalyst after oxidation-coupling reaction did not show any significant changes from the fresh catalysts as seen from Fig 4b.15. Also, all the peaks due to MnO₂ and Mn₂O₃ were consistent and no new peaks were observed. Thus, there was no increase in the oxide component after recycling the catalyst suggesting that MnOx(OH) acts as a stable catalyst under the reaction conditions.

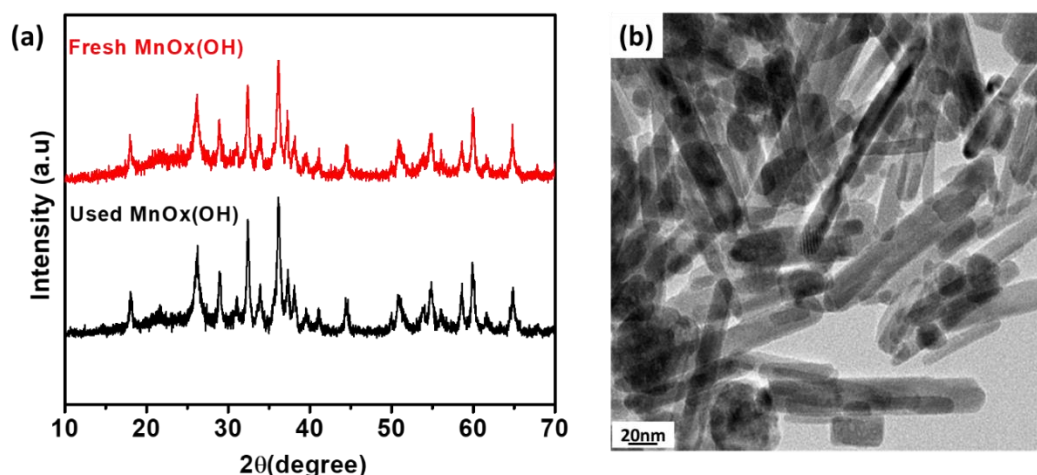
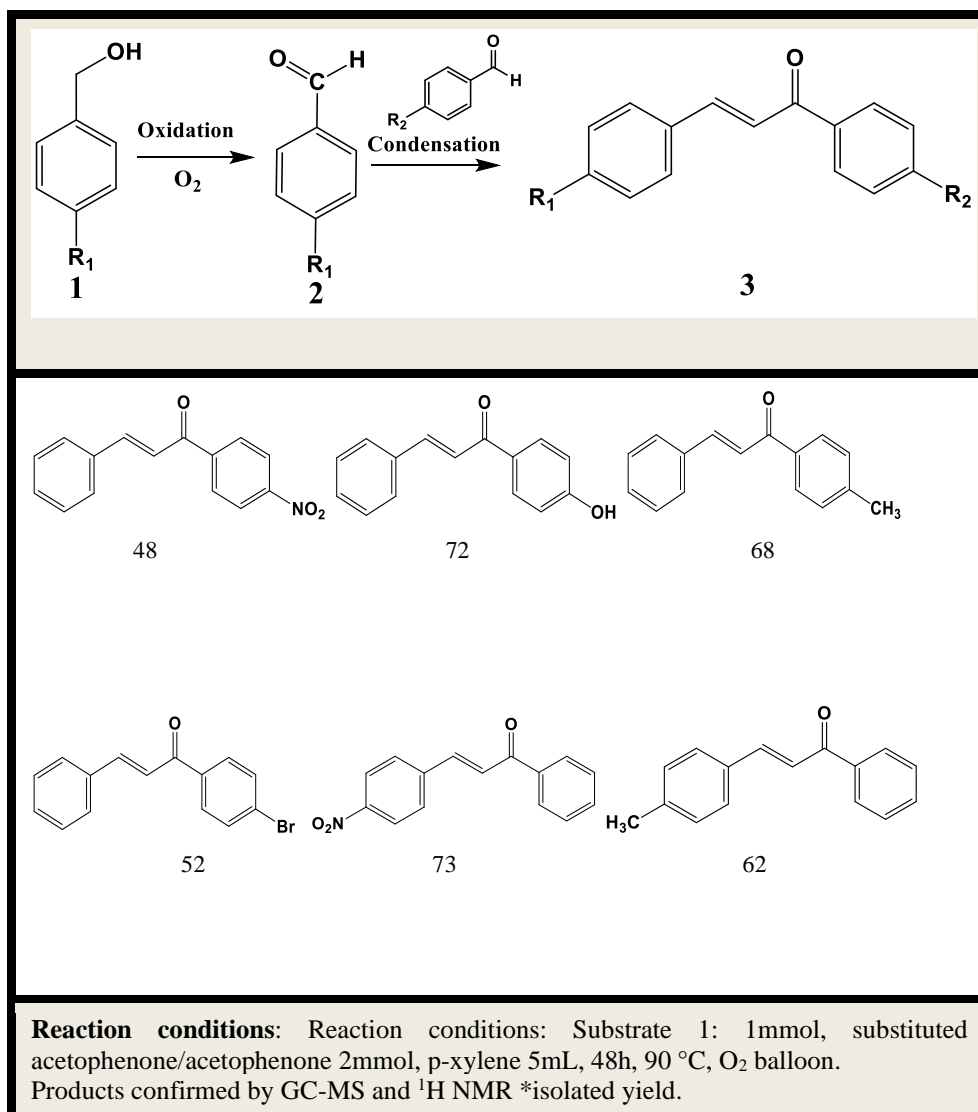


Fig 4b.15: a) XRD of Fresh and used MnO_x(OH) b) TEM of used MnO_x(OH)

4b.3.2.5: Substrate Scope

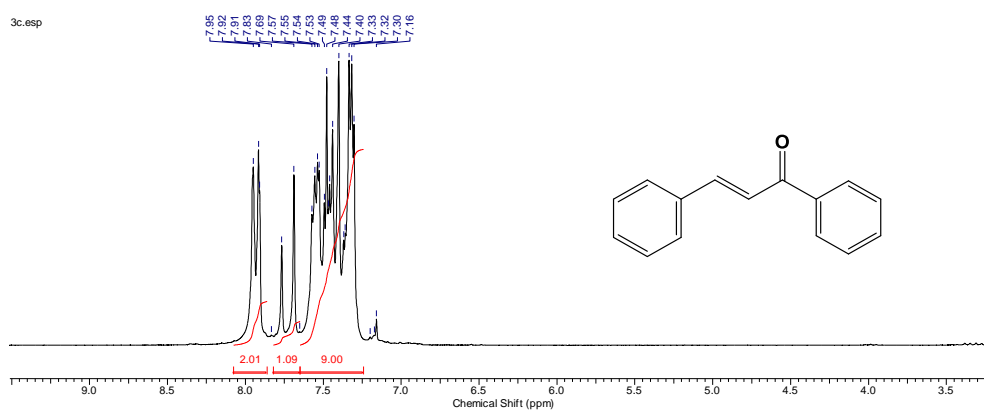
To explore the versatility of MnO_x(OH) as a catalyst, our study was extended for other substrates by studying other substituted aromatic alcohols as well as substituted acetophenones. (Table 4b.5) For example, 4-nitro benzyl alcohol on tandem oxidation-condensation with acetophenone gave 48% yield, whereas electron donating 4-hydroxy benzyl alcohol gave 72% yield. The methyl group on benzyl alcohol in the para position yielded 68% of the product. Para substituted bromine gave 52% yield on tandem reaction with acetophenone. The substituents of acetophenone had an opposite effect on the activity as compared to those on benzyl alcohol. Electron withdrawing substituent -NO₂ on acetophenone gave 73% yield, however the same substituent had a deactivating effect when present on benzyl alcohol in the para position. Also, electron donating -CH₃ on acetophenone gave 62% yield.

Table 4b.5: Substrate Scope exhibited by MnOx(OH)

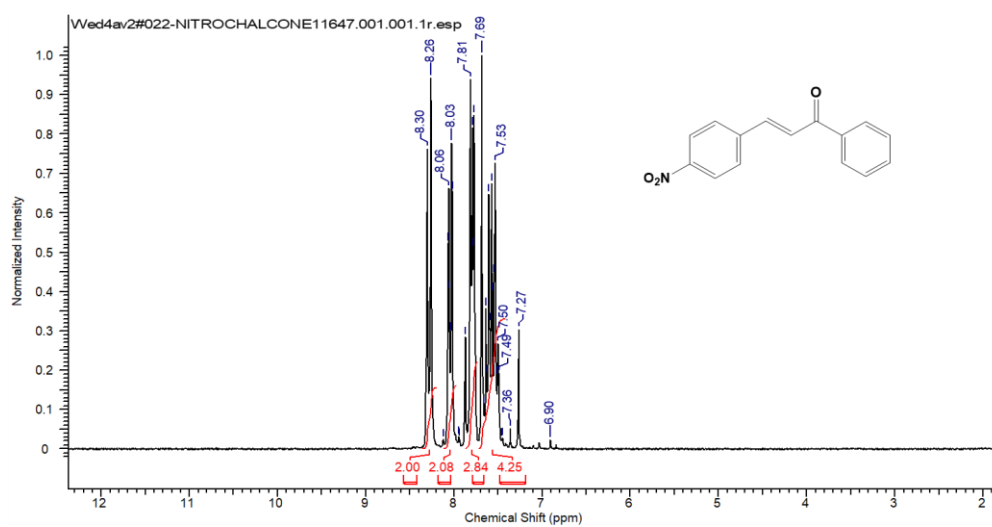


4b.4: Conclusions

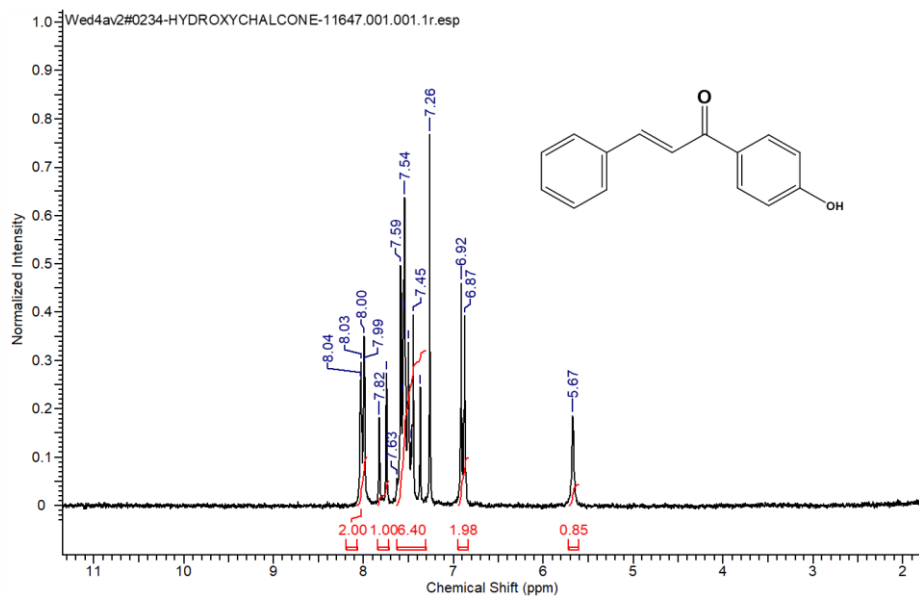
The design and utility of a mixed oxide-oxyhydroxide material, MnOx(OH) was explored for the tandem oxidation-condensation reaction. The material showed structural and compositional differences from pure oxyhydroxide and oxides of manganese. The active sites being the redox active Mn, and the basic sites O²⁻ and O⁻. MnOx(OH) had a larger contribution from O²⁻ as compared to O⁻. Since the oxides phases were formed *in-situ*, the role of oxide-oxyhydroxide interface was important for the catalytic activity. This was the first study on the role of oxide-oxyhydroxide interface in catalytic reactions. This study would open new avenues for designing hybrid oxide-oxyhydroxide nanostructures for a variety of applications in catalytic transformations.

4b.5: ^1H NMR of selected compounds

^1H NMR (200 MHz, CHLOROFORM-*d*) δ ppm 7.24 - 7.65 (m, 10 H) 7.65 - 7.82 (m, 1 H) 7.86 - 8.08 (m, 2 H)



^1H NMR (200 MHz, CHLOROFORM-*d*) δ ppm 7.49 - 7.69 (m, 4 H) 7.77 - 7.81 (m, 3 H) 8.03 - 8.06 (d, 2 H), 8.26-8.30 (d 2H)



^1H NMR (200 MHz, $\text{CHLOROFORM-}d$) δ ppm 8.04 - 7.99 (d, 2 H) 7.82 - 7.79 (m, 1 H) 7.59 - 7.45 (m, 6 H), 6.92-6.87 (d 2H), 5.67 (1H, s)

4b.6: References

- [1] C. K. Remucal, M. Ginder-Vogel, *Environmental Science: Processes & Impacts*, 2014, **16**, 1247-1266.
- [2] R. J. K. Taylor, M. Reid, J. Foot and S. A. Raw, *Accounts of Chemical Research*, 2005, **38**, 851-869.
- [3] P. F. Smith, B. J. Deibert, S. Kaushik, G. Gardner, S. Hwang, H. Wang, J. F. Al-Sharab, E. Garfunkel, L. Fabris, J. Li and G. C. Dismukes, *ACS Catalysis*, 2016, **6**, 2089-2099.
- [4] D. Vernekar, S. Ratha, C. Rode, D. Jagadeesan, *Catalysis Science & Technology*, 2019, **9**, 1154-1164.
- [5] T. W. van Deelen, C. Hernández Mejía and K. P. de Jong, *Nature Catalysis*, 2019, **2**, 955-970.
- [6] A. B. Getsoian, Z. Zhai and A. T. Bell, *Journal of the American Chemical Society*, 2014, **136**, 13684-13697.
- [7] K. Mudiyansele, S. D. Senanayake, L. Faria, S. Kundu, A. E. Baber, J. Graciani, A. B. Vidal, S. Agnoli, J. Evans, R. Chang, S. Axnanda, Z. Liu, J. F. Sanz, P. Liu, J. A. Rodriguez and D. J. Stacchiola, *Angewandte Chemie International Edition*, 2013, **52**, 5101-5105.
- [8] Y. Ning, M. Wei, L. Yu, F. Yang, R. Chang, Z. Liu, Q. Fu and X. Bao, *The Journal of Physical Chemistry C*, 2015, **119**, 27556-27561.
- [9] L. Yu, G. Zhang, C. Liu, H. Lan, H. Liu and J. Qu, *ACS Catalysis*, 2018, **8**, 1090-1096.
- [10] D. Yan, Y. Li, Y. Liu, R. Zhuo, Z. Wu, B. Geng, J. Wang, P. Ren, P. Yan and Z. Geng, *Materials Letters*, 2014, **136**, 7-10.
- [11] X. Gao, G. Sheng and Y. Huang, *Science China Chemistry*, 2013, **56**, 1658-1666.
- [12] P. F. Smith, B. J. Deibert, S. Kaushik, G. Gardner, S. Hwang, H. Wang, J. F. Al-Sharab, E. Garfunkel, L. Fabris and J. Li, *ACS Catalysis*, 2016, **6**, 2089-2099.
- [13] F. Buciuman, F. Patcas, R. Craciun and D. R. T. Zahn, *Physical Chemistry Chemical Physics*, 1999, **1**, 185-190.
- [14] T. Kohler, T. Armbruster and E. Libowitzky, *Journal of Solid State Chemistry*, 1997, **133**, 486-500.
- [15] S. Gnanam and V. Rajendran, *Journal of sol-gel science and technology*, 2011, **58**, 62-69.
- [16] M. Newville, *Reviews in Mineralogy and Geochemistry*, 2014, **78**, 33-74.
- [17] E. S. Ilton, J. E. Post, P. J. Heaney, F. T. Ling and S. Kerisit, *Applied Surface Science*, 2016, **366**, 475-485.
- [18] A. J. Fatiadi, in *Organic Syntheses by Oxidation with Metal Compounds*, Springer, 1986, pp. 119-260.
- [19] M. Ramstedt, A. Shchukarev, S. Sjöberg, *Surface and Interface Analysis: An International Journal devoted to the development and application of*

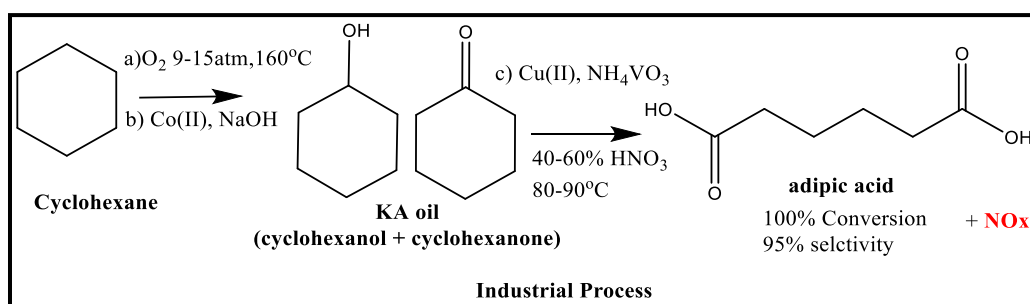
- techniques for the analysis of surfaces, interfaces and thin films* , 2002, **34**, 632-636.
- [20] D. Vernekar, S. S. Sakate, C. V. Rode and D . Jagadeesan, *Journal of Catalysis*, 2019, **378**, 80-89.
- [21] M.-L. Bailly, C. Chizallet, G. Costentin, J.-M. Krafft, H. Lauron-Pernot and M. Che, *Journal of Catalysis*, 2005, **235**, 413-422.

Chapter 5

Amorphous WCoFeO(OH) for oxidant-free liquid phase catalytic conversion of cyclohexane to adipic acid

5.1 Introduction

Among the most widely available commercial aliphatic dicarboxylic acids, adipic acid is at the forefront primarily due to its use as a feedstock for the production of nylon 66 resin, polyurethanes, food additives, plasticizers and pharmaceuticals.[1, 2] Rapidly expanding global construction industry is also projected to drive the product demand in building components such as exterior panels, insulation materials, and house hold electronics. Growing automotive and packaging industries are also contributing toward the market growth of adipic acid. The global market size for adipic acid (AA) is projected to reach 8 billion pounds by 2024 based on a new report by Grand View Research, Inc. [3] Importantly, almost 50% of the production of adipic acid is carried out by the oxidation of cyclohexane. The current industrial process involves a harsh oxidation of cyclohexane using cobalt based catalyst to a mixture of cyclohexanol and cyclohexanone, commonly known as KA oil (Scheme 5.1). Subsequently, the use of homogeneous vanadium-based catalysts and HNO₃ convert KA oil to adipic acid in high yield.[4] The overall process consumes large amounts of energy as well as emits toxic NO_x.



Scheme 5.1: Industrial process for Adipic Acid production from cyclohexane oxidation[4]

Other preparation routes involve selective oxidation of cyclohexene, cyclohexanone and n-hexane.[5] Catalytic pathways involving lignocellulose-derived chemicals such as 5-hydroxymethylfurfural, D-glucose, γ -valerolactone and compounds representative of lignin and lignin-derived bio-oils are also explored.[5] The direct conversion of cyclohexane to adipic acid using molecular oxygen or H₂O₂ is an appealing process due to its clean and ideal oxidation conditions.[6] H₂O₂ in fact has high content of ‘active’ oxygen, and the probable by-product is water alone; moreover H₂O₂ is cheaper and safer than other peroxides. Hence, these processes are utilized in pursuit of the goal of ‘green chemistry’. Thus, there is an obvious need

to develop a green strategy to efficiently produce bulk chemicals like adipic acid. Many efforts have been taken in this direction. Direct conversion of cyclohexane into AA involves formation of KA oil as an intermediate in the first step followed by its subsequent oxidation to yield AA. Catalysts such as $\text{Mn}(\text{OAc})_2/\text{Co}(\text{OAc})_2$, [7] μ_3 -oxo-bridged Co/Mn cluster complex, [8] microporous FeAlPO-31, [9] Mn/HTS-1 and manganese porphyrins have been shown to carry out the reaction using molecular O_2 . [10, 11] Similarly, H_2O_2 as an oxidizing agent has been interestingly used predominantly along with tungsten-based catalysts. For example, Silver supported tungsten oxide, [12] silica-functionalized ammonium tungstate, [13] $\text{Na}_2\text{WO}_4/\text{H}_3\text{PO}_4$, [14] $\text{H}_2\text{WO}_4/\text{TS}-1$ [4] are few of the reported materials. Literature studies showed that the active sites required for the conversion of cyclohexane to KA oil and then to AA are different. In $\text{H}_2\text{WO}_4/\text{TS}-1$ catalyst, titania sites are important for the KA oil generation whereas W sites play vital role in the C-C cleavage of KA oil intermediates to AA. Similarly, in the case of shape selective FeAlPO-31 catalyst, the role of transition metal Fe was pivotal for cyclohexane to cyclohexanol oxidation. Hence, a bifunctional catalyst containing two different active sites for two different steps of the reaction sequence would be highly beneficial. Moreover, the direct synthesis of AA from cyclohexane involves activation of C-H bond of cyclohexane in the first step. Also, in the second step, tautomerization takes place assisted by proton abstraction of cyclohexanone. We looked keenly into these aspects and attempted to explore a potential mixed metal oxyhydroxide catalyst as the surface hydroxyl groups can provide the necessary active sites. For this purpose, the combination of $\text{FeO}(\text{OH})$ and $\text{CoO}(\text{OH})$ oxyhydroxide catalysts was explored, which have been known for oxidation properties and oxygen evolution reactions. [15, 16] The use of tungsten (W) having redox characteristic, in the matrix composite containing Co and Fe oxyhydroxide was expected to provide suitable active sites and modulate the overall electron density required for each step of the catalysis reaction such as C-H bond activation, proton abstraction and C-C bond cleavage and oxidation properties. Metal oxyhydroxide $\text{MO}(\text{OH})$ is an interesting class of material containing abundant surface hydroxyl groups than metal oxides along with M-O-M linkages. The predominant advantage of using $\text{MO}(\text{OH})$ for these applications is due to the nano size and presence of dissociable hydroxyl groups.

5.2: Experimental Section:

Materials used: tungsten chloride (WCl_6), cobalt chloride ($CoCl_2$), ferric chloride anhydrous ($FeCl_3$), ethanol (EtOH), Propylene oxide, Deionized water, cyclohexane, acetone.

5.2.1: Synthesis of mixed metal oxyhydroxides

WCoFeOOH: This material was prepared by a modified sol-gel technique.[17] The tungsten, cobalt and iron precursors in the form of anhydrous WCl_6 (0.9mmol), $CoCl_3$ (0.9mmol) and $FeCl_6$ (0.9mmol) were dissolved in 2mL ice cooled ethanol in a glass vial. To this, a solution of ethanol 2mL in DI water (0.18mL) was then added. All the liquids were ice cooled to prevent uncontrolled hydrolysis of the metal salts. Controlled hydrolysis was done using 1mL of propylene oxide added slowly to the above solution and formation of dark green gel. This gel was aged for different time intervals (24h, 48h, 72h) and then dried at 60 °C to obtain WCoFeOOH.

WCoOOH/WFeOOH/CoFeOOH:

The same material synthesis protocol was followed as described above with only two metal precursors used.

FeO(OH): 4 g $FeCl_2 \cdot 4H_2O$ was dissolved in distilled water. To this, 1 M NaOH was added until the pH of the solution reached 6.5-6.8 forming greenish black deposits. Oxygen was bubbled through this solution for 20 minutes to obtain orange deposits i.e. γ -FeO(OH) which were separated by filtration and washed with ethyl alcohol and distilled water several times and dried at 60 °C.

CoO(OH): 50 mL of 0.1 mol/L NaOH solution was added drop wise into 80 mL of 0.05 mol cobaltous nitrate solution at 45 °C. A pink precipitate was produced Which was then filtered and washed 3 times with deionized water. The precipitate was dissolved in 5 mL of 8 mol NaOH along with 2 mL of 30% H_2O_2 and kept at 45 °C for 18 h. The final brown precipitate was filtered and washed with deionized water 3 times. The precipitate was collected and dried at 65 °C.

5.2.2 Cyclohexane oxidation: One pot oxidation of cyclohexane was performed in a 25 mL Teflon lined autoclave equipped with a magnetic stirrer. Typically, 2.1g (25 mmol) of cyclohexane along with 0.05g of catalyst was mixed in a 12 mL of

acetone. The autoclave was sealed and kept in an oil bath maintained at 90 C and stirred for 24h. After the reaction, the catalyst was filtered and the unreacted cyclohexane, cyclohexanol and cyclohexanone were identified using GC-MS. Adipic acid and other overoxidation compounds such as succinic acid, glutaric acid and valeric acid were identified using Agilent HPLC using a RP-18 column and using water: Methanol 9:1 with a phosphate buffer (0.001M) as the mobile phase.

5.2.3 Acidity measurements: *In situ* pyridine adsorption/dissociation Infrared Spectroscopy measurements were done using PerkinElmer 2000 Frontier FT-IR equipped with Praying Mantis™ assembly using MCT (HgCdTe) detector. 10µL of pyridine was injected into the port from which the injected molecule was driven under nitrogen flow (50mL/min) and adsorbed on the weighed sample. The FTIR measurements were performed and data was then analyzed using the spectrum software and compared with the blank measurements.

Emeis Equations

$$C_L = K_L \times A_{1450} = (\pi / \text{IMEC}_L) \times (r^2/w) \times A_{1450} \quad \text{----- (I)}$$

$$C_B = K_B \times A_{1540} = (\pi / \text{IMEC}_B) \times (r^2/w) \times A_{1540} \quad \text{----- (II)}$$

Where,

C_L and C_B = concentration of pyridine on Lewis and Brønsted acid sites.

A_{1450} and A_{1540} = integrated area of band at 1450 cm^{-1} and 1540 cm^{-1}

K_L and K_B = molar extinction constant for Lewis acid sites and Brønsted acid sites

IMEC_L = integration molar extinction coefficient (2.22 $\text{cm}/\mu\text{mol}$) for Lewis acid sites

IMEC_B = integration molar extinction coefficient (1.67 $\text{cm}/\mu\text{mol}$) for Brønsted acid sites

r = radius of self-supporting disk of praying mantis assembly

weight of sample pressed into self-supporting disk of praying mantis assembly.

5.3 Results and Discussion

5.3.1 Material Characterization

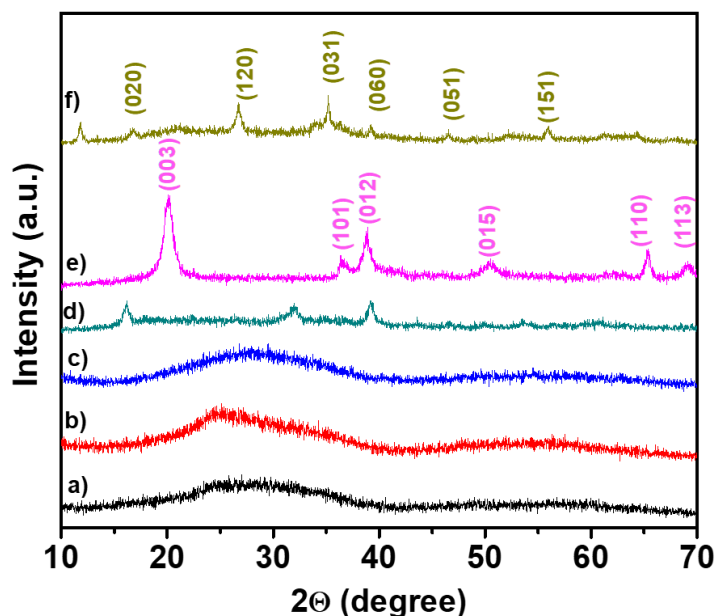


Fig 5.1: X-ray Diffraction pattern for (a) WFeCoO(OH) (b) WFeO(OH) (c) WCoO(OH) d) CoFeO(OH) e) CoO(OH) f) FeO(OH)

WFeCoO(OH) was synthesized using a modified procedure of a reported method. The details are given in the experimental section. The methodology involves using equimolar quantities of Fe, Co and W precursors with controlled incorporation of W^{6+} in CoFe oxyhydroxides in a homogeneous manner. Fig 5.1 shows the XRD pattern of the synthesized WFeCoO(OH). Broad peaks occurred around $2\theta = 30^\circ$. There were no sharp peaks that could be assigned to any crystalline phases. In contrast, FeO(OH) (JCPDS card no 73-2326) and CoO(OH) (JCPDS card No. 01-073-1213) showed a crystalline morphology in consonance with standard JCPDS data. The presence of large W atom (1.93 \AA) in the Co-Fe matrix ($1.56\text{-}1.52 \text{ \AA}$) led to an altered amorphous feature. Whereas, W^{6+} bereft samples showed crystalline behaviour with distinct peaks. The infrared spectrum (Fig 5.2) of WFeCoO(OH) (trace a) showed broad metal-oxygen linkages in the region between $600\text{-}900 \text{ cm}^{-1}$. The presence of hydroxyl groups was also noticed due to the broad band around 3200 cm^{-1} .

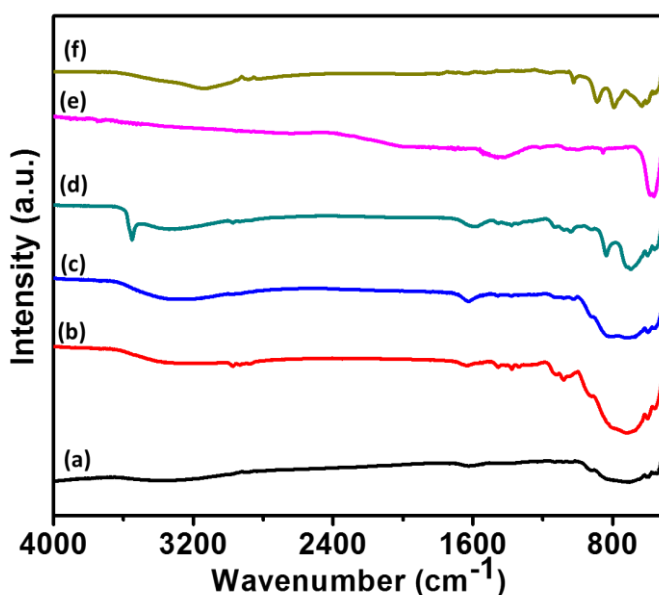


Fig 5.2: Infrared Spectrum of (a) WFeCoO(OH) (b) WFeO(OH) (c) WCoO(OH) (d) CoFeO(OH) (e) CoO(OH) (f) FeO(OH)

A broad band at $590\text{--}710\text{ cm}^{-1}$ can be assigned to W–O–W, W–O–H, and W–O· · ·HO–W stretch vibrations. [18] The infrared spectrum of CoO(OH) shows bands at $560, 727, 875,$ and 1427 cm^{-1} . [19] For FeO(OH) (trace f) bands around $620\text{--}680\text{ cm}^{-1}$ are due to Fe–O symmetric stretching. Bands in the region of $750\text{--}1000\text{ cm}^{-1}$ are characteristic due to –OH bending and stretching vibrations. [20] Electron Microscopy studies of WFeCoO(OH) (Fig 5.3a) indicated that the amorphous nature with no any distinct metal oxide features such as crystal planes, particle size and surface area suggest that the material was oxyhydroxide. [21] Electron diffraction pattern (Fig 5.3b) of the material too confirmed the amorphous nature of WFeCoO(OH). Elemental Analysis presented in Figs 5.3c and d showed atomic percent for Fe, Co, W as 38, 34 and 27 %, respectively, indicating a near homogeneous distribution of the metals. The surface composition of WFeCoO(OH) was studied using X-ray Photoelectron Spectroscopy (XPS). The full scan XPS spectra is presented in Fig 5.4a. Peaks due to Fe2p, Co2p, W4f and O1s could be easily identified. Deconvoluted O1s XPS spectra (Fig 5.1b) confirmed contributions from three kinds of oxygen species a) oxygen involved in M–O–M linkages b) the surface hydroxyl groups and c) chemisorbed and physisorbed water.

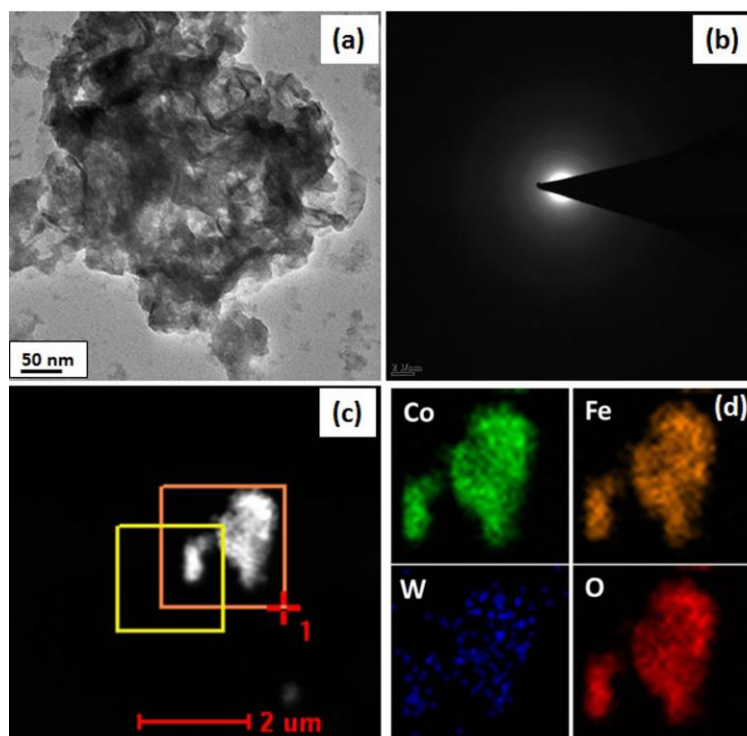


Fig 5.3. a) Transmission Electron Microscopy image of WFeCoO(OH) b) Electron Diffraction pattern c) HAADF STEM image and d) elemental mapping of the selected orange portion in c).

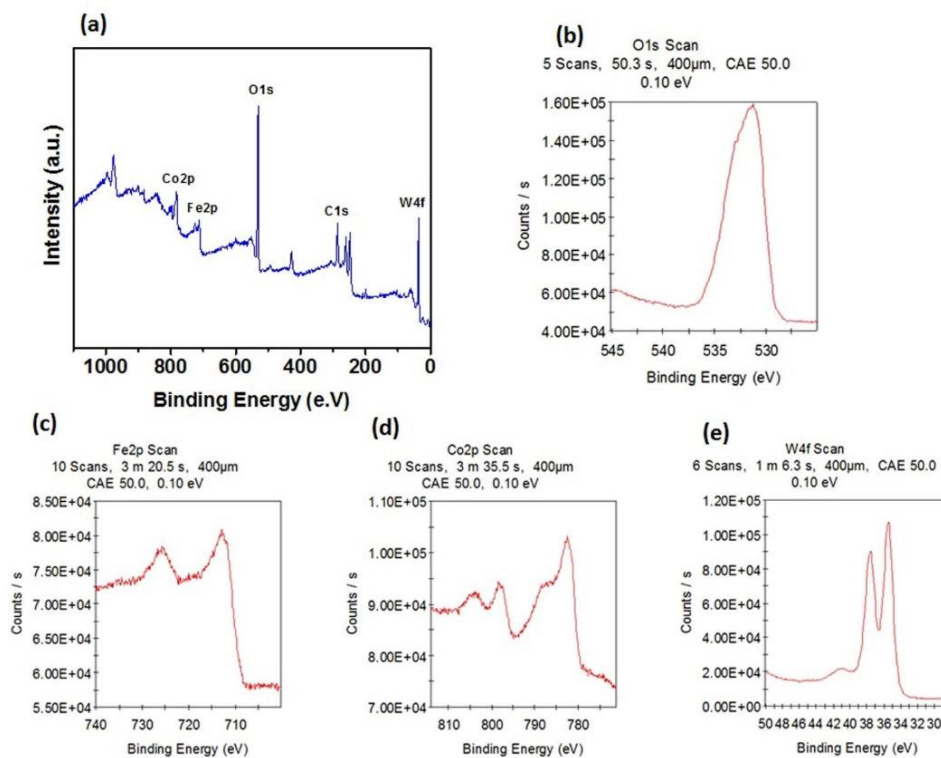


Fig 5.4. XPS spectra of a) full scan of WFeCoO(OH) b) O1s c) Fe2p d) Co2p e) W4f of WFeCoO(OH)

The XPS signal of Fe2p (Fig 5.4c) showed two peaks due to Fe2p_{3/2} and Fe2p_{1/2} at 710.6 eV and 724.1 eV respectively. High-resolution Co 2p spectrum (Fig 5.4d) show spin-orbit splitting into 2p_{1/2} and 2p_{3/2} components.[19] In addition to the normal core photoelectron lines, satellite line structure can be observed in the late 3d transition metal compounds. These additional spectral lines have been related either to a coupling between unpaired electrons in the atom (multiplet splitting) or a multiple electron excitation (the so-called ‘shakeup’).[22] In the case of tungsten (Fig 5.4 e), peaks at 37.9 eV and 35.8 eV can be attributed to W4f_{7/2} and W4f_{5/2} of W⁶⁺ species.[4]

5.3.2 Catalyst activity

The direct cyclohexane to adipic acid conversion was performed over a variety of catalysts and the results of which are presented in Table 5.1 First, pure single metal oxyhydroxides such as FeO(OH) and CoO(OH) were tested however, a poor conversion of 2-3% (Table 5.1, Entry 2) was observed for FeO(OH). Whereas, CoO(OH) gave a higher conversion of 16% but with a selectivity 80% to KA oil (Table 5.1 Entry 3). The role of active Co for KA oil synthesis is well known;[7] hence this result isn’t surprising. The double metal oxyhydroxides (Table 5.1 Entries 5 and 6) again showed a poor conversion (5-6%) but WCoO(OH) (Table 5.1 Entry 4) showed a 90% selectivity to adipic acid with a conversion of 19%. This indicated that W and Co sites together can help to achieve 90 % selectivity to adipic acid however, the conversion being marginal. Interestingly, our material WFeCoO(OH) gave a 40% conversion with 67 % selectivity to adipic acid (Table 5.1, Entry 7). On increasing the reaction time to 48h, conversion of cyclohexane increased to 56% and 90% selectivity to adipic acid was achieved (Table 5.1 Entry 10). This is an encouraging result considering the reported values of conversion and selectivity by various heterogenous catalysts. [4] Moreover, no any additional oxidizing agent such as H₂O₂ or excess of O₂ was used. The control reaction involving H₂O₂ (Table 5.1, Entry 11) did not improve the conversion and in contrast was detrimental to the overall activity (conversion 20%, AA selectivity 54%).

Table 5.1: Cyclohexane to Adipic Acid conversion using various catalysts

Sr No	Catalyst	Conversion (%)	Selectivity (%)		
			cyclohexanol + cyclohexanone	Adipic acid	others
1	No catalyst	0	-	-	-
2	FeO(OH)	2-3	92	8	-
3	CoO(OH)	16	80	20	-
4	WCoO(OH)	19	6	90	4
5	CoFeO(OH)	5	82	8	10
6	WFeO(OH)	6	78	16	6
7	WFeCoO(OH)	40	25	67	8
8	WFeCoO(OH) ^a	71	14 ^d	73	13
9	WFeCoO(OH) ^b	84	-	83	17
10	WFeCoO(OH) ^c	56	5	90	5
11	WFeCoO(OH) ^e	20	34	54	12
12	WCl ₆	No reaction	-	-	-
13	CoCl ₃	No reaction	-	-	-

25 mmol cyclohexane, 50 mg Catalyst, Acetone 12 mL, sealed autoclave, 90 °C, 24h, others include glutaric acid, succinic acid, valeric acid, ^a cyclohexanol as starting reactant instead of cyclohexane, ^{b d} Cyclohexanone, ^c 48 h reaction, ^e reaction carried out in the presence of 2.7 mL 30% H₂O₂ as an oxidizing agent. Conversion (GC MS) = [Initial cyclohexane concentration (mmol) - Final cyclohexane concentration (mmol)] / 100

This is because, H₂O₂ probably deactivated the WFeCoO(OH) as change in physical appearance (colour) in the catalyst was evident after addition of H₂O₂ and a brisk effervescence was observed. More studies are needed to conclusively ascertain the deactivation of the material in the presence of H₂O₂. On starting the reaction using cyclohexanol (Table 5.1, Entry 8) and cyclohexanone selectivities were obviously improved to 73 and 83% (Table 5.1, Entry 9), respectively, as the first step of cyclohexane oxidation was not needed. Cyclohexanone is easily activated by proton abstraction to form an enol[4] and hence, gives a higher activity as compared to cyclohexanol. The precursors, WCl₆ and CoCl₃ were also tested for this reaction which showed no any conversion. Having identified the active catalyst under the

given reaction conditions, the effect of change in catalyst amount and effect of temperature on the catalytic activity were also studied, keeping other parameters unchanged. The results are shown in Fig.s 5a and b.

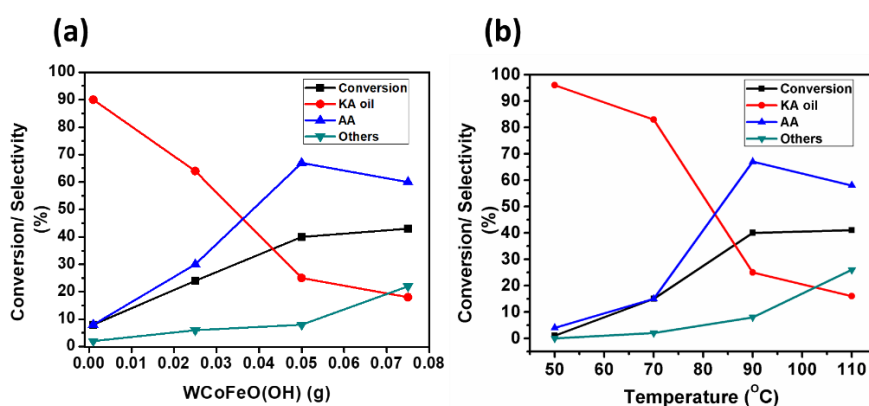


Fig 5.5: a) Effect of Catalyst amount and b) Effect of reaction temperature on activity:

The catalyst amount was varied between 10 mg to 75mg. The optimal conversion and selectivity results were obtained for 50mg of catalyst. Increasing the catalyst amount beyond 50 mg led to an increase in the concentration of the side product. Similarly, the temperature around 90 °C gave the maximum adipic acid yields (67%) (Fig 5.5b).

5.3.3 Active sites

5.3.3.1 Acidity of WFeCoO(OH)

The insights gained into the mechanistic pathway from literature have set forth the rational design of bifunctional heterogeneous catalysts containing Brønsted acid and metal sites as the primary way of getting high adipic acid yields.[23] To understand the reason for this high conversion and selectivity for the reaction the pyridine IR measurements of the sample were performed. The difference spectra obtained from subtracting pure spectra from pyridine adsorbed spectra is given in Fig 5.6a. Pyridine, being a base can get easily adsorbed to acid sites and can be identified using Infrared spectroscopy. The Lewis acidic interaction of the metals with pyridine was observed to be predominant at 1446 cm^{-1} . The weak Brønsted acidity due to interaction of the Brønsted acid sites and pyridine forming pyridinium ion were observed at 1541 cm^{-1} . Unspecified peak also occurred at 1487 cm^{-1} .

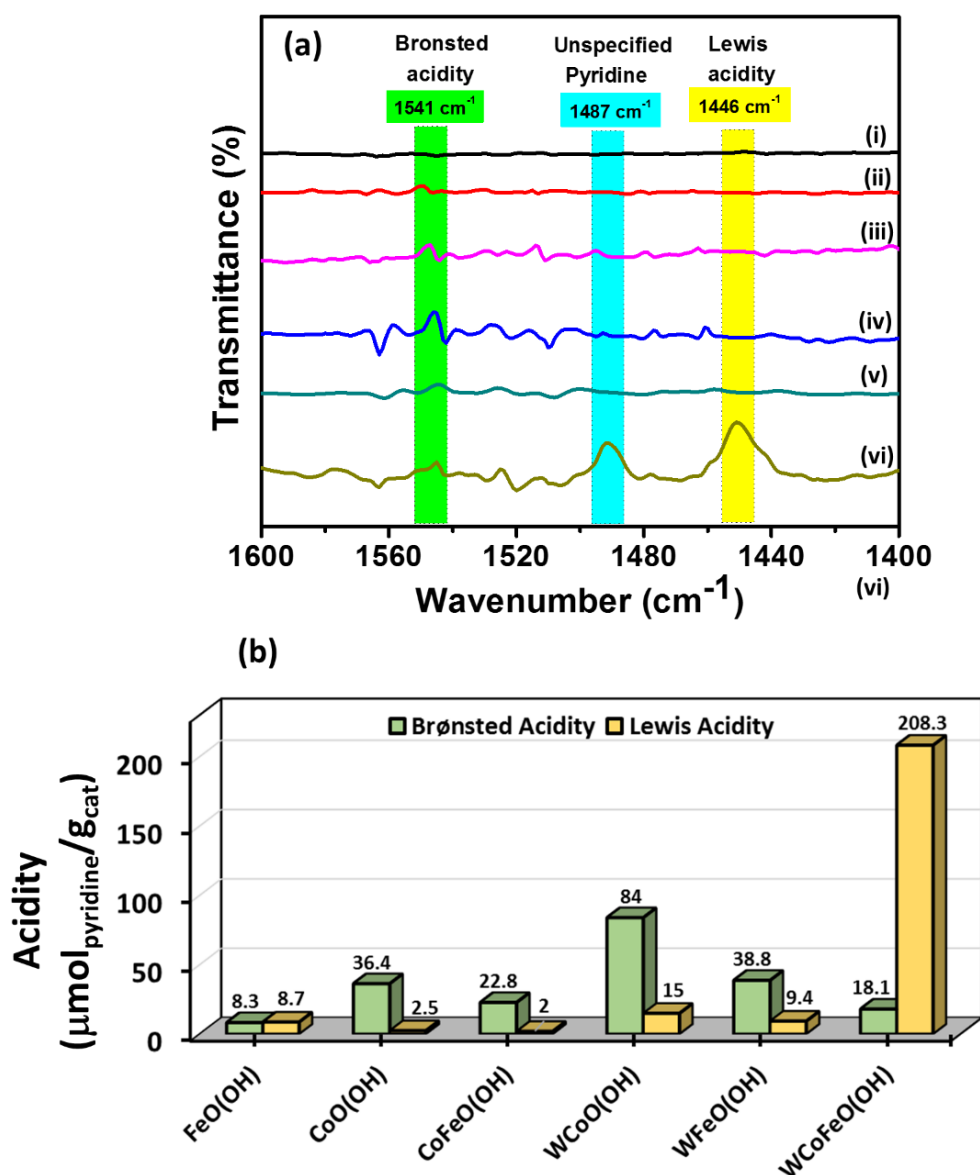
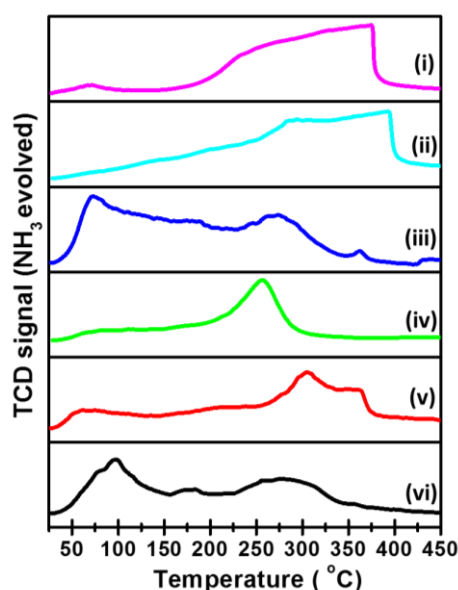


Fig 5.6: a) Pyridine IR difference spectra for (vi) WFeCoO(OH) (v) WFeO(OH) (iv) WCoO(OH) (iii) CoFeO(OH) (ii) CoO(OH) (i) FeO(OH) b) Quantified Brønsted and Lewis acidity for the samples

Both Brønsted and Lewis acidity were quantified based on Emmis algorithm. The details are provided in the experimental section. The quantified data is plotted as Fig 5.6b. FeO(OH) had a better Lewis acidity ($8.7 \mu\text{mol}/\text{g}$) as compared to CoO(OH) ($2.5 \mu\text{mol}/\text{g}$). Additional presence of W^{6+} appeared to increase the Brønsted acidity in WFeO(OH) and WCoO(OH) as compared to tungsten bereft counterparts. Most importantly, in the case of WFeCoO(OH), Lewis acidity value increased to $208.3 \mu\text{mol}/\text{g}$ which was almost 14 times the next best Lewis acidity value. This surge was clearly evident in trace (vi) in Fig 5.6a. This strong Lewis acidity could be one of the reasons for the high activity of WFeCoO(OH). Hence, the controlled incorporation

of W^{6+} in CoFe oxyhydroxides in a homogeneous manner must be responsible for this high acidity. Another factor responsible for the high acidity of $WFeCoO(OH)$ could be the substitution of a W dopant at a Co^{4+}/Fe^{3+} site resulting in (i) due to the high charge of W which prefers the W^{6+} formal oxidation state there could be migration of protons away from W, towards oxygen at Co sites, and (ii) compressive strain of larger W atoms on the surrounding Co/Fe sites.[17] As a result, these geometric and electronic changes provide optimal adsorption energetics for the intermediates and hence improving its activity. NH_3 TPD of our sample was also performed to quantify the acidity of $WFeCoO(OH)$. The acidity in terms of 5.1 mmol/g of NH_3 desorbed was observed (Fig 5.7) which was again better than other controls. All the other controls gave acidity value in the range 2-3 mmol/g. This data was consistent with the Pyridine IR data.



Sr. No	Catalyst	Acidity (Ammonia TPD) mmol _{ammonia} /g _{cat}
1.	$WFeCoO(OH)$	5.1
2.	$WCoO(OH)$	2.8
3.	$WFeO(OH)$	3.1
4.	$CoFeO(OH)$	2.3
5.	$CoO(OH)$	2.5
6.	$FeO(OH)$	2.7

Fig 5.7: Ammonia TPD plot for (i) $FeO(OH)$ (ii) $CoO(OH)$ (iii) $WCoO(OH)$ (iv) $WFeO(OH)$ (v) $CoFeO(OH)$ (vi) $WFeCoO(OH)$ and their calibrated acidity values

5.3.4 DFT Calculations

Calculations for the deprotonation energies (DPE) for the Co-based oxyhydroxides were performed using plane wave density functional theory (DFT) code as implemented in Vienna ab initio simulation package (VASP-5.3.5 version).[24] These calculations were performed by Prof Haider's group in IIT-Delhi. The core

electrons were described using PAW potentials,[25] whereas Kohn Sham one electron valence states were expanded in a plane wave basis function. All the calculations were performed under spin-polarized condition, with Hilbert U_{eff} parameters of value 3.32 eV and 5.3 eV employed for Co and Fe, respectively[17]. The plane-wave basis sets were truncated at a cut-off energy of 396 eV. Revised Perdew-Burke-Ernzerhof (RPBE) exchange correlation functional developed by Hammer et al.[26] was used for all the calculations.

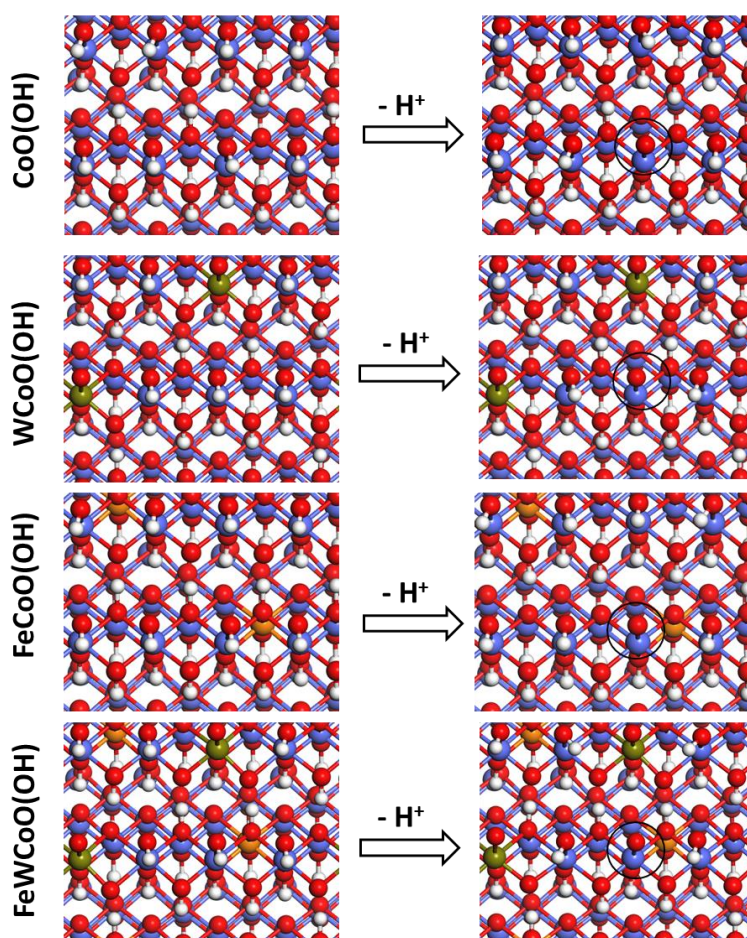


Fig 5.8: DFT optimized geometries of CoO(OH), WCoO(OH), FeCoO(OH) and FeWCoO(OH) catalyst surface and respective configuration after deprotonation.

Crystal structure of β -CoO(OH) was adapted from Materials Project database (materials ID. mp-31526).[27] The CoO(OH) surface was obtained by terminating the surface along the (01-12) direction, as suggested by Zhang et al.[17]. The surface terminal oxygens were passivated with hydrogen (Figure 1). The W, Fe and both W, Fe doped CoO(OH) surfaces was obtained as suggested in the reported work [17], are shown in Fig 5.8. The surface slabs were modelled using a slab of 4 layers of size

4 x 4, as given in Fig 5.8. The bottom two layers were fixed while the upper half along with the terminal hydrogens were allowed to relax. A Monkhorst-Pack k point grid with 3 x 3 x 1 mesh was used to sample the Brillouin zones.[28] The slabs were periodically repeated along the (001) direction with 20 Å vacuum between the slabs to mimic the surface and subsurface restructuring. The convergence criteria for force and energy were set to 0.05 eV/Å and 10⁻⁴ eV, respectively.

To calculate the deprotonation energy, a hydrogen is removed from each of the four Co-based oxyhydroxide surface, as shown in Fig 5.8. The hydrogen was assigned charge +1, whereas the deprotonated oxyhydroxide surfaces were assigned -1 charge.

The deprotonation energy (DPE) is calculated as,

$$\text{DPE} = (E_{\text{oxyhydroxide-DP}^{-1}} + E_{\text{H}^{+1}}) - E_{\text{oxyhydroxide}}$$

Where $E_{\text{oxyhydroxide}}$ and $E_{\text{oxyhydroxide-DP}^{-1}}$ are the DFT calculated energies of oxyhydroxide surfaces, respective deprotonated oxyhydroxide surfaces. $E_{\text{H}^{+1}}$ is the energy of proton in gas-phase.

5.3.4.1 Results of DFT studies:

To understand the adipic acid selectivity of the Co-based oxyhydroxides, DPE is calculated using DFT method. DPE has been shown to be an important descriptor to analyze the trends in acid catalyzed reaction over solid acid catalyst like HPA[3, 29-31] and zeolites[32, 33], as has been shown by Neurock, Iglesia, van Santen and co-workers. The DPE value for the undoped CoO(OH) can be calculated as 1665 kJ/mol, which is higher to the DPE values observed for HPAs (1082 kJ/mol for H₃PW₁₂O₃₀), but comparable to the ones obtained for Brønsted acidic MFI zeolites [33] The DPE was found to decrease drastically on doping CoO(OH) with W (DPE ~ 1244 kJ/mol for WCoO(OH)), which is slightly higher compared to the DPE values of HPAs. (Fig 5.9) When Fe is used as dopant to CoO(OH) no drastic change in the DPE values is observed, DPE of FeCoO(OH) ~ 1662 kJ/mol. Co-doping Fe and W with CoO(OH) in FeWCoO(OH) provide the moderate decrease in DPE values (DPE ~ 1434 kJ/mol), which is lower than parent CoO(OH) but higher compared to WCoO(OH).

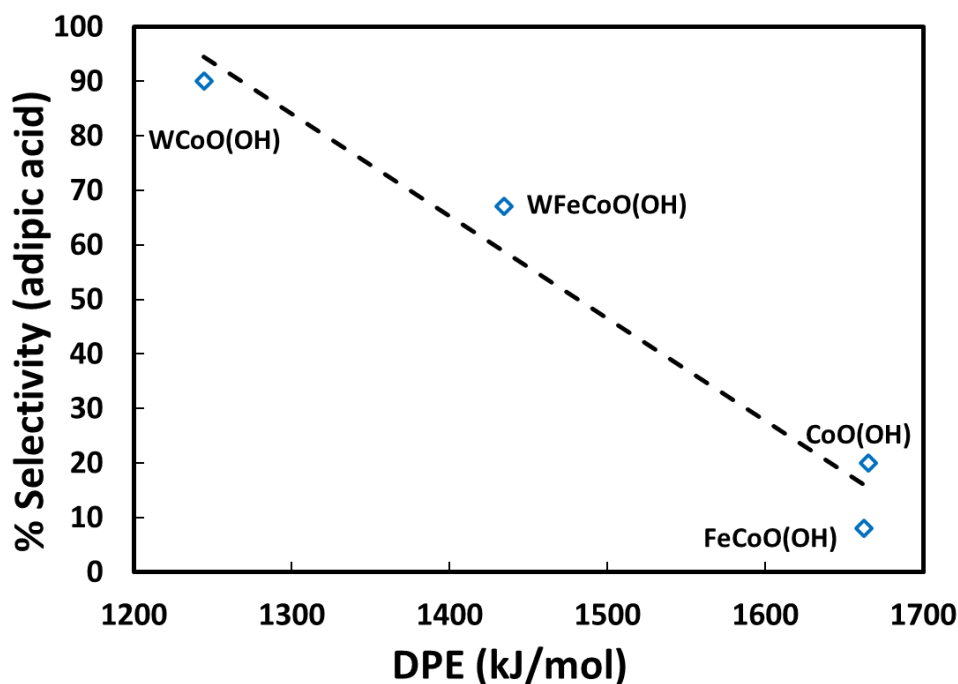


Fig 5.9: A plot of DPE vs adipic acid selectivity for the various catalysts.

In overall the DPE trends for the W, Fe doped CoO(OH) is: $\text{WCoO(OH)} < \text{WFeCoO(OH)} < \text{FeCoO(OH)} \sim \text{CoO(OH)}$. As proposed in the mechanism for the formation of adipic acid through the ring-opening of cyclohexanone, the Brønsted acidity plays a pivotal role, which will determine the adipic acid selectivity in the cyclohexane oxidation reaction. The selectivity to adipic acid observed in the experiment shows a linear correlation with the calculated DPE values of the respective catalyst, as shown in the Fig 5.9.

5.3.5 Recyclability and catalyst stability studies:

The efficiency of WFeCoO(OH) catalyst was established by its recycle studies (Fig. 5.10). After completion of the first run, the catalyst was separated by filtration, washed several times with acetone and dried at 100 °C and then used for four subsequent runs. Fig. 5.10 shows that the cyclohexane conversion did drop from 40% to 31% in four cycles. However, during this period, the adipic acid selectivity fluctuated between 67-65 % with minor losses. Though, there was a gradual drop in the conversion, the selectivity to the required product was stable. More studies were needed to identify the loss in conversion as XRD of the fresh and used catalysts did not show any significant changes Fig 5.11.

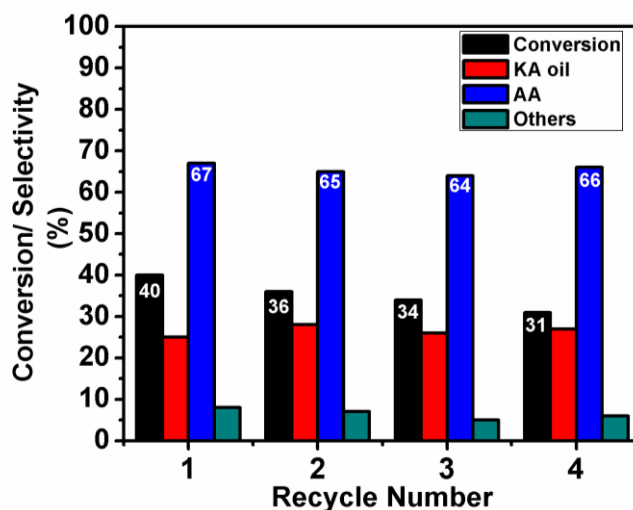


Fig 5.10: Recycle studies for WFeCoO(OH)

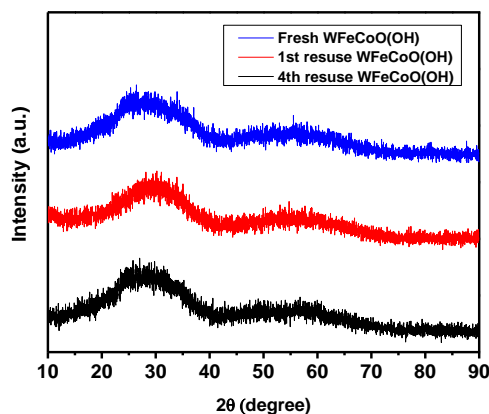


Fig 5.11: XRD before and after the catalytic studies

5.4 Conclusions:

An unique mixed metal oxyhydroxide WFeCoO(OH) was developed using controlled hydrolysis of the metal precursors. The material was structurally characterized using XRD, IR, TEM, Pyridine IR and NH₃ TPD. The material was tested for a one pot oxidation of cyclohexane to adipic acid which gave 56% conversion and 90% selectivity to adipic acid. The higher extent of Lewis acidity of WFeCoO(OH) and high oxidation states of the metals were proposed to be responsible for the observed activity. DFT calculations indicated that a decrease in deprotonation energies for WFeCoO(OH) as compared to undoped CoO(OH). Further work is needed to understand the mechanism of the reaction over WFeCoO(OH)

5.5 References

- [1] A. Castellan, J. Bart and S. Cavallaro, *Catalysis Today*, 1991, **9**, 237-254.
- [2] R. Roew, J. Sheskey and E. Quinn, *Handbook of pharmaceutical excipients*, 2009, 11-12.
- [3] Adipic Acid Market Size, Share & Trends Analysis Report By Application (Nylon 66 Fiber, Nylon 66 Resin, Polyurethane, Adipate Ester), By Region (APAC, North America, Europe, MEA, CSA), And Segment Forecasts, 2018 - 2024
- [4] J. Dai, W. Zhong, W. Yi, M. Liu, L. Mao, Q. Xu and D. Yin, *Applied Catalysis B: Environmental*, 2016, **192**, 325-341.
- [5] S. Van de Vyver and Y. Román-Leshkov, *Catalysis Science & Technology*, 2013, **3**, 1465-1479.
- [6] K. Sato, M. Aoki and R. Noyori, *Science*, 1998, **281**, 1646-1647.
- [7] T. Iwahama, K. Sjojyo, S. Sakaguchi, Y. Ishii, *Organic Process Research & Development*, 1998, **2**, 255-260.
- [8] S. Chavan, D. Srinivas and P. Ratnasamy, *Journal of Catalysis*, 2002, **212**, 39-45.
- [9] M. Dugal, G. Sankar, R. Raja and J. Thomas, *Angewandte Chemie*, 2000, **112**, 2399-2402.
- [10] G. Zou, W. Zhong, Q. Xu, J. Xiao, C. Liu, Y. Li, L. Mao, S. Kirk and D. Yin, *Catalysis Communications*, 2015, **58**, 46-52.
- [11] H. Li, Y. She, H. Fu, M. Cao, J. Wang and T. Wang, *Canadian Journal of Chemistry*, 2015, **93**, 696-701.
- [12] S. Ghosh, S. S. Acharyya, S. Adak, L. S. Konathala, T. Sasaki and R. Bal, *The Journal of Physical Chemistry C*, 2014, **16**, 2826-2834.
- [13] M. Vafaezadeh and M. Hashemi, *Catalysis Communications*, 2014, **43**, 169-172.
- [14] M. Shang, T. Noël, Q. Wang, Y. Su, K. Miyabayashi, V. Hessel and S. Hasebe, *Chemical Engineering Journal*, 2015, **260**, 454-462.
- [15] I. S. Pinto, P. H. Pacheco, J. V. Coelho, E. Lorençon, J. D. Ardisson, J. D. Fabris, P. P. de Souza, K. W. Krambrock, L. C. Oliveira and M. Pereira, *Applied Catalysis B: Environmental*, 2012, **119**, 175-182.
- [16] H. Wang, E. Feng, Y. Liu and C. Zhang, *Journal of materials chemistry A*, 2019, **7**, 7777-7783.
- [17] B. Zhang, X. Zheng, O. Voznyy, R. Comin, M. Bajdich, M. García-Melchor, L. Han, J. Xu, M. Liu and L. Zheng, *Science*, 2016, **352**, 333-337.
- [18] S. Y. Hou, Z. H. Zhou, T. R. Lin and H. Wan, *European journal of inorganic chemistry*, 2006, **8**, 1670-1677.
- [19] J. Yang, H. Liu, W. N. Martens and R. Frost, 2010, *The Journal of Physical Chemistry C*, **114**, 111-119.
- [20] D. Vernekar, S. S. Sakate, C. V. Rode and D. Jagadeesan, *Journal of Catalysis*, 2019, **378**, 80-89.

- [21] J.-P. Jolivet, M. Henry and J. Livage, *Metal oxide chemistry and synthesis: from solution to solid state*, Wiley-Blackwell, 2000.
- [22] N. McIntyre and M. Cook, *Analytical chemistry*, 1975, **47**, 2208-2213.
- [23] P. Bhanja, S. Chatterjee, A. K. Patra and A. Bhaumik, *Journal of colloid and interface science*, 2018, **511**, 92-100.
- [24] G. Kresse and J. Furthmüller, *Phys. Rev. B*, 54 1996, **54**, 11169.
- [25] D. Vanderbilt, *Physical review B*, 1990, **41**, 7892.
- [26] B. Hammer, L. B. Hansen and J. Nørskov, *Physical review B*, 1999, **59**, 7413.
- [27] A. Jain, S. Ong, G. Hautier, W. Chen, W. Richards, S. Dacek, S. Cholia, D. Gunter, D. Skinner, G. Ceder, *APL Materials*, 2013, **1**, 011002. ISSN 2166532X.
- [28] H. J. Monkhorst and J. Pack, *Physical review B*, 1976, **13**, 5188.
- [29] J. Macht, M. J. Janik, M. Neurock and E. Iglesia, *Journal of the American Chemical Society*, 2008, **130**, 10369-10379.
- [30] J. Macht, M. J. Janik, M. Neurock and E. Iglesia, *Angewandte Chemie International Edition*, 2007, **46**, 7864-7868.
- [31] M. J. Janik, J. Macht, E. Iglesia and M. Neurock, *The Journal of Physical Chemistry C*, 2009, **113**, 1872-1885.
- [32] R. Van Santen and G. Kramer, *Chemical Reviews*, 1995, **95**, 637-660.
- [33] A. J. Jones and E. Iglesia, *Acs Catalysis*, 2015, **5**, 5741-5755.

Chapter 6

Summary and Future Scope

6.1: Summary

This thesis describes the design and development of metal oxyhydroxide based catalyst systems for organic multistep reactions. The whole work is organised in total six chapters, which is summarised below.

Chapter 1 gives a general introduction to metal oxyhydroxides, their structures, synthesis methods and applications. The metal oxyhydroxides as heterogeneous catalysts for tandem reactions was hardly known until now and this work could be the first detail contribution in this area. The reason for multifunctionality of the material is explained based on the chemical equilibrium of surface hydroxyl groups and is explored in tandem catalysis in this chapter. This chapter also discusses the analytical tools used to explain results obtained related to the tandem catalysis. Finally, this chapter provides a blueprint of the motivation of this work.

Chapter 2 discusses the acid-base bifunctional behavior of the three hierarchically condensed phases namely, metal hydroxides $M(OH)_x$, metal oxyhydroxides $MO(OH)$ and metal oxides $M_x(O)_y$. CO_2 -TPD, NH_3 -TPD and Pyridine IR data showed the presence of acid and basic sites. The strength of acid sites was found to be higher for $MO(OH)$ while, $M(OH)_x$ possesses stronger basic sites. The presence of two types of active sites OH/O^- and O^{2-} on $MO(OH)$ surface was shown spectroscopically. $MO(OH)$ was found to be a versatile catalyst due to its stability and recyclability.

Chapter 3a: $MO(OH)$ is known for existing in several polymorphs. Polymorphs have identical chemical composition but different crystal structures. The acid-base bi-functional catalytic activity of the polymorphs of $FeO(OH)$ namely α , β , γ and δ was explored for the first time for deacetylation-Henry reaction. The polymorphs exhibited selectivity to different products which could be tuned to some extent by changing the time of reaction and sample composition. The origin of acid and base bifunctional sites was due to the surface chemical equilibrium between $FeO(OH)$ and $FeOO^-$ groups. The role of water in establishing the chemical equilibrium is also discussed in this chapter. The difference in the selectivity for the products with different polymorphs was explained based on the presence of variation of the density of active sites present on the crystal facets of the polymorphs. The results of this

work is published in Catalysis Science and Technology. (*Catalysis Science & Technology*, **2015**, 5(8), pp.4029-4038.)

Chapter 3b presents the use of γ -FeO(OH) as an environmental friendly, cost effective base catalyst for transformation of citral to pseudoionones (PS) and its analogues. Combined presence of Brønsted basic O^- and Lewis basic O^{2-} was effective for the PS synthesis. *In situ* CO₂ adsorption studies confirmed the presence of singly, double and triply coordinated hydroxyl groups with the active singly coordinated species in abundance. Experimental evidences clearly showed that externally added water promoted the formation of Brønsted basic O^- sites on FeO(OH) by deprotonating the surface hydroxyl groups. This O^- was responsible for drastic improvement in activity. The basicity on FeO(OH) obtained by water activation is chemically different from those present on other solid bases explored in literature for PS synthesis. Our studies also indicated that basicity due to (O^-) was superior and easily controllable based on water content in the system. The material also exhibited a wide substrate scope. The results of this work is published in Journal of Catalysis. (*Journal of Catalysis*, **2019**, 378, pp.80-89.)

Chapter 4a describes the design and utility of K- α -CrO(OH) as a bifunctional catalyst explored in sequential transformation of benzyl alcohol to a variety of C-C and C-N coupling products. The transformations were feasible because of the co-existence of redox Cr(III) and basic sites (O^- and O^{2-}) on the surface of the K- α -CrO(OH). The presence of electron rich sites (O^{2-}) due to doping of K and the surface hydroxyl groups were found to be the basic sites on the catalysts using spectroscopy and thermal probe studies. This being the first report on use of K- α -CrO(OH) in multifunctional catalysis, there is a promising scope to utilize this material for other catalytic transformations useful in fine chemical and pharmaceutical industries where multistep transformations are needed. The results of this is published in Catalysis Science and Technology. (*Catalysis Science & Technology*, **2019**, 9(5), pp.1154-1164.)

Chapter 4b discusses the design and utility of an mixed oxide-oxyhydroxide material MnOx(OH) was explored for the tandem oxidation-condensation reaction. The material showed structural and compositional difference from pure oxyhydroxide and oxides. The active sites being the redoxible Mn species, while

the basicity was exhibited by O^{2-} and O^- species. $MnO_x(OH)$ showed a larger contribution from O^{2-} as compared to O^- . Since the oxide phases were formed *in-situ*, the role of oxide-oxyhydroxide interface was important for activity. This was the first study on the role of oxide-oxyhydroxide interface in catalysis.

Chapter 5 includes the studies on an unique mixed metal oxyhydroxide $WFeCoO(OH)$, obtained by controlled hydrolysis of the respective metal precursors. The material was characterized using XRD, IR, TEM, Pyridine-IR and NH_3 -TPD and was tested for one pot conversion of cyclohexane to adipic acid with 56% conversion and 90% selectivity to adipic acid. The strong Lewis acidity of $WFeCoO(OH)$ and high oxidation states of the metals responsible for the observed activity. DFT calculations indicated a decrease in deprotonation energies for $WFeCoO(OH)$ as compared to undoped $CoO(OH)$ responsible for the high activity.

6.2 Salient outcome of the present thesis.

- Demonstrated the acid-base catalytic activity in $MO(OH)$ for the first time.
- Demonstrated the polymorph-dependent bifunctional catalytic activity in $MO(OH)$ for the first time.
- Role of H_2O in the acid-base activity of the catalysts studied in the present work.
- Extended the bifunctional activity beyond acid-base reactions to redox-base catalysis
- Demonstrated the use of $MO(OH)$ in the synthesis of industrially important chemicals such as PS and adipic acid for the first time.
- Conclusive experimental evidences established the nature of active sites of $MO(OH)$. Acidity in metal oxyhydroxides was due to the surface hydroxyl groups ($-OH$) and Lewis acidic metal centers. Basicity in metal oxyhydroxides was due to the deprotonated surface hydroxyl group (O^-) and oxide ion (O^{2-}). Redox activity in metal oxyhydroxides was due to the metal centers existing in variable oxidation states.

6.3 Future Scope

Metal oxyhydroxides as active catalysts were explored for the first time in this research work. Our work on mixed metal oxyhydroxide showed improved activity for industrially important oxidation reactions such as adipic acid production from cyclohexane. The novel properties of such naturally available minerals can be useful for further applications in several catalytic reactions of practical importance. Combining any other active site (e.g. redox active site) with acid-base sites on MO(OH) opens up possibilities of many new catalyst materials would be useful in fine chemical and pharmaceutical industries where multistep transformations are needed. Hence, this work could give new direction for the present-day heterogeneous catalysis by incorporating various metal oxyhydroxides as supports or active catalysts.

List of Publications

1. *Tunable acid–base bifunctional catalytic activity of FeO(OH) in an orthogonal tandem reaction*

Dnyanesh Vernekar, Dinesh Jagadeesan Catalysis Science & Technology 5, 4029-4038, 10, 2015.

2. *Efficient bifunctional reactivity of K-doped CrO (OH) nanosheets: exploiting the combined role of Cr (III) and surface –OH groups in tandem catalysis*

Dnyanesh Vernekar, Satyajit Ratha, Chandrashekhar Rode, and Dinesh Jagadeesan Catalysis Science & Technology 9 (5), 1154-1164, 2019

3. *Water-promoted surface basicity in FeO(OH) for the synthesis of Pseudoionones (PS) and their analogues*

Dnyanesh Vernekar, Sachin S. Sakate, Chandrashekhar V. Rode, and Dinesh Jagadeesan, Journal of Catalysis, 378, 80-89, 2019.

4. *New Opportunities in Heterogeneous Catalysis*

Dinesh Jagadeesan, **Dnyanesh Vernekar**, Sharad Gupta and Garima Jaiswal Proceedings of the Indian National Science Academy 85 (1), 23-41, 2019.

5. *Iron-carbon nanohybrid particles as environmentally benign electrode for supercapacitor*

Satyajit Ratha, **Dnyanesh Vernekar**, Kavin Sivaneri, Dinesh Jagadeesan and Chandra Sekhar Rout Journal of Solid State Electrochemistry 21 (6), 1665-1674, 1, 2017.

6. *Earth abundant iron-rich N-doped graphene based spacer and cavity materials for surface plasmon-coupled emission enhancements*

Venkatesh Srinivasan, **Dnyanesh Vernekar**, Garima Jaiswal, Dinesh Jagadeesan and Sai Sathish Ramamurthy ACS applied materials & interfaces 8 (19), 12324-12329, 8, 2016.

7. *Role of surface hydroxyl groups on hierarchically condensed phases (Hydroxides, Oxyhydroxides & Oxides) : Insight into surface acidity and basicity*

Dnyanesh Vernekar, Chandrashekhar Rode, and Dinesh Jagadeesan (to be submitted)

8. *Role of oxide-oxyhydroxide interface in defect $MnO_x(OH)$ for redox-base tandem activity*

Dnyanesh Vernekar, P Varsha, Chandrashekhar Rode and Dinesh Jagadeesan (to be submitted)

9 *Amorphous $WCoFeO(OH)$ for oxidant-free liquid phase catalytic conversion of cyclohexane to adipic acid*

Dnyanesh Vernekar, Mohammad Dayyan, M. Ali Haider, Chandrashekhar Rode and Dinesh Jagadeesan (to be submitted)

About the Author

Dnyanesh Vinayak Vernekar was born on 10th August 1990 at Ankola in Uttara Kannada district of Karnataka, India. He completed his Bachelors in Chemistry (Honours) from Sri Sathya Sai Institute of Higher Learning, Brindavan Campus Bangalore (2008-2011). He went on to pursue Masters in Chemistry (2011-2013) from Sri Sathya Sai Institute of Higher Learning, Prashanthi Nilayam Campus and was awarded the Gold medal for topping the course. He then joined as a Project Assistant (2013-2015) at CSIR-National Chemical Laboratory, Pune under Dr Dinesh Jagadeesan. Having secured the DST-INSPIRE fellowship for PhD, he registered for his doctorate degree in January 2015 with AcSIR under the supervision of Dr. Chandrashekhar Rode, Chief Scientist in Chemical Engineering and Process Development Division, CSIR-NCL, Pune and co-supervision of Dr Dinesh Jagadeesan, Assistant Professor, IIT-Palakkad. His work mainly focuses on design and development of metal oxyhydroxide based catalyst systems for organic multistep reactions, which have been presented in this thesis.

10%

SIMILARITY INDEX

PRIMARY SOURCES

- 1** R. M. Cornell, U. Schwertmann. "The Iron Oxides", Wiley, 2003 176 words — 9%
Crossref
 - 2** Yanning Cao, Xiaoli Hu, Xubin Lin, Yan Lin, Ronghai Huang, Lilong Jiang, Kemei Wei. "Low-Temperature Desulfurization on Iron Oxide Hydroxides: Influence of Precipitation pH on Structure and Performance", Industrial & Engineering Chemistry Research, 2015 13 words — 1%
Crossref
-

EXCLUDE QUOTES ON

EXCLUDE MATCHES OFF

EXCLUDE BIBLIOGRAPHY ON



CrossMark
click for updates

Cite this: *Catal. Sci. Technol.*, 2015, 5, 4029

Tunable acid–base bifunctional catalytic activity of FeOOH in an orthogonal tandem reaction†

D. Vernekar and D. Jagadeesan*

In this report, we have explored the acid–base bifunctional catalytic activity of iron oxohydroxides (FeOOH) by catalyzing deacetalization and Henry condensation reactions successively in a single pot. The crystalline polymorphs of FeOOH, namely goethite (α FeOOH), akaganéite (β FeOOH), lepidocrocite (γ FeOOH) and δ FeOOH, were chemically prepared and tested for the catalytic activity. All the polymorphs of FeOOH exhibited acid–base bifunctional catalytic activity. The relative selectivity for products varied with the polymorphs of FeOOH. Whereas α FeOOH produced benzaldehyde in high yield, the polymorphs β FeOOH, γ FeOOH and δ FeOOH showed high selectivity for *trans*- β -nitrostyrene. In addition, β FeOOH also exhibited a unique activity towards the formation of 1,3-dinitro-2-phenylpropane. The difference in the catalytic activity of FeOOH polymorphs was explained based on the strength and density of acidic and basic active sites on the surface. Selectivity for the products was tuned by changing the synthesis parameters of the catalysts and reaction conditions.

Received 11th March 2015,
Accepted 26th May 2015

DOI: 10.1039/c5cy00361j

www.rsc.org/catalysis

Biosynthetic pathways in living organisms are excellent examples for tandem catalysis. A substrate is acted upon by enzymes in a sequential manner thereby efficiently pushing the chemical equilibrium towards products in high selectivity.^{1,2} In the last decade, several attempts have been made to mimic nature's strategy on heterogeneous catalyst systems to develop multi-functional catalysts for orthogonal tandem reactions.^{2,3} Multifunctional catalysts that are capable of carrying out orthogonal tandem reactions are important to the pharmaceutical industry in which significant savings on cost, energy and time can be achieved. From the materials perspective, a multifunctional catalyst must bear suitable active sites for each step of the tandem reaction. The active sites must be so positioned on the catalyst surface that they do not compromise their functions but act independently and sometimes cooperatively leading to a unique activity. Recently, nanostructured materials containing spatially isolated acidic and basic sites were found to be efficient as bifunctional catalysts for one-pot tandem reactions involving hydrolysis and condensation steps. The bifunctional nano-materials were obtained by selectively functionalizing the outer and inner walls of hollow silica nanoparticles with acidic ($-\text{SO}_3\text{H}$ groups grafted on silica or $-\text{Si}-\text{OH}$ groups) or basic (covalently anchored $-\text{NH}_2$) sites in a spatially separated

manner.^{4–6} Selectivity for products was tuned by controlling the chemical nature of acidic and basic sites and their location.^{4–8} Distribution, stability and activity of the active sites were highly dependent on the method of synthesis such as co-condensation or post-synthesis grafting. However, the major drawbacks of this method were the laborious steps of preparation and the use of toxic alkoxide reagents. Recently, acid–base bifunctional catalytic activity has been reported in organic–inorganic hybrid zeolites.^{9,10} These catalysts exhibited acidic properties due to Al^{3+} sites in zeolites and basic properties due to the uncalcined organic structure directing agents. Besides the surface functionalized silica and hybrid zeolites, the literature of bifunctional catalysts for tandem reactions is limited. This presents interesting challenges in materials chemistry to develop new materials with robust and efficient bifunctional active sites without spatially isolating acidic and basic groups on a surface. A number of acid–base equilibrium within a single species is well known in chemistry and a careful use of these systems can create bifunctional catalysts. The acidic and basic sites in such catalysts may be randomly distributed but will be useful as they are simple to produce without involving multiple steps of surface functionalization. It is our opinion that inorganic metastable phases such as metal oxohydroxides are ideal as robust, inexpensive and easily scalable acid–base bifunctional catalysts. These materials, which are usually prepared by hydrolytic sol–gel methods, can be considered as intermediates between hydroxylated metal sol precursors and completely condensed dense oxide phases. Iron oxohydroxides (FeOOH) are interesting candidates for bifunctional catalytic applications because

Physical and Materials Chemistry Division, CSIR National Chemical Laboratory, Dr. Homi Bhabha Road, Pune – 411 008, India. E-mail: d.jagadeesan@ncl.res.in; Fax: +91 020 25902636; Tel: +91 020 2590 3046

† Electronic supplementary information (ESI) available. See DOI: 10.1039/c5cy00361j



Water-promoted surface basicity in FeO(OH) for the synthesis of pseudoionones (PS) and their analogues

Dnyanesh Vernekar^{a,b}, Sachin S. Sakate^{a,c}, Chandrashekhar V. Rode^{a,b,*}, Dinesh Jagadeesan^{d,*}

^a Chemical Engineering and Process Development Division, CSIR-National Chemical Laboratory, Pashan, Pune 411008, India

^b Academy of Scientific and Innovative Research (ACSIR), Ghaziabad 201002, India

^c P. E. Society's Modern College of Arts, Science and Commerce (Autonomous), Shivajinagar, Pune 411005, India

^d Department of Chemistry, Indian Institute of Technology Palakkad, Palakkad 678 557, Kerala, India

ARTICLE INFO

Article history:

Received 8 March 2019
Revised 17 August 2019
Accepted 19 August 2019

Keywords:

Pseudoionones
Iron (III) oxyhydroxide
Knoevenagel condensation
Brønsted basicity
Surface hydroxyl groups

ABSTRACT

Use of Iron oxyhydroxide (γ -FeO(OH)) as a robust catalyst for the synthesis of important intermediates like pseudoionones and their analogues through the C-C bond formation reactions like Knoevenagel and aldol condensation is explored. These motifs are the building blocks for the construction of the sesquiterpenes as well as the diterpenes such as retinoic acid, Vitamin A etc. Iron oxyhydroxide (γ -FeO(OH)) was synthesized and well characterized using XRD, FT-IR, TEM, XPS and adsorption studies to establish the catalytic activity. A thorough investigation on the nature of basic sites and the role of water as a promoter was explored based on dye adsorption, *in situ* methanol dissociation and CO₂ adsorption studies. The catalyst also showed a wide range of substrate scope with active methylene groups involving various functional groups such as cyanides, esters and acetophenones along with its stability and reproducibility.

© 2019 Elsevier Inc. All rights reserved.

1. Introduction

Pseudoionones (PS) are special monoterpenoids used in the synthesis of industrially important chemical intermediates such as α -, β - and γ -ionones [1]. PS are synthesized in large scale by aldol condensation between citral and acetone in the presence of a base (Scheme 1) [2]. The product yields vary between 50 and 80% depending upon the reaction conditions and the catalysts used. Heterogeneous base catalysts such as alkaline metal oxides [3], basic zeolites [4], and Mg-Al hydrotalcites [5] are preferred over homogeneous bases due to non-toxicity, non-corrosion, minimal waste and recyclability. Recently, LiOH·H₂O [6], aluminophosphates (ALPO) [7], anionic clays [8], choline hydroxide/MgO [9], KF·Al₂O₃ [10] and Mg-Al mixed oxides containing rare earth elements [11] have been shown to catalyze the synthesis of PS. Among various catalysts, hydrotalcites are quite interesting as the studies on the reconstructed hydrotalcites (Mg₆Al₂(OH)₁₈·4H₂O) showed that a combination of O²⁻ (Lewis basic) and intercalated OH⁻ anions (Brønsted base) provide a high activity [12]. The presence of charge-compensating Brønsted base (OH⁻ ions) in the Mg-Al hydrotalcite matrix was shown to increase the selectivity of PS

from 60% to >90% as compared to the catalysts with just O²⁻ sites. Unfortunately, these intercalated OH⁻ ions have a tendency to leach away into the solvent due to their non-covalent bonding, leading to a severe loss in the activity. Taking a cue from this work, we wanted to explore the use of Iron oxyhydroxides FeO(OH) as a catalyst for the synthesis of PS. FeO(OH) are metastable intermediates during the synthesis of iron oxides from its hydroxide gel precursors. It naturally contains abundant concentration of potential Brønsted basic sites such as —O⁻ and Lewis basic sites such as O²⁻ in the crystal structure (Scheme 2a). [13] Most importantly, the basic sites (O⁻ & O²⁻) are chemically bonded to the metal and occur in close proximity to O²⁻ sites of FeO(OH) crystal. The structure is therefore suitable for a high and stable activity in the synthesis of PS [14]. For the first time, we report the use of FeO(OH) as stable and highly active catalyst for the synthesis of PS. In addition to that, we also provide an overwhelming evidence that H₂O promotes the catalytic activity of FeO(OH).

2. Experimental section

2.1. Materials & methods

Ferrous chloride (FeCl₂·4H₂O) and Sodium hydroxide (NaOH) were purchased from Thomas-Baker. Citral and other active methylene substrates were obtained from Sigma-Aldrich.

* Corresponding authors.

E-mail addresses: cv.rode@ncl.res.in (C.V. Rode), d.jagadeesan@itpkd.ac.in (D. Jagadeesan).

<https://doi.org/10.1016/j.jcat.2019.08.026>

0021-9517/© 2019 Elsevier Inc. All rights reserved.

Cite this: *Catal. Sci. Technol.*, 2019,
9, 1154

Efficient bifunctional reactivity of K-doped CrO(OH) nanosheets: exploiting the combined role of Cr(III) and surface –OH groups in tandem catalysis†

Dnyanesh Vernekar,^{ab} Satyajit Ratha,^c
Chandrashekhar Rode^{ab} and Dinesh Jagadeesan^{id}*^d

This work reports the bifunctional catalytic activity of layered K-doped α -CrO(OH). The combined action of the redox active Cr(III) and the surface hydroxyl groups was efficiently used to carry out 2–3 oxidation reactions in tandem followed by condensation/coupling reactions in one pot. Oxidation of benzyl alcohol followed by Knoevenagel condensation or coupling reactions forming C–C and C–N linkages in one pot is demonstrated. The catalyst has been characterized using XRD, IR, TGA, CO₂-TPD, cyclic voltammetry, XPS and microscopic techniques to gain insight into the nature of active sites. The role of O[–] and O^{2–} on the CrO(OH) catalyst in the bifunctional activity was studied using analytical techniques. Recyclability and leaching tests confirmed that K- α -CrO(OH) is a stable and environmentally safe catalyst.

Received 15th November 2018,
Accepted 11th January 2019

DOI: 10.1039/c8cy02345j

rsc.li/catalysis

Introduction

Synthesis of complex organic molecules is usually carried out over several steps of functional group transformations. Reaction sequences in such synthesis strategies often involve separation and purification of intermediate products and change of catalysts.¹ It is exciting to think of a possibility to carry out the full sequence of synthesis in a single pot so that the yield of the target molecule and the environmental benevolence of the reaction are enhanced.^{2,3} One of the strategies to achieve this may require carrying out all the catalyzed steps of a reaction sequence in a single pot by introducing a common heterogeneous catalyst.⁴ For example, a reaction sequence requiring a combination of two or more active sites such as an acid, a base, or a reduction or an oxidation site (for reaction steps like hydrolysis, condensation or oxidation) may be carried out in tandem in a single pot in the presence of a single catalyst possessing all such required sites on its surface. One

can envisage that such bifunctional catalysts capable of catalyzing a sequence of oxidation and condensation/coupling reactions in tandem shall be useful in efficiently synthesizing biologically active molecules such as chalcones, benzylidene malononitriles, and imines.^{5–7}

The synthesis and applications of multifunctional heterogeneous catalysts are of contemporary interest with promising outcomes.⁸ Literature pertaining to the catalysis of sequential oxidation–condensation reactions revealed that the majority of the catalysts employed expensive noble metals and a base.^{9,10} In fact, one could classify the heterogeneous catalysts for the sequential oxidation–coupling organic transformations into two major types. The first type of catalysts are predominantly noble metals on inert oxides such as Ag–Al₂O₃,¹¹ Pd/AlOOH,¹² Pd–Si–Pr–NiXantphos/SiO₂,¹³ and Pt–Sn/C–Al₂O₃.¹⁴ These catalysts employ external bases such as K₃PO₄, LiOH, and Cs₂CO₃ to complete the reaction. The second type of catalysts are noble metals on basic oxides or supports with basic functional groups such as amines, e.g. Au@Cu(II)-MOF,¹⁵ Pd(0)@UiO-68-AP,¹⁶ Au–Pd/HT,¹⁷ Cu_xAg_{1–x}/HT,¹⁸ and Pd–Au@Mn(II)-MOF.¹⁹ Examples of non-noble metal based bifunctional catalysts without using an external base are rare. Notable ones are Co on N-doped carbon,²⁰ Tris-LDH-X₄(PW₉)₂ (ref. 21) and CeO₂.^{22,23}

Our group reported that –OH and –O[–] groups on the surface of iron oxyhydroxides could catalyze organic transformation requiring sequential acid and base catalyzed steps in a single pot.²⁴ Importantly, we also showed that oxyhydroxides are much simpler acid–base bifunctional catalysts as they do

^a Chemical Engineering and Process Development Division, CSIR-National Chemical Laboratory, Pune-411008, India

^b Academy of Scientific and Innovative Research (ACSIR), Ghaziabad-201002, India

^c School of Basic Sciences, Indian Institute of Technology, Bhubaneswar, Odisha, 751013, India

^d Indian Institute of Technology Palakkad, Kozhippara P.O., Palakkad – 678 557, India. E-mail: d.jagadeesan@iitpkd.ac.in

† Electronic supplementary information (ESI) available. See DOI: 10.1039/c8cy02345j

Review Article**New Opportunities in Heterogeneous Catalysis**DINESH JAGADEESAN^{1,*}, DNYANESH VERNEKAR², SHARAD GUPTA³ and GARIMA JAISWAL⁴¹*Department of Chemistry, Indian Institute of Technology Palakkad, Kozhippara, Palakkad 678 557, Kerala, India*²*Chemical Engineering and Process Development Division, CSIR-National Chemical Laboratory, Pashan, Pune 411 008, Maharashtra, India**Academy of Scientific and Innovation Research (ACSIR), Ghaziabad 201 002, India*³*Inorganic Chemistry and Catalysis Division, CSIR-National Chemical Laboratory, Pashan, Pune 411 008, Maharashtra, India**Academy of Scientific and Innovation Research (ACSIR), Ghaziabad 201 002, India*⁴*Organic Chemistry Division, CSIR-National Chemical Laboratory, Pashan, Pune 411 008, Maharashtra, India**Academy of Scientific and Innovation Research (ACSIR), Ghaziabad 201 002, India*

(Received on 02 May 2018; Revised on 10 July 2018; Accepted on 11 August 2018)

Nearly 80% of the processes involved in the chemical production of bulk or fine chemicals employ heterogeneous catalysts that are typically solids. The heart of the heterogeneous catalyst is the surface active site which must be highly active, selective and stable during several hundred cycles of reaction. Although it is not always possible to determine the structure of an active site in a heterogeneous catalyst, the emphasis of modern day research has not only been to understand the structure of an active site but also synthesize and study them. The article will describe some of the challenges from this perspective with examples from the authors research.

Keywords: Heterogeneous Catalysis; Multifunctional Catalysts; Hydrogenation; Dehydrogenation**Introduction**

Catalysts are defined as chemical substances that transform reactants to products through uninterrupted and repeated cycles of elementary steps in which the catalyst is regenerated to its original form by the end of a cycle. Catalysts bind with reactants in a specific manner and cause an accelerated rate of transformation to products by lowering the activation energy. Heterogeneous catalysis involves studies of catalysts that are in a physical phase different from that of reactants and products. Typically, heterogeneous catalysts are solids, while the reactants and products are liquids or gases or a mixture of both. Heterogeneous catalyst science and technology is a matured branch in chemistry with several pivotal contributions to major economic transformations in

the human history. For example, iron oxide catalyst promoted with K_2O , CaO , SiO_2 or Al_2O_3 was used to produce fertilizers by converting N_2 to NH_3 . This reaction helped quadruple the productivity of agricultural lands which was desperately needed during the world war (Jacobsen *et al.*, 2001). Another important example is the refining of crude oil by hydrocracking, hydrodesulfurization, hydrodenitrogenation, hydrodechlorination over Mo based catalysts and zeolite catalysts to produce useful distillates. This reaction was responsible for the large scale production of fuel grade gasoline and diesel in addition to several low molecular weight hydrocarbons and aromatic compounds useful in chemical industry (Matar *et al.*, 1998). Besides large scale production of fuels and chemicals, heterogeneous catalysts are also extensively used in automobiles in catalytic converters

*Author for Correspondence: E-mail: d.jagadeesan@iitpkd.ac.in

Earth Abundant Iron-Rich N-Doped Graphene Based Spacer and Cavity Materials for Surface Plasmon-Coupled Emission Enhancements

Venkatesh Srinivasan,[†] Dnyanesh Vernekar,[‡] Garima Jaiswal,[#] Dinesh Jagadeesan,^{*,[†]} and Sai Sathish Ramamurthy^{*,[†]}

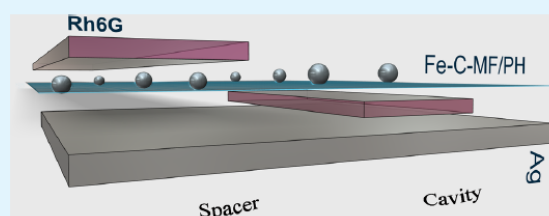
[†]Plasmonics Laboratory, Department of Chemistry, Sri Sathya Sai Institute of Higher Learning, Prasanthi Nilayam Campus, Anantapur, Andhra Pradesh, India 515134

[‡]Chemical Engineering and Process Development Division, [#]Catalysis Division, and [†]Physical and Materials Chemistry Division, CSIR – National Chemical Laboratory, Pune, Maharashtra, India 411008

Supporting Information

ABSTRACT: We demonstrate for the first time the use of Fe-based nanoparticles on N-doped graphene as spacer and cavity materials and study their plasmonic effect on the spontaneous emission of a radiating dipole. Fe–C–MF was produced by pyrolyzing FeOOH and melamine formaldehyde precursor on graphene, while Fe–C–PH was produced by pyrolyzing the Fe-phenanthroline complex on graphene. The use of the Fe–C–MF composite consisting of Fe-rich crystalline phases supported on N-doped graphene presented a spacer material with 116-fold fluorescence enhancements. On the other hand, the Fe–C–PH/Ag based cavity resulted in an 82-fold enhancement in Surface Plasmon-Coupled Emission (SPCE), with high directionality and polarization of Rhodamine 6G (Rh6G) emission owing to Casimir and Purcell effects. The use of a mobile phone as a cost-effective fluorescence detection device in the present work opens up a flexible perspective for the study of different nanomaterials as tunable substrates in cavity mode and spacer applications.

KEYWORDS: surface plasmon-coupled emission, fluorescence enhancements, Casimir effect, Purcell factor, iron carbides, N-doped graphene



INTRODUCTION

Two-dimensional electron systems have recently drawn great research interest.¹ Graphene and its nanocomposites in particular have been extensively used in numerous photonics and electronic applications owing to their intrinsic 2D plasmons.^{2–4} The intrinsic graphene plasmons are unique and different from that of metallic nanoparticles.⁵ Grigorenko et al. explain that in order to trail the incident electric field, the π -electrons in graphene move outward and are dragged back due to disturbance of charge and overshoot again, leading to an oscillation of the electron cloud.⁶ In addition to this, it is also known that the plasmon losses in graphene are lesser than that in metallic nanoparticles. The electronic oscillations on metal thin films - surface plasmons, on the other hand, have also been exploited widely for plasmonic applications.⁷ SPCE phenomenon in this context makes use of the fluorescence of a radiating dipole situated near a metal thin film, to couple with the surface plasmons, resulting in a polarized, directional, and enhanced emission.⁸ In addition to the fluorophore–metal thin film interaction, low-dimensional carbon materials with a delocalized π -electron cloud have also been known to couple with the fluorescent molecules such as Rhodamine 6G.⁹ Graphene and fullerene have previously been reported as spacers in plasmon-

coupled emission studies giving 40- and 30-fold enhancements, respectively.^{10,11} Moreover, metal nanoparticles of gold and silver also exhibit substantial fluorescence enhancements.¹² In our earlier work, we have demonstrated the use of single layered graphene, carbon nanotubes, and fullerenes (C_{60} and C_{70}) as spacers that help in the coupling of fluorescence with the surface plasmons.¹³

In the current study, we utilize the unique plasmonic properties of magnetic nanocomposites of doped graphene to achieve augmented fluorescence emission from a radiating dipole. So far a judicious combination of earth-abundant ceramic nanomaterials with cost-effective transition metals and π -conjugated materials as cavity materials and spacers in plasmon-coupled emission studies has not been reported. In this context, we have investigated the use of nanocomposites containing particles of iron carbides, oxides, and nitrides on N-doped graphene (Fe–C) as a hybrid spacer material for SPCE substrates. We report the preparation of an iron carbide-graphene nanocomposite (Fe–C) type of materials by

Received: December 10, 2015

Accepted: April 29, 2016

Published: April 29, 2016

Iron-carbon nanohybrid particles as environmentally benign electrode for supercapacitor

Satyajit Ratha¹ · Dnyanesh Vernekar² · Kavin Sivaneri³ · Dinesh Jagadeesan³ · Chandra Sekhar Rout¹

Received: 11 October 2016 / Revised: 17 January 2017 / Accepted: 8 February 2017 / Published online: 21 February 2017
© Springer-Verlag Berlin Heidelberg 2017

Abstract In this work, we report the synthesis and electrode applications of iron-carbon nanohybrid particles prepared by carbonization of a nanocomposite of FeOOH nanoneedles and melamine-formaldehyde resin. The chemical composition and microstructure of the material have been characterized using ICP-AES, FT-IR, XRD, FESEM, TEM and XPS. The supercapacitor properties of the MF-Fe-C are studied in detail. A thorough comparison of the supercapacitor performances of MF-Fe-C and bare MF-C has been carried out through detailed electrochemical characterisations employing both two and three-electrode techniques. The nanohybrid showed an enhanced energy density of 127.75 WhKg⁻¹, specific capacitance of ~408 F g⁻¹ at 1 mVs⁻¹ scan rate, and excellent cyclic stability even after 1000 charge-discharge cycles, making it an intriguing material for high energy density supercapacitor devices.

Keywords Electrochemistry · Nanohybrid · Supercapacitor · Energy density

Electronic supplementary material The online version of this article (doi:10.1007/s10008-017-3537-z) contains supplementary material, which is available to authorized users.

✉ Dinesh Jagadeesan
d.jagadeesan@ncl.res.in

✉ Chandra Sekhar Rout
csrout@iitbbs.ac.in

¹ School of Basic Sciences, Indian Institute of Technology – Bhubaneswar, Bhubaneswar, Odisha 751 013, India

² Chemical Engineering and Process Development Division, CSIR – National Chemical Laboratory, Pune, Maharashtra 411 008, India

³ Physical and Materials Chemistry Division, CSIR – National Chemical Laboratory, Pune, Maharashtra 411 008, India

Introduction

Riveting properties such as large specific surface area, better transportation of electrons, and electric double layer capacitance in terms of charge separation at the electrode-electrolyte interface are some of the fundamental factors for the indispensable use of graphitic carbon in electrodes for energy conversion and storage materials [1–6]. Last decade has seen several efforts to improve the electrochemical properties of carbon-based materials by doping heteroatoms (e.g., N, O, B, P, S) [7–13] in the carbon matrix with an aim to alter the electron density over neighboring carbon atoms. Among the dopants, the effect of nitrogen is widely studied because of its atomic size equivalent to carbon and ease of incorporation on to the carbon matrix or the edge as functional group. In addition, energy and power densities of carbon materials were increased by taking advantage of pseudocapacitance of transition metal oxide nanocomposites such as NiO, Mn₃O₄, Bi₂O₃, Co₃O₄, TiO₂, and Fe₃O₄, which can essentially multiply capacitance values due to the fast faradic reactions resulting from multielectron transfer [14–18]. Great number of physical and chemical approaches have been studied for adjusting the nitrogen content for altering the electrochemical properties using techniques such as ammonia treatment, chemical vapor deposition, and others [19, 20]. Although there have been a number of reports discussing electrode applications of N-doped carbon or metal oxides, literature on the synthesis and electrochemical properties N-doped carbon/metal oxide is limited [21]. In this report, we demonstrate the electrode application of an iron-carbon nanohybrid material in supercapacitor. We believe doping of nitrogen in carbon accompanied by decoration of inorganic metal oxide nanoparticles with active storage functional sites were achieved efficiently by carbonizing suitable precursors. Importantly, the material is inexpensive and composed of earth-abundant